ACOUSTIC TRANSDUCTION – MATERIALS AND DEVICES

Period 31 July 1996 to 31 December 1997

Annual Report

VOLUME VII

OFFICE OF NAVAL RESEARCH
Contract No: N00014-96-1-1173

Kenji Uchino

PENNSTATE

1855

THE MATERIALS RESEARCH LABORATORY
UNIVERSITY PARK, PA

19980910 007

REPORT DOCUMENTATION PAGE

Public reporting burden for this collection of information is estimated to average 1 hour per response, including the time for reviewing instructions, searching existing data sources, gathering and maintaining the data needed, and completing and reviewing the collection of information. Send comments regarding this burden estimate or any other aspect of this collection of information, including suggestions for reducing this burden, to Washington Headquarters Services, Directorate for Information Operations and Reports, 1215 Jefferson Davis Highway, Suite 1204, Arlington, VA 22202-4302, and to the Office of Management and Budget, Paperwork Reduction Project (0704-0188), Washington, DC 20503.

1. AGENCY USE ONLY (Leave blank)	2. REPORT DATE 05/01/98	3. REPORT TYPE AND DATES COVERED ANNUAL REPORT 07/31/96-12/31/97

4. TITLE AND SUBTITLE

ACOUSTIC TRANSDUCTION -- MATERIALS AND DEVICES

5. FUNDING NUMBERS
ONR CONTRACT NO:
N00014-96-1-1173

6. AUTHOR(S)

KENJI UCHINO

7. PERFORMING ORGANIZATION NAME(S) AND ADDRESS(ES)

Materials Research Laboratory
The Pennsylvania State University
University Park, PA 16802

8. PERFORMING ORGANIZATION REPORT NUMBER

9. SPONSORING/MONITORING AGENCY NAME(S) AND ADDRESS(ES)

Office of Naval Research
ONR 321SS
Ballston Centre Tower One
800 N Quincy Street
Arlington, VA 22217-5660

Office of Naval Research
Regional Office Chicago
536 S Clark Str., Rm 208
Chicago IL 60605-1588

10. SPONSORING/MONITORING AGENCY REPORT NUMBER

11. SUPPLEMENTARY NOTES

12a. DISTRIBUTION/AVAILABILITY STATEMENT

12b. DISTRIBUTION CODE

13. ABSTRACT (Maximum 200 words)

SEE FOLLOW PAGE

14. SUBJECT TERMS

15. NUMBER OF PAGES

16. PRICE CODE

17. SECURITY CLASSIFICATION OF REPORT	18. SECURITY CLASSIFICATION OF THIS PAGE	19. SECURITY CLASSIFICATION OF ABSTRACT	20. LIMITATION OF ABSTRACT

NSN 7540-01-280-5500

GENERAL INSTRUCTIONS FOR COMPLETING SF 298

The Report Documentation Page (RDP) is used in announcing and cataloging reports. It is important that this information be consistent with the rest of the report, particularly the cover and title page. Instructions for filling in each block of the form follow. It is important to *stay within the lines* to meet *optical scanning requirements*.

Block 1. Agency Use Only (Leave blank).

Block 2. Report Date. Full publication date including day, month, and year, if available (e.g. 1 Jan 88). Must cite at least the year.

Block 3. Type of Report and Dates Covered. State whether report is interim, final, etc. If applicable, enter inclusive report dates (e.g. 10 Jun 87 - 30 Jun 88).

Block 4. Title and Subtitle. A title is taken from the part of the report that provides the most meaningful and complete information. When a report is prepared in more than one volume, repeat the primary title, add volume number, and include subtitle for the specific volume. On classified documents enter the title classification in parentheses.

Block 5. Funding Numbers. To include contract and grant numbers; may include program element number(s), project number(s), task number(s), and work unit number(s). Use the following labels:

C	-	Contract	PR	- Project
G	-	Grant	TA	- Task
PE	-	Program Element	WU	- Work Unit Accession No.

Block 6. Author(s). Name(s) of person(s) responsible for writing the report, performing the research, or credited with the content of the report. If editor or compiler, this should follow the name(s).

Block 7. Performing Organization Name(s) and Address(es). Self-explanatory

Block 8. Performing Organization Report Number. Enter the unique alphanumeric report number(s) assigned by the organization performing the report.

Block 9. Sponsoring/Monitoring Agency Name(s) and Address(es). Self-explanatory.

Block 10. Sponsoring/Monitoring Agency Report Number. (If known)

Block 11. Supplementary Notes. Enter information not included elsewhere such as: Prepared in cooperation with...; Trans. of...; To be published in.... When a report is revised, include a statement whether the new report supersedes or supplements the older report.

Block 12a. Distribution/Availability Statement. Denotes public availability or limitations. Cite any availability to the public. Enter additional limitations or special markings in all capitals (e.g. NOFORN, REL, ITAR).

DOD - See DoDD 5230.24, "Distribution Statements on Technical Documents."
DOE - See authorities.
NASA - See Handbook NHB 2200.2.
NTIS - Leave blank.

Block 12b. Distribution Code.

DOD - Leave blank.
DOE - Enter DOE distribution categories from the Standard Distribution for Unclassified Scientific and Technical Reports.
NASA - Leave blank.
NTIS - Leave blank.

Block 13. Abstract. Include a brief (*Maximum 200 words*) factual summary of the most significant information contained in the report.

Block 14. Subject Terms. Keywords or phrases identifying major subjects in the report.

Block 15. Number of Pages. Enter the total number of pages.

Block 16. Price Code. Enter appropriate price code (*NTIS only*)

Blocks 17. - 19. Security Classifications. Self-explanatory. Enter U.S. Security Classification in accordance with U.S. Security Regulations (i.e., UNCLASSIFIED). If form contains classified information, stamp classification on the top and bottom of the page.

Block 20. Limitation of Abstract. This block must be completed to assign a limitation to the abstract. Enter either UL (unlimited) or SAR (same as report). An entry in this block is necessary if the abstract is to be limited. If blank, the abstract is assumed to be unlimited.

ABSTRACT

The report documents work carried out over the period 31 July 1996 to 31 December 1997 on a Multi-University Research Initiative (MURI) program under Office of Naval Research (ONR) sponsorship. The program couples transducer materials research in the Materials Research Laboratory (MRL), design and testing studies in the Applied Research Laboratory (ARL) and vibration and flow noise control in the Center for Acoustics and Vibration (CAV) at Penn State.

The overarching project objective is the development of acoustic transduction materials and devices of direct relevance to Navy needs and with application in commercial products. The initial focus of studies is upon high performance sensors and high authority high strain actuators. This objective also carries the need for new materials, new device designs, improved drive and control strategies and a continuing emphasis upon reliability under a wide range of operating conditions.

In *Material Studies*, undoubtedly major breakthroughs have occurred in the ultra-high strain relaxor ferroelectric systems. Earlier reports of unusual piezoelectric activity in single crystal perovskite relaxors have been amply confirmed in the lead zinc niobate : lead titanate, and lead magnesium niobate : lead titanate systems for compositions of rhombohedral symmetry close to the Morphotropic Phase Boundary (MPB) in these solid solutions. Analysis of the unique properties of 001 field poled rhombohedral ferroelectric crystals suggests new intrinsic mechanisms for high strain and carries the first hints of how to move from lead based compositions. A major discovery of comparable importance is a new mode of processing to convert PVDF:TrFE copolymer piezoelectric into a relaxor ferroelectric in which electrostrictive strains of 4% have been demonstrated at high fields. Both single crystal and polymer relaxors appear to offer energy densities almost order of magnitude larger than in earlier polycrystal ceramic actuators.

Transducer Studies have continued to exploit the excellent sensitivity and remarkable versatility of the cymbal type flextensional element. Initial studies of a small cymbal arrays show excellent promise in both send and receive modes, and larger arrays are now under construction for tests at ARL. New studies in constrained layer vibration damping and in flow noise reduction are yielding exciting new results.

In *Actuator Studies*, an important advance in piezoelectric generated noise control now permits wider use of acoustic emission as a reliability diagnostic technique. Joint studies with NRL, Washington have developed a completely new d_{15} driven torsional actuator and the CAV program element has designed an exciting high strain high force inchworm.

Finite element analysis continues to be an important tool for understanding the more complex composite structures and their beam forming capability in water. *Thin and Thick Thin Film Studies* are gearing up to provide the material base for micro-tonpilz arrays. New exploitation of ultra sensitive strain and permittivity measurements is providing the first reliable data of electrostriction in simple solids, and suggesting new modes for separating the polarizability contributors in dielectrics and electrostrictors.

APPENDICES

VOLUME I

GENERAL SUMMARY PAPERS

1. Ito, Y. and K. Uchino, Wiley Encyclopedia of Electrical and Electronics Engineering, J. G. Webster, Edit., (Partial Charge "Piezoelectricity"), John Wiley & Sons (1998). [in press].
2. Newnham, R.E., "Molecular Mechanisms in Smart Materials," MRS Bulletin (May 1997).
3. Swartz, S.L., T.R. Shrout, and T. Takenaka, "Electronic Ceramics R&D in the U.S., Japan, Part I: Patent History," The American Ceramic Society Bulletin **76** (8) (1997).

2.0 MATERIALS STUDIES

2.1 *Polycrystal Perovskite Ceramics*

4. Alberta, E.F., and A.S. Bhalla, "Piezoelectric Properties of $Pb(InNb)_{1/2}O_3$-$PbTiO_3$ Solid Solution Ceramics," J. Korean Phys. Soc. **32**, S1265-S1267 (February 1998).
5. Alberta, E.F. and A.S. Bhalla, "High Strain and Low Mechanical Quality Factor Piezoelectric $Pb[Sc_{1/2}Nb_{1/2})_{0.575}Ti_{0.425}]O_3$ Ceramics" (1997).
6. Zhang, Q.M. and J. Zhao, "Polarization Responses in Lead Magnesium Niobate Based Relaxor Ferroelectrics," Appl. Phys. Lett. **71** (12, 1649-1651 (1997).
7. Glazounov, A.E., J. Zhao, and Q.M. Zhang, "Effect of Nanopolar Regions on Electrostrictive Coefficients of a Relaxor Ferroelectric," Proceedings Williamsburg Meeting, Williamsburg, Virginia (1998).
8. Zhao, J. A.E. Glazounov, Q.M. Zhang, and B. Toby, "Neutron Diffraction Study of Electrostrictive Coefficients of Prototype Cubic Phase of Relaxor Ferroelectric $PbMg_{1/3}Nb_{2/3}O_3$," Appl. Phys. Lett. **72** (9), 1-3 (1998).
9. Park, S.-E., T.R. Shrout, P. Bridenbaugh, J. Rottenberg, and G.M. Loiacono, "Electric Field Induced Anisotropy in Electrostrictive $Pb(Mg_{1/3}Nb_{2/3})O_3$ - $PbTiO_3$ Crystals," Ferroelectrics (1997).
10. You, H. and Q.M. Zhang, "Diffuse X-Ray Scattering Study of Lead Magnesium Niobate Single Crystals," Phys. Rev. Lett. **79** (20), 3950-3953 (1997).
11. Zhao, J., V. Mueller, and Q.M. Zhang, "The Influence of the External Stress on the Electromechanical Response of Electrostrictive $0.9Pb(Mg_{1/3}Nb_{2/3})O_3$–$0.1PbTiO_3$ in the DC Electrical Field Biased State," J. Mat. Res. (1998).

VOLUME II

12. Yoon, S.-J., A. Joshi, and K. Uchino, "Effect of Additives on the Electromechanical Properties of $Pb(Zr,Ti)O_3$–$Pb(Y_{2/3}W_{1/3})O_3$ Ceramics," J. Am. Ceram. Soc **80** (4), 1035-39 (1997).
13. Hackenberger, W., M.-J. Pan, V. Vedula, P. Pertsch, W. Cao, C. Randall, and T. Shrout, "Effect of Grain Size on Actuator Properties of Piezoelectric Ceramics," Proceedings of the SPIE's 5th International Symposium on Smart Structures and Materials, San Diego, CA (March 1-5, 1998).

THIS PAGE LEFT INTENTIONALLY BLANK

14. Mueller, V. and Q.M. Zhang, "Shear Response of Lead Zirconate Titanate Piezoceramics," J. Appl. Phys. (1998).

15. Park, S.-E., M.-J. Pan, K. Markowski, S. Yoshikawa, and L.E. Cross, "Electric Field Induced Phase Transition of Antiferroelectric Lead Lanthanum Zirconate Titanate Stannate Ceramics," J. Appl. Phys. **82** (4), 1798-1803 (1997).

16. Yoshikawa, S., K. Markowski, S.-E. Park, M.-J. Pan, and L.E. Cross, "Antiferroelectric-to-Ferroelectric Phase Switching Lead Lanthanum Zirconate Stannate Titanate (PLZST) Ceramics)," Proceedings of SPIE's 4th Annual Symposium on Smart Structures and Materials, San Diego, CA (March 3-6, 1997).

17. Pan, M.-J., S.-E. Park, K.A. Markowski, W.S. Hackenberger, S. Yoshikawa, and L.E. Cross, "Electric Field Induced Phase Transition in Lead Lanthanum Stannate Zirconate Titanate (PLSnZT) Antiferroelectrics: Tailoring Properties through Compositional Modification" (1997).

18. Pan, M.-J., P. Pertsch, S. Yoshikawa, T.R. Shrout, and V. Vedula, "Electroactive Actuator Materials: Investigations on Stress and Temperature Characteristics," Proceedings of the SPIE's 5th International Symposium on Smart Structures and Materials, San Diego, CA (March 1-5, 1998).

19. Pan, M.-J. and S. Yoshikawa, "Effect of Grain Size on the Electromechanical Properties of Antiferroelectric-to-Ferroelectric Phase Switching PLSnZT Ceramics" (1997).

2.2 *Relaxor Ferroelectric Single Crystal Systems*

20. Service, R.F., "Shape-Changing Crystals Get Shiftier," Science **275**, 1878 (28 March 1997).

21. Shrout, T.R., S.-E. Park, C.A. Randall, J.P. Shepard, L.B. Hackenberger, "Recent Advances in Piezoelectric Materials" (1997).

22. Park, S.-E. and T.R. Shrout, "Ultrahigh Strain and Piezoelectric Behavior in Relaxor Based Ferroelectric Single Crystals," J. Appl. Phys. **82** (4), 1804-1811 (1997).

23. Park, S.-E. and T. R. Shrout, "Characteristics of Relaxor-Based Piezoelectric Single Crystals for Ultrasonic Transducers," IEEE Transactions, Ferroelectrics, and Frequency Control **44** (5), 1140-1147 (1997).

24. Park, S.-E. and T.R. Shrout, "Relaxor Based Ferroelectric Single Crystals for Electro-Mechanical Actuators," Mat. Res. Innov. **1**, 20-25 (1997).

25. Park, S.-E., M.L. Mulvihill, G. Risch, and T.R. Shrout, "The Effect of Growth Conditions on the Dielectric Properties of $Pb(Zn_{1/3}Nb_{2/3})O_3$ Single Crystals," Jpn. J. Appl. Phys. **36**, 1154-1158 (1997).

26. Mulvihill, M.L., L.E. Cross, W. Cao, and K. Uchino, "Domain-Related Phase Transionlike Behavior in Lead Zinc Niobate Relaxor Ferroelectric Single Crystals," J. Am. Ceram. Soc. **80** (6), 1462-68 (1997).

27. Park, S.-E., P.D. Lopath, K.K. Shung, and T.R. Shrout, "Relaxor-Based Single Crystal materials for Ultrasonic Transducer Applications" (1997).

28. Lopath, P.D., S.-E. Park, K.K. Shung, and T.R. Shrout, "$Pb(Zn_{1/3}Nb_{2/3})O_3/PbTiO_3$ Single Crystal Piezoelectrics for Ultrasonic Transducers" (1997).

29. Lopath, P.D., S-E. Park, K.K. Shung, and T.R. Shrout, "Single Crystal $Pb(Zn_{1/3}Nb_{2/3})O_3/PbTiO_3$ (PZN/PT) in Medical Ultrasonic Transducers" (1997).

2.3 New High Strain Polymer Materials

30. Su. J., Q.M. Zhang, C.H. Kim, R.Y. Ting, and R. Capps, "Effect of Transitional Phenomena on the Electric Field Induced Strain–Electrostrictive Response of a Segmented Polyurethane Elastomer" (1997).
31. Su, J., Q.M. Zhang, and R.Y. Ting, "Space-Charge-Enhanced Electromechanical Response in Thin-Film Polyurethane Elastomers," Appl. Phys. Lett **71** (3), 386-388 (1997).

VOLUME III

32. Su, J., Q.M. Zhang, P.-C. Wang, A.G. MacDiarmid, K.J. Wynne, "Preparation and Characterization of an Electrostrictive Polyurethane Elastomer with Conductive Polymer Electrodes," Polymers for Adv. Tech. (1998).
33. Zhang, Q.M., V. Bharti, and X. Zhao, "Giant Electrostriction and Relaxor Ferroelectric Behavior in Electron Irradiated Poly(vinylidene Fluoride-Trifluoroethylene) Copolymer," Science (1998).

3.0 TRANSDUCER STUDIES

3.1 Cymbal : Moonie : BB Composites

34. Newnham, R.E., "Composite Sensors and Actuators" (1997).
35. Steele, B.CH., R.E. Newnham, and A.G. Evans, "Ceramics, Composites, and Intergrowth," Current Opinion in Solid State & Materials Science **2**, 563-565 (1997).
36. Tressler, J.F. S. Alkoy, and R.E. Newnham, "Piezoelectric Sensors and Sensor Materials" (1997).
37. Tressler, J.F., S. Alko, A. Dogan, and R.E. Newnham, "Functional Composites for Sensors, Actuators, and Transducers" (1997).
38. Dogan, A., K. Uchino, R.E. Newnham, "Composite Piezoelectric Transducer with Truncated Conical Endcaps 'Cymbal'," IEEE Transactions on Ultrasonics, Ferroelectrics, and Frequency Control **44** (3), 597-605 (1997).
39. Dogan, A., J.F. Fernandez, K. Uchino, and R.E. Newnham, "The 'Cymbal' Electromechanical Actuator" (1997).
40. Tressler, J.F., W. Cao, K. Uchino, and R.E. Newnham, "Ceramic-Metal Composite Transducers for Underwater Acoustic Applications" (1997).
41. Tressler, J.F. and R.E. Newnham, "Doubly Resonant Cymbal-Type Transducers," IEEE Transactions on Ultrasonics, Ferroelectrics, and Frequency Control **44** (5), 1175-1177 (1997).
42. Tressler, J.F., W. Cao, K. Uchino, and R.E. Newnham, "Finite Element Analysis of The Cymbal-Type Transducer" (1997).
43. Tressler, J.F., W.J. Hughes, W. Cao, K. Uchino, and R.E. Newnham, "Capped Ceramic Underwater Sound Projector" (1997).

VOLUME IV

44. Alkoy, S., P.D. Lopath, R.E. Newnham, A.-C. Hladky-Hennion, and J.K. Cochran, "Focused Spherical Transducers for Ultrasonic Imaging" (1997).
45. Alkoy, S., A. Dogan, A.-C. Hladky, P. Langlet, J.K. Cochran, and R.E. Newnham, "Miniature Piezoelectric Hollow Sphere Transducers (BBs)" (1997).
46. Zipparo, M.J., K.K. Shung, and T.R. Shrout, "Piezoceramics for High-Frequency (20 to 100 MHz) Single-Element Imaging Transducers," IEEE Transactions on Ultrasonics, Ferroelectrics, and Frequency Control **44** (5), 1038-1048 (1997).

3.2   Frequency Agile Transducers

47. Davis, C. and G.A. Lesieutre, "An Actively-Tuned Solid State Piezoelectric Vibration Absorber" (1997).
48. Davis, C.L., G.A. Lesieutre, and J. Dosch, "A Tunable Electrically Shunted Piezoceramic Vibration Absorber" (1997).
49. Lesieutre, G.A. and U. Lee, "A Finite Element for Beams Having Segmented Active Constrained Layers with Frequency-Dependent Viscoelastic Material Properties" (1997).
50. Hebert, C.A. and G.A. Lesieutre, "Rotocraft Blade Lag Damping Using Highly Distributed Tuned Vibration Absorbers," American Institute of Aeronautics and Astronautics (AIAA 98-2001).
51. Lesieutre, G.A. and C.L. Davis, "Can a Coupling Coefficient of a Piezoelectric Device be Higher than Those of its Active Material?," SPIE 4th Annual Symposium on Smart Structures and Materials, San Diego, CA (March 1997).

3.3   3-D Acoustic Intensity Probes

52. Lauchle, G.C., J.R. MacGillivray, and D.C. Swanson, "Active Control of Axial-flow Fan Noise," J. Acoust. Soc. Am **101** (1), 341-349 (1997).
53. McGuinn, R.S., G.C. Lauchle, and D.C. Swanson, "Low Flow-Noise Microphone for Active Noise Control Applications," AIAA Journal **35** (1), 29-34 (1997).
54. McGuinn, R.S., G.C. Lauchle, and D.C. Swanson, "Low Flow-Noise Pressure Measurements Using a "Hot-Mic," AIAA -97-1665-CP.
55. Capone, D.E., and G.C. Lauchle, "Designing a Virtual Sound-Level Meter in LabVIEW," Education/Acoustics, LabVIEW, National Instruments.

VOLUME V

4.0   ACTUATOR STUDIES

4.1   Materials : Designs : Reliability

56. Uchino, K., "Piezoelectric Actuators" (1997).
57. Uchino, K., "Overview: Materials Issues in Design and Performance of Piezoelectric Actuators," SPIE Mtg. (1997).
58. Uchino, K., "Shape Memory Ceramics," Chapter 8 (1997).

Actuator Studies–continued

59. Aburatani, H., S. Yoshikawa, K. Uchino, and J.W.C. deVries, "A Study of Acoustic Emission in Piezoelectric Multilayer Ceramic Actuator," Jpn. J. Appl. Phys. **37**, 204-209 (1998).
60. Aburatani, H. and K. Uchino, "Acoustic Emission (AE) Measurement in Piezoelectric Ceramics" (1997).
61. Aburatani, H. and K. Uchino, "The Application of Acoustic Emission (AE) Method for Ferroelectric Devices and Materials," 8th US-Japan Seminar (1997).
62. Uchino, K., "Reliability of Ceramic Actuators" (1997).

4.2   Photostrictive Actuators

63. Tonooka, K. P. Poosanaas, and K. Uchino, "Mechanism of the Bulk Photovoltaic Effect in Ferroelectrics," Proceedings of the 5th SPIE Mtg., San Diego, CA (1998).
64. Poosanass, P. A. Dogan, S. Thakoor, and K. Uchino, "Dependence of Photostriction on Sample Thickness and Surface Roughness for PLZT Ceramics," Proceedings of the 1997 IEEE Ultrasonics Symposium, Toronto, Ontario, Canada (October 1997).
65. Poosanaas, P. A. Dogan, A.V. Prasadarao, S. Komarneni, and K. Uchino, "Photostriction of Sol-Gel Processed PLZT Ceramics," J. Electroceramics **1** (1), 105-111 (1997).

VOLUME VI

66. Poosanaas, P., A. Dogan, A.V. Prasadarao, S. Komarneni, and K. Uchino, "Effect of Ceramic Processing Methods on Photostrictive Ceramics," J. Adv. Perf. Mat. (1997).
67. Thakoor, S., P. Poosanaas, J.M. Morookian, A. Yavrovian, L. Lowry, N. Marzwell, J. Nelson, R.R. Neurgaonkar, and K. Uchino, "Optical Microactuation in Piezoceramics" (1997).

4.3   New Torsional Amplifier/Actuators

68. Glazounov, A.E., Q.M. Zhang, and C. Kim, "Piezoelectric Actuator Generating Torsional Displacement from Piezoelectric d_{15} Shear Response," Appl Phys. Lett. (1997).
69. Glazounov, A.E., Q.M. Zhang, and C. Kim, "A New Torsional Actuator Based on Shear Piezoelectric Response," Proceedings of SPIE Smart Materials, San Diego, CA (March 1998).

4.4   High Force Amplifiers and Inchworms

70. Uchino, K., J. Zheng, A. Joshi, S. Yoshikawa, S. Hirose, S. Takahashi, and J.W.C. deVries, "High Power Characterization of Piezoelectric Materials" (1997).
71. Uchino, K., "High Electromechanical Coupling Piezoelectrics - How High Energy Conversion Rate is Possible," Mat. Res. Soc. Symp. Proc. **459**, 3-14 (1997).
72. Park, S.-E., V. Vedula, M.-J. Pan, W.S. Hackenberger, P. Pertsch, and T.R. Shrout, "Relaxor Based Ferroelectric Single Crystals for Electromechanical Actuators," Proceedings of the SPIE's 5th International Symposium on Smart Structures and Materials, San Diego, CA (March 1998).

73. Koopmann, G.H. G.A. Lesieutre, B.R. Dershem, W. Chen, and S. Yoshikawa, "Embeddable Induced Strain Actuators Using Framed 3-3 Piezoceramic Stacks: Modeling and Characterization," Proceedings of the SPIE's 4th Annual International Symposium on Smart Structures and Materials, San Diego, CA (March 1997).

74. Driesch, P.L., G.H. Koopmann, J. Dosch, and H. Iwata, "Development of a Surface Intensity Probe for Active Control Applications," IMECE, Dallas, Texas (November 1997).

75. Galante, T., J. Frank, J. Bernard, W. Chen, G.A. Lesieutre, and G.H. Koopmann, "Design, Modeling, and Performance of a High Force Piezoelectric Inchworm Motor" (1997).

76. Galante, T.P., "Design and Fabrication of a High Authority Linear Piezoceramic Actuator: The PSU H3 Inchworm," Master of Science Thesis, The Pennsylvania State University (August 1997).

77. Lesyna, M.W., "Shape Optimization of a Mechanical Amplifier for Use in a Piezoceramic Actuator," Master of Science Thesis, The Pennsylvania State University (May 1998).

VOLUME VII

78, Uchino, K., "Piezoelectric Ultrasonic Motors: Overview," J. Smart Materials and Structures–Special Issue (1997).

79. Uchino, K., "Compact Piezoelectric Ultrasonic Motors," J. Medical Ultrasonics 24 (9), 1191-92 (1997).

5.0 MODELING and CHARACTERIZATION

5.1 Finite Element Methods

80. Qi, W. and W. Cao, "Finite Element Analysis and Experimental Studies on the Thickness Resonance of Piezocomposite Transducer," Ultrasonic Imaging 18, 1-9 (1996).

81. Qi, W. and W. Cao, "Finite Element Study on Random Design of 2-2 Composite Transducer," SPIE 3037, 176-180 (1997).

82. Geng, X. and Q.M. Zhang, "Evaluation of Piezocomposites of Ultrasonic Transducer Applications–Influence of the Unit Cell Dimensions and the Properties of Constituents on the Performance of 2-2 Piezocomposites," IEEE Transactions on Ultrasonics, Ferroelectrics, and Frequency Control 44 (4), 857-872 (1997).

83. Zhang, Q. and X. Geng, "Acoustic Properties of the Interface of a Uniform Medium-2-2 Piezocomposite and the Field Distributions in the Composite," Jpn. J. Appl. Phys. 36, 6853-6861 (1997).

84. Geng, X. and Q.M. Zhang, "Analysis of the Resonance Modes and Losses in 1-3 Composites for Ultrasonic Transducer Applications," IEEE UFFC (1997).

APPENDIX 78

PIEZOELECTRIC ULTRASONIC MOTORS : OVERVIEW

Kenji Uchino
International Center for Actuators and Transducers
Intercollege Materials Research Laboratory, The Pennsylvania State University
University Park, PA 16802, USA

ABSTRACT

This paper reviews recent developments of ultrasonic motors using piezoelectric resonant vibrations. Following the historical background, ultrasonic motors using the standing and traveling waves are introduced. Driving principles and motor characteristics are explained in comparison with the conventional electromagnetic motors. After a brief discussion on speed and thrust calculation, finally, reliability issues of ultrasonic motors are described.

1.   INTRODUCTION

In office equipment such as printers and floppy disk drives, market research indicates that tiny motors smaller than 1 cm^3 would be in large demand over the next ten years. However, using the conventional electromagnetic motor structure, it is rather difficult to produce a motor with sufficient energy efficiency. Piezoelectric ultrasonic motors, whose efficiency is insensitive to size, are superior in the mm-size motor area.

In general, piezoelectric and electrostrictive actuators are classified into two categories, based on the type of driving voltage applied to the device and the nature of the strain induced by the voltage: (1) rigid displacement devices for which the strain is induced unidirectionally along an applied dc field, and (2) resonating displacement devices for which the alternating strain is excited by an ac field at the mechanical resonance frequency (ultrasonic motors). The first category can be further divided into two types: servo displacement transducers (positioners) controlled by a feedback system through a position-detection signal, and pulse-drive motors operated in a simple on/off switching mode, exemplified by dot-matrix printers.

The AC resonant displacement is not directly proportional to the applied voltage, but is, instead, dependent on adjustment of the drive frequency. Although the positioning accuracy is not as high as that of the rigid displacement devices, very high speed motion due to the high frequency is an attractive feature of the ultrasonic motors. Servo displacement transducers, which use feedback voltage superimposed on the DC bias, are used as positioners for optical and precision machinery systems. In contrast, a pulse drive motor generates only on / off strains, suitable for the impact elements of dot-matrix or ink-jet printers.

The materials requirements for these classes of devices are somewhat different, and certain compounds will be better suited for particular applications. The ultrasonic motor, for instance, requires a very hard piezoelectric with a high mechanical quality factor Q, in order to minimize heat generation and maximize displacement. Note that the resonance displacement is equal to $\alpha\cdot dEL$, where d is a piezoelectric constant, E, applied electric field, L, sample length and α is an amplification factor proportional to the mechanical Q. The servo-displacement transducer suffers most from strain hysteresis and, therefore, a PMN electrostrictor is preferred for this application. Notice that even in a feedback system the hysteresis results in a much lower response speed. The pulse-drive motor requires a low permittivity material aiming at quick response with a limited power supply rather than a small hysteresis, so that soft PZT piezoelectrics are preferred to the high-permittivity PMN for this application.

This paper deals with ultrasonic motors using resonant vibrations. Following the historical background, various ultrasonic motors are introduced. Driving principles and motor characteristics are explained in comparison with the conventional electromagnetic motors. After a brief discussion on speed and thrust calculation, finally, reliability issues of ultrasonic motors are described.

2.   CLASSIFICATION OF ULTRASONIC MOTORS

2.1   Historical Background

Electromagnetic motors were invented more than a hundred years ago. While these motors still dominate the industry, a drastic improvement cannot be expected except through new

discoveries in magnetic or superconducting materials. Regarding conventional electromagnetic motors, tiny motors smaller than $1cm^3$ are rather difficult to produce with sufficient energy efficiency. Therefore, a new class of motors using high power ultrasonic energy -- ultrasonic motor, is gaining wide spread attention. Ultrasonic motors made with piezoceramics whose efficiency is insensitive to size are superior in the mini-motor area. Figure 1 shows the basic construction of ultrasonic motors, which consist of a high-frequency power supply, a vibrator and a slider. Further, the vibrator is composed of a piezoelectric driving component and an elastic vibratory part, and the slider is composed of an elastic moving part and a friction coat.

Though there had been some earlier attempts, the practical ultrasonic motor was proposed firstly by H. V. Barth of IBM in 1973.[1] As shown in Fig. 2, the rotor was pressed against two horns placed at different locations. By exciting one of the horns, the rotor was driven in one direction, and by exciting the other horn, the rotation direction was reversed. Various mechanisms based on virtually the same principle were proposed by V. V. Lavrinenko[2] and P. E. Vasiliev[3] in the former USSR. Because of difficulty in maintaining a constant vibration amplitude with temperature rise, wear and tear, the motors were not of much practical use at that time.

In 1980's, with increasing chip pattern density, the semiconductor industry began to request much more precise and sophisticated positioners which do not generate magnetic field noise. This urgent request has accelerated the developments in ultrasonic motors. Another advantage of ultrasonic motors over the conventional electromagnetic motors with expensive copper coils, is the improved availability of piezoelectric ceramics at reasonable cost. Japanese manufacturers are producing piezoelectric buzzers around 30 - 40 cent price range at the moment.

Let us summarize the merits and demerits of the ultrasonic motors:

---

merits

1. Low speed and high torque   -- Direct drive
2. Quick response, wide velocity range, hard brake and no backlash
                                        -- Excellent controllability
                                        -- Fine position resolution
3. High power / weight ratio and high efficiency
4. Quiet drive
5. Compact size and light weight
6. Simple structure and easy production process
7. Negligible effect from external magnetic or radioactive fields,
   and also no generation of these fields

Demerits

8. Necessity for a high frequency power supply
9. Less durability due to frictional drive
10. Drooping torque vs. speed characteristics

3

2.2   Classification and Principles of Ultrasonic Motors

From a customer's point of view, there are rotary and linear type motors. If we categorize them from the vibrator shape, there are rod type, π-shaped, ring (square) and cylinder types, which are illustrated in Fig. 3. Two categories are being investigated for ultrasonic motors from a vibration characteristic viewpoint: a standing-wave type and a propagating-wave type. Refresh your memory on the wave formulas. The standing wave is expressed by

$$u_S(x,t) = A \cos kx \cdot \cos \omega t, \qquad (1)$$

while the propagating wave is expressed as

$$u_p(x,t) = A \cos (kx - \omega t). \qquad (2)$$

Using a trigonometric relation, Eq. (2) can be transformed as

$$u_p(x,t) = A \cos kx \cdot \cos \omega t + A \cos (kx - \pi/2) \cdot \cos (\omega t - \pi/2). \qquad (3)$$

This leads to an important result, i. e. a propagating wave can be generated by superimposing two standing waves whose phases differ by 90 degree to each other both in time and in space. This principle is necessary to generate a propagating wave on a limited volume/size substance, because only standing waves can be excited stably in a finite size.

Standing Wave Type

The standing-wave type is sometimes referred to as a vibratory-coupler type or a "woodpecker" type, where a vibratory piece is connected to a piezoelectric driver and the tip portion generates flat-elliptical movement. Figure 4 shows a simple model proposed by T. Sashida.[4] A vibratory piece is attached to a rotor or a slider with a slight cant angle θ. Take the x-y coordinate so that the x axis is normal to the rotor face. When a vibration displacement

$$u_x = u_0 \sin (\omega t + \alpha) \qquad (4)$$

is excited at the piezoelectric vibrator, the vibratory piece generates bending because of restriction by the rotor, so that the tip moves along the rotor face between A --> B, and freely between B --> A. If the vibratory piece and the piezo-vibrator are tuned properly, they form a resonating structure, and if the bending deformation is sufficiently small compared with the piece length, the tip locus during the free vibration (B --> A) is represented by

$$x = u_0 \sin (\omega t + \alpha),$$
$$y = u_1 \sin (\omega t + \beta), \qquad (5)$$

which is an elliptical locus. Therefore, only the duration A --> B provides a unidirectional force to the rotor through friction, i. e. intermittent rotational torque or thrust. However, because of the inertia of the rotor, the rotation speed ripple is not large to be observed. The standing-wave type, in general, is low in cost (one vibration source) and has high

4

efficiency (up to 98% theoretically), but lack of control in both clockwise and counterclockwise directions is a problem.

<u>Propagating Wave Type</u>

By comparison, the propagating-wave type (a surface-wave or "surfing" type) combines two standing waves with a 90 degree phase difference both in time and in space. The principle is shown in Fig. 5. A surface particle of the elastic body draws an elliptical locus due to the coupling of longitudinal and transverse waves. This type requires, in general, two vibration sources to generate one propagating wave, leading to low efficiency (not more than 50 %), but it is controllable in both the rotational directions.

3. STANDING WAVE TYPE MOTORS

3.1 Rotary Motors

T. Sashida developed a rotary type motor similar to the fundamental structure.[4] Four vibratory pieces were installed on the edge face of a cylindrical vibrator, and pressed onto the rotor. This is one of the prototypes which triggered the present development fever on ultrasonic motors. A rotation speed of 1500rpm, torque of 0.08 N·m and output of 12 W (efficiency 40%) were obtained under an input of 30 W at 35 KHz. This type of ultrasonic motor can provide a speed much higher than the inchworm types, because of high frequency and an amplified vibration displacement at the resonance frequency.

Hitachi Maxel significantly improved the torque and efficiency by using a torsional coupler replacing Sashida's vibratory pieces (Fig. 6), and by the increasing pressing force with a bolt.[5] The torsional coupler looks like an old fashioned TV channel knob, consisting of two legs which transform longitudinal vibration generated by the Langevin vibrator to a bending mode of the knob disk, and a vibratory extruder. Notice that this extruder is aligned with a certain cant angle to the legs, which transforms the bending to a torsion vibration. This transverse moment coupled with the bending up-down motion leads to an elliptical rotation on the tip portion, as illustrated in Fig. 6(b). The optimum pressing force to get the maximum thrust is obtained, when the ellipse locus is deformed roughly by half. A motor with 30mm x 60mm in size and 20 - 30° in cant angle between a leg and a vibratory piece provided the torque as high as 1.3 N·m and the efficiency of 80%. However, this type provides only unidirectional rotation. Notice that even the drive of the motor is intermittent, the output rotation becomes very smooth because of the inertia of the rotor.

The Penn State University has developed a compact ultrasonic rotory motor as tiny as 3 mm in diameter. As shown in Fig. 7, the stator consists of a piezoelectric ring and two concave/convex metal endcaps with "windmill" shaped slots bonded together, so as to generate a coupled vibration of up-down and torsional type.[6] Since the component number and the fabrication process were minimized, the fabrication price would be decreased remarkably, and it would be adaptive to the disposable usage. When driven at 160 kHz, the maximum revolution 600 rpm and the maximum torque 1 mN·m were obtained for a 11 mmφ motor.

Tokin developed a piezoelectric ceramic cylinder for a torsional vibrator (Fig. 8).[7] Using an interdigital type electrode pattern printed with 45° cant angle on the cylinder surface, torsion vibration was generated, which is applicable to a simple ultrasonic motor.

5

S. Ueha proposed a two-vibration-mode coupled type (Fig. 9), i. e. a tortional Langevin vibrator was combined with three multilayer actuators to generate larger longitudinal and transverse surface displacement of the stator, as well as to control their phase difference.[8] The phase change can change the rotation direction.

3.2 Linear Motors

K. Uchino invented a π-shaped linear motor.[9] This linear motor is equipped with a multilayer piezoelectric actuator and fork-shaped metallic legs as shown in Fig. 10. Since there is a slight difference in the mechanical resonance frequency between the two legs, the phase difference between the bending vibrations of both legs can be controlled by changing the drive frequency. The walking slider moves in a way similar to a horse using its fore and hind legs when trotting. A test motor 20 x 20 x 5 mm^3 in dimension exhibited a maximum speed of 20 cm/s and a maximum thrust of 0.2 kgf with a maximum efficiency of 20%, when driven at 98kHz at 6V (actual power = 0.7 W). Figure 11 shows the motor characteristics of the linear motor. This motor has been employed in a precision X-Y stage.

Tomikawa's rectangular plate motor is also intriguing.[10] As shown in Fig. 12, a combination of the two modes forms an elliptical displacement motion. The two modes chosen were the 1st longitudinal mode (L_1 mode) and the 8th bending mode (B_8), whose resonance frequencies were almost the same. By applying voltages with a phase difference of 90 degree to the L-mode and B-mode drive electrodes, elliptical motion in the same direction can be obtained at both ends of this plate, leading to rotation of the rollers in contact with these points. Anticipated applications are paper or card senders. The reader can find other linear motor ideas in Ueha and Tomikawa's book.[11]

4. PROPAGATING WAVE TYPE MOTORS

4.1 Linear Motors

T. Sashida and S. Ueha et al. manufactured a linear motor as illustrated in Fig. 13.[12,13] The two piezoelectric vibrators installed at both ends of a transmittance steel rod excite and receive the traveling transverse wave (antisymmetric fundamental Lamb wave mode). Adjusting a load resistance in the receiving vibrator leads to a perfect traveling wave. Exchanging the role of exciting and receiving piezo-components provided a reverse moving direction.

The bending vibration transmitting via the rail rod is represented by the following differential equation:

$$(\partial^2 w(x,t)/\partial t^2) + (E\,I\,/\,\rho\,A)\,(\partial^4 w(x,t)/\partial x^4) = 0, \qquad (6)$$

where $w(x,t)$ is a transverse displacement (see Fig. 5), x, the coordinate along the rod axis, E, Young's modulus of the rod, A, the cross sectional area, ρ, density and I is the moment of inertia of the cross-section. Assuming a general solution of Eq. (6) as

$$w(x,t) = W(x)\,(A\,\sin\,\omega t + B\,\cos\,\omega t), \qquad (7)$$

the wave transmission velocity v and wavelength λ are caluculated as

6

$$v = (E\,I\,/\,\rho\,A)^{1/4}\,\sqrt{\omega},\tag{8}$$

$$\lambda = 2\pi\,(E\,I\,/\,\rho\,A)^{1/4}\,/\,\sqrt{\omega}.\tag{9}$$

Using the bending vibration, the wavelength λ can be easily chosen as short as several mm to satisfy a stable surface contact with the slider by changing the cross-section area A or the moment of inertia I of the transmission rod. In the case of Fig. 13, $\lambda = 26.8$ mm.

A slider, the contact face of which is coated with rubber or vinyl resin sheet, clamps the transmission rod with an appropriate force. The transmission efficiency is strongly affected by the vibration source position on the rod, showing a periodic change with the distance from the free end of the rod to the position of the vibrator. Taking account of the wave phase, the vibration source should be fixed at the distance of the wavelength λ (i. e. 26.8 mm) from the rod end.

The slider made of a steel clamper 60 mm in length, which theoretically covers two waves, was driven at a speed of 20 cm/s with a thrust of 50 N at 28 kHz. A serious problem with this type is found in low efficiency around 3% because the whole rod must be excited even when only a small portion is utilized for the output. Thus, ring type motors were invented by Sashida, where the whole rod can be utilized, because the lengths of the stator and rotor are the same.

4.2   Rotary Motors

When we deform the rod discussed in the previous section to make a ring by connecting the two ends topologically, we can make a rotary type motor using a bending vibration. Two types of "ring" motor designs are possible; (a) bending mode and (b) extensional mode.[14] Though the principle is similar to the linear type, more sophisticated structures are employed in the ceramic poling and in the mechanical support mechanism.

Principle of "Surfing" Rotary Motors

In general, when a vibration source is driven at one position on a closed ring (circular or square) at a frequency corresponding to the resonance of this ring, only a standing wave is excited, because the vibration propagates in two directions symmetrically to the vibration source and interferes with each other. When multiple vibration sources are installed on the ring, displacements can be obtained by superimposing all the waves (two waves from each vibration source). Using this superposition principle, we can generate a propagating wave which is a rotation of the standing-wave shape, even in a closed ring.

Assuming a vibration source of $A \cos \omega t$ at the point $\theta = 0$ of the elastic ring, the n-th mode standing wave can be expressed by

$$u(\theta,t) = A \cos n\theta \cos \omega t,\tag{10}$$

and the traveling wave by

$$u(\theta,t) = A \cos (n\theta - \omega t). \tag{11}$$

Since the traveling wave can be expressed as a superimposition of two standing waves as

$$u(\theta,t) = A \cos n\theta \cos \omega t + A \cos (n\theta - \pi/2) \cos (\omega t - \pi/2), \tag{12}$$

we derive an important principle: a propagating wave can be generated by superimposing two standing waves whose phases differ by 90 degree to each other both in time and in space. More generally, the phase difference can be chosen arbitrarily (except 0, $-\pi$, π), as far as the phase difference is the same in space and in time. The vibration source positions for generating a propagating wave on a ring are illustrated in Fig. 14. In principle, the excitation at only two parts of the ring is sufficient to generate a traveling wave. However, in practice, the number of the vibration sources is increased to as many as possible to increase the mechanical output. The symmetry of the electrode structure needs to be considered.

Examples of "Surfing" Rotary Motors

Figure 15 shows the famous Sashida motor.[15] By means of the traveling elastic wave induced by a thin piezoelectric ring, a ring-type slider in contact with the "rippled" surface of the elastic body bonded onto the piezoelectric is driven in both directions by exchanging the sine and cosine voltage inputs. Another advantage is its thin design, which makes it suitable for installation in cameras as an automatic focusing device. Eighty percent of the exchange lenses in Canon's "EOS" camera series have already been replaced by the ultrasonic motor mechanism. Most of the studies on ultrasonic motors done in the US and Japan have been modifications of Sashida's type.

The PZT piezoelectric ring is divided into 16 positively and negatively poled regions and two asymmetric electrode gap regions so as to generate a 9th mode propagating wave at 44 kHz. A proto-type was composed of a brass ring of 60 mm in outer diameter, 45 mm in inner diameter and 2.5 mm in thickness, bonded onto a PZT ceramic ring of 0.5 mm in thickness with divided electrodes on the back-side. The rotor was made of polymer coated with hard rubber or polyurethane. Figure 16 shows Sashida's motor characteristics.

Canon utilized the "surfing" motor for a camera automatic focusing mechanism, installing the ring motor compactly in the lens frame. It is noteworthy that the stator elastic ring has many teeth, which can magnify the transverse elliptical displacement and improve the speed. The lens position can be shifted back and forth through a screw mechanism. The advantages of this motor over the conventional electromagnetic motor are:

1. Silent drive due to the ultrasonic frequency drive and no gear mechanism (i. e. more suitable to video cameras with microphones).
2. Thin motor design and no speed reduction mechanism such as gears, leading to space saving.
3. Energy saving.

A general problem encountered in these traveling wave type motors is the support of the stator. In the case of a standing wave motor, the nodal points or lines are generally supported; this causes minimum effects on the resonance vibration. To the contrary, a traveling wave does not have such steady nodal points or lines. Thus, special considerations are necessary. In Fig. 15, the stator is basically fixed very gently along the axial direction through felt so as not to suppress the bending vibration. It is important to

note that the stop pins which latch onto the stator teeth only provide high rigidity against the rotation.

Matsushita Electric proposed a nodal line support method using a higher order vibration mode (see Fig. 17(b)).[16] Figure 17(a) shows the stator structure, where a wide ring was supported at the nodal circular line and "teeth" were arranged on the maximum amplitude circle to get larger revolution.

Seiko Instruments miniaturized the ultrasonic motor to as tiny as 10 mm in diameter using basically the same principle.[17] Figure 18 shows the construcion of this small motor with 10 mm diameter and 4.5 mm thickness. A driving voltage of 3 V and a current 60 mA provides 6000 rev/min (no-load) with torque of 0.1 mN·m. AlliedSignal developed ultrasonic motors similar to Shinsei's, which would be utilized as mechanical switches for launching missiles.[18]

It is important to note that the unimorph (bonded type of a piezoceramic plate and a metal plate) bending actuation can not provide high efficiency theoretically, because the electromechanical coupling factor k is usually less than 10%. Therefore, instead of the unimorph structure, a simple disk was directly used to make motors.[19,20] Figure 19 shows (1,1), (2,1) and (3,1) modes of a simple disk, which are axial-asymmetric modes. Both the inner and outer circumferences can provide a rotation like a "hula hoop."

Another intriguing design is a "plate-spinning" type proposed by Tokin.[21] Figure 20 shows its principle. A rotary bending vibration was excited on a PZT rod by a combination of sine and cosine voltages, then a cup was made to contact the "spinning" rod with the internal face for achieving rotation.

4.3 Comparison among Various Ultrasonic Motors

The standing-wave type, in general, is low in cost (one vibration source) and has high efficiency (up to 98% theoretically), but lack of control in both clockwise and counterclockwise directions is a problem. By comparison, the propagating-wave type combines two standing waves with a 90 degree phase difference both in time and in space. This type requires, in general, two vibration sources to generate one propagating wave, leading to low efficiency (not more than 50 %), but is controllable in both rotational directions.

Table I summarizes the motor characteristics of the vibration coupler standing wave type (Hitachi Maxel), surface propagating wave type (Shinsei Industry) and a compromised "teeth" vibrator type (Matsushita).[22]

5. MICRO-WALKING MACHINES

Recent biomedical experiments and medical surgery require sophisticated tiny actuators for micro-manipulation of optical fibers, catheters, micro surgery knives etc. Thus, microactuators, particularly micro-walking devices have been studied intensively.

The first systematic study was performed by T. Hayashi on PVDF bimorph actuators.[23] Figure 21 shows two designs of micro-machines. The devices were fabricated using two 30 μm-thick PVDF films bonded together with a curvature of 1 cm^{-1}. The curved bimorph is electrically driven at the mechanical resonance, which generates a large opening and

closing motion at the contact point with the floor. In order to control the device in both clockwise and counter-clockwise rotations, a slight difference of the leg width between the right and left legs was intentionally made, so as to provide a slight difference between their resonance frequencies. By choosing a suitable drive frequency, the right or left leg pair is more mechanically excited, leading to curving.

The π-shape ustrasonic motor described in Section 3.2 can be modified to be driven in a propagating wave manner. K. Ohnishi et al. developed a motor as shown in Fig. 22, where two multilayer actuators were installed at the two corners of the π-shaped frame, and driven with a 90 degree phase difference, revealing a "trotting" leg motion.[24]

One ceramic multilayer component actuator was proposed by Mitsui Sekka.[25] Figure 23 shows the electrode pattern. Only by the external connection, a combined vibration of the longitudinal L_1 and bending B_2 modes could be excited. The motor characteristics are shown in Fig. 24.

Let us introduce a surface acoustic wave motor proposed by Kurosawa and Higuchi.[26] As shown in Fig. 25(a), Rayleigh waves were excited in two crossed directions on a 127.8°-rotation Y-LiNbO$_3$ plate with two pairs of interdigital electrode patterns. Figure 25(b) shows a slider structure with three balls as legs. The driving vibration amplitude and the wave velocity of the Rayleigh waves were adjusted to 6.1 nm and 22 cm/sec for both x and y directions. It is important to note that even though the up-down vibrational amplitude is much smaller ($< 1/10$) than the surface roughness of the LiNbO$_3$, the slider was transferred smoothly. The mechanism has not been clarified yet, it might be due to the locally enhanced friction force through a ball-point contact. This may be categorized as a nano-actuator.

6. SPEED/THRUST CALCULATION

We will introduce the speed and thrust calculation for ultrasonic motors roughly in this section.[27] These calculations depend on the type of motors as well as the contact conditions. The intermittent drive must be considered for the vibratory coupler type motors, while the surface wave type provides the continuous drive in the calculation. The contact models include:

(1) Rigid slider & rigid stator,
(2) Compliant slider & rigid stator,
(3) Compliant slider & compliant stator.

6.1 Surface Wave Type

If the rigid slider and rigid stator model is employed, the slider speed can be obtained from the horizontal velocity of the surface portion of the stator (see Fig. 26). If the frequency and wavelength of the stator vibration are f and λ, respectively, and the normal vibration amplitude (up-down) is Z, and the distance between the surface and the neutral plane is e0, the wave propagation speed is given by

$$V = f \cdot \lambda. \tag{13}$$

This is the sound phase velocity of the vibration mode! To the contrary, the speed of the slider is given by

$$v = 4\pi^2 Z e_0 f / \lambda. \tag{14}$$

It is noteworthy that the slider moves in the opposite direction with respect to the wave traveling direction.

6.2   Vibration Coupler Type

Here, the compliant slider : rigid stator model is introduced. As shown in Fig. 27, the horizontal and vertical displacements of the rigid stator are given by

$$a = a_0 \cos \omega t,$$
$$b = b_0 \sin \omega t. \tag{15}$$

Thus, the horizontal velocity becomes

$$v_h = (\partial a / \partial t) = - a_0 \omega \sin \omega t. \tag{16}$$

We ususally employ the following three hypotheses for futher calculations:

Hypothesis 1: Normal force is given as follows, using a characteristic angle ϕ (between P_1 and P_2):

$$n = \beta [\sin \omega t - \cos(\phi/2)] \quad \text{for } (\pi/2 - \phi/2) < \omega t < (\pi/2 + \phi/2)$$
$$\text{(in contact)}$$
$$n = 0 \quad \text{for } 0 < \omega t < (\pi/2 - \phi/2), (\pi/2 + \phi/2) < \omega t < 2\pi$$
$$\text{(out of contact)} \tag{17}$$

Hypothesis 2: The slider speed is constant (V_0).
Hypothesis 3: The maximum thrust is given by the dynamic friction constant μ_d:

$$f = - \mu_d n \qquad \text{- Accelerating force}$$
$$\text{for } (\pi/2 - \psi/2) < \omega t < (\pi/2 + \psi/2)$$
$$f = \mu_d n \qquad \text{- Dragging force} \tag{18}$$
$$\text{for } (\pi/2 - \phi/2) < \omega t < (\pi/2 - \psi/2), (\pi/2 - \psi/2) < \omega t < (\pi/2 + \phi/2)$$

The main results are summarized. If we know ϕ experimentally (or theoretically taking into account the geometry and elasticity) under a certain normal force N, we can calculate the no-load speed V_0 from

$$V_0 = - a_0 \omega \sin (\phi/2) / (\phi/2), \tag{19}$$

and no-slip position angle ψ from the following relation:

$$\cos(\psi/2) = \sin(\phi/2) / (\phi/2). \tag{20}$$

Then, finally, we can obtain the thrust from

$$F = \mu_d N \{1 - 2 [\sin(\psi/2) - (\psi/2)\cos(\phi/2)] / [\sin(\phi/2) - (\phi/2)\cos(\phi/2)]\}. \tag{21}$$

In the case of $\phi = 0$, $\psi = 0$, $V_0 = -a_0\omega$, $F = -0.155 \mu_d N$; while in the case of $\phi = \pi$, $\cos(\psi/2) = 2/\pi$, $V_0 = -(2/\pi) a_0\omega$, and $F = -0.542 \mu_d N$. With increasing contact period of the vibratory piece, the thrust F increases by sacrificing the speed.

For other model calculations, refer to the book.[11]

7. RELIABILITY OF ULTRASONIC MOTORS

In the development of the ultrasonic motors, the following themes should be systematically studied:

1. Measuring Methods for High-Field Electromechanical Couplings
2. Materials Development (low loss & high vibration velocity)
3. Piezo-Actuator Designs
   a. Heat generation mechanism
   b. Degradation mechanisms
   c. New multilayer actuator designs
4. USM Designs
   a. Displacement magnification mechanisms (horn, hinge-lever)
   b. USM types (standing-wave type, propagating-wave type)
   c. Frictional contact part
5. Drive/Control
   a. High frequency/high power supply
   b. Resonance/antiresonance usage

We will discuss the reliability issues in this section: heat generation, friction materials and drive/control techniques in the ultrasonic motors.

7.1 Heat Generation

The largest problem in ultrasonic motors is heat generation, which sometimes drives temperatures up to 120°C and causes a serious degradation of the motor characteristics through depoling of the piezoceramic. Therefore, the ultrasonic motor requires a very hard type piezoelectric with a high mechanical quality factor Q, leading to the suppression of heat generation. It is also notable that the actual mechanical vibration amplitude at the resonance frequency is directly proportional to this Q value.

Figure 28 shows mechanical Q versus basic composition x at effective vibration velocity $v_0 = 0.05$ m/s and 0.5 m/s for $Pb(Zr_xTi_{1-x})O_3$ doped with 2.1 at.% of Fe.[28] The decrease in mechanical Q with an increase of vibration level is minimum around the rhombohedral-tetragonal morphotropic phase boundary (52/48). In other words, the worst material at a small vibration level becomes the best at a large vibration level, and the data

12

obtained by a conventional impedance analyzer does not provide data relevant to high power materials.

Figure 29 shows an important notion on heat generation from the piezoelectric material. The resistances R_d and R_m in the equivalent electrical circuit are separately plotted as a function of vibration velocity.[29] Note that R_m, mainly related to the mechanical loss, is insensitive to the vibration velocity, while R_d, related to the dielectric loss, changes significantly around a certain critical vibration velocity. Thus, the resonance loss at a small vibration velocity is mainly determined by the mechanical loss, and with increasing vibration velocity, the dielectric loss contribution significantly increases. We can conclude that heat generation is caused by dielectric loss (i. e. P-E hysteresis loss).

Zheng et al. reported the heat generation from various sizes of multilayer type piezoelectric ceramic actuators.[30] The temperature change was monitored in the actuators when driven at 3 kV/mm and 300 Hz, and Fig. 30 plots the saturated temperature as a function of V_e/A, where V_e is the effective volume (electrode overlapped part) and A is the surface area. This linear relation is reasonable because the volume V_e generates the heat and this heat is dissipated through the area A. Thus, if you need to suppress the heat, a small V_e/A design is preferred.

7.2   Frictional Coating and Life Time

Figure 31 plots the efficiency and maximum output of various friction materials.[31] High ranking materials include PTFE (poly tetra fluoro ethylene, Teflon), PPS (Ryton), PBT (poly butyl terephthalate) and PEEK (poly ethyl ethyl ketone). In practical motors, Econol (Sumitomo Chemical), Carbon Fiber Reinforced Plastic (Japan Carbon), PPS (Sumitomo Bakelite) and Polyimide have been popularly used. Figure 32 shows the wear and driving period for CFRP, which indicates that the 0.5 mm thick coat corresponds to 6000 - 8000 hours life.[32] Although the life time of the ultrasonic motor is limited by the characteristics of the friction material, this problem has been nearly solved in practice for some case. The durability test of the Shinsei motor (USR 30) is shown below:

> Continuous Drive (CW 1min & CCW 1min) under revolution 250 rpm and
> load 0.5 kg·cm:
> > --> After 2000 hours, the revolution change is less than 10 %
>
> Intermittent Drive (CW 1 rotation & CCW 1 rotation) under no-load
> > --> After 250 million revolutions, no degradation in motor
> > characteristics

Taking into account the usual lifetime specifications, e. g. 2000 - 3000 hours for VCR's, the lifetime of the ultrasonic motor is no longer a problem.

Of course, the lifetime of the motor itself is not identical to the lifetime installed in a device system. We need further clarification in this issue under severe drive conditions such as large load and high temperature and humidity.

7.3   Drive/Control Technique

Figure 33 summarizes the control methods of the ultrasonic motors. Taking account of the controllability and efficiency, pulse width modulation is most highly recommended.

Driving the motor at the antiresonant frequency, rather than at the resonant state, is also an intriguing technique to reduce the load on the piezo-ceramic and the power supply. Mechanical quality factor Q_m and temperature rise have been investigated on a PZT ceramic rectangular bar, and the results for the fundamental resonance (A-type) and antiresonance (B-type) modes are plotted in Fig. 34 as a function of vibration velocity.[33] It is recognized that Q_B is higher than Q_A over the whole vibration velocity range. In other words, the antiresonance mode can provide the same mechanical vibration level without generating heat. Moreover, the usage of "antiresonance," whose admittance is very low, requires low current and high voltage for driving, in contrast to high current and low voltage for the "resonance." This means that the conventional inexpensive power supply may be utilized for driving the ultrasonic motor.

8. SUMMARIES

8.1 Merits and Demerits of Ultrasonic Motors

Ultrasonic motors are characterized by "low speed and high torque," which are contrasted with "high speed and low torque" of the conventional electromagnetic motors. Thus, the ultrasonic motors do not require gear mechanisms, leading to very quiet operation and space saving. Negligible effects from external magnetic or radioactive fields, and no generation of these fields are suitable for the application to electron beam lithography etc. relevant to the semiconductor technology. Moreover, high power / weight ratio, high efficiency, compact size and light weight are very promising for the future micro actuators adopted to catheter or tele-surgery.

8.2 Classifications of Ultrasonic Motors

There are various categories to classify ultrasonic motors such as:

    (1)   operation: rotary type and linear type
    (2)   device geometry: rod type, π-shaped, ring (square) and cylinder types
    (3)   generating wave: standing wave type and propagating wave type.

8.3 Contact models for speed/thrust calculations

The following medels have been proposed to calculate the speed/thrust of the ultrasonic motors:

    (1) rigid slider & rigid stator,
    (2) compliant slider & rigid stator,
    (3) compliant slider & compliant stator.

8.4 The ultrasonic motor developments require

For the further applications of the ultrasonic motors, systematic investigations on the following issues will be required:

    (1) low loss & high vibration velocity piezo-ceramics,
    (2) piezo-actuator designs with high resistance to fracture and good heat dissipation,
    (3) USM designs;
        a. displacement magnification mechanisms (horn, hinge-lever),
        b. USM types (standing-wave type, propagating-wave type),
        c. frictional contact part,
    (4) high frequency/high power supplies.

15

REFERENCES

1) H. V. Barth: IBM Technical Disclosure Bull. 16, 2263 (1973).
2) V. V. Lavrinenko, S. S. Vishnevski and I. K. Kartashev: Izvestiya Vysshikh Uchebnykh Zavedenii, Radioelektronica 13, 57 (1976).
3) P. E. Vasiliev et al.: UK Patent Application GB 2020857 A (1979).
4) T. Sashida: Oyo Butsuri 51, 713 (1982).
5) A. Kumada: Jpn. J. Appl. Phys., 24, Suppl. 24-2, 739 (1985).
6) B. Koc: Ph. D. Thesis, Electrical Engineering Dept., The Pennsylvania State University (1997).
7) Y. Fuda and T. Yoshida: Ferroelectrics, 160, 323 (1994).
8) K. Nakamura, M. Kurosawa and S. Ueha: Proc. Jpn. Acoustic Soc., No.1-1-18, p.917 (Oct., 1993).
9) K. Uchino, K. Kato and M. Tohda: Ferroelectrics 87, 331 (1988).
10) Y. Tomikawa, T. Nishituka, T. Ogasawara and T. Takano: Sonsors and Mater., 1, 359 (1989).
11) S. Ueha and Y. Tomikawa: "Ultrasonic Motors," Monographs in Electr. & Electron. Engin. 29, Oxford Science Publ., Oxford (1993).
12) Nikkei Mechanical, Feb. 28 issue, p.44 (1983).
13) M. Kurosawa, S. Ueha and E. Mori: J. Acoust. Soc. Amer., 77, 1431 (1985).
14) S. Ueha and M. Kuribayashi: Ceramics 21, No.1, p.9 (1986).
15) T. Sashida: Mech. Automation of Jpn., 15 (2), 31 (1983).
16) K. Ise: J. Acoust. Soc. Jpn., 43, 184 (1987).
17) M. Kasuga, T. Satoh, N. Tsukada, T. Yamazaki, F. Ogawa, M. Suzuki, I. Horikoshi and T. Itoh: J. Soc. Precision Eng., 57, 63 (1991).
18) J. Cummings and D. Stutts: Amer. Ceram. Soc. Trans. "Design for Manufacturability of Ceramic Components", p.147 (1994).
19) A. Kumada: Ultrasonic Technology 1 (2), 51 (1989).
20) Y. Tomikawa and T. Takano: Nikkei Mechanical , Suppl., p.194 (1990).
21) T. Yoshida: Proc. 2nd Memorial Symp. Solid Actuators of Japan: Ultra-precise Positioning Techniques and Solid Actuators for Them, p.1 (1989).
22) K. Uchino: Solid State Phys., Special Issue "Ferroelectrics" 23 (8), 632 (1988).
23) T. Hayashi: Proc. Jpn. Electr. Commun. Soc., US84-8, p.25 (June, 1984).
24) K. Ohnishi, K. Naito, T. Nakazawa and K. Yamakoshi: J. Acoust. Soc. Jpn., 47, 27 (1991).
25) H. Saigo: 15th Symp. Ultrasonic Electronics (USE 94), No. PB-46, p.253 (Nov. 1994).
26) M. Takahashi, M. Kurosawa and T. Higuchi: Proc. 6th Symp. Electro-Magnetic Dynamics '94, No. 940-26 II, D718, p.349 (July, 1994).
27) K. Uchino: "Piezoelectric Actuators and Ultrasonic Motors," Kluwer Academic Publishers, MA (1996).
28) S. Takahashi and S. Hirose: Jpn. J. Appl. Phys., 32, Pt.1, No.5B, 2422 (1993).
29) S. Hirose, M. Aoyagi, Y. Tomikawa, S. Takahashi and K. Uchino: Proc. Ultrasonics Int'l. '95, Edinburgh, p.184 (1995).
30) J. Zheng, S. Takahashi, S. Yoshikawa, K. Uchino and J. W. C. de Vries: J. Amer. Ceram. Soc. 79, 3193 (1996).
31) Y. Tada, M. Ishikawa and N. Sagara: Polymer Preprints 40, 4-17-23, 1408 (1991).
32) K. Ohnishi et al.: SAW Device 150 Committee, Jpn. Acad. Promotion Inst., Abstract 36th Mtg., p.5 (Aug., 1993).
33) S. Hirose, S. Takahashi, K. Uchino, M. Aoyagi and Y. Tomikawa: Proc. Mater. for Smart Systems, Mater. Res. Soc. Vol.360, p.15 (1995).

FIGURE & TABLE CAPTIONS

Table I Comparison of the motor characteristics of the vibraion coupler standing wave type (Hitachi Maxel), surface propagating wave type (Shinsei Industry) and a compromised "teeth" vibrator type (Matsushita).
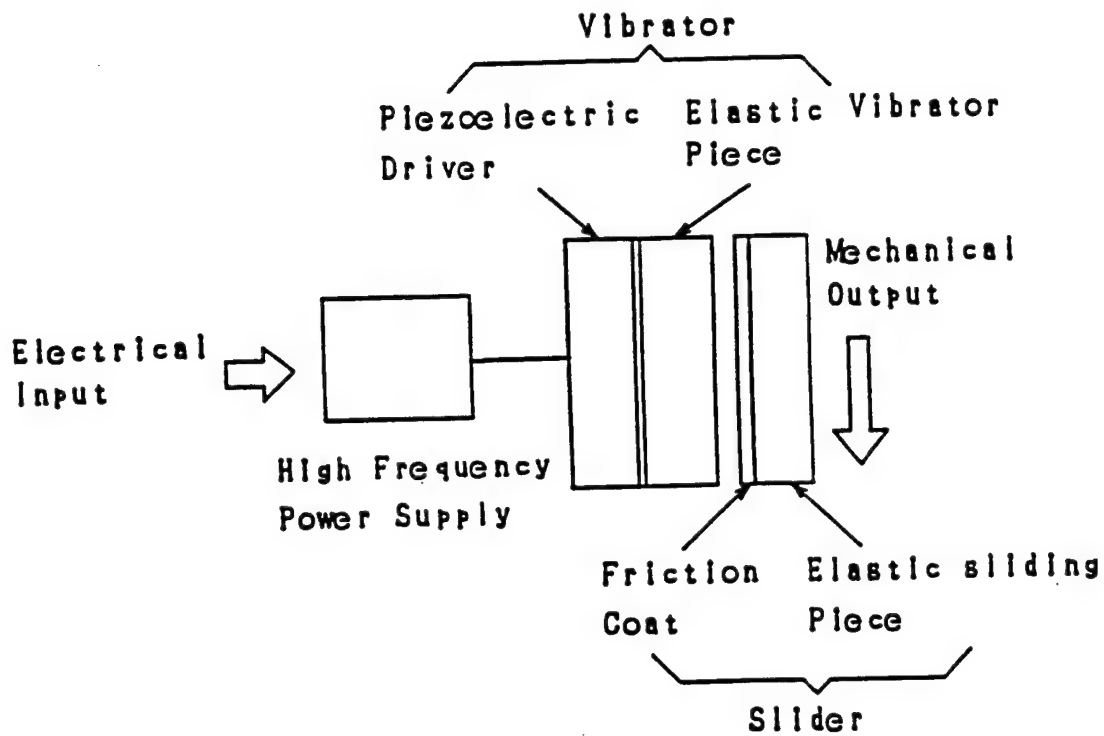
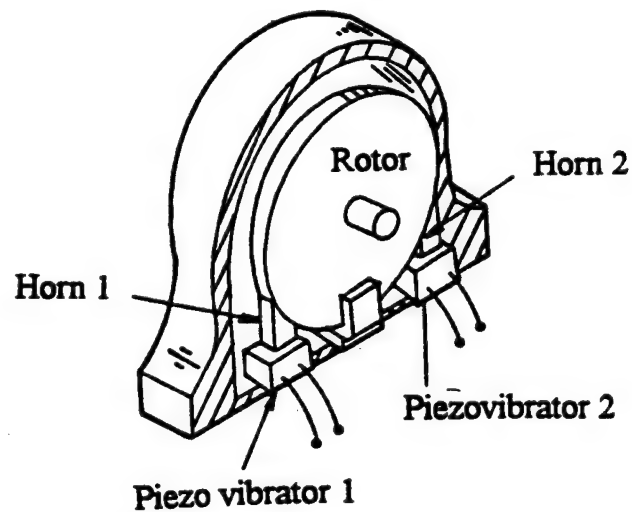Fig. 1 Fundamental construction of ultrasonic motors.
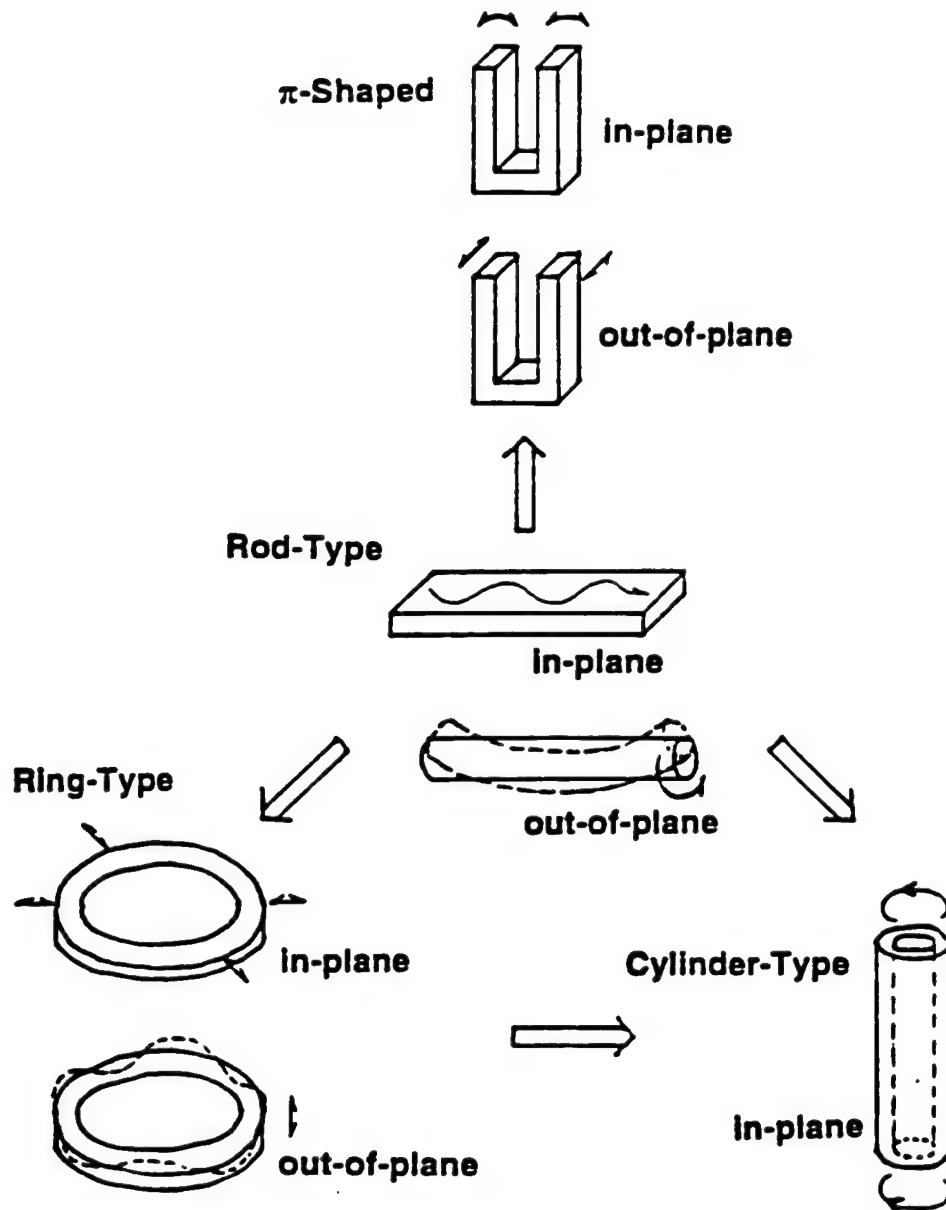
Fig. 2 Ultrasonic motor by Barth.

Fig. 3 Vibrator shapes for ultrasonic motors.

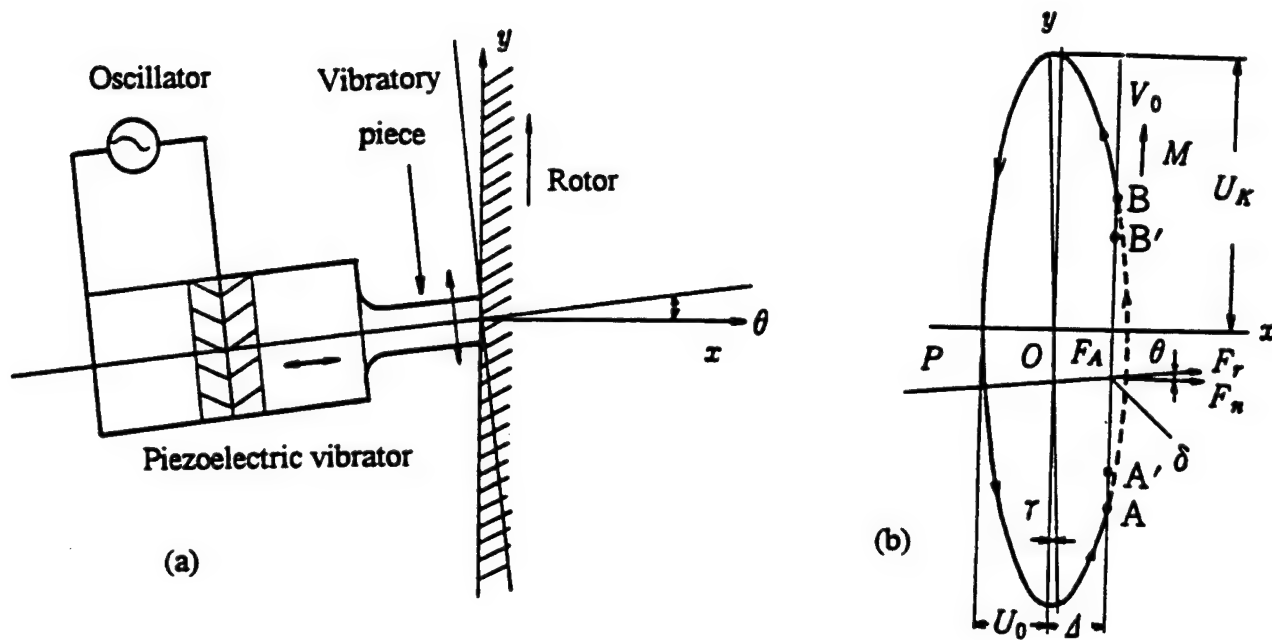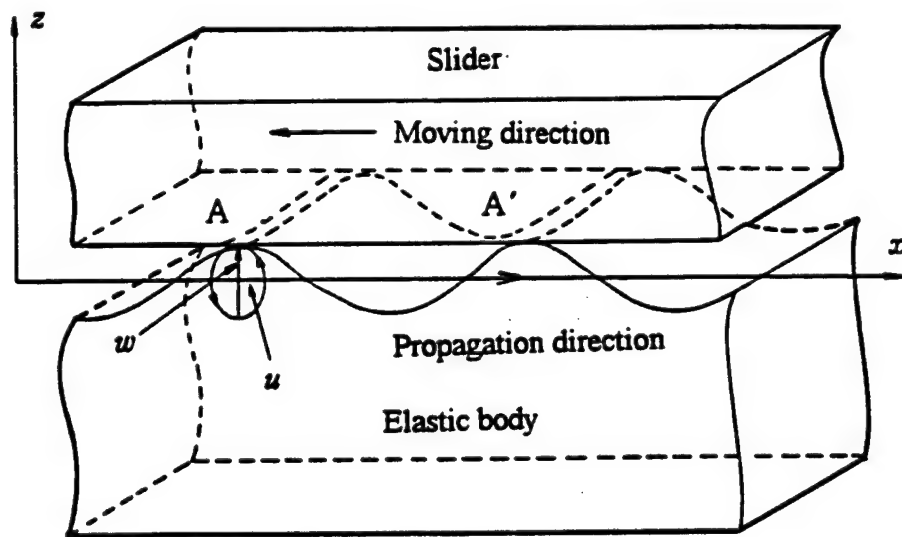Fig. 4 Vibratory coupler type motor (a) and its tip locus (b).
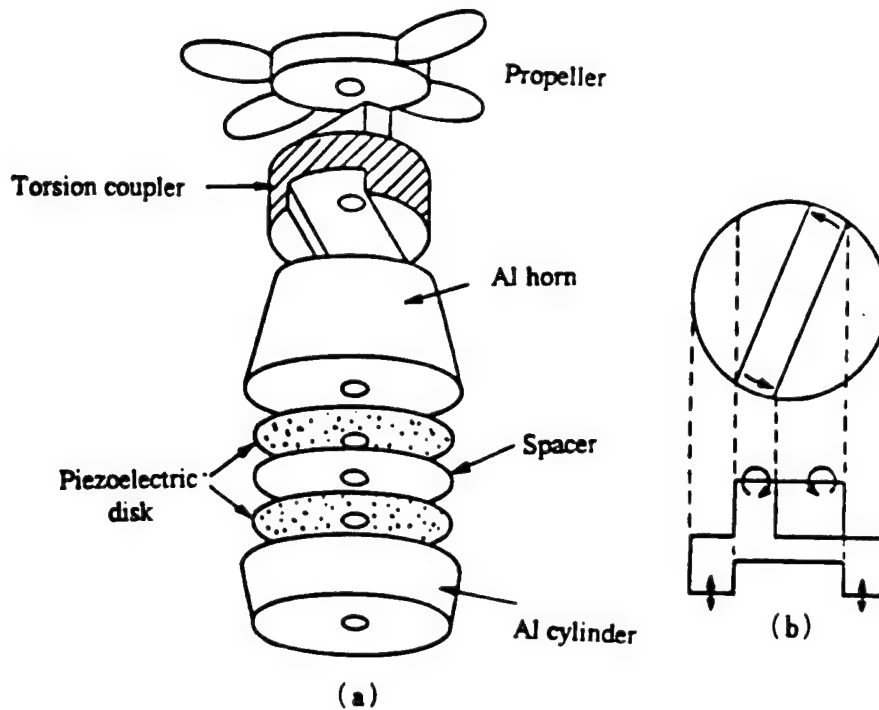
Fig. 5 Principle of the propagating wave type motor.

Fig. 6 Torsional coupler ultrasonic motor (a) and the motion of the torsional coupler (b).

Fig. 7 "Windmill" motor with a disk-shaped torsional coupler.

Fig. 8 Piezoelectric cylinder torsional vibrator (a) and the electrode pattern (b).

Fig. 9 Two-vibration-mode coupled type motor.

Fig. 10 π-shaped linear ultrasonic motor. (a) construction and (b) walking principle. Note the 90 degree phase difference like human walk.

Fig. 11 Motor characteristics of the π-shaped motor.

Fig. 12 L_1 and B_8 double-mode vibrator motor.

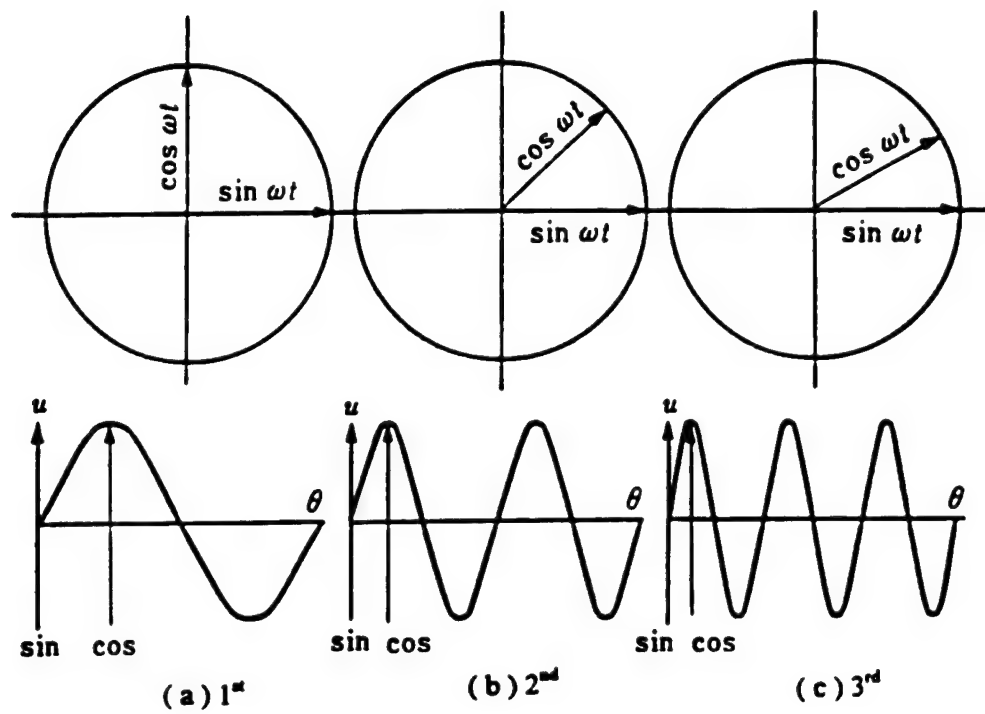Fig. 13 Linear motor using a bending vibration.

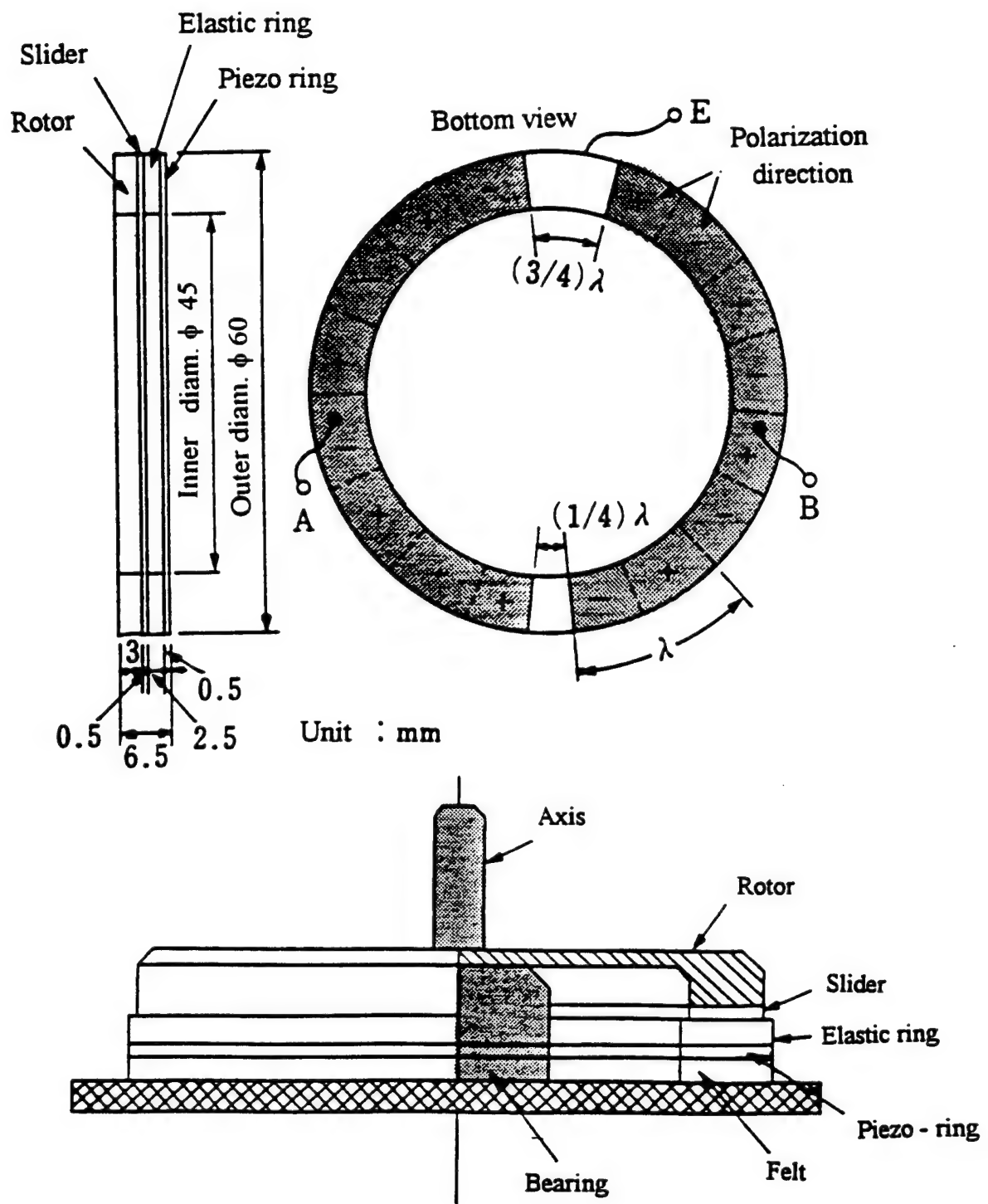Fig. 14 Vibration source positions for generating a propagating wave in a ring.

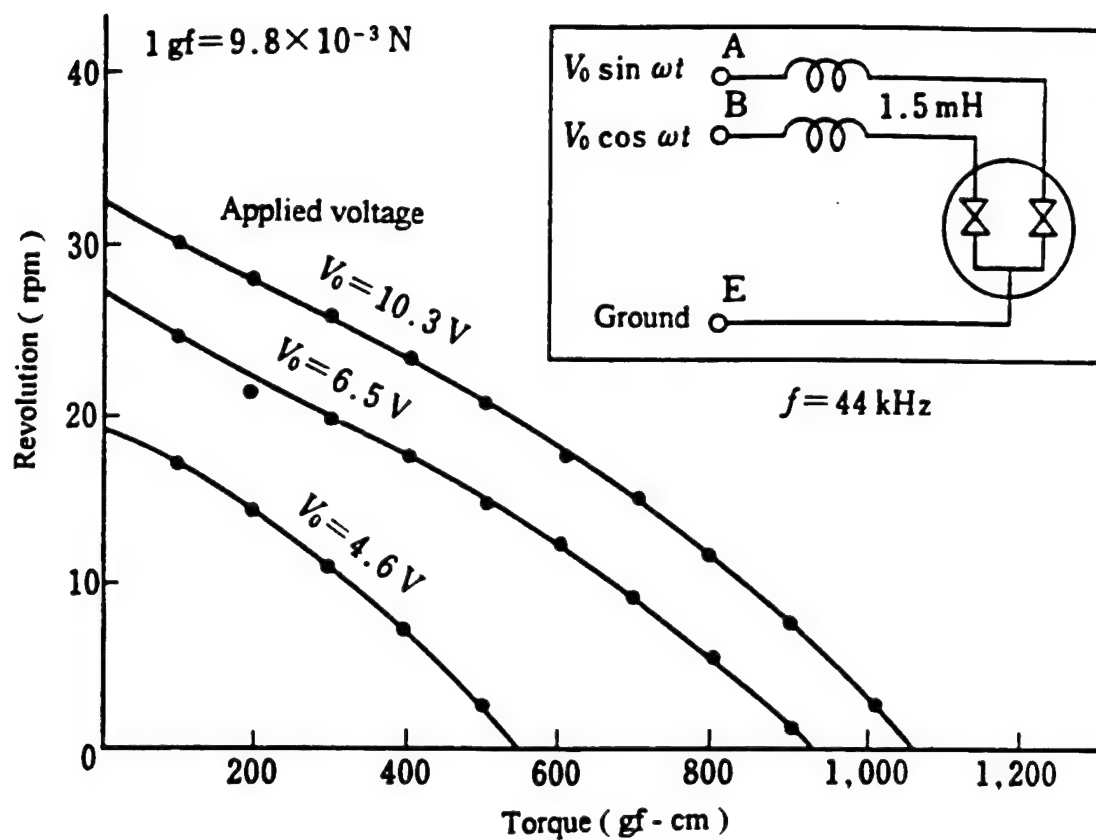Fig. 15 Stator structure of Sashida's motor.

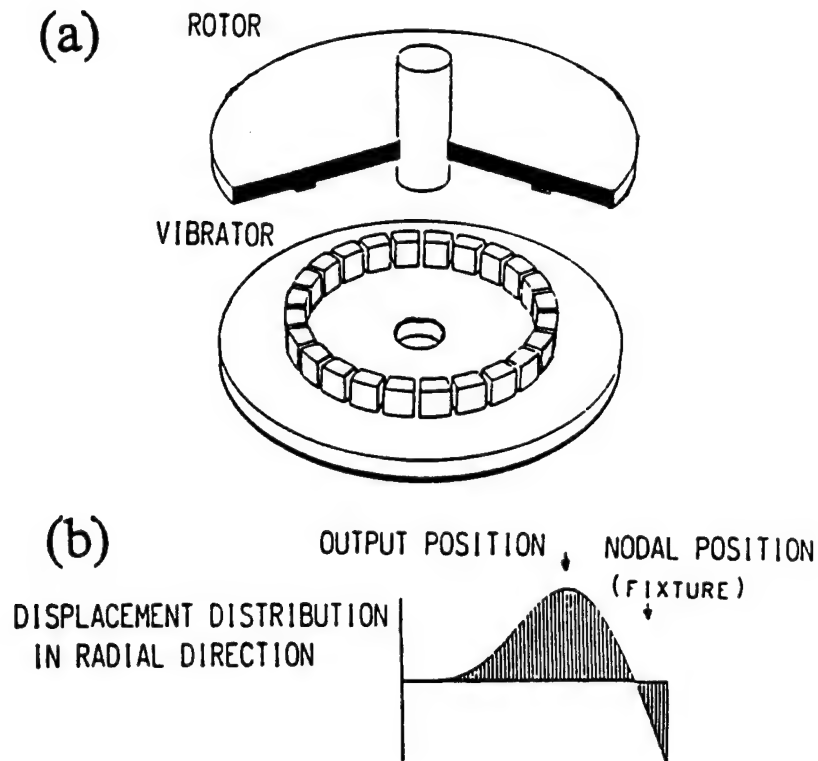Fig. 16 Motor characteristics of Sashida's motor.

Fig. 17 (a) Tooth shaped stator and (b) a higher order vibration mode with a nodal line for fixing.
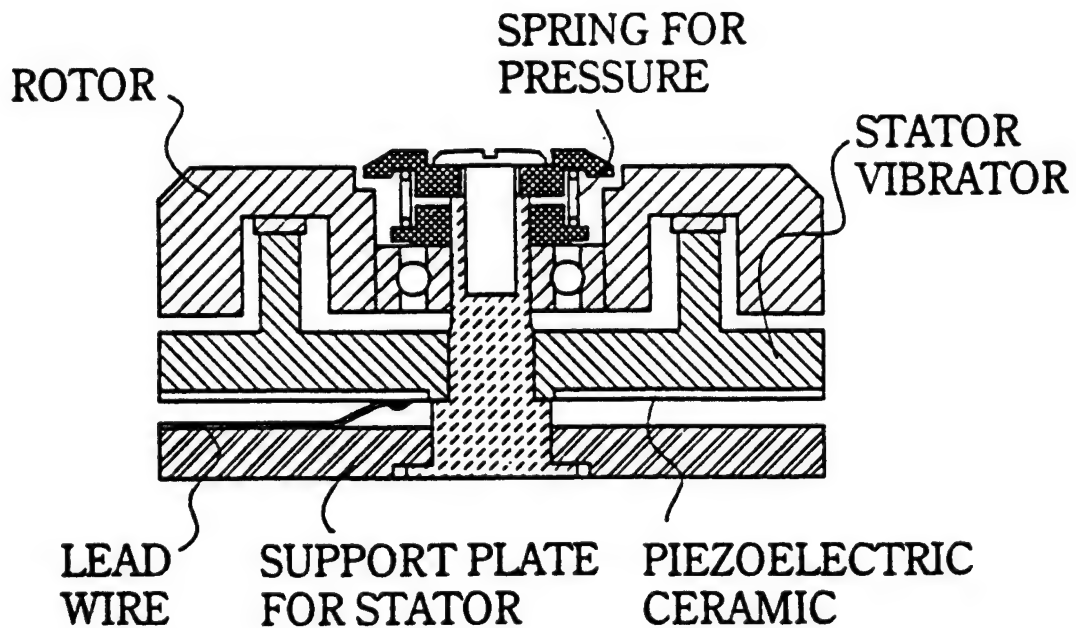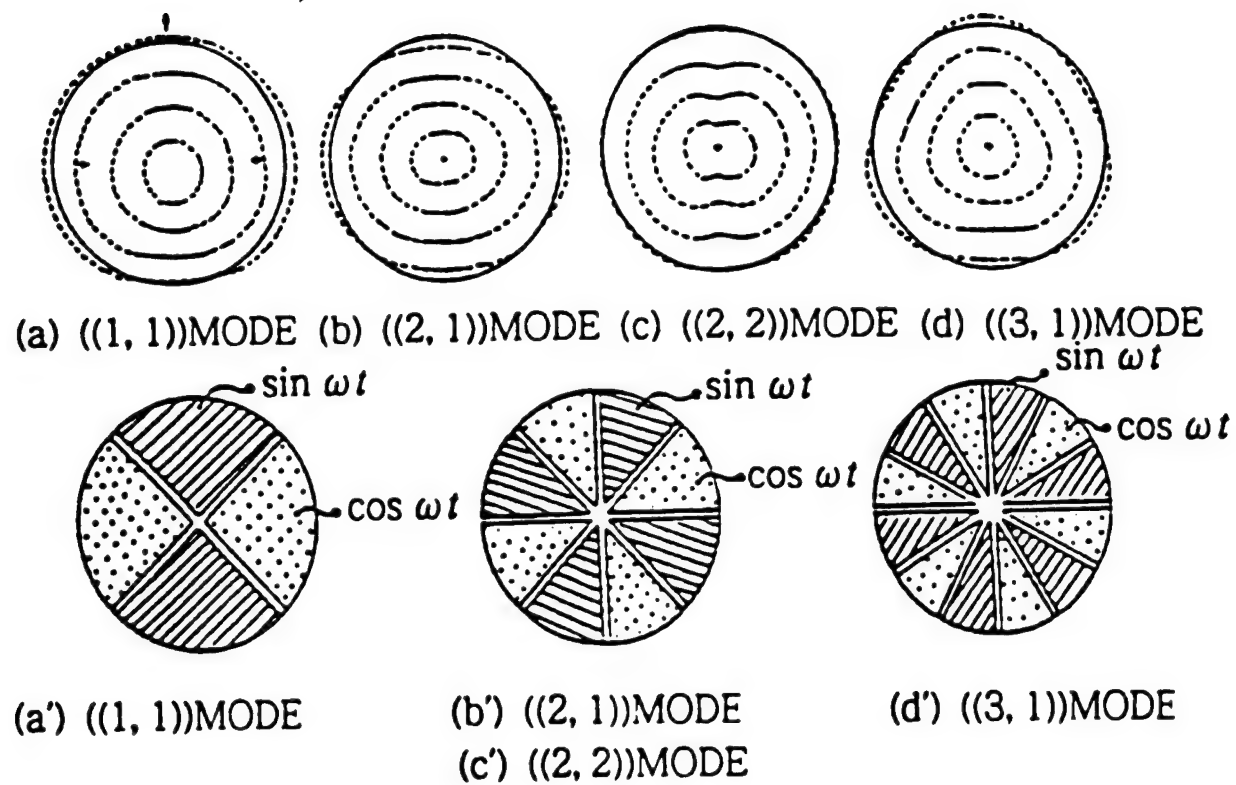
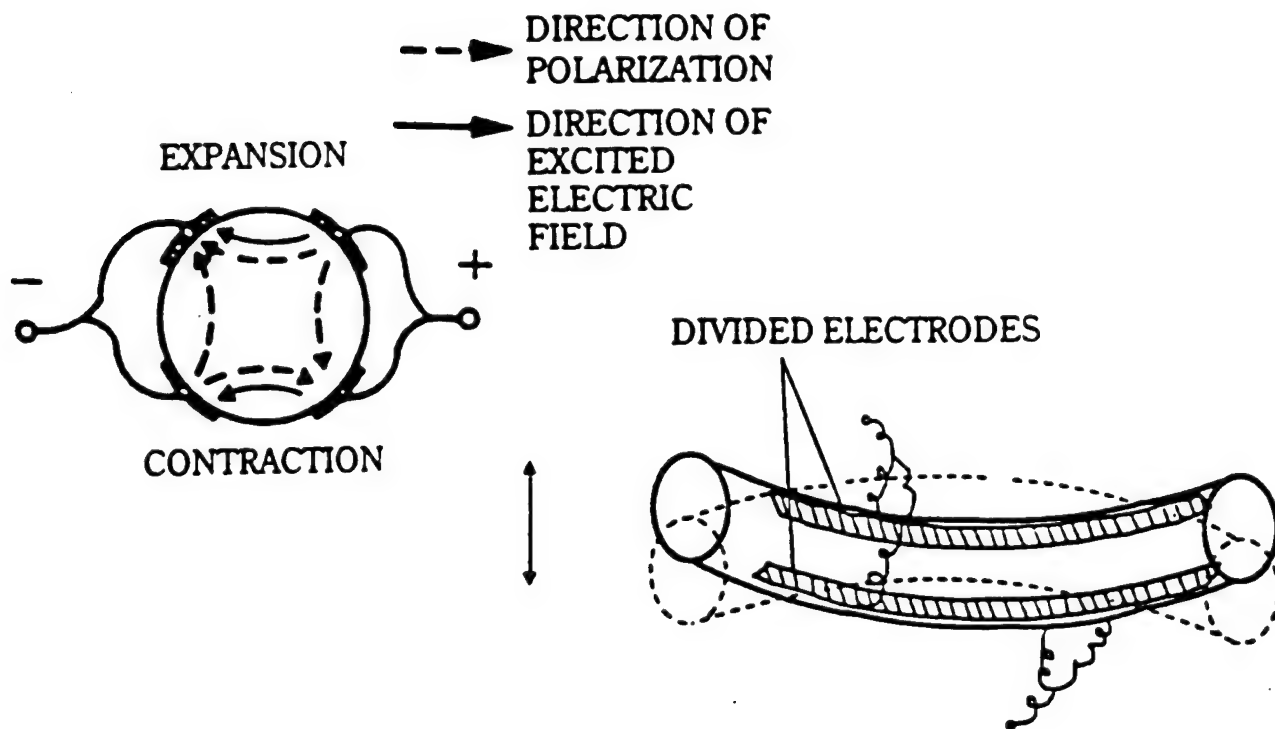Fig. 18 Construction of Seiko's motor.

Fig. 19 Disk type hula-hoop motor.
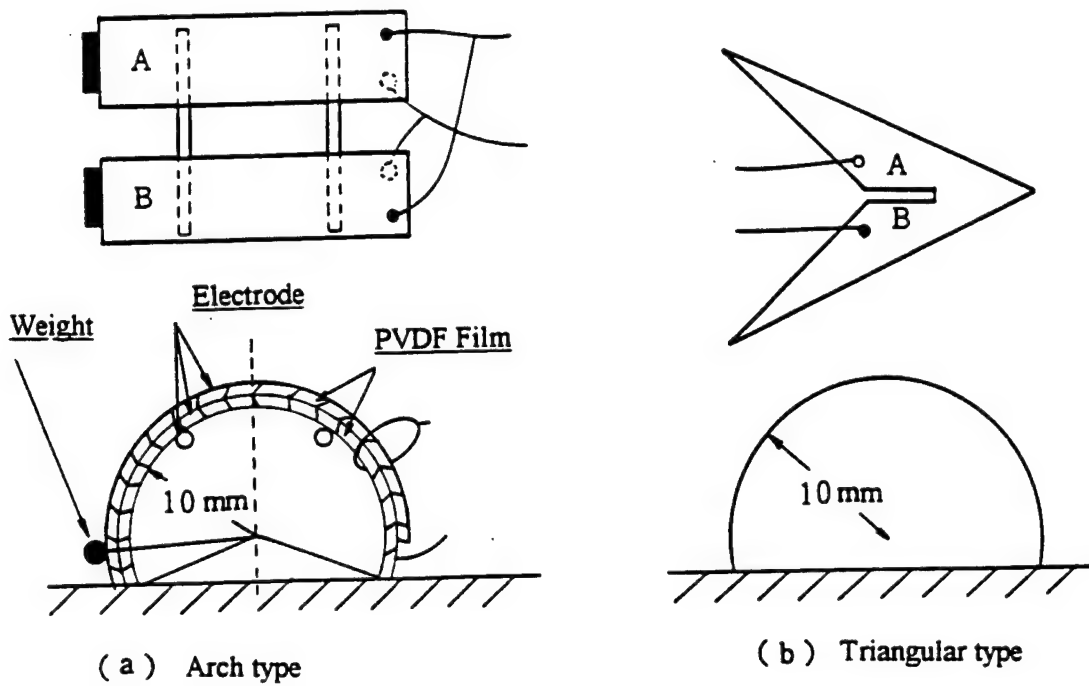
Fig. 20 "Plate-spinning" type motor by Tokin.
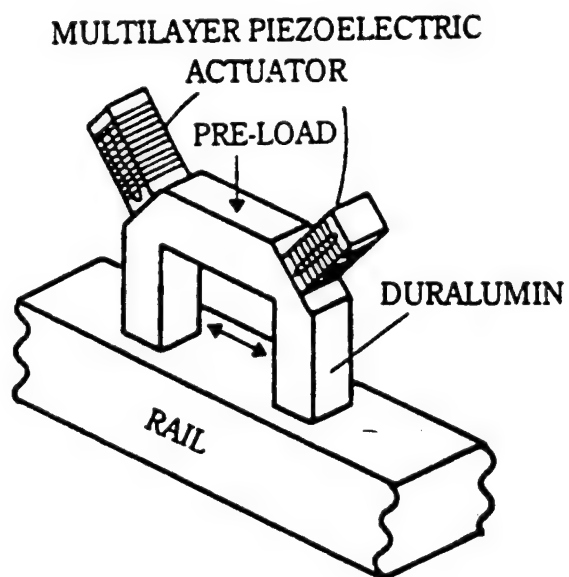
Fig. 21 PVDF walking mechanism.

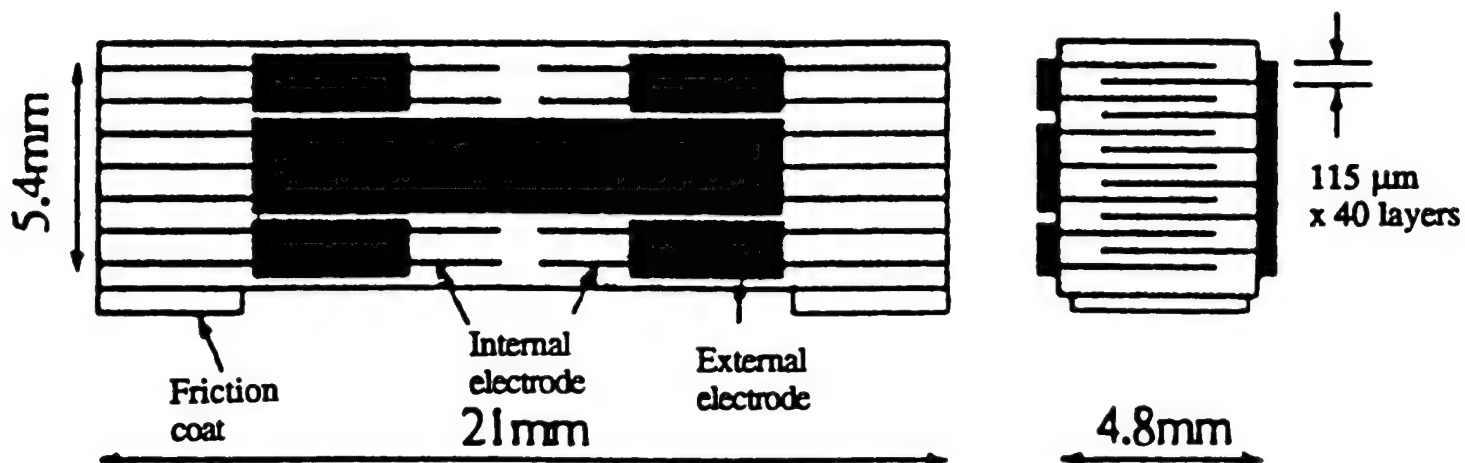Fig. 22 π-shaped ultrasonic linear motor.

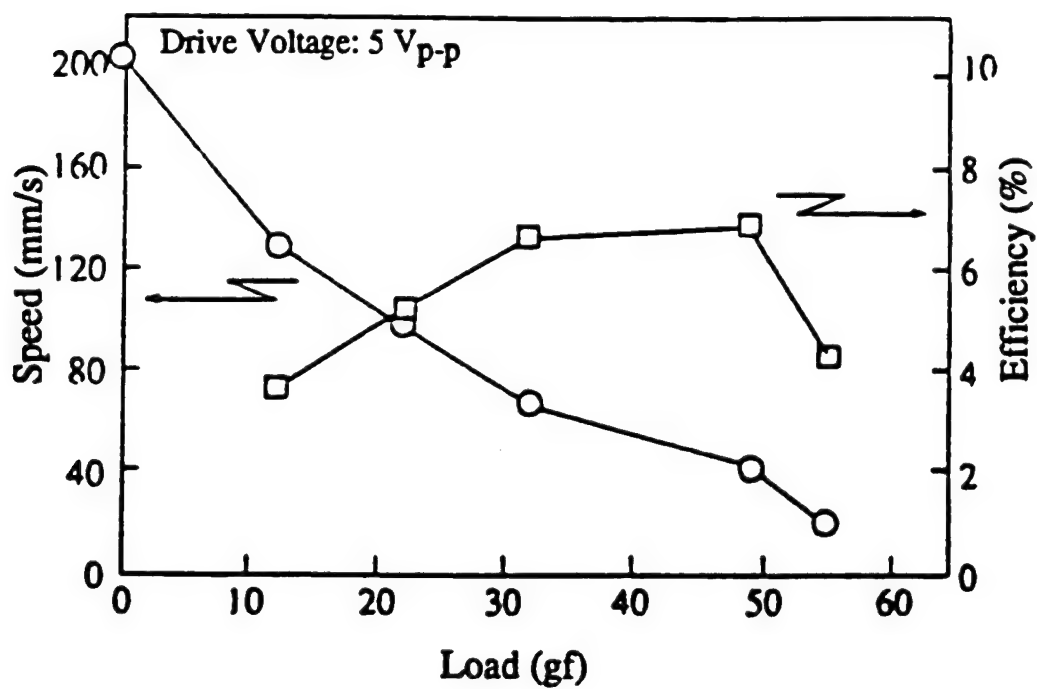Fig. 23 Multilayer ceramic simple linear motor.

Fig. 24 Motor characteristics of the Mitsui-Sekka motor.
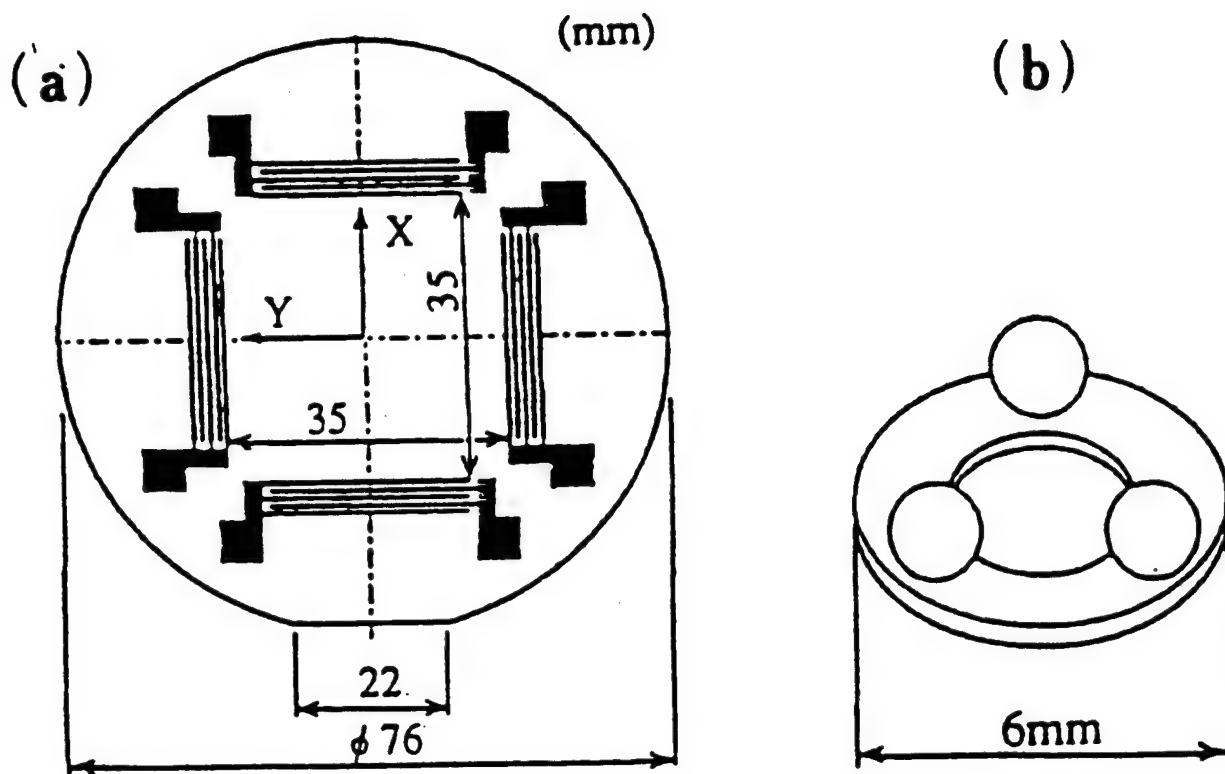
Fig. 25 (a) Stator structure of the surface acoustic wave motor. (b) Slider structure of the SAW motor.
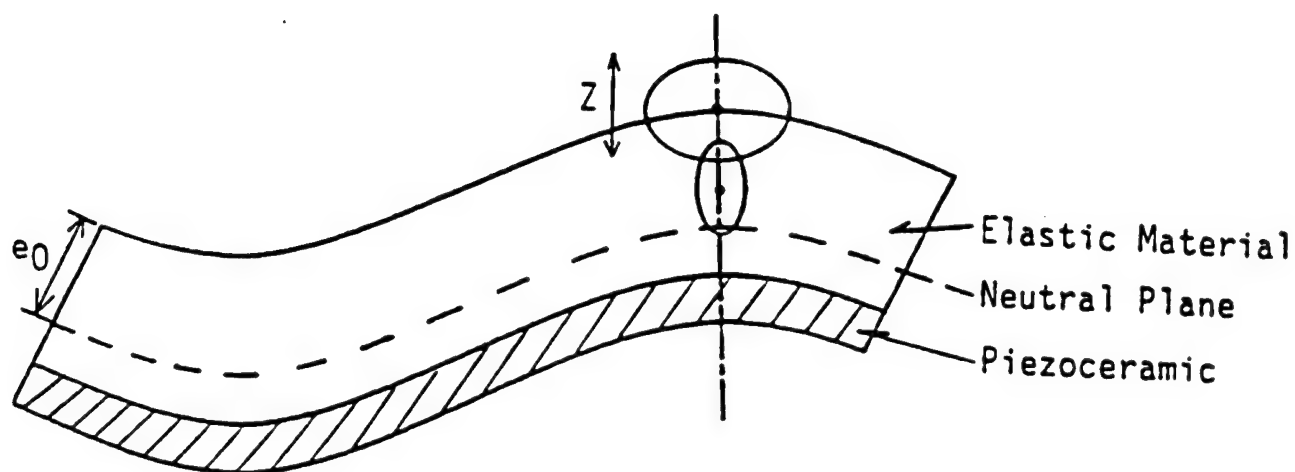
Fig. 26 Displacement configuration of the stator of the surface wave type motor.

Fig. 27 Compliant slider and rigid stator model.

Fig. 28 Mechanical quality factor Q vs. basic composition x at vibration velocity v_0 = 0.05 and 0.5 m/s for $Pb(Zr_xTi_{1-x})O_3 + 2.1$ at% Fe ceramics.

Fig. 29 Vibration velocity dependence of the resistances R_d and R_m in the equivalent electric circuit.

Fig. 30 Temperature rise versus V_e/A (3 kV/mm, 300 Hz), where V_e is the effective volume generating the heat and A is the surface area dissipating the heat.

Fig. 31 Efficiency and maximum output of the Shinsei ultrasonic motor for various friction materials.

Fig. 32 Wear and driving period of the ultrasonic motor for CFRP friction material.

Fig. 33 Control methods of the ultrasonic motor.

Fig. 34 Vibration velocity dependence of the quality factor Q and temperature rise for both A (resonance) and B (antiresonance) type resonances of a longitudinally vibrating PZT rectangular transducer through d_{31}.

Table I Comparison of the motor characteristics of the vibraion coupler standing wave type (Hitachi Maxel), surface propagating wave type (Shinsei Industry) and a compromised "teeth" vibrator type (Matsushita).

CHARACTERISTICS / TYPES	Rotation	Rotation Speed [rpm]	Rotation Torque [kgf·cm]	Efficiency [%]	Size	Analogy
Vibratory Coupler Type	Uni-Direction	600	13	80	Slim & Long	Euglena
Compromise Type	Reversible	600	1	45	- - -	Paramecium
Surface Wave Type	Reversible	600	0.5	30	Wide & Thin	Ameba

Fig. 1 Fundamental construction of ultrasonic motors.

Fig. 2 Ultrasonic motor by Barth.

π-Shaped   in-plane

out-of-plane

Rod-Type

in-plane

out-of-plane

Ring-Type

in-plane

Cylinder-Type

out-of-plane

in-plane

Fig. 3 Vibrator shapes for ultrasonic motors.

Fig. 4 Vibratory coupler type motor (a) and its tip locus (b).

Fig. 5 Principle of the propagating wave type motor.

Fig. 6 Torsional coupler ultrasonic motor (a) and the motion of the torsional coupler (b).

Fig. 7 "Windmill" motor with a disk-shaped torsional coupler.

Fig. 8 Piezoelectric cylinder torsional vibrator (a) and the electrode pattern (b).

Fig. 9 Two-vibration-mode coupled type motor.

Fig. 10 π-shaped linear ultrasonic motor. (a) construction and (b) walking principle.

Note the 90 degree phase difference like human walk.

Fig. 11 Motor characteristics of the π-shaped motor.

Fig. 12 L1 and B8 double-mode vibrator motor.

Fig. 13 Linear motor using a bending vibration.

Fig. 14 Vibration source positions for generating a propagating wave in a ring.

Slider
Elastic ring
Piezo ring
Rotor

Bottom view

E

Polarization
direction

Inner diam. φ 45
Outer diam. φ 60

(3/4) λ

(1/4) λ

A

B

λ

3
0.5
0.5
2.5
6.5

Unit : mm

Axis

Rotor

Slider

Elastic ring

Piezo - ring

Bearing

Felt

Fig. 15 Stator structure of Sashida's motor.

1 gf $= 9.8 \times 10^{-3}$ N

Applied voltage

$V_0 = 10.3$ V

$V_0 = 6.5$ V

$V_0 = 4.6$ V

$V_0 \sin \omega t$ A

$V_0 \cos \omega t$ B   1.5 mH

Ground   E

$f = 44$ kHz

Fig. 16   Motor characteristics of Sashida's motor.

Fig. 17 (a) Tooth shaped stator and (b) a higher order vibration mode with a nodal line for fixing.

Fig. 18 Construction of Seiko's motor.

(a) ((1, 1))MODE (b) ((2, 1))MODE (c) ((2, 2))MODE (d) ((3, 1))MODE

(a') ((1, 1))MODE

(b') ((2, 1))MODE

(c') ((2, 2))MODE

(d') ((3, 1))MODE

Fig. 19 Disk type hula-hoop motor.

Fig. 20 "Plate-spinning" type motor by Tokin.

Fig. 21 PVDF walking mechanism.

Fig. 22 π-shaped ultrasonic linear motor.

Fig. 23 Multilayer ceramic simple linear motor.

Fig. 24 Motor characteristics of the Mitsui-Sekka motor.

Fig. 25   (a) Stator structure of the surface acoustic wave motor. (b) Slider structure of the

SAW motor.

Fig. 26 Displacement configuration of the stator of the surface wave type motor.

Fig. 27 Compliant slider and rigid stator model.

Fig. 28 Mechanical quality factor Q vs. basic composition x at vibration velocity v0 =

0.05 and 0.5 m/s for Pb(Zr$_x$Ti$_{1-x}$)O$_3$ + 2.1 at% Fe ceramics.

Fig. 29 Vibration velocity dependence of the resistances R$_d$ and R$_m$ in the equivalent

electric circuit.

Fig. 30 Temperature rise versus V_e/A (3 kV/mm, 300 Hz), where V_e is the effective volume generating the heat and A is the surface area dissipating the heat.

Fig. 31 Efficiency and maximum output of the Shinsei ultrasonic motor for various friction materials.

(a) Pressing force vs. wear

$$\text{Wear L (µm)} = \alpha\, F\, H$$

$\alpha = 0.0275$

F: pressing force (kgf)

H: drive period (hr)

■ 3kg

(b) Driving period vs. wear

Fig. 32 Wear and driving period of the ultrasonic motor for CFRP friction material.

1) Voltage change
   lack of slow motion

2) Frequency change
   lack of slow motion

3) Phase change
   low efficiency

4) Pulse Width Modulation

Fig. 33 Control methods of the ultrasonic motor.

Fig. 34 Vibration velocity dependence of the quality factor Q and temperature rise for both
A (resonance) and B (antiresonance) type resonances of a longitudinally vibrating
PZT rectangular transducer through d31.

APPENDIX 79

COMPACT PIEZOELECTRIC ULTRASONIC MOTORS

Kenji Uchino
International Center for Actuators and Transducers
Intercollege Materials Research Laboratory, The Pennsylvania State
University
University Park, PA 16802, USA

ABSTRACT

Electromagnetic motors were invented more than a hundred years ago. While these motors still dominate the industry, a drastic improvement cannot be expected except through new discoveries in magnetic or superconducting materials. Regarding conventional electromagnetic motors, tiny motors smaller than $1cm^3$ are rather difficult to produce with sufficient energy efficiency. Therefore, a new class of motors using high power ultrasonic energy -- ultrasonic motor, is gaining wide spread attention. Ultrasonic motors made with piezoceramics whose efficiency is insensitive to size are superior in the mini-motor area.

This paper reviews recent developments of miniature ultrasonic motors using piezoelectric resonant vibrations, which will be a promising candidate for intravascular and intraureteral applications. Following the historical background, ultrasonic motors using the standing and traveling waves are introduced. Driving principles and motor characteristics are explained in comparison with the conventional electromagnetic motors. Finally, reliability issues of ultrasonic motors are described.

The ultrasonic motor is characterized by "low speed and high torque," which is contrasted with "high speed and low torque" of the electromagnetic motors. Two categories are being investigated for ultrasonic motors: a standing-wave type and a propagating-wave type.

The standing-wave type is sometimes referred to as a vibratory-coupler type or a "woodpecker" type, where a vibratory piece is connected to a piezoelectric driver and the tip portion generates flat-elliptical movement. Attached to a rotor or a slider, the vibratory piece provides intermittent rotational torque or thrust. The standing-wave type has, in general, high efficiency, but lack of control in both clockwise and counterclockwise directions is a problem. An ultrasonic linear motor equipped with a multilayer piezoelectric actuator and fork-shaped metallic legs has been developed. Since there is a slight difference in the mechanical resonance frequency between the two legs, the phase difference between the bending vibrations of both legs can be controlled by changing the drive frequency.

The walking slider moves in a way similar to a horse using its fore and hind legs when trotting. A trial motor 20x20x5 mm^3 in dimension exhibited a maximum speed of 20 cm/s and a maximum thrust of 0.2 kgf with a maximum efficiency of 20 %, when driven at 98 kHz of 6 V. This motor has been employed in a precision X-Y stage. A compact ultrasonic rotory motor as tiny as 3 mm in diameter has also been developed. The stator consists of a piezoelectric ring and two concave/convex metal endcaps with "windmill" shaped slots bonded together, so as to generate a coupled vibration of up-down and tortional type. Since the component number and the fabrication process were minimized, the fabrication price would be decreased remarkably, and it would be adaptive to the disposable usage. When diven at 160 kHz, the maximum revolution 600 rpm and the maximum torque 1 mN·m were obtained for an 11 mm dia motor.

By comparison, the propagating-wave type (a surface-wave or "surfing" type) combines two standing waves with a 90 degree phase difference both in time and in space, and is controllable in both rotational directions. By means of the traveling elastic wave induced by the thin piezoelectric ring, a ring-type slider in contact with the "rippled" surface of the elastic body bonded onto the piezoelectric is driven in both directions by exchanging the sine and cosine voltage inputs. Another advantage is its thin design, which makes it suitable for installation in cameras as an automatic focusing device.

In the development of the reliable ultrasonic motors, the following themes should be systematically studied: 1. low loss and high vibration velocity piezoelectric materials development, 2. piezo-actuator designs taking account of heat generation and degradation mechanisms, 3. USM designs including displacement magnification mechanisms and frictional contact parts.

MODELING AND CHARACTERIZATION

Finite Element Methods

APPENDIX 80

Finite Element Analysis and Experimental Studies on the Thickness Resonance of Piezocomposite Transducers

Wenkang Qi* and Wenwu Cao*·†

*Intercollege Materials Research Laboratory, †Department of Mathematics, The Pennsylvania State University, University Park, Pennsylvania 16802

Finite element method (FEA) has been used to calculate the thickness resonance frequency and electromechanical coupling coefficient k_t for 2-2 piezocomposite transducers. The results are compared with that of the effective medium theory and also verified by experiments. It is shown that the predicted resonance frequencies from the effective medium theory and the unit cell modeling using FEA deviate from the experimental observations for composite systems with a ceramic aspect ratio (width/length) more than 0.4. For such systems, full size FEA modeling is required which can provide accurate predictions of the resonance frequency and thickness coupling constant k_t.

KEY WORDS: Aspect ratio; composite transducers; effective medium theory; finite element analysis; piezocomposites. © 1996 Academic Press, Inc.

1. INTRODUCTION

A transducer is usually characterized by two major properties: sensitivity and resolution. The sensitivity is related to the electromechanical coupling coefficient, while the resolution is related to the center frequency and bandwidth. At the beginning of the ultrasonic imaging industry, two types of piezoelectric materials were used as transducer materials: lead zirconate titanate (PZT) and polyvinylidene fluoride (PVDF). PZT has high acoustic impedance, making it very difficult to send ultrasonic energy into the human tissue, which has very low acoustic impedance. In addition, the Q value of PZT is very high so that the bandwidth is narrow resulting in poor resolution due to ringing effects. On the other hand, PVDF has a very good acoustic impedance match with human tissue, but its electromechanical coupling coefficient is very low, resulting in low sensitivity. In addition, the low dielectric constant of PVDF also creates the problem of electric impedance mismatch, which limits the application of PVDF in array transducers (Table I).

The advent of piezoelectric composites greatly improved this situation [1,2]. Piezocomposites have large coupling coefficients as well as low acoustic impedance, making them ideal transducer materials. Nowadays, piezoelectric composites are widely used in making underwater acoustic and medical ultrasonic transducers [2–4]. However, due to the biphase nature and the large difference in the elastic stiffness between the polymer and the ceramic, the surface displacement is often nonuniform [5–8]. It is therefore difficult to accurately predict the resonance frequency of the composite transducers using simplified models.

The most commonly-used method for designing composite transducers is the effective medium model [4]. Experience reveals that the actual resonance frequency of the designed

TABLE I
Material Properties of PZT and Epoxy

	Elastic compliance (10^{-12} m^2/N)					
	s_{11}^E	s_{33}^E	s_{12}^E	s_{13}^E	s_{44}^E	s_{66}^E
PZT	16.5	20.7	−4.78	−8.45	43.5	42.6
Epoxy	286.7	286.7	−97.9	−97.9	769	769

Piezoelectric constants, d_{ij}, (10^{-12} C/N) dielectrics constants, k_{ij}, (ϵ_0) coupling constants, $k_{iλ}$ and k_t, and density $ρ$ (kg/m^3)

	d_{15}	d_{31}	d_{33}	$\epsilon_{11}^1/\epsilon_0$	$\epsilon_{33}^1/\epsilon_0$	k_{15}	k_{31}	k_{33}	k_t	$ρ$
PZT	741	−274	593	1700	1470	0.675	0.39	0.75	0.50	7800
Epoxy				4.0	4.0					1097

composite transducer is often lower than the theoretical estimates from the effective medium theory. Motivated by this discrepancy, we have conducted a combined experimental and finite element analysis to give a detailed assessment of the effective medium model and to derive the conditions for the application of such theoretical estimates. We also intended to evaluate the validity of the commonly used unit cell FEA modeling [9–11]. For simplicity, we only analyze a 2-2 composite transducer, but the conclusions are also valid for 1-3 type composite transducers.

2. EFFECTIVE MEDIUM MODEL FOR 2-2 PIEZOCOMPOSITES

A typical 2-2 composite is shown in figure 1. It is a layered structure of alternating polymer and piezoceramic constituents.

The constitutive relations for the polymer phase can be written as the following,

$$T_1 = c_{11}S_1 + c_{12}S_2 + c_{12}S_3 \tag{1a}$$

$$T_2 = c_{12}S_1 + c_{11}S_2 + c_{12}S_3 \tag{1b}$$

$$T_3 = c_{12}S_1 + c_{12}S_2 + c_{11}S_3 \tag{1c}$$
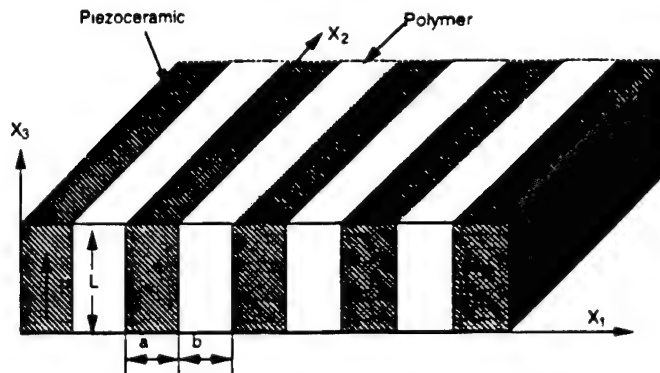
FIG. 1.   Configuration of 2-2 composite investigated in this study.

$$T_4 = c_{44}S_4 \tag{1d}$$

$$T_5 = c_{44}S_5 \tag{1e}$$

$$T_6 = c_{44}S_6 \tag{1f}$$

$$D_1 = \epsilon_{11}E_1 \tag{1g}$$

$$D_2 = \epsilon_{11}E_2 \tag{1h}$$

$$D_3 = \epsilon_{11}E_3 \tag{1i}$$

Here, T_l and S_l ($l = 1, 2, \ldots 6$) are the stress and strain components, respectively, in Voigt notation [12], E_i and D_i ($i = 1, 2, 3$) are the electric field and electric displacement respectively, c_{ij} are the elastic stiffness constants and ϵ_{ij} are the dielectric constants.

Similarly, if we take the x_3-direction as the poling direction, the constitutive relations in the ceramic phase can be written as:

$$T_1 = c_{11}^E S_1 + c_{12}^E S_2 + c_{13}^E S_3 - e_{31}E_3 \tag{2a}$$

$$T_2 = c_{12}^E S_1 + c_{11}^E S_2 + c_{13}^E S_3 - e_{31}E_3 \tag{2b}$$

$$T_3 = c_{13}^E S_1 + c_{13}^E S_2 + c_{33}^E S_3 - e_{33}E_3 \tag{2c}$$

$$T_4 = c_{44}^E S_4 - e_{15}E_2 \tag{2d}$$

$$T_5 = c_{44}^E S_5 - e_{15}E_1 \tag{2e}$$

$$T_6 = c_{66}^E S_6 \tag{2f}$$

$$D_1 = e_{15}S_5 + \epsilon_{11}^S E_1 \tag{2g}$$

$$D_2 = e_{15}S_4 + \epsilon_{11}^S E_2 \tag{2h}$$

$$D_3 = e_{31}S_1 + e_{31}S_2 + e_{33}S_3 - \epsilon_{33}^S E_3 \tag{2i}$$

where e_{il} are the piezoelectric constants, and the superscripts, E and S, refer to quantities at constant electric field and strain, respectively.

We can follow the same procedure as in [4] and use all the assumptions proposed there to derive the effective properties (denoted with an overbar) of a 2-2 composite.

$$\overline{c_{33}^E} = V\left[c_{33}^E - V'\frac{(c_{12} - c_{13}^E)^2}{V'c_{11}^E + Vc_{11}}\right] + V'c_{11} \tag{3a}$$

$$\overline{e_{33}} = V\left[e_{33} - V'e_{31}\frac{(c_{13}^E - c_{12})}{V'c_{11}^E + Vc_{11}}\right] \tag{3b}$$

$$\overline{\epsilon_{33}^S} = V\left[\epsilon_{33}^E + \frac{e_{31}^2 V'}{V'e_{11}^E + Vc_{11}}\right] \tag{3c}$$

$$\overline{c_{33}^D} = \overline{c_{33}^E} + \frac{\overline{e_{33}^2}}{\overline{\epsilon_{33}^S}} \tag{3d}$$
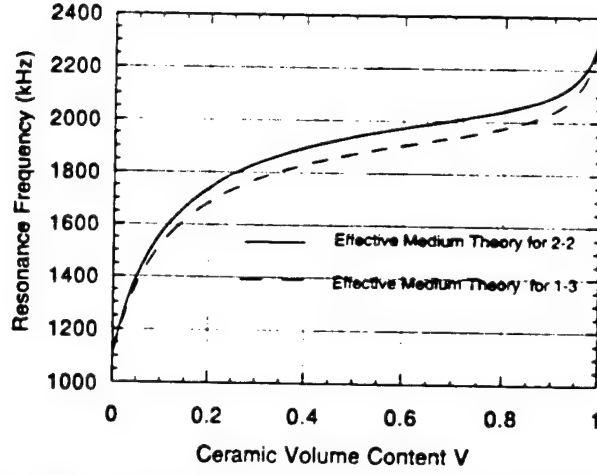
FIG. 2. Resonance frequencies for 2-2 and 1-3 composites calculated using the effective medium theory for different ceramic volume content.

$$\overline{h_{33}} = \frac{\overline{e_{33}}}{\overline{\epsilon_{33}^S}} \tag{3e}$$

$$\overline{\beta_{33}^S} = \frac{1}{\overline{\epsilon_{33}^S}} \tag{3f}$$

$$\overline{\rho} = V\rho^C + V'\rho^P \tag{3g}$$

In the above expressions, V and V' are the volume percentages of ceramic and polymer, respectively, $V' = 1 - V$, and ρ^P and ρ^c are the densities of the ceramic and polymer. Using the conventional definition, one can derive all the relevant effective quantities for the thickness mode operation,

$$\overline{k}_t = \frac{\overline{h_{33}}}{\sqrt{\overline{c_{33}^D}\overline{\beta_{33}^S}}} = \frac{\overline{e_{33}}}{\overline{c_{33}^D}\overline{\epsilon_{33}^S}} \tag{4}$$

$$\overline{Z} = \sqrt{\overline{c_{33}^D}\overline{\rho}} \tag{5}$$

$$\overline{v_l} = \sqrt{\frac{\overline{c_{33}^D}}{\overline{\rho}}} \tag{6}$$

$$f_r = \frac{\overline{v_l}}{2L} \tag{7}$$

$\overline{v_l}$ and L are the longitudinal wave speed and the thickness of the composite in the poling (x_3) direction and f_r is the resonance frequency givenby the effective medium theory.

Using the above equations, we have calculated the effective thickness resonance frequency for a 2-2 composite of 1 mm thick. Compared with a 1-3 composite transducer of the same thickness, the resonance frequency of a 2-2 composite is higher than that of a 1-3 composite of the same ceramic volume content (Fig. 2). The same is true also for the thickness coupling constant $\overline{k}_t$ (Fig. 3).
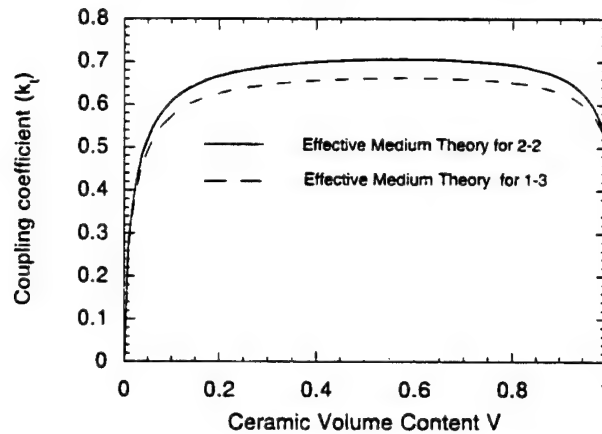
FIG. 3. Coupling constant k_t calculated for 2-2 and 1-3 composites of different ceramic volume content.

Although the effective medium theory is relatively simple and sometimes gives reasonable estimate for the resonance frequency, it fails to account for the aspect ratio effect, which can be substantial if the a/L (width/length) ratio is not sufficiently small [6,7]. For systems with large a/L ratio and low ceramic content, the isostrain assumption is no longer valid.

In addition, since a real transducer always contains a finite number of cells, one would not expect a very good match with experimental results from a unit cell model that automatically assuming periodic boundary conditions. For this reason, we have performed FEA on 2-2 composite transducers using both the unit cell and full dimension models.

3. FINITE ELEMENT ANALYSIS

The nonuniform displacement at the surface of composite transducers has been observed experimentally [5.8]. This inhomogeneity can greatly affect the overall performance of a transducer. For low frequencies, the situation may be treated by using elasticity theory and describing the two constituents separately. Some approximations can be used in solving the low frequency problem since there are no significant phase differences in the structure [6–8]. However, when the operating frequency is high and close to the thickness resonance, we must use FEA for an accurate theoretical prediction.

A commercial package ANSYS was used in our study and two models were analyzed: (1) A unit cell model, which was also analyzed by several other researchers [9–11]; (2) A finite real dimensional system. These FEA results are checked against our experiment results.

After some test runs, we found that the results from a 2-D model are almost the same as those from a 3-D model for the geometry we have chosen. Therefore, for computational efficiency, we performed only 2-D modeling. The models and the coordinate system are shown in figure 4.

One of our objectives is to study the change of the thickness resonance frequency and the electromechanical coupling coefficient k_t with respect to the change of ceramic aspect
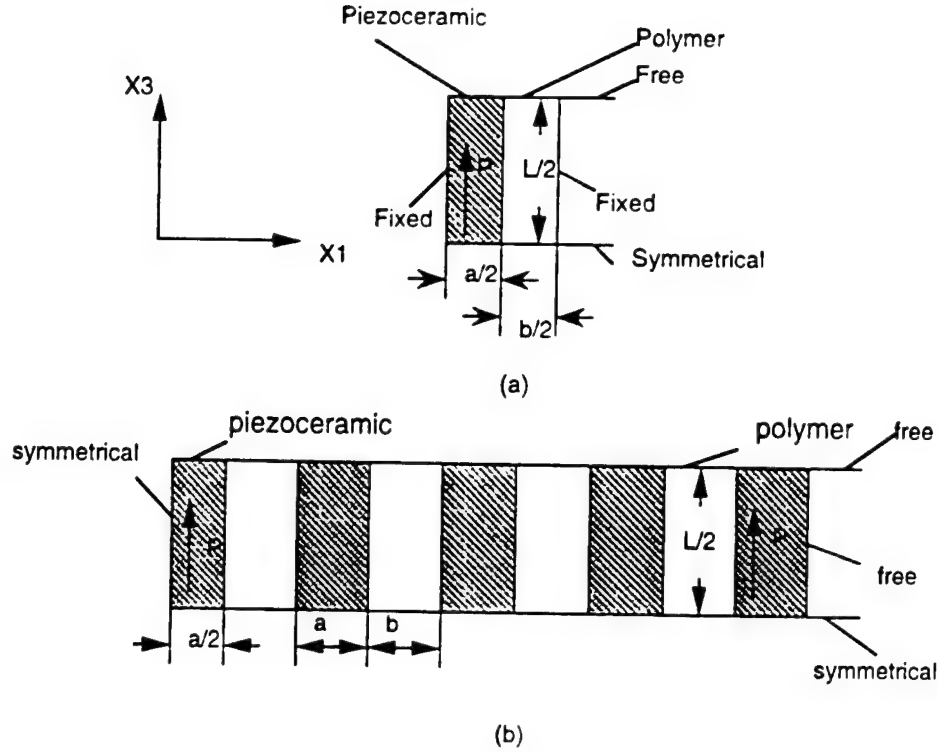
(a)

(b)

FIG. 4. 2-D models used in the finite element analysis (a) unit cell model; (b) full dimension model.

ratio. Both the thickness resonance and the anti-resonance frequencies were calculated. The resonance frequency is calculated under short circuit condition (constant E) while the anti-resonance frequency is calculated in open circuit condition (constant D) [13]. From these two resonance frequencies, the electromechanical coupling coefficient k_t can be calculated using the formula,

$$k_t^2 = \frac{\pi f_r}{2f_a} \tan\left(\frac{\pi(f_a - f_r)}{2f_a}\right) \tag{8}$$

where f_r and f_a are the resonance and anti-resonance frequencies, respectively.

First, we performed analysis on the unit cell model. Only a quarter of the unit cell is needed due to symmetry (Fig. 4a). A composite of real dimensions was then analyzed. Again, only a quarter of the piece was analyzed due to symmetry (Fig. 4b). The results are plotted in figure 5 together with the experiment results.

4. RESULTS AND DISCUSSIONS

In order to verify the theoretical results, we made a series of 2-2 composite transducers using PZT-5H and Spurrs epoxy. The dimension along the x_2-axis (into the paper) is made large enough so that the system can be treated as two dimensional. We start by making
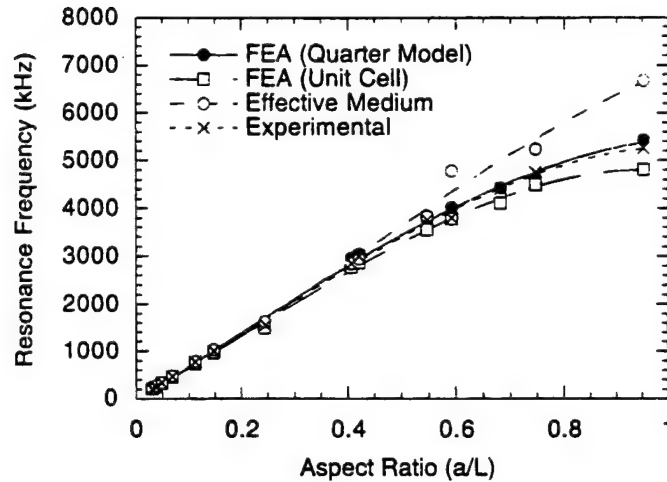
FIG. 5. Comparison of observed resonance frequencies and theoretical predictions from the effective medium theory, unit cell and full dimension finite element models at different ceramic aspect ratios. The widths of the ceramic and polymer are $a = 0.273$ mm and $b = 0.362$ mm, respectively.

a thick 2-2 piezocomposite in the x_3-dimension, and later gradually increased the a/L ratio by shortening L, i.e., shortening the x_3-dimension without changing the other dimensions. After each cutting, the sample is re-electroded and the resonance frequency measured using a HP 4194A impedance analyzer. From the impedance curves, the resonance and anti-resonance frequencies can be obtained, and the electromechanical coupling coefficient k_t can be determined using Eq. (8).

Another experiment was also performed to check the dimensional effect in the x_1-direction. In other words, reducing the number of cells in the composite structure to see if it affects the resonance frequency in the x_3-dimension. Impedance measurements were also used as the means to characterize this effect.

Figure 5 shows the comparison of the resonance frequencies calculated by the effective medium theory, unit cell FEA and real dimensional model FEA together with the experimental results. When the ceramic ratio a/L is less than 0.4, all theoretical models agree quite well with the experimental observations. But for a/L greater than 0.4, the effective medium theory prediction is too high while the prediction from the unit cell FEA model is too low. Only the real dimensional model provide accurate prediction for the resonance frequency.

The coupling constant k_t calculated from effective medium theory is independent of the aspect ratio Fig. 3. However, experimental results demonstrate a fluctuation of k_t with change of aspect ratio Fig. 6. This fluctuation is mainly caused by the coupling between the thickness mode and other lateral modes or their higher harmonics.

When the thickness, L, is reduced, the resonance frequency is shifted to higher frequencies. Whenever the resonance frequency approaches one of the lateral modes or their higher harmonics, energy will be lost to the lateral modes and the coupling constant k_t is reduced. Further increase of the thickness resonance frequency may recover some of the lost energy through mode decoupling until reaching the next lateral mode, which causes another reduction of the coupling constant. Therefore, we expect the k_t value to
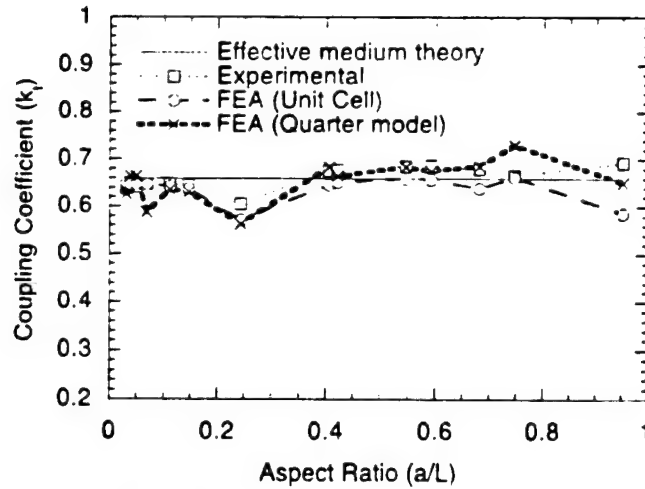
FIG. 6. Comparison of observed coupling constant k_t and theoretical calculations from the effective medium theory, unit cell and full dimension finite element models at different ceramic aspect ratios. The widths of the ceramic and polymer are $a = 0.273$ mm and $b = 0.362$ mm. respectively.

go up and down with the decrease in L. As shown in figure 6, this mode coupling effect is well accounted for by the FEA. Both the unit cell model and the real dimensional model show this fluctuating feature and the real dimensional model provides better agreement with the experimental observations.

The difference between unit cell and real dimensional model indicate that the resonance frequency in the x_3-dimension will also depend on the composite size in the x_1-dimension (number of cells). However, this effect is weak when the a/L ratio is small.

5. SUMMARY AND CONCLUSIONS

We have performed both experimental and FEa investigations on the resonance frequency of a 2-2 piezoelectric composite transducer and compared with the effective medium theory estimation. It is found that the effective medium theory gives good estimates when the a/L ratio is less than 0.4, but the calculation of the coupling constant is incorrect whenever the thickness mode gets close to one of the lateral modes. When the a/L ratio is larger than 0.4, the effective medium theory prediction will be higher than the actual resonance frequency of the composite transducer. The FEA results depend strongly on the details of the model. Unit cell modeling seems to underestimate the resonance frequency for composites with large a/L ratio but the fluctuation of k_t can be reasonably predicted. The most accurate modeling is the real dimensional FEA, which gave good predictions for both resonance frequency and coupling constant for all aspect ratios investigated.

ACKNOWLEDGMENTS

REFERENCES

[1] Newnham, R. E., Bowen, L. J., Klicker, K. A., and Cross, L. E., Composite piezoelectric transducer, *Materials in Engineering 2*, 93–106 (1980).

[2] Smith, W. A., The Role of Piezocomposites in Ultrasonic Transducers, in *1989 IEEE Ultrasonic Symposium Proceedings*, pp. 755–766.

[3] Hayward, G., and Hossack, J. A., Unidimensional Modeling of 1-3 Composite Transducer, in *1989 Ultrasonic International Conference Proceedings*, pp. 531–536.

[4] Smith, W. A., Modeling 1-3 composite piezoelectric: thickness-mode oscillations, *IEEE Trans. Ultrason. Ferroelect. Freq. Contr. 38*, 40–47 (1991).

[5] Auld, B. A., Kunkel, H. A., Shui, Y. A., and Wang, Y., Dynamic Behavior of Periodic Piezoelectric Composites, in *1983 IEEE Ultrasonics Symposium*, pp. 554–558.

[6] Cao, W., Zhang, Q., and Cross, L. E., Theoretical study on the static performance of piezoelectric ceramic-polymer composites with 2-2 connectivity, *IEEE Trans. Ultrason. Ferroelec. Freq. Contr. 40*, 103–109 (1993).

[7] Cao, W., Zhang, Q., and Cross, L. E., Theoretical study on the static performance of piezoelectric ceramic-polymer composites with 1-3 connectivity, *J. Appl. Phys. 72*, 5814–5821 (1992).

[8] Zhang, Q. M., Cao, W., Zhao, J., and Cross, L. E., Piezoelectric performance of piezoceramic-polymer composites with 2-2 connectivity—a combined theoretical and experimental study, *IEEE Trans. Ultrason. Ferroelec. Freq. Contr. 41*, 556–564 (1994).

[9] Hossack, J. A., and Hayward, G., Finite-element analysis of 1-3 composite transducers, *IEEE Trans. Ultrason. ferroelec. Freq. Contr. 38*, 618–629 (1991).

[10] Hladky-Hennion, A., and Decarpigny, J., Finite element modeling of active periodic structures: application to 1-3 piezocomposites, *J. Acoust. Soc. Am. 94*, 621–635 (1993).

[11] Hossack, J. A., Auld, B. A., and Batha, H. D., Techniques for Suppressing Spurious Resonant Modes in 1:3 Composite Transducers, in *1991 IEEE Ultrasonics Symposium*, pp. 651–655.

[12] Wallace, W. C., Thermoelastic theory of stressed crystals and high-order elastic constants, *Solid State Phys.: 25*, 301–405 (1970).

[13] Lerch, R., Simulation of piezoelectric devices by two- and three-dimensional finite elements, *IEEE Trans. Ultrason. Ferroelec. Freq. Contr. 37*, 233–246 (1990).

APPENDIX 81

Finite element study on random design of 2-2 composite transducer

Wenkang Qi and Wenwu Cao

Whitaker Center for Medical Ultrasonic Transducer Engineering
Materials Research Laboratory
The Pennsylvania State University, university park, Pennsylvania, 16802

ABSTRACT

Random 2-2 composite transducers are studied using FEM(ANSYS®). Admittance curves as well as beam patterns in the nearfield are calculated and used to evaluate the performance of random 2-2 composite designs. First, the pressure and the normal velocity distributions at the interface of water and transducer are calculated using ANSYS, then, these pressure and velocity data are used to calculate the beam pattern using Helmholtz integral. Different random configurations are studied and the results are discussed.

Keywords: ultrasound, transducer, composite, piezoelectric, FEM.

1. INTRODUCTION

Piezoelectric composite has advantages over single phase piezoelectric ceramics and polymer materials for transducer applications[1-6]. It has lower acoustic impedance than that of ceramic, higher electromechanical coupling coefficient and lower Q than that of pure ceramic and much higher sensitivity than the piezoelectric polymer. But at high frequencies, its periodic structure causes spurious lateral modes, which interfere the thickness resonance. The coupling of these lateral modes with the thickness mode will reduce the thickness electromechanical coupling coefficient and prolong the ringdown. Conventional method to eliminate the coupling is to reduce the pitch size so that the lateral resonance is pushed up to twice of the thickness resonance frequency[7]. However, the thinnest blade of a diamond saw available now is around 20 microns, which limits the frequency range of the composite transducers made by dice and fill technique to less than 20 MHz.

It is shown that the lateral resonance may be destroyed by introducing randomness into the composite structure[8-10]. In this paper, we further investigate this idea by introducing randomness into the polymer phase in low ceramic percentage composite. Various random patterns have been tested, and the beam pattern in the nearfield is studied by using ANSYS® combined with direct integration of the Helmholtz equation[11].

2. RESONANCE MODES IN 2-2 COMPOSITE

Fig.1 shows the thickness mode [Fig.1(B)] and the lateral mode[Fig.1(C)]. This lateral mode shown in Fig 1(C) is the first lateral pitch resonance, in which the ceramic and polymer constituents are vibrating out of phase. This transducer is designed to have 44% PZT ceramic and the filler is spurs epoxy. The dimensions are: thickness 1.12mm, ceramic width 0.273mm, polymer width 0.362mm.

(a) One half of a 2-2 composite model, larger phase(darker color) is polymer.

(b) The thickness anti resonance mode at 1.5MHz.

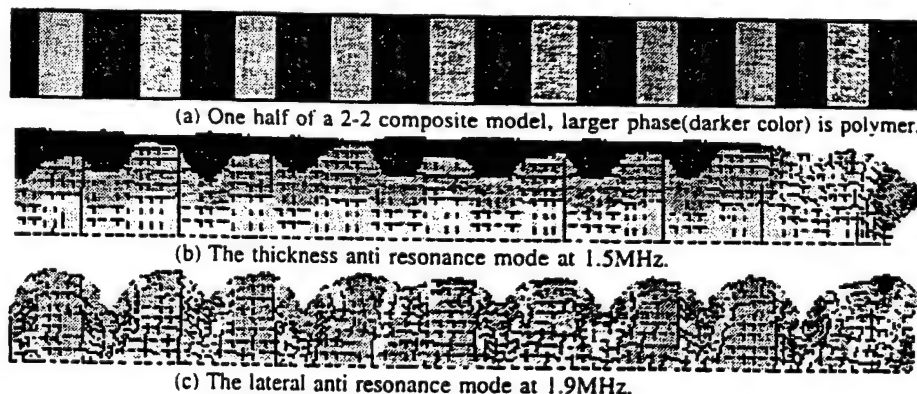(c) The lateral anti resonance mode at 1.9MHz.

Fig.1

Fig.2 (a) and (b) are admittance curves from ANSYS calculation and experiment, respectively. The two peaks represent the thickness and the pitch resonance, respectively. We can see that the two modes strongly couple to each other in this design. In this case, the thickness coupling coefficient is rather low, $k_t \approx 0.5$.

In order to suppress the pitch resonance, we randomize the width of the kerfs which are filled with polymer. Fig. 3 shows the admittance curve for the case of 100% random kerf width. Although the electric admittance of random composite shows encouraging results, we need to further examine the performance of this random composite by considering the beam pattern.
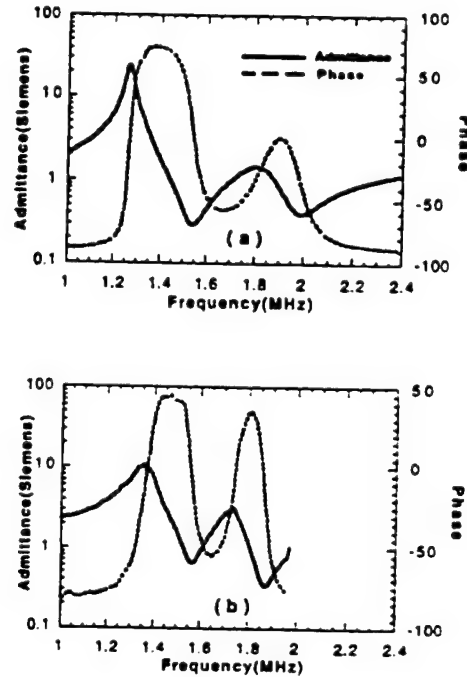
Fig.2 (a) The admittance curve of a 33 layer periodic 2-2 composite calculated by FEM.
(b) The measured admittance curve of a 33 layer periodic 2-2 composite.
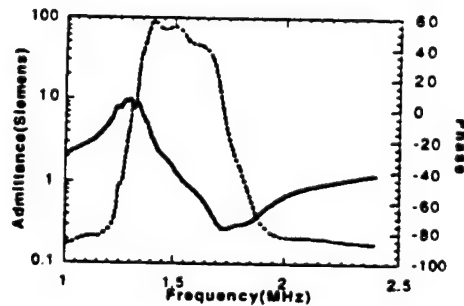
Fig.3 The calculated admittance of a 33 layer random 2-2 composite using ANSYS®

3. BEAM PATTERN

In medical imaging, we are interested in the beam characteristics in vicinity of the focal point, which is different from sonar applications. In order to accurately calculate the beam pattern, we have to consider the effect of water loading. This can be accomplished by using Fluid Structure Interface element in ANSYS®. Harmonic analysis using FEM can provide pressure distribution as well as normal velocity distribution at the interface. These distributions will then be used to do the Helmholtz integral to calculate the nearfiled beam pattern. Since the Green's function and its derivative have some singularity points at the

integration surface, we can not do the integration in the original coordinate plane. Coordinate transformation has been performed to resolve the singularity problem. This procedure has been applied to calculate the beam pattern for the random composite transducer and the result is shown in Fig. 4.
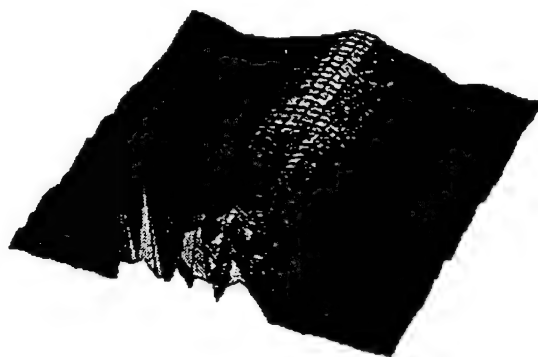

Fig.4 The beam pattern of a 33 layer random composite transducer immersed in water.

One can see several problems with this design: First, because the transducer is not symmetric in the x-direction, we lose the symmetry of the beam pattern. This is not desirable in medical imaging application since it causes imaging distortion. Second, although theoretically we can randomize the kerf, it is not feasible to dice with too many different kerfs in practice. Third, the beam width is wider than that of a periodic composite transducer, which means this design will not have better lateral resolution.

The first problem can be overcome by introducing symmetry in the x-direction while keeping the random kerfs in half of the composite. The beam pattern produced by the symmtrized random composite is shown in Fig.5. We can see that the beam pattern becomes symmetric again.
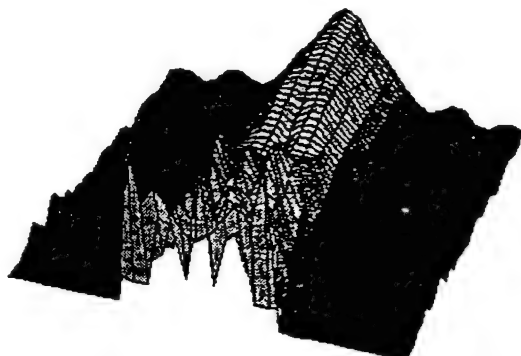
Fig.5 The nearfield of the random composite with symmetry in the x-direction.

However for the second and third problem, we have to investigate other random designs. From FEM study, we found that it is not necessary to randomize every kerf, instead, a repeated sequence of different size kerfs can give reasonable reduction of the lateral mode. Figs. 6(a-e) are admittance curves of 2-2 composites with 33 cells and different sequential kerf configurations [Note that all the configurations have symmetry in the x-direction to keep the beam pattern symmetric].

In Fig.6(a), the first 16 kerfs are randomly chosen with a fixed volume percentage of ceramic, while the last 16 kerfs are obtained from mirror symmetry of the first 16 kerfs. The 17th is set equal to the first one. In Fig.6(b), the first 5 kerfs are randomly chosen, then repeat this pattern 3 times, the 16th is the same as the first one and the 17th is the same as the second. The other 16 kerfs are mirror symmetry of the first 16. In Fig.6(c), the first 4 kerfs are random, and the pattern is repeated 4 times, while the 17th is equal to the first. The other 16 kerfs are mirror symmetry of the first 16. In Fig.6(d), the first 3 kerfs are random, and then repeat this pattern 5 times, the 16th is equal to the first, while the 17th is equal to the second. In Fig.6(e), the first 2 kerfs have different sizes, and then the pattern is repeated 8 times, the 17th is equal to the first. The other 16 kerfs are mirror symmetry of the first 16.

178

As we can see in Fig.6(a), the admittance curve is almost the same as that in Fig. 3, in which every kerf size is randomly chosen, except there is a small bump around 1.2MHz. Interestingly, as we reduce the sequential random number from 17 down to 3, little change occurred for the admittance curve. However, when the sequential random number becomes 2, there is a new lateral mode showing clearly in the admittance curve as shown in Fig. 6(e).
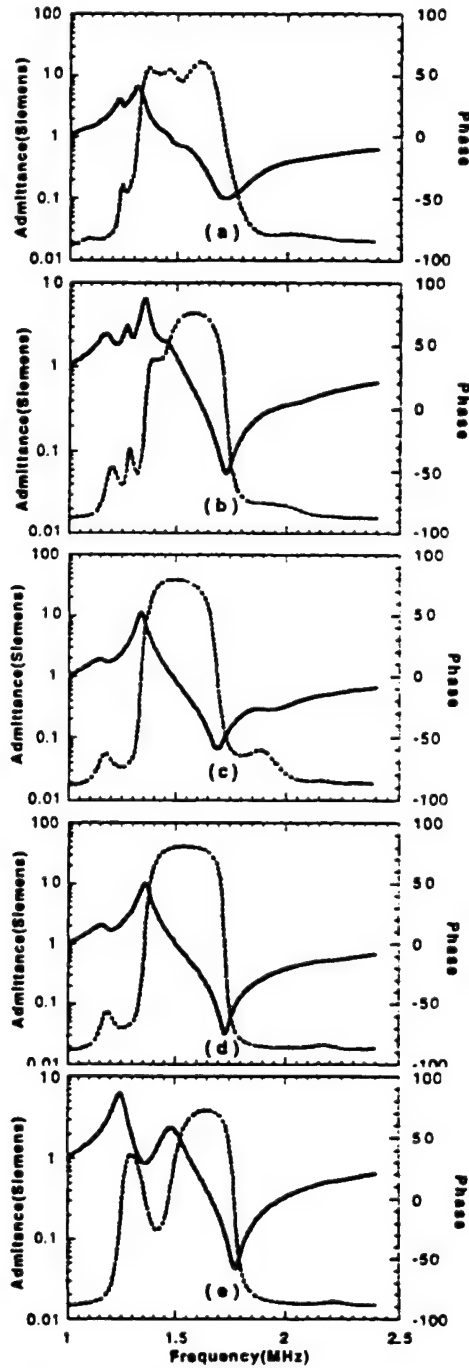

Fig.6   (a) Sequential number is 16; (b) Sequential number is 5;
            (c) Sequential number is 4; (d) Sequential number is 3;
            (e) Sequential number is 2.

As mentioned above, we can not use the admittance curve as the sole criterion, the beam pattern must also be investigated for designing random 2-2 composite transducers.

In Fig.7, the pressure profiles near the focal point were compared for three different sequential numbers 3, 4, and 5. The beam width shows little change. Therefore, there are not much advantages for making higher sequential number composite transducers.
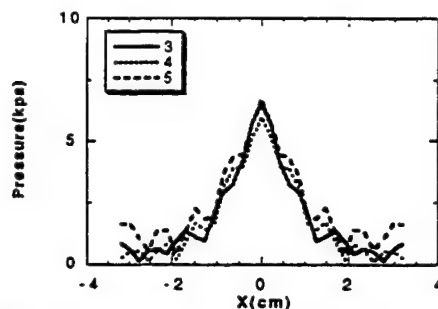
Fig.7 Pressure profile near the focal point for sequential number 3,4,5, respectively.

4. CONCLUSION

In a periodic 2-2 composite transducer, lateral modes are produced and they will couple to the thickness mode for high frequency operation. This coupling effect and the manufacture difficulties limit the current frequency range of composite transducer to less than 20 MHz. We show that these lateral modes may be suppressed through randomization of kerf width [3-4]. However, FEM analysis shows that the randomization will introduce distortion to the beam pattern. In order to maintain the symmetry of the beam pattern, it is necessary to keep the 2-2 composite structure symmetric in the x-direction.

From practical point of view, it is not feasible to randomize every kerf in a 2-2 composite due to production difficulties. A series of composites with sequential kerf width are explored using FEM. From the calculated admittance curves, the lateral mode can almost be suppressed when the sequential number is 3 or 4. By looking at the nearfield beam pattern, the sequential number 3 is preferred. It is also easier to fabricate for low sequential number than for higher sequential numbers.

ACKNOWLEDGMENT

REFERENCES

[1]. R.E. Newnham, L.J. Bowen, K.A. Klicker, and L.E. Cross, "Composite piezoelectric transducer." Materials in Engineering, Vol.2, pp. 93-106, 1980.

[2]. W.A. Smith, "The role of piezocomposites in ultrasonic transducers," Proc. 1989 IEEE Ultrason. Symp., 1989, pp. 755-766.

[3]. G. Hayward and J.A. Hossack, "Unidimensional modeling of 1-3 composite transducer," Ultrason. Int. 89 Conf. Proc., 1989, pp. 531-536.

[4]. H.A. Kunkel, etal, "Finite-Element Analysis of Vibration Modes in Piezoelectric Ceramic Disks,", IEEE transaction on ultrasonic, ferroelectrics, and frequency control, Vol. 37, No. 4, July 1990.

[5]. John A. Hossack and Gordon Hayward, "Finite-Element Analysis Of 1-3 Composite Transducers", IEEE transactions on ultrasonic, ferroelectrics, and frequency control, Vol. 38, No.6, Nov. 1991.[6]. Anne-Christine, "Finite element modeling of active periodic structures: Application to 1-3 piezocomposites," J. Acoust. Soc. Am. 94(2), Pt. 1, Aug., 1993.

[6]. Yukio Kagawa, etal, "Finite Element Simulation of a Composite Piezoelectric Ultrasonic Transducer," IEEE transactions on sonic and ultrasonics, Vol. Su-26, No. 2, Mar. 1979.

[7] Smith, W.A., "Modeling 1-3 composite piezoelectric: thickness-mode oscillations", IEEE Trans. Ultrasonic. Ferroelect. Freq. Contr. 38, 40-47(1991).

[8] Hayward, G., and Hossack, J.A., "Unidimensional Modelling of 1-3 composite transducer", in 1989 Ultrasonic International Conference Proceeding, PP. 531-536.

[9] Wenwu Cao and Wenkang Qi, "Plane wave propagation in finite 2-2 composite", J. Appl.. Phys. Vol. 78, PP. 4627-4632, 1995.

[10] Wenwu Cao and Wenkang Qi, "Multisource excitations in a stratified biphase structure",J. Appl. Phys. vol. 78, pp. 4640-4646, 1995.

[11] D.T. Wilton. 1978. "Acoustic Radiation and Scattering from Elastic Structures," International Journal for nummerical Methods in Engineering, 13:123-138.

APPENDIX 82

Evaluation of Piezocomposites for Ultrasonic Transducer Applications—Influence of the Unit Cell Dimensions and the Properties of Constituents on the Performance of 2-2 Piezocomposites

Xuecang Geng and Q. M. Zhang

Abstract—A theoretical model on piezoceramic polymer composites with laminar periodic structure is presented. A salient feature of this model is that it can treat explicitly how the unit cell dimensions and other material properties influence the performance of an ultrasonic transducer made of 2-2 piezocomposites. The model predicts that there exist a series of modes associated with the periodic structure of a composite, which is beyond the stop-band edge resonance prediction. One of the main concerns in designing a composite transducer is how the surface vibration profile changes with frequency and how this is influenced by the aspect ratio of the ceramic plate. It was predicted that as long as the thickness resonance is below the first lateral mode frequency, there is always a frequency f_1 which is near the thickness resonance and at which the polymer and ceramic vibrate in unison. The effect of aspect ratio is to change the position of f_1 with respect to the thickness resonance frequency and the bandwidth in which polymer and ceramic have nearly the same vibration amplitude and phase. It is also predicted that, when operated in a fluid medium such as water, there will be a resonance mode which has a frequency determined by the velocity of the fluid medium and the unit cell length d and is associated with the oscillation of the fluid. The behavior of a composite plate as an acoustic transmitter and receiver and the influence of the aspect ratio of the ceramic plate on them are also investigated.

I. INTRODUCTION

TO PRODUCE a high performance ultrasonic transducer requires the transducer material. which performs the energy conversion between the mechanical form and electrical form. to have a high electromechanical coupling factor, broad operation frequency bandwidth. and adjustable acoustic impedance which can be tuned to match that of the medium. With single phase piezoelectric materials, it is difficult to simultaneously meet all the requirements. Piezoceramic polymer composite materials. which combine the high electromechanical activity of piezoceramics and the low acoustic impedance of polymeric materials, have provided new opportunities to meet these requirements [1],

[2]. Since their inception in the seventies, the piezoceramic polymer composites have become one of the most important transducer materials and are being widely used in many areas such as medical imaging. nondestructive evaluation of materials, underwater vision. etc.

Being a diphasic material, the properties of a piezocomposite can be tailored over a wide range by adjusting the material properties and geometric shapes of constituent phases [3], [4]. It has also been observed that the properties of a composite vary with frequency [5]. The challenge of understanding the seemingly complex relationship between the performance of a composite and the properties of its constituents and the great opportunities provided by these materials have stimulated, in the past two decades. extensive investigations. both experimental and theoretical. on this class of materials.

The classic work of Newnham *et al.*. [6] which classified piezocomposite materials according to the connectivity of the constituent phases, has greatly facilitated the analysis of the composites as the connectivity is one of the key parameters in determining the performance of a composite. For composites with 1-3 and 2-2 connectivities. both analytical and finite element modelings have been carried out which have provided useful guidelines in the design of composite transducers [7]–[13]. The isostrain models developed by Smith and Auld [3] and Hashimoto and Yamaguchi [4] linked the material parameters of the constituents to the effective piezoelectric properties of 1-3 and 2-2 composites, respectively. and predicted that the thickness coupling factor k_t of a composite can approach the longitudinal coupling factor k_{33}^l of the piezoceramic rod and k_{33}^w of the plate, respectively. which is in good agreement with experiments for composites with a high aspect ratio t/d. where t is the thickness and d is the periodicity of the composites. Auld *et al.* [7]. using the Floquet theory. investigated wave propagations in both the 2-2 and 1-3 composites and showed that, due to the periodic structure of these composites, there exist pass bands and stop bands. similar to the band structure in a crystal solid, and that there are piezoelectric resonances associated with the stop band edge resonances [7]–[10]. For the design of composite transducers. the recognition of the existence of these modes and the precise prediction of their frequencies are of

prime importance since, quite often, it is the interference of these modes with the thickness mode of a composite that deteriorates the performance. especially at high frequency operations. Craciun *et al.* [11] examined the coupling between these lateral modes and thickness mode using a phenomenological approach, and the results provided qualitative understanding between the coupling of the two modes and the material properties. The results from these investigations have played important roles in the development of ultrasonic composite transducers. However, due to the approximations used in the analysis. there are severe limitations. For instance, various features related to the dynamic behavior of a composite transducer were not treated in a consistent manner, and the effect of finite thickness of a composite on the material properties. that has been shown to be crucial in determining the performance of a piezocomposite, cannot be treated in these analyses. To address these realistic issues of a composite material, finite element analysis has been employed by many authors [12]–[15]. For example, the dispersion curves have been evaluated for various modes in a composite and the dependence of the electromechanical coupling factor on the ceramic volume content and the ceramic rod shape was investigated.

For a piezoceramic polymer composite, it has to be recognized that it is the ceramic phase which performs the energy conversion between the electric and mechanical forms and the polymer phase merely acts as a carrier which transfers acoustic energy between the piezoceramic and the external medium. Hence. if the elastic coupling between the two constituents is not very effective, even if the material exhibits a perfect acoustic impedance matching with the medium and the electromechanical coupling factor is large. the electromechanical performance of the material is still poor. These observations clearly indicate that in modeling piezoceramic polymer composites. one cannot simply use an effective medium approach and has to take into account explicitly this internal degree of freedom.

Recently. we developed an analytical model on the dynamic problem of a piezocomposite material with the 2-2 connectivity [16]–[18]. In the model. we avoided the approximations made in the earlier works and, hence. can address the dynamic responses of 2-2 piezocomposites. such as the frequencies of various modes. the mode coupling, the electromechanical coupling factor. the vibration profiles of composites under different external driving conditions. etc.. in a realistic and consistent manner. For example, one of the misconceptions in the early studies of the dynamic behavior of piezocomposites is the direct linkage between the non-uniform surface vibration profile in a composite and the aspect ratio of the ceramic plate (in 2-2 composites) or rod (in 1-3 composites). Here. we will show. which was verified by experiment. that for a composite plate. as long as the thickness resonance frequency is below that of the lateral mode. there is always a frequency near the thickness resonance where the vibration profile of the composite is uniform. The influence of the
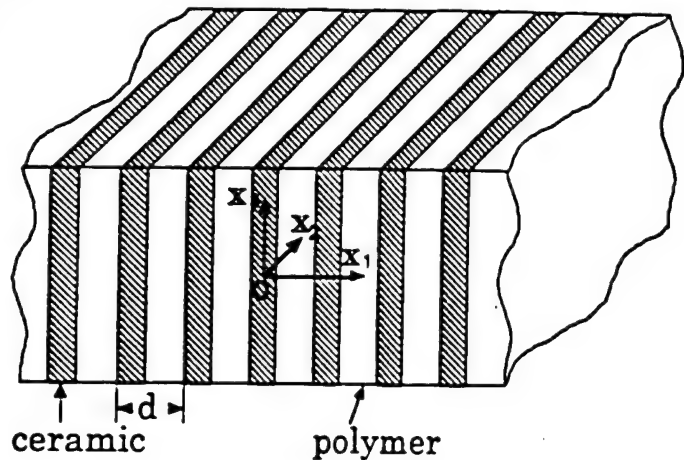
(a)
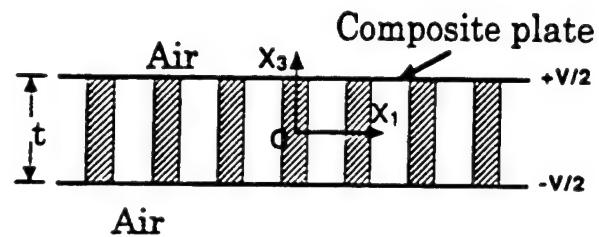
(b)

Fig. 1. (a) Schematic drawing of a 2-2 piezoceramic polymer composite which is unbounded in all three orthogonal directions. The period of the composite is d. (b) Schematic drawing of a 2-2 piezoceramic polymer composite plate with a thickness t situated in air. An external voltage is applied to the composite.

aspect ratio is on the frequency bandwidth in which the polymer and ceramic vibrate in unison.

The approach taken here to solve the vibration problem in a finite thickness composite plate is based on the method of partial wave expansion where the various elastic and electric fields are expanded in terms of the eigenmodes of the structure as shown in Fig. 1(a) and the coefficients for each eigen-mode are determined by the boundary conditions at $x_3 = t/2$ [Fig. 1(b)]. Some of the results have been presented in early publications. In this paper, we would like to summarize briefly these early results and then. discuss many issues pertinent to the design of piezocomposite ultrasonic transducers based on the results from the model analysis. The paper is organized as the following: First, the details of derivation of the eigenfunctions for a 2-2 piezoceramic polymer composite will be presented. Based on the results, the wave propagation in an unbounded 2-2 composite is analyzed. For the finite thickness composites, various features of a piezocomposite plate under an external driving electric field in both air and water media are treated. The response behavior of the composite plate under external pressure is also treated. Experiments were conducted to provide comparison with the theoretical re-

sults. From the results, we will show explicitly how the aspect ratio t/d influences the transduction performance of a composite plate.

II. GENERAL SOLUTIONS FOR WAVE PROPAGATION IN A 2-2 PIEZOCOMPOSITE

Shown in Fig. 1(a) is a schematic drawing of a 2-2 composite (unbounded in the x_3-direction), where plates of piezoceramic and polymer form a parallel array. The coordinate system is chosen such that the x_3-axis is along the ceramic poling direction, the x_1-axis is perpendicular to the ceramic polymer interface, and x_2-axis is in the plane of the plates. For a typical 2-2 composite, the dimensions in the x_1- and x_2-directions are much larger than the period d and thickness t. In the treatment here, they can be taken as infinite without much error in the results. Under these conditions, the composite is clamped in the x_2-direction so that $S_2 = 0$, where S_2 is the strain in the x_2-direction, and the problem becomes a two-dimensional one with no dependence on the x_2-coordinate.

The governing equations for the dynamics of a 2-2 composite are [19]–[21]:

$$\frac{\partial T_1}{\partial x_1} + \frac{\partial T_5}{\partial x_3} = \rho \frac{\partial^2 u_1}{\partial t^2}$$
$$\frac{\partial T_5}{\partial x_1} + \frac{\partial T_3}{\partial x_3} = \rho \frac{\partial^2 u_3}{\partial t^2} \qquad (1)$$
$$\frac{\partial D_1}{\partial x_1} + \frac{\partial D_3}{\partial x_3} = 0.$$

The symbols adopted in this paper are summarized here: T_i and S_i are the stress and strain tensor components, where the Voigt notation is used, u_i is the elastic displacement vector, ρ is the density, and D_i is the electric displacement vector. E_i is the electric field. The relevant material coefficients are: e_{ij} is the piezoelectric coefficient, c_{ij} is the elastic stiffness, and ε_i is the dielectric permittivity. Equation (1) holds for both the polymer and ceramic phases.

The constitutive equations, relating stress T, strain S, electric displacement D, and electric field E, are:

$$[T] = [c^E][S] - [e_t][E] \qquad (2a)$$
$$[D] = [e][S] + [\varepsilon^S][E]. \qquad (2b)$$

For the polymer phase, e_{ki} in (2) are zero. The superscripts E and S indicate that the coefficients are under the constant E field and constant strain conditions, respectively. Here $[e_t]$ is the transposed $[e]$ array. Under the quasi-electrostatic approximation, the electric field E can be expressed as:

$$\vec{E} = -\nabla \Phi \qquad (3)$$

where Φ is the electrical potential.

Combining (1), (2), and (3) yields three second order differential equations, governing the elastic displacement u_1, u_3, and electric potential Φ in the ceramic plate, respectively:

$$c_{44}^E u_{3.11} + (c_{13}^E + c_{44}^E)u_{1,13} + c_{33}^E u_{3,33}$$
$$+ (e_{33}\Phi_{,33} + e_{15}\Phi_{,11}) = \rho \ddot{u}_3$$
$$c_{11}^E u_{1.11} + (c_{13}^E + c_{44}^E)u_{3,13} + c_{44}^E u_{1.33}$$
$$+ (e_{31} + e_{15})\Phi_{,13} = \rho \ddot{u}_1 \qquad (4)$$
$$e_{15}u_{3.11} + (e_{15} + e_{31})u_{1,13} + e_{33}u_{3.33}$$
$$- (\varepsilon_{33}^S \Phi_{,33} + \varepsilon_{11}^S \Phi_{,11}) = 0.$$

For the polymer phase, e_{ij} in (4) should be taken to zero.

For an unbounded composite, the solutions to (4) have the form:

$$u_3 = A \exp(j(hx_1 + \beta x_3 - \omega t))$$
$$u_1 = B \exp(j(hx_1 + \beta x_3 - \omega t)) \qquad (5)$$
$$\Phi = C \exp(j(hx_1 + \beta x_3 - \omega t))$$

where A, B, and C are three constants, ω is the angular frequency, h and β are the wave vector components in the x_1- and x_3-directions, respectively.

Substituting (5) into (4) yields three homogeneous equations with the undetermined constants A, B, and C,

$$[M_{ij}][A_i] = 0 \qquad (6)$$

where $[A_i] = [A, B, C]^T$ and

$$[M_{ij}] = \begin{pmatrix} c_{33}^E\beta^2 + c_{44}^E h^2 - \rho\omega^2 & (c_{13}^E + c_{44}^E)h\beta & e_{33}\beta^2 + e_{15}h^2 \\ (c_{13}^E + c_{44}^E)h\beta & c_{11}^E h^2 + c_{44}^E\beta^2 - \rho\omega^2 & (e_{15} + e_{31})h\beta \\ e_{33}\beta^2 + e_{15}h^2 & (e_{15} + e_{31})h\beta & -(\varepsilon_{11}^S h^2 + \varepsilon_{33}^S\beta^2) \end{pmatrix}.$$

$$(7)$$

The condition for a nontrivial solution is such that the determinant of the coefficient matrix vanishes, i.e.,

$$|M_{ij}| = 0 \qquad (8)$$

Equation (8) is a cubic equation of h^2. For a given ω and β, (8), in general, has three roots of h^2, denoted as h_1^c, h_2^c, and h_3^c, corresponding to the quasi-electromagnetic, quasi-longitudinal, and quasi-shear waves in the piezoelectric plate, respectively. For each h_i^c, the ratio among A, B, and C can be determined from (6). Since we are concerned only with the waves in the x_3 direction which correspond to piezo-active modes in a finite thickness composite plate, the general solutions become:

$$u_3^c = \sum_i R_i^c f_i^c \cos(h_i^c x_1) \sin(\beta x_3)$$
$$u_1^c = \sum_i R_i^c g_i^c \sin(h_i^c x_1) \cos(\beta x_3) \qquad (9)$$
$$\Phi^c = \sum_i R_i^c t_i^c \cos(h_i^c x_1) \sin(\beta x_3)$$

where i runs from 1 to 3. f_i, g_i and t_i are the cofactors of $A_{k1}(i)$, $A_{k2}(i)$, and $A_{k3}(i)$ of the determinant (8) (where

h is replaced by h_i^c for $i = 1, 2,$ and 3, respectively). The $\exp(-j\omega t)$ term in (9) is omitted.

Following the similar procedure, the solutions for the polymer phase can be obtained (the center of the polymer plate is at $x_1 = d/2$):

$$u_3^P = \sum_i R_i^P f_i^P \cos\left(h_i^P\left(x_1 - \frac{d}{2}\right)\right)\sin(\beta x_3)$$

$$u_1^P = \sum_i R_i^P g_i^P \sin\left(h_i^P\left(x_1 - \frac{d}{2}\right)\right)\cos(\beta x_3)$$

$$\Phi^P = C^P \cosh\left(\beta\left(x_1 - \frac{d}{2}\right)\right)\sin(\beta x_3)$$

(10)

where $i = 1, 2$. f_i^P and g_i^P are the cofactors of $A_{k1}(i)$. $A_{k2}(i)$ of the determinant (8) with all the material parameters replaced by those of the polymer phase, and

$$(h_1^P)^2 = (k_L^P)^2 - \beta^2 \text{ and } (h_2^P)^2 = (k_T^P)^2 - \beta^2$$

where $k_L^P = \frac{\omega}{\nu_L^P}$, $k_T^P = \frac{\omega}{\nu_T^P}$, ν_L^P, and ν_T^P are the longitudinal and shear wave velocities of the polymer phase, respectively.

The expressions of the stresses and the electric displacement in the ceramic plate can be obtained by substituting (9) into (2):

$$T_1^C = \sum_i T_{11}^C(i)R_i^C \cos(h_i^C x_1)\cos(\beta x_3)$$

$$T_3^C = \sum_i T_{33}^C(i)R_i^C \cos(h_i^C x_1)\cos(\beta x_3)$$

(11)

$$T_5^C = \sum_i T_{31}^C(i)R_i^C \sin(h_i^C x_1)\sin(\beta x_3)$$

where

$$T_{11}^C(i) = c_{11}^E h_i^C g_i^C + (c_{13}^E f_i^C + e_{31}t_i^C)\beta$$

$$T_{33}^C(i) = c_{13}^E h_i^C g_i^C + (c_{33}^E f_i^C + e_{33}t_i^C)\beta$$

(12)

$$T_{31}^C(i) = -c_{44}^E(\beta g_i^C + h_i^C f_i^C) - e_{15}h_i^C t_i^C$$

where $i = 1, 2, 3$ for ceramic phase. The electric displacements are:

$$D_1^C = \sum_i D_1^C(i)R_i^C \sin(h_i^C x_1)\sin(\beta x_3)$$

(13a)

$$D_3^C = \sum_i D_3^C(i)R_i^C \cos(h_i^C x_1)\cos(\beta x_3)$$

(13b)

where $D_1^C(i) = -e_{15}(\beta g_i^C + h_i^C f_i^C) + \varepsilon_{11}^S h_i^C t_i^C$ and $D_3^C(i) = e_{31}h_i^C g_i^C + e_{33}3f_i^C - \varepsilon_{33}^S \beta t_i^C$. Similar expressions can be obtained for the polymer plate. For instance, the electric displacements are:

$$D_1^P = -\varepsilon_{11}^P \beta C^P \sinh\left(\beta\left(x_1 - \frac{d}{2}\right)\right)\sin(\beta x_3)$$

(14a)

$$D_3^P = -\varepsilon_{11}^P \beta C^P \cosh\left(\beta\left(x_1 - \frac{d}{2}\right)\right)\cos(\beta x_3)$$

(14b)

Making use of the boundary conditions at the ceramic polymer interface($x_1 = \nu d/2$, where ν is the volume fraction of the ceramic in a composite), which are:

$$u_1^C = u_1^P, u_3^C = u_3^P, T_1^C = T_1^P \text{ and } T_5^C = T_5^P$$

(15a)

$$\text{and } \Phi^C = \Phi^P \text{ and } D_1^C = D_1^P$$

(15b)

R_i^C, R_j^P and C^P, ($i = 1, 2, 3$ and $j = 1, 2$) can be determined. Expanding (15) in terms of (9), (10), (11), (13), and (14) yields the following six homogeneous linear equations:

$$\begin{pmatrix} K_{11} & K_{12} & K_{13} & K_{14} & K_{15} & 0 \\ K_{21} & K_{22} & K_{23} & K_{24} & K_{25} & 0 \\ K_{31} & K_{32} & K_{33} & K_{34} & K_{35} & 0 \\ K_{41} & K_{42} & K_{43} & K_{44} & K_{45} & 0 \\ 0 & 0 & K_{53} & K_{54} & K_{55} & K_{56} \\ 0 & 0 & K_{63} & K_{64} & K_{65} & K_{66} \end{pmatrix}\begin{pmatrix} R_1^P \\ R_2^P \\ R_1^C \\ R_2^C \\ R_3^C \\ C^P \end{pmatrix} = 0$$

(16)

where the matrix elements K_{ij} are functions of β, ω, d, ν, and the material parameters of both the polymer and piezoceramic. The condition that the determinant

$$|K_{ij}| = 0$$

(17)

yields the relationship between ω and β, the dispersion relations in the composite. For each pair of ω and β, the relationships among R_i^C, R_j^P, and C^P can be obtained. Hence, the various stress, strain, electric field distributions in the composite can be determined.

III. DISPERSION CURVES, MODES, AND MODES COUPLING OF A 2-2 PIEZOCOMPOSITE

Equation (17) allows us to determine the relationship between β and ω, the dispersion curves, for a composite if the materials parameters of piezoceramic and polymer and the geometric parameters, such as d and ν, are known. Equation (17) is a transcendental function which cannot be solved analytically. A computer code was developed and the dispersion curves were evaluated numerically.

Shown in Fig. 2 (the solid curves) are the two lowest branches of the dispersion curves for a 2-2 composite made of PZT-5H piezoceramic and Spurr epoxy with the ceramic volume fraction of 44%.[1] For all the composites discussed in this paper, except otherwise specified, PZT-5H piezoceramic and Spurr epoxy are used as the constituents. The parameters of PZT-5H and Spurr epoxy are presented in Table I. The general trend of the dispersion curves in Fig. 2 resembles that of the symmetric Lamb waves in a plate [19]. As will be shown later, at small βd limit, the first branch corresponds to the longitudinal wave propagation along the x_3-direction, that is, u_3 is the dominant displacement which is more or less uniform and in phase in the x_1-direction, and its phase velocity is the effective longitudinal

---

[1]PZT-5H is the trade-mark of Morgan Mattroc Inc., Beddford, OH 44146, for one of its PZT piezoceramics. Spurr epoxy is the trademark of Polysciences, Inc., Warrington, PA 18976.
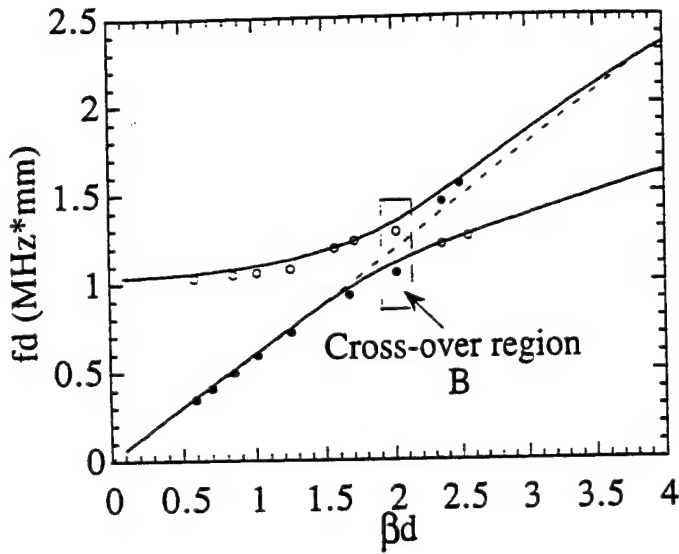
Fig. 2. The first and second branches of the dispersion curves (solid lines) and the experimentally measured thickness mode (solid circles) and lateral mode (open circles) for a 2-2 composite made of PZT-5H and Spurr epoxy with 44% ceramic content. After the crossover region, the thickness mode jumps to the second branch. The criterion for the thickness mode is that it is the one with the larger effective coupling factor.

TABLE I

THE MATERIAL PROPERTIES OF PZT-5H AND SPURR EPOXY USED FOR THE 2-2 COMPOSITES IN THE INVESTIGATION.

PZT-5H: $e_{33} = 23.09$ C/m^2, $e_{31} = -6.603$ C/m^2, $e_{15} = 17.0$ C/m^2. $c_{11} = 12.72 * 10^{10}$ N/m^2, $c_{44} = 2.3 * 10^{10}$ N/m^2, $c_{33} = 11.74 * 10^{10}$ N/m^2, $c_{13} = 8.47 * 10^{10}$ N/m^2, $K_{11} = 1700$, $K_{33} = 1470$. $\rho = 7500$ kg/m^3.
Spurr epoxy: $c_{11} = 5.4 * 10^9$ N/m^2, $c_{44} = 1.3 * 10^9$ N/m^2, $\rho = 1100$ kg/m^3.

wave velocity of the composite. The second branch corresponds to the lateral resonance which arises from the periodic structure of the composite, that is. it is a stationary shear wave along the x_1-direction, and it can be shown that the displacement u_3 of the polymer phase is much larger than that of the ceramic phase and the phase difference between them is 180°. Hence, it is the so-called stop-band edge resonance as predicted by Auld et al. [7], [8].

Under the assumption that the wave length λ in the x_3-direction ($\beta = 2\pi/\lambda$) is equal to two times the composite thickness t (the condition for the thickness resonance), the theoretical dispersion curves can be compared with the experimental results, obtained from composites with different thickness. At low βd on the dispersion curves, where d is the period of the composite. the frequency of the fundamental thickness mode from the experiment falls on the first branch as marked by the black dots. and the frequency of the first lateral mode falls on the second branch as marked by the open circles. After the crossover region B, the modes interchange the positions on the dispersion curves where the thickness mode is in the second branch while there is a weak resonance at a frequency below the
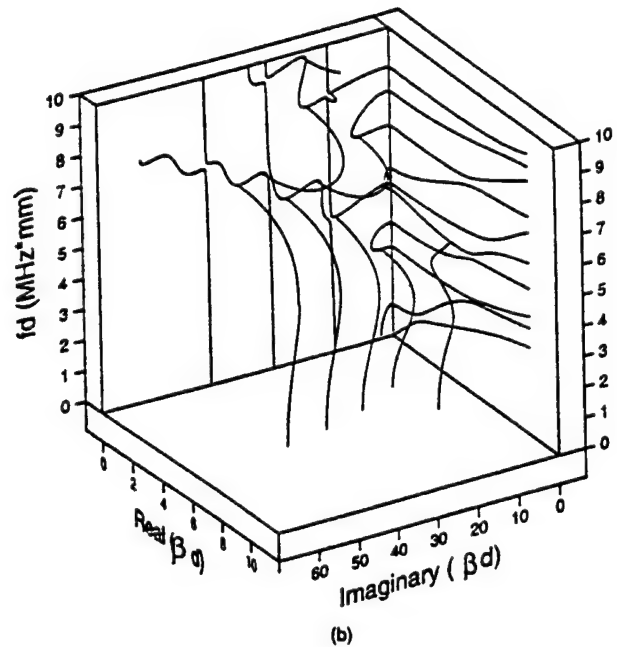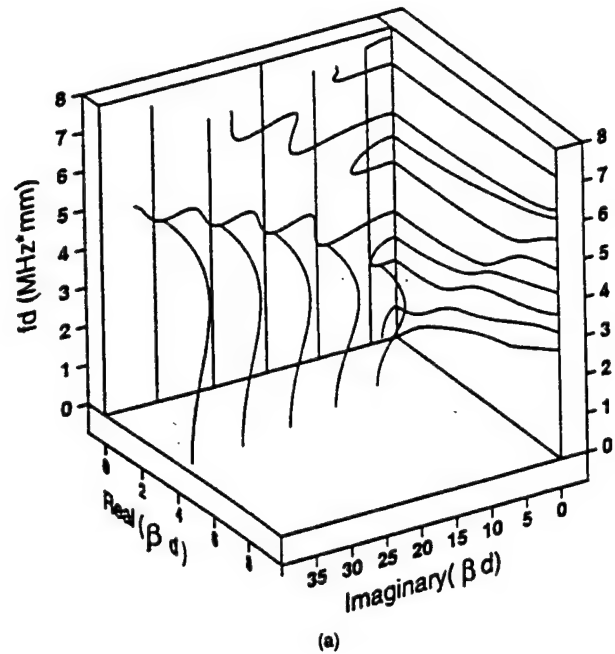

(a)

(b)

Fig. 3. The dispersion curves for a 2-2 composite [Fig. 1(a)] made of PZT-5H and Spurr epoxy for (a) 15% ceramic volume content and (b) 44% ceramic volume content.

thickness mode, and it falls on the first branch. Here, the thickness mode is defined as the one with higher electromechanical coupling factor. The mode on the first branch gradually diminishes at high βd values. The result is presented in Fig. 2. Clearly, there is an excellent accord between the theoretically derived resonance frequencies and experimentally observed ones.

Shown in Figs. 3(a) and 3(b) are the 3-dimensional dispersion curves for 2-2 composites with 15% and 44% ceramic volume fraction, respectively. Obviously, there are imaginary and complex branches of the dispersion curves. The modes on these branches are non-propagating
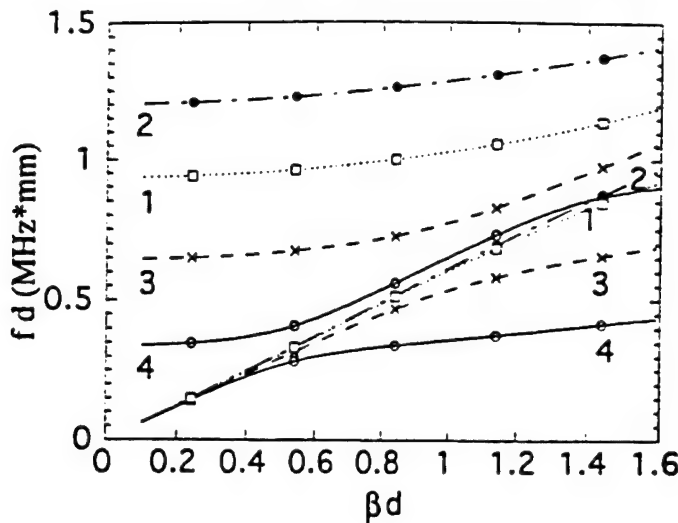
Fig. 4. The effect of the properties of the polymer matrix on the dispersion curves of 2-2 composites with PZT-5H ceramic, derived from the model. The properties of the polymer phase are: curve 1: $c_{11} = 7.72 * 10^9$ N/m^2, $c_{44} = 1.588 * 10^9$ N/m^3; curve 2: $c_{11} = 1.3634 * 10^{10}$ N/m^2, $c_{44} = 3.432 * 10^9$ N/m^2, $\rho = 1610$ kg/m^3; curve 3: $c_{11} = 3.173 * 10^9$ N/m^2, $c_{44} = 0.696 * 10^9$ N/m^2, $\rho = 1060$ kg/m^3; curve 4: $c_{11} = 1.622 * 10^9$ N/m^2, $c_{44} = 1.646 * 10^8$ N/m^2, $\rho = 890$ kg/m^3.

modes (imaginary branches) and attenuated modes (complex branches), respectively. These modes do not exist in an unbounded composite, however, they are important in the vibration problems of finite thickness plates as well as in semi-infinite mediums, where they correspond to the evanescent waves at the surface which will be discussed later in the paper.

Fig. 4 presents the effect of the stiffness of the polymer phase on the dispersion curves of a 2-2 composite with 30% ceramic content where PZT-5H is used as the piezoceramic phase. It is apparent that the frequency position of the second branch is very sensitive to properties of the polymer phase. This is quite understandable since, as will be shown later, the frequency position of this branch is directly related to the shear velocity of the polymer matrix for composites at this ceramic content. The lower the shear wave velocity of the polymer phase is, the lower the frequency of the second branch will be. Therefore, for a transducer operated at high frequencies, in order to avoid the interference from the lateral modes, a polymer matrix with a high shear velocity should be utilized even though the thickness coupling factor k_t of this composite may be reduced as a result of the stiffer polymer matrix [3], [4].

In order to further elucidate the origins of these resonant modes, it is instructive to make a comparison between the dispersion curves of a composite and those of single piezoceramic and polymer plates with appropriate boundary conditions [22]. In general, in piezoceramic polymer composites, the elastic stiffness of the piezoceramic is more than one order of magnitude higher than that of the polymer. It is reasonable to assume that the piezoceramic plates in a 2-2 composite are stress free at the ceramic-polymer interface, that is, the stress components T_1 and T_5
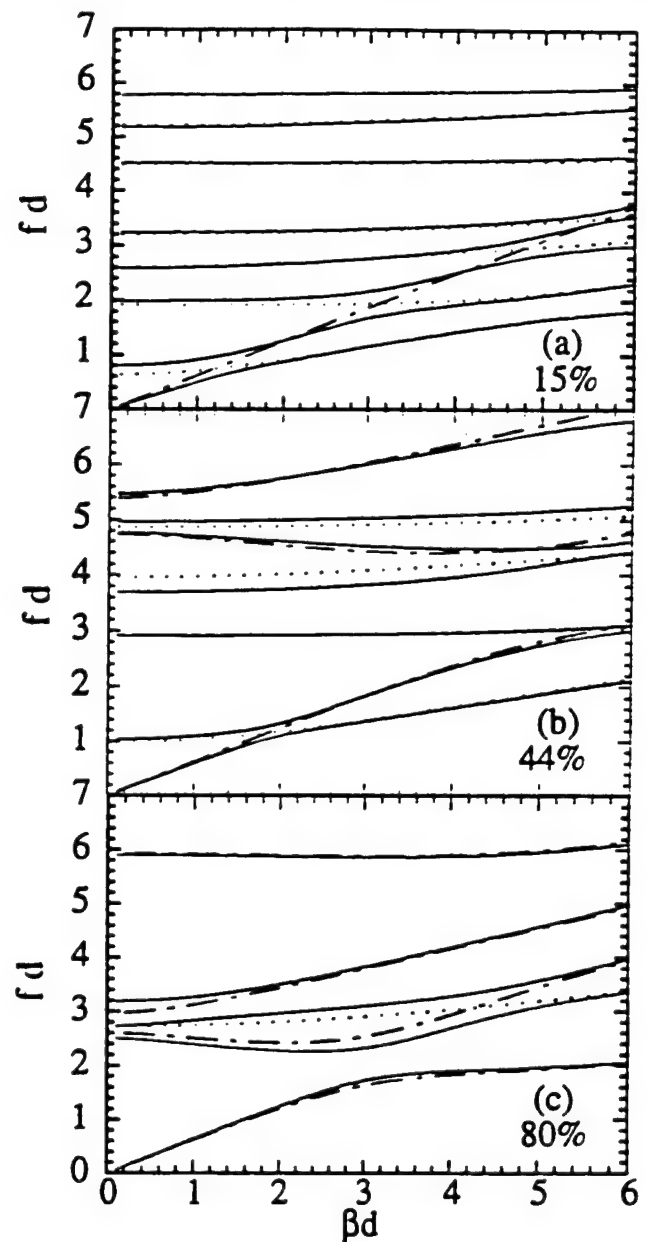

Fig. 5. Comparison of the dispersion curves in 2-2 composites with those in a single piezoceramic plate and a polymer plate for composites with (a) 15% ceramic content; (b) 44% ceramic; and (c) 80% ceramic content. PZT-5H is used as the piezoceramic and Spurr epoxy as the polymer phase.

are zero at the interface. Similarly, the polymer plates can be approximated as under the fixed boundary conditions, that is, u_1 and u_3 are zero at the interface. Under these assumptions, the dispersion curves of both single ceramic and single polymer plates are calculated for the plates with different widths corresponding to 2-2 composites with different ceramic volume fractions. The results are presented in Figs. 5(a), 5(b), and 5(c) corresponding to 2-2 composites with 15%, 44%, and 80% ceramic content, respectively. In these figures, the solid lines are the dispersion curves of the 2-2 composites, the dashed lines are those of the ceramic plate, and dotted lines are the dispersion curves of the polymer plate.

The results from these figures reveal that there are many resemblances between the dispersion curves of 2-2 composites and the dispersion curves of the single ceramic and single polymer plates with appropriate boundary conditions. For instance, at small βd, the first branch in the dispersion curves of the 2-2 composites with 44% and 80% ceramic volume content is very close to the first branch of the ceramic plate. On the other hand, for 2-2 composites with low ceramic volume content, a large difference between these two is found for the first branch. These results are consistent with those from Smith and Auld [3] and from Hashimoto and Yamaguchi [4] based on an effective medium model. For the second branch which corresponds to the lateral resonant mode in a composite plate, at low and medium ceramic volume content, it is close to the first branch of the polymer plate which frequency at small βd is equal to $V_T^P/2d_P$ where V_T^P and d_P are shear wave velocity and width of the polymer plate, respectively. However, for composites with high ceramic volume content such as the one shown here (80%), the second branch is related to the longitudinal resonance of the ceramic plate along the width- (or x_1-) direction while the shear resonance associated with the polymer plate lies on the third branch of the dispersion curves.

Obviously, the coupling between the two phases through the interface boundary conditions will influence the dispersion curves of the waves in the two phases. It is well known that the dispersion curves for the uncoupled waves are split at their crossover points when coupling is introduced [11]. Far from the crossover region, the coupled wave dispersion curves should nearly coincide with those of the uncoupled waves. If the coupling is very strong as for the 15% and 44% piezocomposites, the coupled waves exhibit large departure from the uncoupled curves in the crossover region, which is clearly shown in Figs. 5(a) and 5(b). While for the composite with 80% ceramic content, the coupling between the first and the second branches is through the coupling of P wave and SV wave in the ceramic plate where the interface does not have a significant effect on it.

IV. VIBRATION OF A FINITE THICKNESS COMPOSITE PLATE UNDER AN ELECTRIC FIELD IN AIR

In the previous section, the properties of guided wave propagation in laminated 2-2 piezocomposites have been analyzed. In spite of the fact that many effective parameters of the material can be derived by this simple method, one key issue in the design of a composite transducer, i.e., the influence of the aspect ratio of the ceramic plates (or the unit cell) in a composite on the performance of the transducer cannot be addressed. In this section, we will treat the vibration problem of a finite thickness composite plate under an external driving electric field and situated in air. From the analysis, one can obtain detailed information on how the surface vibration profile changes with frequency and its dependence on the aspect ratio of the ceramic plate (or the unit cell dimension), the possible resonant modes in a composite transducer, and the de-

pendence of the electromechanical coupling factor on the aspect ratio of the ceramic plate, etc. We will also show that, as long as the thickness resonance frequency is below the lateral mode frequency, the aspect ratio will not have a direct effect on the vibration uniformity of a composite near the thickness resonance. The influence is on the bandwidth in which the ceramic and polymer vibrate with nearly the same amplitude and phase.

A composite plate with a thickness t is drawn schematically in Fig. 1(b). For the problem treated here, the two free surfaces of the composite plate are electroded with conducting material and an AC electric field of a frequency f is applied between the two electrodes.

It is well known that there exist no simple solutions for the vibration problem of a finite thickness plate such as the piezocomposite treated here. One of the most frequently used approximation methods is to expand the elastic and electric fields in a material in terms of the eigenfunctions in an unbounded one [21]. Different techniques such as the variational technique and the method of least squares can be used to determine the expansion coefficients. For the composite plate treated here, we found that the variational technique is more appropriate in treating the boundary problem than the method of least squares because of the large difference in the vibration amplitudes between the two phases in the composite.

For the ceramic phase in the composite plate, the elastic displacements u_3 and u_1, and the electric potential Φ are expended in terms of the eigenfunctions derived:

$$u_3^C = \sum_{n=1}^{m}\sum_{i=1}^{3} R_{ni}^C f_{ni}^C \cos(h_{ni}^C x_1)\sin(\beta_n x_3)A_n$$

$$u_1^C = \sum_{n=1}^{m}\sum_{i=1}^{3} R_{ni}^C g_{ni}^C \sin(h_{ni}^C x_1)\cos(\beta_n x_3)A_n$$
$$\div C R_0^C \sin(h_{01}^C x_1) \tag{18}$$

$$\Phi^C = \sum_{n=1}^{m}\sum_{i=1}^{3} R_{ni}^C t_{ni}^C \cos(h_{ni}^C x_1)\sin(\beta_n x_3)A_n + C x_3.$$

Similarly, for the polymer phase in the composite plate:

$$u_3^P = \sum_{n=1}^{m}\sum_{i=1}^{2} R_{ni}^P f_{ni}^P \cos\left(h_{ni}^P\left(x_1-\frac{d}{2}\right)\right)\sin(\beta_n x_3)A_n$$

$$u_1^P = \sum_{n=1}^{m}\sum_{i=1}^{2} R_{ni}^P g_{ni}^P \sin\left(h_{ni}^P\left(x_1-\frac{d}{2}\right)\right)\cos(\beta_n x_3)A_n$$
$$\div C R_0^P \sin\left(h_{01}^P\left(x_1-\frac{d}{2}\right)\right) \tag{19}$$

$$\Phi^P = \sum_{n=1}^{m} C_n^P \cosh\left(\beta_n\left(x_1-\frac{d}{2}\right)\right)\sin(\beta_n x_3)A_n + C x_3$$

where R_{n1}^C, R_{n2}^C, R_{n3}^C, R_{n1}^P, R_{n2}^P, and C_n^P are determined in (16). β_n, h_{ni}^C, and h_{ni}^P are the wave vector components of the nth mode in the x_3- and x_1-directions where the superscripts c and p stand for the ceramic and polymer, respectively. h_{01}^C and h_{01}^P are related to the mode in which

β is equal to zero: $h_{01}^C = \sqrt{\frac{\rho^C}{c_{11}^C}}\omega$ and $h_{01}^P = \sqrt{\frac{\rho^P}{c_{11}^P}}\omega$. R_0^C and R_0^P are determined by (16) in which β is set to zero. The mode with $\beta = 0$ is generated due to the fact that the velocity of the electromagnetic wave is much faster than that of the elastic waves and the composite plate is clamped in the x_3-direction ($S_3 = 0$). A_n and C are the coefficients which will be determined by the boundary conditions which are traction free and $\Phi = \pm V/2$ (here $\exp(-j\omega t)$ is omitted) at $x_3 = \pm t/2$.

The stresses T_3, T_5 and electric displacement D_3 are expressed as:

$$T_3^C = \sum_{n=1}^{m}\sum_{i=1}^{3} T_{33}^C(n,i)\cos(h_{ni}^C x_1)\cos(\beta_n x_3)A_n$$
$$+ (e_{33} + T_0^C \cos(h_{01}^C x_1))C \tag{20a}$$

$$T_5^C = \sum_{n=1}^{m}\sum_{i=1}^{3} T_{13}^C(n,i)\sin(h_{ni}^C x_1)\sin(\beta_n x_3)A_n \tag{20b}$$

$$D_3^C = \sum_{n=1}^{m}\sum_{i=1}^{3} D_3^C(n,i)\cos(h_{ni}^C x_1)\cos(\beta_n x_3)A_n$$
$$+ (-\varepsilon_{33}^S + D_0^C \cos(h_{01}^C x_1))C \tag{20c}$$

$$T_3^P = \sum_{n=1}^{m}\sum_{i=1}^{2} T_{33}^P(n,i)\cos\left(h_{ni}^P\left(x_1-\frac{d}{2}\right)\right)\cos(\beta_n x_3)A_n$$
$$+ T_0^P \cos\left(h_{01}^P\left(x_1-\frac{d}{2}\right)\right)C \tag{20d}$$

$$T_5^P = \sum_{n=1}^{m}\sum_{i=1}^{2} T_{13}^P(n,i)\sin\left(h_{ni}^P\left(x_1-\frac{d}{2}\right)\right)\sin(\beta_n x_3)A_n \tag{20e}$$

$$D_3^P = \sum_{n=1}^{m}\sum_{i=1}^{2} D_3^P(n,i)\cos\left(h_{ni}^P\left(x_1-\frac{d}{2}\right)\right)\cos(\beta_n x_3)A_n$$
$$- \varepsilon_{11}^P C \tag{20f}$$

where $T_{33}^C(n,i)$, $T_{13}^C(n,i)$, $D_3^C(n,i)$, $T_{33}^P(n,i)$, $T_{13}^P(n,i)$, and $D_3^P(n,i)$ are the same as $T_{33}^C(i)$, $T_{31}^C(i)$, $D_3^C(i)$, $T_{33}^P(i)$, $T_{31}^P(i)$, and $D_3^P(i)$ in (11) to (14) if the subscript i there is replaced by n and i for i-th partial wave of n-th mode here. And

$$T_0^C = c_{13}^E h_{01}^C R_0^C, \quad T_0^P = c_{12}^P h_{01}^P R_0^P, \quad D_0^C = e_{31} h_{01}^C R_0^C.$$

The number of the eigenfunctions, m, required in the expansion is determined by the accuracy needed for the solution. For the problem treated here, we found that it is adequate to use eight eigen-modes in the expansion. In the frequency range studied ($fd < 2$ MHz*mm), there are two branches having real β and the other branches having either imaginary or complex β, which corresponds to the modes confined at the surface of $x_3 = \pm t/2$.

For the problem treated here, all the stress components in air are zero and for the sake of simplicity, D in air is also assumed to be zero since the dielectric permittivity of the composite is much higher than air. Under these conditions,

the variational formula takes the following form:

$$\int_V [(T_{kl,k} - \rho\ddot{u}_l)\delta u_l^* + D_{k,k}\delta\Phi^*]dV$$
$$+ \int_S [(-T_{kl})\delta u_l^* + (\Phi - \overline{\Phi})\delta D_k^*]dS = 0 \tag{21}$$

where the integration over time has been performed to take into account the complex notations for the quantities in the integrands [19], [21]. The * represents the complex conjugate of the corresponding quantity. The first integral is over the volume of the 2-2 composite plate, and it can be shown that it is equal to zero since all the quantities in the integrand satisfy (1). The second integral is over the surfaces of the composite plate at $x_3 = \pm t/2$ where $\overline{\Phi} = \pm V/2$ at $x_3 = \pm t/2$ where V is the applied voltage. The periodic condition of the composite in the x_1-direction and the symmetric condition of the solutions and the boundary conditions about the plane of $x_3 = 0$ allow the second integration to be performed over one unit cell at $x_3 = t/2$.

Substituting T_3, T_5, u_1, u_3, Φ, and D_3 into (21) yields the following linear algebraic equation:

$$(M_{ij})(A_j) = (V_i) \tag{22}$$

where (M_{ij}) is a 9×9 matrix, $(A_j) = (A_1, A_2, A_3, A_4, A_5, A_6, A_7, A_8, C)^T$, (V_i) is a 9×1 matrix whose elements depend only on V, the applied voltage. For a given frequency f, one can solve (22) to obtain A_j and C. From A_j and C, (18), (19), and (20) yield all the characteristic properties related to the vibration of a 2-2 composite plate with different thickness and different ceramic volume fraction such as the electrical impedance, surface displacement distribution, resonant modes, electromechanical coupling coefficient, etc.

For the composite plate treated here, the electrical impedance for a single repeating unit can be found from:

$$Z = \frac{V}{I} \tag{23}$$

where I is the current which is equal to $I = \frac{dQ}{dt} = -j\omega Q = -j2\omega b \int_0^{d/2} D_3 dx_1$, where Q and b are the electric charge and the length in the x_2-direction of the plate, respectively. To compare with the experimental result, the current I should be multiplied by N, the number of repeating unit in a composite plate.

Shown in Fig. 6(a) is the electric impedance curve calculated from (22) and (23) for a composite plate with $t/d = 4.5$ and the ceramic volume fraction $\nu = 44\%$. The electric impedance measured experimentally from the same composite plate is shown in Fig. 6(b) and clearly the theoretical impedance curve reproduces the experimental data quite well. The difference in the sharpness of the resonant peaks between the experimental data and the theoretical curve is due to the fact that in the theoretical analysis, the electrical and mechanical losses of the ceramic and polymer phases were not included.
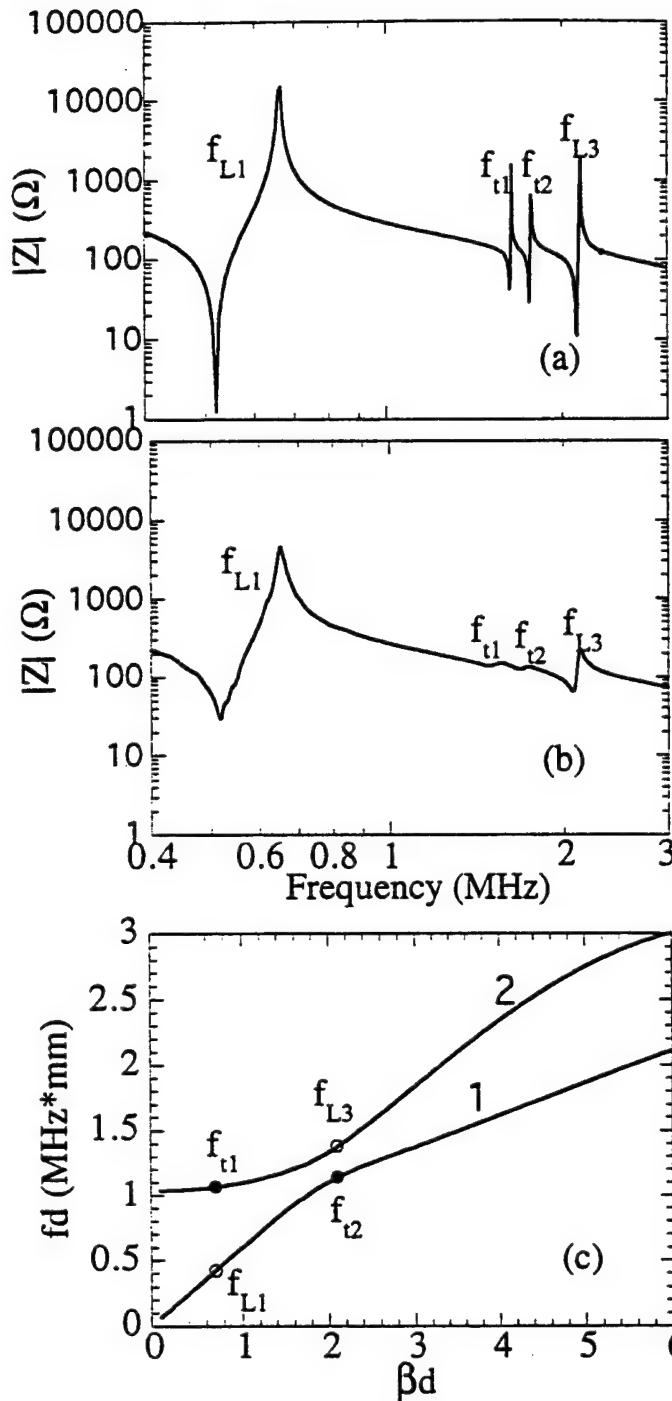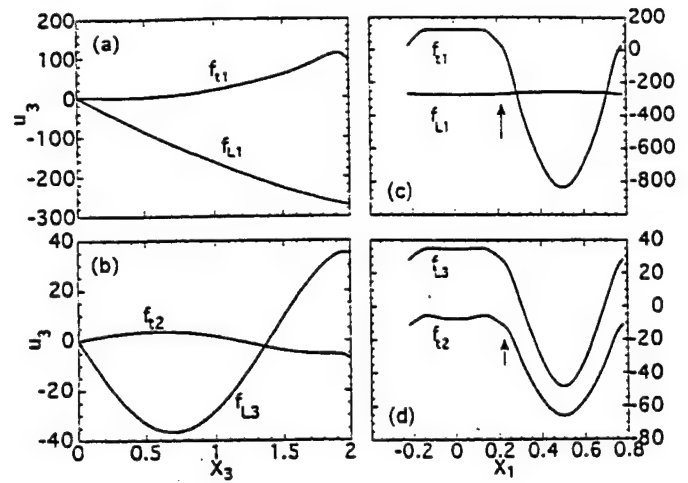
Fig. 7. The distribution of the elastic displacement u_3 for f_{L1}, f_{L3}, f_{t1}, and f_{t2} of a 2-2 composite with $t/d = 4$, where (a) and (b) are the distributions along the x_3-direction when $x_1 = 0$ [at the center line of the ceramic plate, Fig. 1(b)], $x_3 = 0$ is at the center and $x_3 = 2$ is at the ceramic surface; (c) and (d) are surface vibration profiles at $x_3 = 2$. $x_1 = 0$ corresponds to the center of the ceramic plate and $x_1 = 0.5$ is at the center of the polymer plate.

Fig. 6. The electric impedance curve for a 2-2 composite plate with PZT-5H and Spurr epoxy (44% ceramic) measured in air: (a) the theoretical curve and (b) the experimental curve. The thickness t of the composite is $t/d = 4.5$ and $d = 0.635$ mm. f_{L1} and f_{L3} are the fundamental and third harmonic of the thickness mode and $t1$ and $t2$ are the modes arose from the periodicity of the composite. (c) The dispersion curves elucidating the origin of the resonant modes f_{t1} and f_{t2}. In general, any modes on the dispersion curves will show up whenever $3d = (2n + 1)/2$, $n = 0, 1, 2, \ldots$ is satisfied, where $\beta = 2\pi/\lambda$ and $\lambda = 2t$.

In Fig. 6(c), the peak positions from the experimental data are compared with the dispersion curves for this composite which shows excellent agreement between the two. In order to elucidate the nature of these modes, the spatial distribution of u_3 at each mode at the composite surface is presented in Fig. 7 which are evaluated based on (18) and (19). Apparently, f_{L1} is the fundamental thickness resonance and f_{t1} is the first lateral mode as revealed by the fact that the ceramic and polymer vibrate 180° out of phase at this mode, as predicted in the earlier theoretical work [7], [8]. The frequency position and the distribution of u_3 along the x_3 axis indicate that f_{L3} is the third harmonic of the thickness mode. However, the appearance of f_{t2} is not expected from the earlier theoretical works in which the ceramic and polymer vibrate in phase. By examining the equations of the boundary conditions at $x_3 = \pm t/2$, it can be deduced that a resonance will occur whenever $\beta = (1 + 2n)\pi/t$, i.e., $\cos(\beta t/2) = 0$. Hence, the dispersion curves of real β, as shown in Fig. 6(c), reveal that the fundamental thickness resonance and the first lateral resonance occur at $\beta = \pi/t$ (f_{L1} and f_{t1}). Similarly, when $\beta = 3\pi/t$, the third harmonic of the thickness mode will occur at f_{L3}. In addition, a mode f_{t2} will also show up at the branch 1 which is at a frequency near and above f_{t1}. By the same argument, it would be expected that f_{L5}, f_{t3}, etc. may also be observed, depending on the electromechanical coupling factors of these modes. As shown later, the effective coupling factor for the modes in the first branch will decrease with increasing βd, i.e., reducing thickness, and on the other hand, the effective coupling factor for the modes in the second branch will increase with β. As the ratio of t/d decreases, the frequency of the thickness mode will gradually move toward the first lateral mode which will become stronger (coupling factor increases), and the second lateral mode (f_{t2}) becomes weaker and finally it
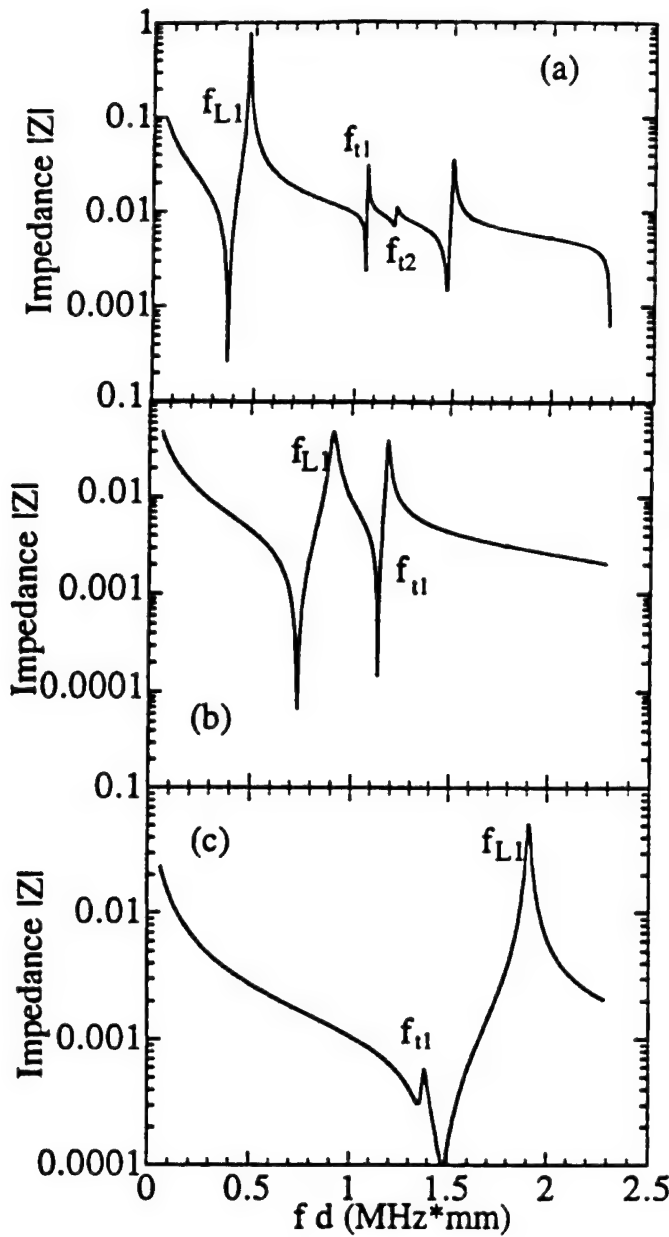
Fig. 8. The evolution of various modes in a 2-2 composite made of PZT-5H (44% ceramic) and Spurr epoxy with the thickness t of composite plate: (a) $t/d = 4$. (b) $t/d = 2$, and (c) $t/d = 1$. There is already substantial coupling between the thickness and lateral modes at $t/d = 2$ for this composite. At low t/d values (thin samples), the lateral mode will disappear.

will disappear. These features are summarized in Fig. 8 which provide understanding on the earlier experimental observations on how various modes change with temperature (which causes reduction of the shear velocity of the polymer phase) and the composite thickness [5].

Both the experimental results and the theoretical data indicate that the ceramic and polymer vibrate in phase for all the modes on the first branch and out of phase for modes on the second branch.

The electromechanical coupling factor for the thickness resonance can be evaluated based on the definition
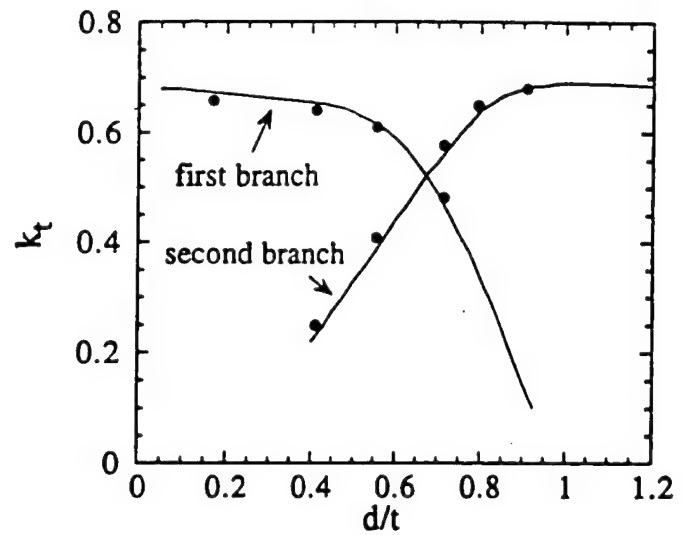
Fig. 9. The evolution of the coupling factor for the modes on the first and second branches of the dispersion curves with the composite thickness d/t for a composite made of PZT-5H and Spurr epoxy with 44% ceramic content.

of IEEE [20]:

$$k_t^2 = \frac{\pi}{2} \frac{f_s}{f_p} \tan\left(\frac{\pi}{2} \frac{f_p - f_s}{f_p}\right) \qquad (24)$$

where k_t is the thickness mode coupling factor, f_s and f_p are the series and parallel resonance frequencies, respectively. Equation (24) is used here to calculate the coupling factor for the modes in both the first and second branches. Shown in Fig. 9 are the results for a 2-2 composite plate with 44% ceramic volume content for different d/t, where both theoretical and experimental results are presented. As the ratio of d/t increases. the coupling factor of the mode (thickness mode) in the first branch gradually decreases. while the coupling factor of the mode in the second branch gradually increases due to the modes coupling. As d/t increases further, the thickness mode will jump to the second branch when the coupling factor in the second branch surpasses that of the first branch. Although in this region the coupling factor for the thickness mode can still be quite high, the distribution of u_3 is not uniform on the composite surface and the ceramic and polymer vibrate 180° out of phase, which is not desirable since the polymer phase will not be able to perform properly the function of transferring the acoustic energy between the ceramic plates and the external medium.

For a composite plate to work effectively as an electromechanical transduction material, it is required that the ceramic and the polymer plates in the composite vibrate in phase with nearly the same amplitude in the x_3-direction. The evolution of the vibration pattern in the two phases with frequency and the effect of the aspect ratio t/d of a composite plate on this distribution are investigated. Shown in Fig. 10(a) is the variation of the ratio u_3^P/u_3^C at the surface of the composite plate, where u_3^P and u_3^C are u_3 at the centers of the polymer ($x_1 = d/2$) and the ceramic plates ($x_1 = 0$). respectively, with frequency

for the composite plate of $t/d = 4$ where both the experimental results and theoretically calculated curve are presented. The experimental data were acquired using a laser dilatometer [23]. Hence, at frequencies far below any resonant mode, u_3^P/u_3^C is always less than one, which is true as long as the composite is driven electrically. For a given frequency, as t/d increases, this ratio increases and approaches one. These are consistent with the results of the earlier theoretical work on the static properties of composites [24]. As frequency increases, the ratio u_3^P/u_3^C increases toward one. At a frequency f_1 which is near f_s of the thickness mode, $u_3^P/u_3^C = 1$. This ratio will surpass one as the frequency is further increased. This is true as long as $f_{L1} < f_{t1}$. In Fig. 10(b), the change of f_1/f_s vs. the ratio of d/t is presented. Clearly, f_1/f_s is close to, but larger than, one except for composite plates with a small aspect ratio. Hence, the aspect ratio t/d does not have a significant effect on the ratio of u_3^P/u_3^C at frequencies very near f_s of the thickness mode, where u_3^P/u_3^C is always near one if the thickness mode is below the first lateral mode frequency. However, it will affect the bandwidth in which u_3^P/u_3^C is near one. For example, the bandwidth $\Delta f/f_1$, where Δf is defined here as the frequency width in which $0.9 < u_3^P/u_3^C < 1.1$, increases as the ratio of d/t decreases, which is shown in Fig. 10(b). The experimental data points are also presented in Fig. 10(b) and the agreement between the two is quite good.

V. FORCED VIBRATION OF A PIEZOCOMPOSITE PLATE IN A FLUID MEDIUM

Following a similar procedure as outlined in the preceding section, the vibration problem of a composite plate in a fluid medium can also be analyzed, which are more relevant to the practical design and application of a composite transducer. The fluid medium chosen for the study is water and two situations will be investigated: the composite plate as a transmitter, i.e., under a harmonic electric field, and the composite as a receiver, i.e., under a harmonic acoustic pressure in water.

A. Forced Vibration of a Composite Plate in Water under an AC Electric Field

For the sake of convenience, we will treat the system as a symmetric one in which the composite plate is loaded by water on both surfaces, hence, the boundary conditions at the composite-water interface are:

$$T_3^{Cm} = T_3^W, \quad T_5^{Cm} = 0, \quad u_3^{Cm} = u_3^W$$
$$\text{and } \Phi = \pm\frac{V}{2} \text{ at } x_3 = \pm\frac{t}{2} \quad (25)$$

where superscripts Cm and W denote the quantities in the composite and water, and the factor $e^{-j\omega t}$ is omitted in electric potential Φ. The variational formula for this
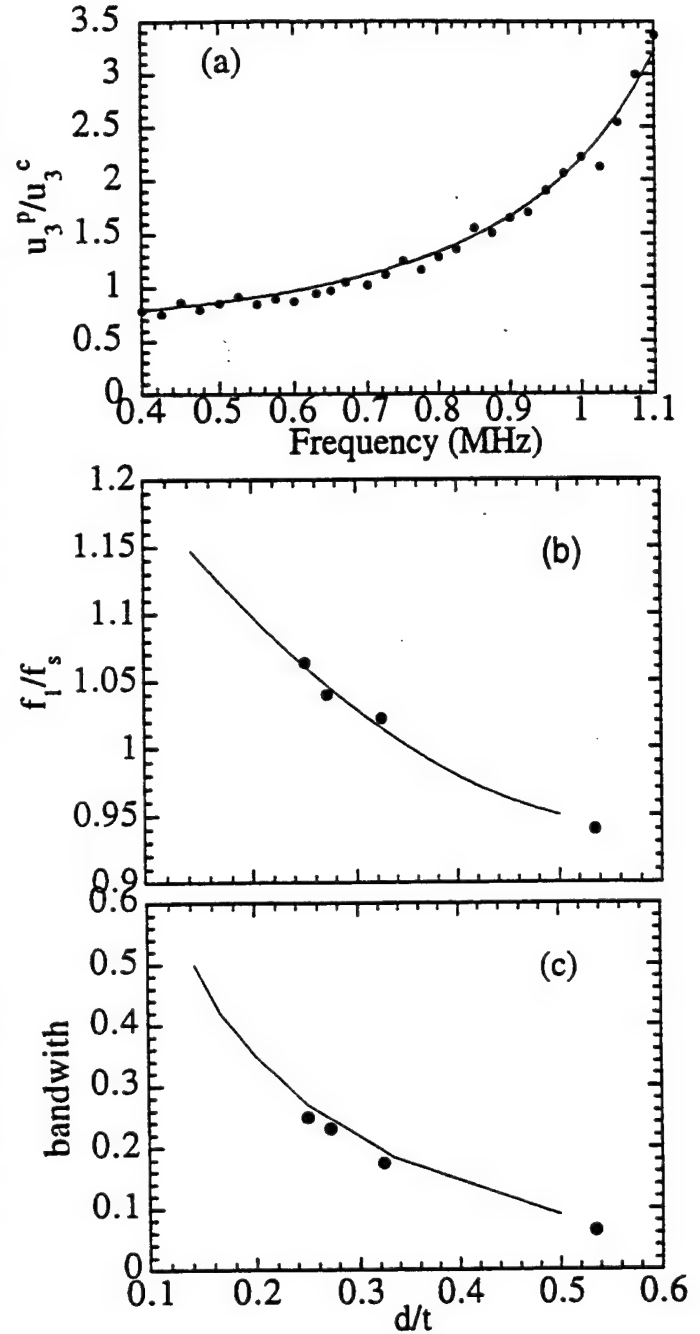

Fig. 10. (a) The ratio of u_3^P/u_3^c vs. frequency for a composite made of PZT-5H and Spurr epoxy (44% ceramic content) at a thickness of $t/d = 4$ ($d = 0.635$ mm) measured in air. u_3^P and u_3^c are the surface displacements at the centers of the polymer plate and ceramic plate, respectively. The black dots are the experimental data measured using a laser dilatometer and the solid line is derived from the model. (b) The ratio f_1/f_s as a function of the ratio d/t of the composite plate, where f_1 is the frequency at which $u_3^P/u_3^c = 1$ and f_s is the series resonant frequency for the thickness mode. The black dots are experimental data and the solid lines are derived from the model calculation. (c) The bandwidth as a function of the ratio d/t of the composite plate. The black dots are experimental data and the solid lines are derived from the model calculation.

problem can be derived as:

$$\int_{S^{\pm}} \frac{1}{2}[(T_3^{W} - T_3^{Cm})(\delta(u_3^{W})^{\cdot} + \delta(u_3^{Cm})^{\cdot})$$

$$+ (u_3^{Cm} - u_3^{W})(\delta(T_3^{W})^{\cdot} + \delta(T_3^{Cm})^{\cdot})]dS$$

$$+ \int_{S^{\pm}} [(\Phi^{Cm} - \overline{\Phi})\delta(D_3^{Cm})^{\cdot} - T_5^{Cm}\delta(u_1^{Cm})^{\cdot}]dS = 0 \quad (26)$$

where $S^{\pm}$ indicates that the integration is over the two composite-water interfaces (at $x_3 = \pm t/2$), and the integration over the volume has been omitted since it is equal to zero.

Here, the expressions for the elastic displacement vectors and the electrical potential Φ in the composite are those in (18) and (19). Because of the periodic nature of the composite plate in the x_1-direction, the solutions in water have the form:

$$u_1^{W} = j\sum_{n=0}^{J} h_n^{W} \sin(h_n^{W} x_1) \exp(\pm j\beta_n^{W} x_3)R_n^{W}$$

$$u_3^{W} = \sum_{n=0}^{J} \beta_n^{W} \cos(h_n^{W} x_1) \exp(\pm j\beta_n^{W} x_3)R_n^{W}$$

$$\quad (27)$$

$$T_3^{W} = jT_0^{W} \sum_{n=0}^{J} \cos(h_n^{W} x_1) \exp(\pm j\beta_n^{W} x_3)R_n^{W}$$

where $h_n^{W} = \frac{2n\pi}{d}$, $\beta_n^{W} = \sqrt{\frac{\omega^2}{(V^W)^2} - (h_n^{W})^2}$, $T_0^{W} = c^{W}(\beta_0^{W})^2$, $\beta_0^{W} = \frac{\omega}{V^W}$, $V^{W} = \sqrt{\frac{c^W}{\rho^W}}$ is the longitudinal wave velocity of water, c^{W} is the bulk modulus of water. $\pm$ correspond to the solutions in $x_3 > 0$ region and $x_3 < 0$ region, respectively. h and β are the wave vector components in the x_1- and x_3-directions in water. R_n^{W} is determined by the boundary conditions through the variational principle formula (26).

Substituting (18), (19), and (27) into (26) yields a set of linear algebraic equations:

$$(M_{ij})(A_j) = (V_i) \quad (28)$$

where (M_{ij}) is a matrix in which its elements are related to the parameters of water, ceramic, and polymer and the geometrical parameters ν and d, as well as ω, β, and h. $(A_j) = (A_1, \ldots, A_m, C, R_0^{W}, \ldots, R_J^{W})$, where m and J are the numbers of the eigenfunctions used in the expansions for the quantities in the composite and in water, respectively, and how many eigenfunctions should be used in the expansion depends on the accuracy desired. In this calculation, $m = 8$ and $J = 6$. Hence, (V_i) is a 16×1 matrix which elements depend on the applied voltage V. Equation (28) is solved numerically.

Shown in Fig. 11(a) is a theoretical electrical impedance curve for a 2-2 composite plate of 44% ceramic volume content and the aspect ratio $t/d = 3.8$ loaded with water. For the comparison, the experimental curve for the
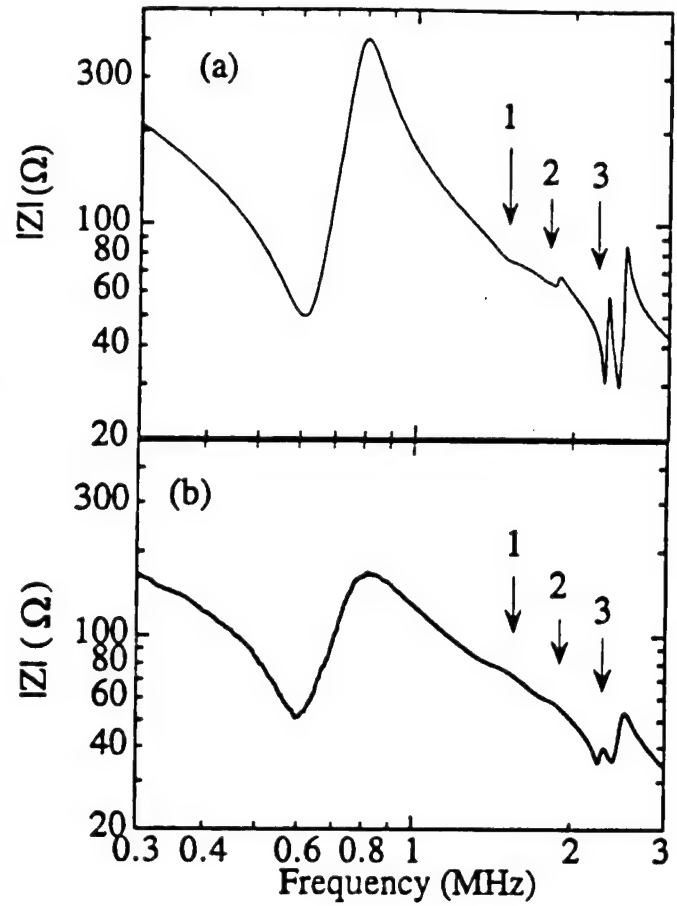

Fig. 11. The electrical impedance magnitude for a 2-2 composite of PZT-5H and Spurr epoxy with 44% ceramic content measured in water. The thickness of the composite is $t/d = 3.8$ and $d = 0.635$ mm. (a) is derived from the model and (b) is the experimental results. The modes 1 and 2 are the lateral modes [f_{t1} and f_{t2} in Fig. 6(c)] and mode 3 arises from the coupling of water to the periodic structure of the composite surface.

same composite plate is shown in Fig. 11(b). The agreement between the experimental result and the theoretical one is quite good. The relatively sharp resonant peaks in the theoretical curve compared with the experimental one are due to the fact that in the theoretical calculation, the elastic and dielectric losses of the composite plate are not included. Comparison between Fig. 11 with Fig. 6, which is the electrical impedance for a similar composite plate in air, reveals that the resonance is severely damped in water as shown by the marked broadening of the resonant peaks in the impedance curve. For the lateral modes (modes 1 and 2 in Fig. 11) which is mainly determined by the shear resonance of the polymer phase in the 2-2 composite investigated, because the acoustic impedance between the polymer and water is very close, the change in the amplitude is quite significant. One interesting feature of the influence of the water loading on a composite plate is the appearance of a mode which is labeled 3 in Fig. 11. It can be shown that the resonant frequency for this mode does not change very much as the thickness of the composite plate changes. From the stress distribution pattern in the water, it is not difficult to show that this mode is related to

the coupling between the composite and water, and its frequency is determined by the periodicity d and the acoustic wave velocity of water ($f = V^w/d$). And it corresponds to the local oscillation of water within one unit cell.

In analogous to the situation in air, it is also found that in water, at frequencies far below any resonant mode, the ratio of u_3^P/u_3^C is always less than one and will approach one as the aspect ratio t/d increases. As the frequency increases toward the thickness resonant frequency, u_3^P/u_3^C increases toward one. At a frequency f_1 near the thickness resonant frequency f_s, this ratio becomes one and above that, this ratio is larger than one [Fig. 12(a)]. Fig. 12(b) presents f_1/f_s and $\Delta f/f_1$ vs. the ratio of d/t for a composite with 44% ceramic content. Clearly, the effect of the aspect ratio t/d on the surface uniformity of a composite plate is to change the frequency position f_1 with respect to the thickness resonance and the frequency width Δf in which u_3^P/u_3^C is near one which are very similar to that found in air. However, the bandwidth $\Delta f/f_1$ in water is larger than that in air, indicating that the surface distribution of the displacement of the two phases is much flatter in water than in air which is quite understandable. Because of the water loading, the vibration amplitude of the polymer phase is significantly reduced. Fig. 12(a) shows how the ratio of u_3^P/u_3^C at the composite surface varies with frequency ($t/d = 4$). One noticeable change between the surface profiles in air and in water is that in water, even at the lateral mode frequency, this ratio does not become very large (not shown in Fig. 12 since the lateral mode frequency is at about 1.5 MHz).

B. Forced Vibration of a Composite Plate in Water under Harmonic Acoustic Pressure

Now we turn to investigate the vibration behavior of a composite plate in water under harmonic acoustic pressure, that is, to study issues related to the receiving sensitivity of a simple 2-2 composite transducer. For simplicity, we shall restrict the treatment to the symmetric system. In this case, as sketched in Fig. 13, the incident acoustic waves impinge normally on the two surfaces of the composite plate from opposite directions and the boundary conditions for this problem are:

$$T_3^{Cm} = T_3^{W}, \quad T_5^{Cm} = 0, \quad u_3^{Cm} = u_3^{W}$$

$$\text{and } D_3^{Cm} = 0 \text{ at } x_3 = \pm\frac{t}{2}. \quad (29)$$

The appropriate variational formula is:

$$\int_{S\pm} \frac{1}{2}[(T_3^{W} - T_3^{Cm})(\delta(u_3^W)^* + \delta(u_3^{Cm})^*)$$

$$+ (u_3^{Cm} - u_3^{W})(\delta(T_3^{W})^* + \delta(T_3^{Cm})^*)]dS$$

$$- \int_{S=} [D_3^{Cm}\delta(\Phi^{Cm})^* + T_5^{Cm}\delta(u_1^{Cm})^*]dS = 0. \quad (30)$$

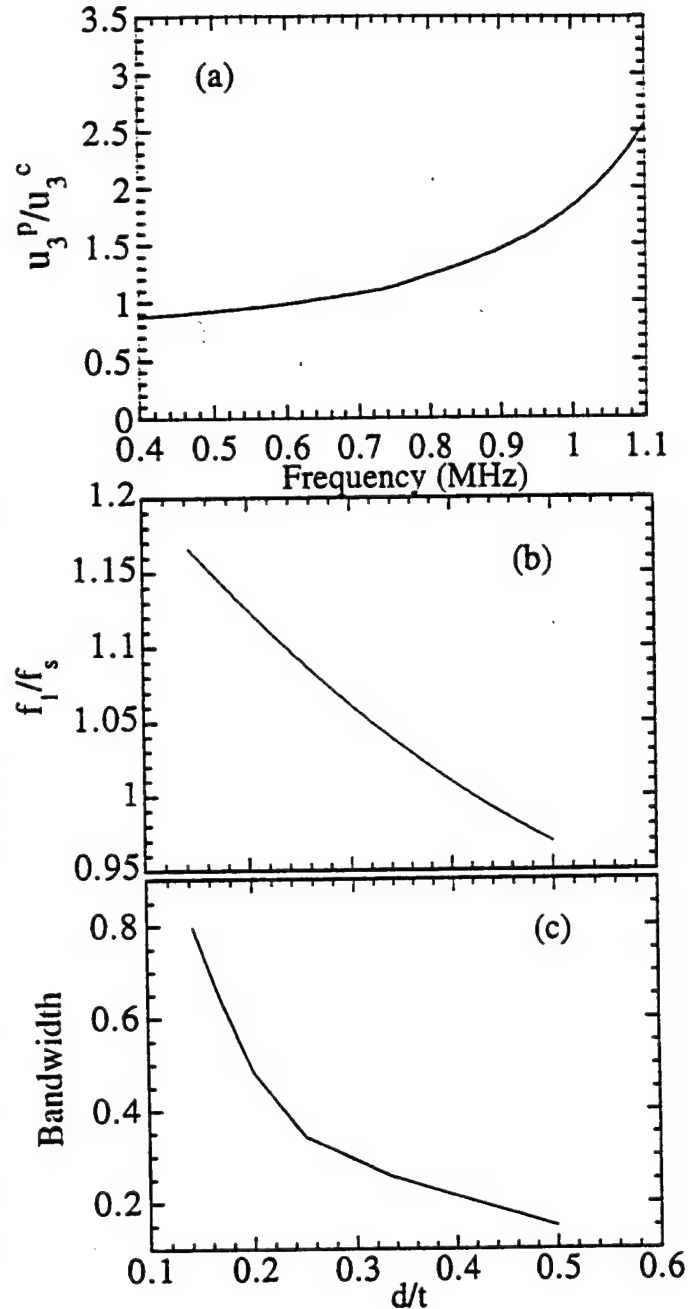The expressions of the displacements and electrical potential in the composite plate are those in (18) and (19) except

Fig. 12. (a) The ratio of u_3^p/u_3^c vs. frequency for a composite made of PZT-5H and Spurr epoxy (44% ceramic content) at a thickness of $t/d = 4$ ($d = 0.635$ mm) measured in water. u_3^p and u_3^c are the surface displacements at the centers of the polymer plate and ceramic plate, respectively. The results are derived from the model. (b) The ratio f_1/f_s as a function of d/t of the composite plate, where f_1 is the frequency at which $u_3^p/u_3^c = 1$ and f_s is the series resonant frequency for the thickness mode. The results are derived from the model. (c) The bandwidth as a function of d/t of the composite plate. The results here can be compared with those in Fig. 10 and apparently, and the water loading improves the uniformity of the vibration profile at the composite surface. The results are derived from the model.
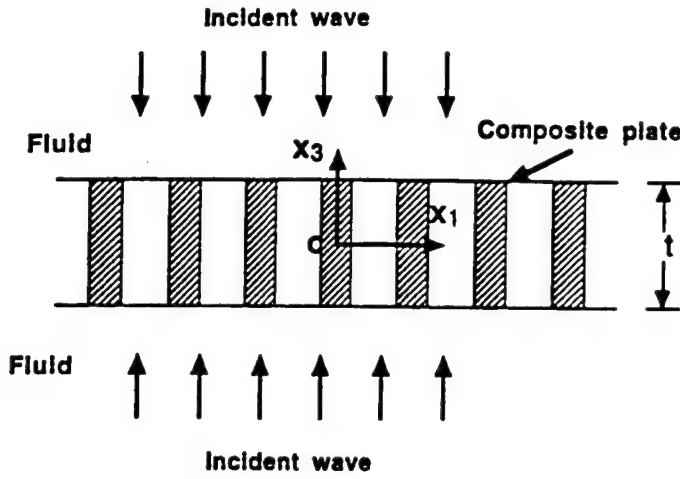
Fig. 13. Schematic drawing of a 2-2 composite plate under normal incident of a pressure wave from the water.

now the mode of $\beta = 0$ should not be included since there is no externally applied electric field. To account for the incident wave in water, (27) is modified and the solutions in the $x_3 > 0$ region are:

$$u_1^W = j \sum_{n=0}^{J} h_n^W \sin(h_n^W x_1) \exp(j\beta_n^W x_3) R_n^W$$

$$u_3^W = -\beta_0 \exp(-j\beta_0 x_3)$$

$$+ \sum_{n=0}^{J} \beta_n^W \cos(h_n^W x_1) \exp(j\beta_n^W x_3) R_n^W$$

$$\tag{31}$$

$$T_3^W = jT_0^W \left[\exp(-j\beta_0 x_3) \right.$$

$$\left. + \sum_{n=0}^{J} \cos(h_n^W x_1) \exp(j\beta_n^W x_3) R_n^W \right]$$

where the term of $-\beta_0 \exp(-j\beta_0 x_3)$ corresponds to the incident plane wave. By substituting (18), (19), and (31) into (30), we obtain a set of linear algebraic equations:

$$(M_{ij})(A_j) = (V_i) \tag{32}$$

where (M_{ij}) is a 15×15 matrix, $(A_j) = (A_1, \ldots, A_m, R_0^W, \ldots, R^W)$ with $m = 8$ and $J = 6$, and (V_i) is a 15×1 matrix related to the incident wave. By solving (32) one can obtain all of the properties related to the behaviors of a composite plate under a harmonic acoustic pressure.

Shown in Fig. 14 is the open circuit voltage receiving sensitivity V/p, where V is the voltage output and p is the pressure of the incident wave, for a 44% 2-2 composite plate at the thickness resonance vs. d/t for the thickness resonance mode where the cross over region (point B in Fig. 2) is at $d/t = 0.65$ [25]. That is, at $d/t < 0.65$, the thickness mode is in the first branch of the dispersion curves and above that, the thickness resonance is at the second branch of the dispersion curves where the polymer and ceramic vibrate out of phase. Since the problems treated in this paper are related only to the piezo-
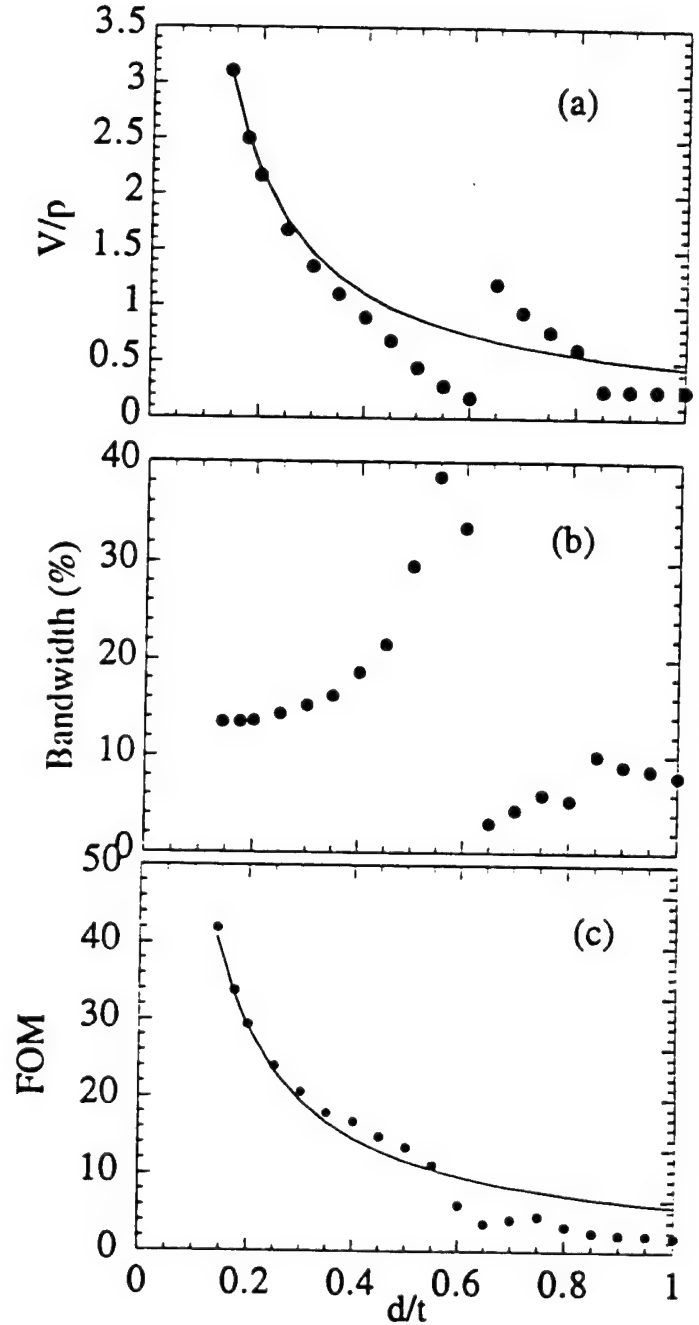

Fig. 14. (a) The influence of the unit cell dimension ratio of d/t on the open circuit voltage sensitivity of a 2-2 composite with 44% PZT-5H and Spurr epoxy matrix. Solid dots are V/p at the peak frequency (f_p) and the solid line is the sensitivity of a single phase material with the effective properties of the composite. The results are derived from the model. (b) The 3 dB bandwidth as a function of d/t for a composite transducer derived from the model. (c) FOM (solid dots, the product of the sensitivity and the bandwidth) for the 2-2 composite in (a) as a function of d/t. The solid line is FOM for a single phase material with the effective properties of the composite. At $d/t > 0.5$, FOM drops much below the single phase material value. The results are derived from the model.

materials. the open-circuit receiving sensitivity is used here which, as pointed out by Kojima [25], is a system independent parameter. The bandwidth is defined as the 3 dB width about the peak frequency (f_p for the receiving mode). For a single phase material, it can be derived from the KLM model that the sensitivity here should be proportional to t, the thickness of the transducer. Hence, in Fig. 14. the V/p vs. d/t curve for a single phase material should fall off as t (solid line in Fig. 14) while the bandwidth should stay constant. The results show that the sensitivity of the thickness mode for a 2-2 composite decreases slowly as d/t becomes larger than 0.4, but the bandwidth increases gradually. The increase in the bandwidth is due to the merger of the two resonant modes in water. After that, there are anomalous changes in both the bandwidth and the sensitivity in the cross-over region. At higher values of d/t (thin composite plates), both the sensitivity and the bandwidth fall much below the values of single phase material (solid line). If we define the figure of merit (FOM) here as the product of sensitivity and bandwidth, as shown in Fig. 14(b), at $d/t < 0.5$, the FOM falls off with t. At $d/t > 0.5$, the FOM drops to much smaller value. Therefore, in order to gain a high receiving sensitivity and a broad bandwidth of a 2-2 composite transducer, it is desirable to have d/t less than 0.5. The results here can be compared with what is shown in Figs. 2, 8, 9, and 12. At d/t above 0.5, the coupling factor shows a precipitous drop (Fig. 9) and the thickness mode frequency also shows an apparent deviation from the extrapolated value (the dashed line in Fig. 2). Fig. 8 also shows that there is a significant coupling between the two modes. Although the results presented are for a composite with 44% ceramic content. it is approximately true for composites with other volume fractions.

VI. SUMMARY

The details of a theoretical model on piezoceramic polymer composites with laminar periodic structure are presented. The result shows that the various resonant modes in a composite structure can be traced back to the modes in either an isolated ceramic plate or polymer plate with appropriate boundary conditions (stress free for the ceramic plate and strain free for the polymer plate). It also shows that there exist a series of modes associated with the periodic structure of a composite, which is beyond the stop-band edge resonance prediction. One of the main concerns in designing a composite transducer is how the surface vibration profile changes with frequency and how this is influenced by the aspect ratio t/d. It was predicted and verified by experiment that as long as the thickness resonance is below the first lateral mode frequency, there is always a frequency f_1 which is near the thickness resonance and at which the polymer and ceramic vibrate in unison. The effect of t/d is to change the position of f_1 with respect to the thickness resonance frequency and the bandwidth in which polymer and ceramic have nearly the
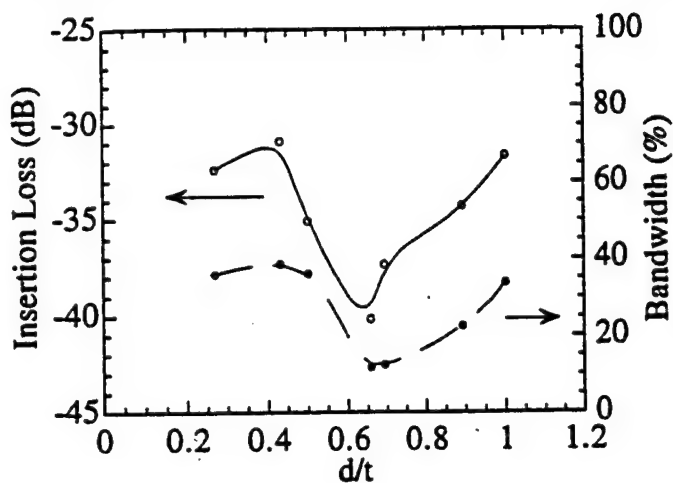

Fig. 15. The experimental data on the insertion loss (open circles) and 6 dB bandwidth (solid dots) of 2-2 composites with 44% volume content of PZT-5H and Spurr epoxy polymer matrix measured by the pulse echo method for different ratio of d/t ($d = 0.635$ mm). The solid lines are drawn to guide eyes.

same vibration amplitude and phase. It is also predicted that. when operated in a fluid medium such as water, there will be a resonance mode whose frequency is determined by the velocity of the fluid medium and the unit cell length d and is associated with the oscillation of the fluid, causing the polymer and ceramic to vibrate 180° out of phase. The difference in the surface vibration profiles between in air and in water indicates the need to characterize the vibration pattern of a composite in a fluid medium since it is much closer to the real application environment.

In general, the maximum transmitting voltage sensitivity of a transducer is at a frequency near f_s and the maximum open circuit receiving sensitivity is near f_p of the thickness mode ($f_p > f_s$), and hence it is expected that the influence of the lateral mode (hence, the aspect ratio t/d) will be more severe on the receiving sensitivity. From the data analysis, it is shown that, when an FOM which is the product of the sensitivity and the bandwidth is introduced as the criterion of the performance of a composite transducer as a receiver. the performance deteriorates when $d/t > 0.5$ for the composite discussed here. Experimental results confirm this finding where, as shown in Fig. 15. the insertion loss of a 2-2 piezocomposite shows large increases at d/t near and above 0.5.

REFERENCES

[1] W. A. Smith, "The application of 1-3 piezocomposites in acoustic transducers," *Proc. 1990 IEEE ISAF7*, Urbana, IL, 1990, pp. 145–152.

[2] T. R. Gururaja, A. Safari, R. E. Newnham. and L. E. Cross. "Piezoelectric ceramic-polymer composites for transducer applications," in *Electronic Ceramics*, L. M. Levinson. Ed. New York: Marcel Dekker, 1987, pp. 92–128.

[3] W. A. Smith and B. A. Auld, "Modeling 1-3 composite piezoelectrics: Thickness-mode oscillations," *IEEE Trans. Ultrason., Ferroelect., Freq. Contr.*, vol. 38. pp. 40-47, 1988.

[4] K. Y. Hashimoto and M. Yamaguchi, "Elastic, piezoelectric and dielectric properties of composite materials." *Proc. IEEE Ultrason. Symp.*, Williamsburg, VA, 1986, pp. 697–702.

[5] T. R. Gururaja, W. A. Schulze, L. E. Cross. R. E. Newnham. B. A. Auld, and J. Wang, "Piezoelectric composite materials for ultrasonic transducer applications. Part I: Resonant modes of vibration of PZT-rod-polymer composites," *IEEE Trans. Sonics Ultrason.*, vol. SU-32, pp. 481–498, 1985.

[6] R. E. Newnham, D. P. Skinner, and L. E. Cross, "Connectivity and piezoelectric-pyroelectric composites," *Mater. Res. Bull.*, vol. 13. pp. 525–536, 1984.

[7] B. A. Auld, H. Kunkel, Y. A. Shui, and Y. Wang, "Dynamic behavior of periodic piezoelectric composites," *Proc. IEEE Ultrason. Symp.*, Atlanta, GA, 1983, pp. 554–558.

[8] B. A. Auld, Y. A. Shui, and Y. Wang, "Elastic wave propagation in three-dimentional periodic composite materials," *J. Physique*, vol. 45, pp. 159–163, 1984.

[9] Y. Wang, E. Schmidt, and B. A. Auld. "Acoustic wave transmission through one-dimensional PZT-epoxy composites." *Proc. IEEE Ultrason. Symp.*, Williamsburg, VA, 1986, pp. 685–689.

[10] Y. Wang, "Waves and vibrations in elastic superlattice composites." Ph.D. dissertation, Stanford University, CA, December 1986.

[11] F. Craciun, L. Sorba, E. Molinari, and M. Pappalardo, "A coupled-mode theory for periodic piezoelectric composites." *IEEE Trans. Ultrason., Ferroelect., Freq. Contr.*, vol. 36. pp. 50–56, 1989.

[12] M. Yamaguchi, K. Y. Hashimoto. and H. Makita. "Finite element method analysis of dispersion characteristics for the 1-3 type piezoelectric composites." *Proc. IEEE Ultrason. Symp.*, Denver. CO, 1987, pp. 657–661.

[13] J. A. Hossack and G. Hayward. "Finite element analysis of 1-3 composite transducers," *IEEE Trans. Ultrason.. Ferroelect.. Freq. Contr.*, vol. 38, pp. 618–629, 1991.

[14] A.-C.. Hladky-Hennion and J.-N. Decarpigny, "Finite element modeling of active periodic structures: Application to 1-3 piezocomposites," *J. Acoust. Soc. Amer.*, vol. 94, pp. 621–635. 1993.

[15] J. Sato. M. Kawabuchi. and J. Fukumoto, "Dependence of electromechanical coupling coefficient on the width to the thickness ratio of plate shaped piezoelectric transducers used in electrically scanned ultrasonic diagnostic systems." *J. Acoust. Soc. Amer.*, vol. 66, pp. 1609–1611, 1979.

[16] Q. M. Zhang and X. Geng, "Dynamic modeling of piezoceramic polymer composite with 2-2 connectivity," *J. Appl. Phys.*, vol. 76. pp. 6014–6016, 1994.

[17] Y. A. Shui, X. Geng. and Q. M. Zhang, "Theoretical modeling of resonant modes of composite ultrasonic transducers." *IEEE Trans. Ultrason.. Ferroelect.. Freq. Contr.*, vol. 42, pp. 766–773, 1995.

[18] X. Geng and Q. M. Zhang. "Dynamic behavior of periodic piezoceramic-polymer composite plates," *Appl. Phys. Lett.*, vol. 67. pp. 3093–3095, 1995.

[19] B. A. Auld, *Acoustic Fields and Waves in Solid*. New York: Wiley. 1973.

[20] IEEE Standard on Piezoelectricity (ANSI/IEEE Standard 176-1987.1988).

[21] H. F. Tiersten. *Linear Piezoelectric Plate Vibrations*. New York: Plennum. 1969.

[22] C. G. Oakley. "Geometric effects on the stopband structures of 2-2 piezoelectric composite plates." *Proc. IEEE Ultrason. Symp.*, pp. 657–661, 1991.

[23] Q. M. Zhang. S. J. Jang. and L. E. Cross. "High-frequency strain response in ferroelectrics and its measurement using a modified Mach-Zehnder interferometer," *J. Appl. Phys.*, vol. 65, pp. 2807–2815. 1989

[24] Q. M. Zhang, W. Cao, J. Zhao, and L. E. Cross. "Piezoelectric performance of piezoceramic-polymer composites with 2-2 connectivity: A combined theoretical and experimental study," *IEEE Trans. Ultrason., Ferroelect., Freq. Contr.*, vol. 41, pp. 556–562. 1994.

[25] T. Kojima. "A new method for estimating the system-independent characteristics of an ultrasonic piezoelectric transducer." *Proc. IEEE Ultrason. Symp.*, pp. 649–654, 1981.

Xuecang Geng received the B.S. degree in physics from Xi'an Jiao tong university, Xi'an, China, in 1983 and the M.S. degree in acoustics from the Institute of Acoustics. Chinese Academy of Sciences, Beijing, China. in 1989. He is currently a candidate for the Ph.D. degree in Materials Research Lab, The Pennsylvania State University.

From 1983 to 1986 he was an engineer at Center of Microelectronics. Chinese Academy of Sciences. Beijing, China. This work focused on the computer aided design of integrated circuit and the computer modeling of integrated circuit and its processing. From 1990 to 1993 as a research assistant at Ultrasonic Lab of the Institute of Acoustics. he worked on the nondestructive evaluation of materials, acoustic wave logging. design. fabrication and characterization of 1-3 piezocomposite materials and ultrasonic transducers. From 1993 to 1995 as a research associate at Materials Research Lab of The Pennsylvania State University, he worked on the modeling of 2-2 and 1-3 piezocomposites. His current research interests are piezoelectric materials. ultrasonic transducers, and transducer array.

Q. M. Zhang was born in ZeiJian. China, in 1957. He received the B.S. degree in physics from Nanjing University, China, in 1981 and the Ph.D. degree in physics from the Pennsylvania State University, University Park, in 1986

He is currently an Associate Professor of Electrical Engineering at the Materials Research Laboratory and Department of Electrical Engineering of the Pennsylvania State University. His research interests involve ferroelectric ceramic. polymer. and composite for actuator. sensor. and transducer applications; new design and modeling of piezocomposites; characterization of piezoelectricity and electrostriction and constitutive relations in ferroelectrics: smart materials and structures; novel. artificial. and nano-composite materials: effects of defect structure on the dielectric. piezoelectric. and elastic properties of ferroelectric materials. From 1986 to 1988, he was a Post-Dr at Materials Research Laboratory of Penn State. From 1988 to 1991. he was a research scientist at Brookhaven National Laboratory, NY, conducting research on interface. surface. and thin films with neutron and synchrotron X-ray scattering techniques.

Dr. Zhang is a member of the American Ceramic Society. IEEE. American Physical Society. and Materials Research Society.

APPENDIX 83

Acoustic Properties of the Interface of a Uniform Medium-2-2 Piezocomposite and the Field Distributions in the Composite

Qiming ZHANG and Xuecang GENG

Materials Research Laboratory and Department of Electrical Engineering,
The Pennsylvania State University, University Park, PA 16802, USA

The acoustic properties of a medium-composite interface and the field distributions in a 2-2 composite are analyzed based on an approach developed recently. It is found that the effective input acoustic impedance Z_{in} of the composite shows marked dependence on the shear stiffness constant of the medium in contact, which is related to the non-uniform vibration distribution at the composite surface. Since for a piezoceramic polymer composite, it is the ceramic phase which performs the energy conversion between the acoustic and electric forms, the amount of acoustic energy which can enter the ceramic region is one of the most important parameters in a composite transducer design. We show that even though the effective transmission coefficient increases as the frequency is increased, the amount of acoustic energy entering the ceramic region actually decreases. From the fact that there is more than 180° phase change in the reflection wave from the medium-composite interface, it is shown that the matching layer thickness is no longer equal to the quarter wavelength, but smaller, and the theoretical predictions are confirmed experimentally.

KEYWORDS: piezocomposite, acoustic properties, ultrasonic transducer, modeling

1. Introduction

Transmission and reflection of a wave at an interface is of great importance in many areas of modern technology such as the optical, electromagnetic, acoustic, and materials nondestructive evaluations. For homogeneous materials, a quantitative understanding of how the material properties at the interface influence the transmission and reflection of various wave components has been well established.[1,2] However, for materials with heterogeneity such as composites, much work remains to be done in order to provide both qualitative and quantitative understandings on how a composite structure affect flows of waves at an interface between a composite and a homogeneous fluid or solid medium.

For the piezoceramic polymer composites used for ultrasonic transducer applications,[3-6] in addition to the wave transmission and reflection at the interface, one has also to deal with the acoustic energy transfer between the two constituents, i.e., the piezoceramic and polymer phases. In a piezoceramic polymer composite, because the energy conversion between the electric and mechanical forms can only be carried out in the ceramic phase the polymer phase acts as a carrier to transfer the acoustic energy between the piezoceramic and the external medium to which the transducer is interacting. Clearly, to establish a structure performance relationship in this type of material, both the propagation of the acoustic energy at the composite-medium interface and the effectiveness of the energy transfer between the polymer and ceramic inside a composite have to be considered.

The objective of this paper is to examine quantitatively how the material properties at the two sides of the interface, i.e., the properties of a piezoceramic polymer composite and a uniform medium, either a liquid or a solid, influence the wave transmission and reflection at the interface and the acoustic energy transfer inside the composite, and how these affect the parameters of

the matching layer at the interface. The approach taken here is based on the eigen-mode expansion method and variational technique.[2,7,8]

The organization of the paper is as follows: In §2, the general formula used to treat the wave propagation at the interface is briefly presented and the results for the fluid-composite interface are analyzed. The definition of the input acoustic impedance Z_{in} of the composite at the interface is also discussed. The acoustic energy transfer between the ceramic and polymer is analyzed. In §3, the wave propagation at a interface between a solid and a piezocomposite is treated where the influence of the shear elastic constant of the solid on Z_{in} of the composite is analyzed. In §4, the issues related to the anti-reflection quarter wave matching layer at a composite-medium interface are examined. And in §5, a brief summary and discussion are presented.

In the paper, the piezoceramic polymer composites used in the model calculations and in experiments are those made of PZT-5H piezoceramic and Spurr epoxy polymer matrix.[9] The composites have a 2-2 connectivity (a terminology introduced by Newnham),[5] i.e., the ceramic and polymer form a periodic laminated structure as shown schematically in Fig. 1(a).

2. Plane Acoustic Wave Propagation at a Fluid-2-2 Composite Interface

The schematic of the interface system is shown in Fig. 1(b) where a plane acoustic wave is normally incident upon the boundary between a fluid and a 2-2 piezocomposite. The coordinate system is chosen such that the x_3-axis is perpendicular to the interface, the x_1-axis is parallel to the interface as shown in the figure, and the x_2-axis is perpendicular to both the x_1 and x_3 axes (pointing out of the paper). The fluid occupies the space of $x_3 < 0$ and the 2-2 composite is in $x_3 > 0$. Since the dimension in the x_2-direction is much larger than the period d of the 2-2 composite and the wave fields are uniform in that direction, it can be taken as infinite without
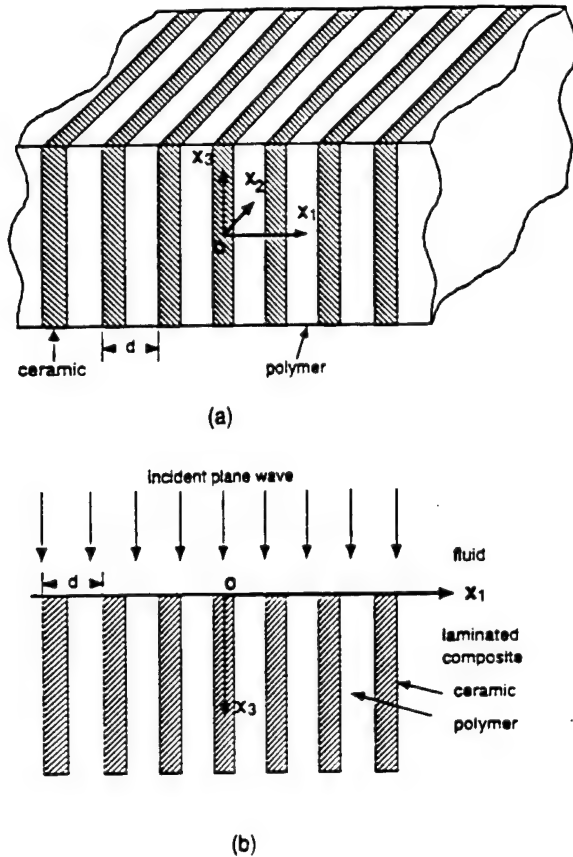
Fig. 1. (a) Schematic of a 2-2 piezoceramic polymer composite where the dimensions in both the x_1 and x_2 directions are much larger than the period d. (b) Schematic of an interface between a fluid and a 2-2 piezocomposite where a plane acoustic wave normally incidents to the interface from the fluid medium. The composite occupies the semi-infinite space $x_3 > 0$.

much error in the results. Hence, for the dynamic problem to be considered, the 2-2 composite can be regarded as elastically clamped in the x_2-direction so that $S_2 = 0$, where S_2 is the strain in that direction, and we have a two dimensional problem with no dependence on the x_2-variable. In the discussion here, the parameters chosen for the fluid medium are those of water.

The governing equations for this problem are

$$T_{ij,i} = \rho \ddot{u}_j$$
$$D_{i,i} = 0 \qquad (1)$$

Where i and $j = 1$ and 3. The symbols adopted in this paper are summarized here: T_{ij} and S_{ij} are the stress and strain tensor components, where the matrix notation is used, u_i is the elastic displacement vector, ρ is the mass density, D_i is the electric displacement vector, and E_i is the electric field. The relevant material coefficients are: e_{ij} is the piezoelectric coefficient, c_{ij} is the elastic stiffness, and ϵ_i is the dielectric permittivity.

The constitutive equations in the composite are:

$$[T] = [c^E][S] - [e][E]$$
$$[D] = [e'][S] + [\epsilon^s][E] \qquad (2)$$

For the polymer phase, e_{ij} in eq. (2) are zero. In the fluid medium, the constitutive relation has the form

$$T_{11} = T_{33} = \lambda^W \left(\frac{\partial u_1}{\partial x_1} + \frac{\partial u_3}{\partial x_3} \right) \qquad (3)$$

where λ^W is the bulk modulus of the fluid.[10] The boundary conditions at the fluid-2-2 composite interface for the problem are

$$T_{33}^{Cm} = T_{33}^W, \quad T_{13}^{Cm} = 0, \quad u_3^{Cm} = u_3^W$$
$$\Phi^{Cm} = \Phi^W, \quad D_3^{Cm} = D_3^W \quad \text{at} \quad x_3 = 0 \quad (4)$$

The superscripts Cm and W represent the 2-2 composite and the fluid. And Φ is the electric potential.

In a 2-2 composite plate, as has been shown in earlier publications,[8,11] the displacements and electrical potential can be expanded in terms of the eigenfunctions in the unbounded 2-2 composite. The field distribution in the fluid medium are periodic function in the x_1-direction due to the composite structure. The variational technique is used to treat the boundary conditions [eq. (4)] and hence to determine the expansion coefficients.[8]

One important parameter related closely to the reflection and transmission of an acoustic wave at an interface is the acoustic impedance of the media at the two sides of the boundary which also depends on the nature of the wave such as plane wave or spherical wave.[2,12] For homogeneous isotropic materials, the acoustic impedance for a plane wave is the characteristic acoustic impedance which is simply the product of the mass density ρ and the wave (longitudinal wave or shear wave) velocity V.[1,2,12] For nonuniform materials (such as piezocomposite materials), on the other hand, no characteristic impedance can be defined in such a simple manner due to the dispersive nature of the properties. However, the acoustic impedance of a material can still be found, for example, from the reflection coefficient or other methods. It should be pointed out that although there exist several definitions for determining the acoustic impedance at an interface (input acoustic impedance), for a heterogeneous material, the results obtained by using different definitions may not be the same.[13,14] However, since the input acoustic impedance is not a direct physical quantity but rather a parameter introduced for the convenience of the analysis, a situation in analogy to the complex notation introduced in many engineering fields, which definition is more appropriate really depends on the situation where it is used. In dealing with the energy transfer across an interface, one might have to use the formula derived under energy flow consideration. On the other hand, in designing matching layers and dealing with the reflection and transmission of acoustic waves in a multilayer medium, the amplitude and phase of the wave components are crucial which may not be included in the coefficients related to the transmission and reflection of the acoustic energy. In the discussion here, we will adopt the definition related to the wave reflection and transmission problems and two different approaches will be used to evaluate Z_{in} of a composite.[2,13]

From the reflection coefficient R, the input acoustic impedance of the composite at the interface can be found as
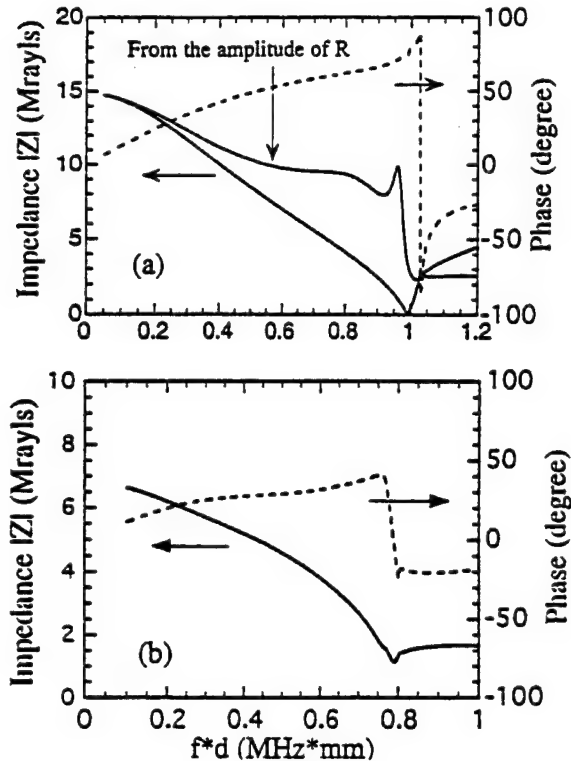
Fig. 2. (a) The effective input acoustic impedance Z_{in} of the 2-2 composite with 44% ceramic content calculated from the reflection coefficient R. For the comparison, Z_{in} calculated from eq. (5) where only the amplitude of R is used. The results demonstrate the importance of the phase in the R. (b) Z_{in} for the 2-2 composite with 15% ceramic volume content.

$$Z_{in} = \frac{1-R}{1+R} Z^{w} \qquad (5)$$

where Z_{in} is the effective input impedance of the 2-2 composite. Z^{w} is the characteristic impedance of water. Using the results of R, the effective input acoustic impedance of 2-2 composites with 44% and 15% ceramic volume content is evaluated and presented in Figs. 2(a) and 2(b). Apparently, there is a large change of the magnitude and phase of the input acoustic impedance as the frequency increases. For the comparison, the acoustic impedance is also evaluated from eq. (5) where only the magnitude of the reflection coefficient is used and shown in Fig. 2(a). Clearly, the results show how erroneous it can be if the phase information in the reflection coefficient is ignored.[15]

In analogy to the electrical impedance, the specific impedance at the interface can also be found from the ratio of the stress (in analogy to the voltage) to the displacement velocity (in analogy to the current):

$$Z(x_1, 0) = \frac{T_3^{Cm}(x_1, 0)}{v_3^{Cm}(x_1, 0)} \qquad (6)$$

where v_3^{Cm} is the particle displacement velocity in the 2-2 composite. Equation (6) is used widely in the equivalent circuit model of transducers.[10,16,17] Apparently, for a 2-2 composite considered, Z from eq. (6) is a function of x_1 due to the variation of T_3 and v_3 in that direction. To eliminate this variation, the approach taken by Miller
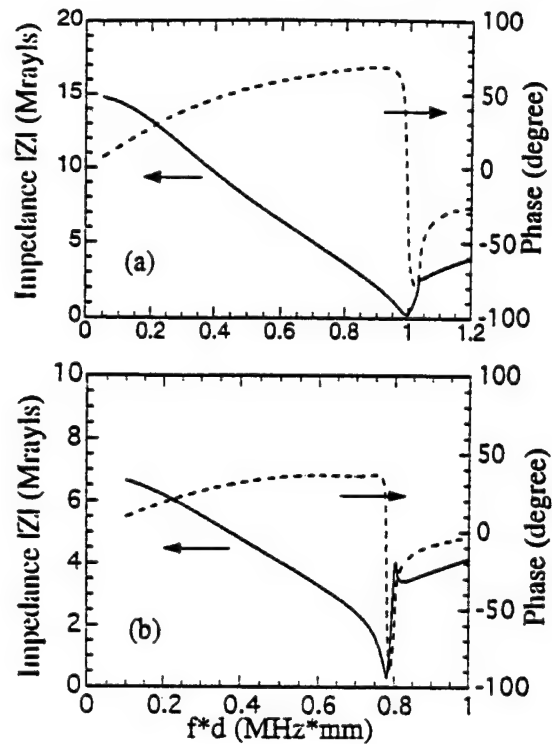
Fig. 3. The effective input impedance Z_{in} calculated from eq. (7) for (a) the composite of 44% ceramic volume content and (b) the composite of 15% ceramic content. The results here are nearly the same as those in Fig. 2 except at frequencies above the first lateral mode.

and Pursey is adopted here.[13] That is, the averaged T_3 and averaged v_3 in the x_1-direction are used:

$$Z_{in} = \frac{\int T_3^{Cm}(x_1, 0) dx_1}{\int v_3^{Cm}(x_1, 0) dx_1} \qquad (7)$$

where the integration is taken in one unit cell. This expression seems physically meaningful since it reflects an averaged mechanical impedance of the composite at the interface. Z_{in} calculated from eq. (7) for composites with 44% and 15% ceramic contents is shown in Fig. 3 which is quite close to those in Fig. 2. In the following discussion, eq. (7) is used to calculate Z_{in} in the composite.

In order to shed light on the large change of the input acoustic impedance with frequency, the surface displacement u_3 is evaluated at the center of the ceramic plate ($x_1 = 0$) and polymer plate ($x_1 = d/2$) and the results are presented in Fig. 4(a). At low frequencies, the surface displacements in the polymer and ceramic regions are in unison which indicate that the isostrain model used in many earlier modelings on ultrasonic composite transducers is valid in this frequency region.[18,19] As the frequency increases, even at frequencies still far below the first lateral mode (at fd near 1), the surface vibration amplitudes in the two regions become quite different. At the frequency near the first lateral mode, the vibrations in the polymer and ceramic regions are 180° out of phase and in this frequency region, the effective input acoustic impedance of the composite becomes very small as
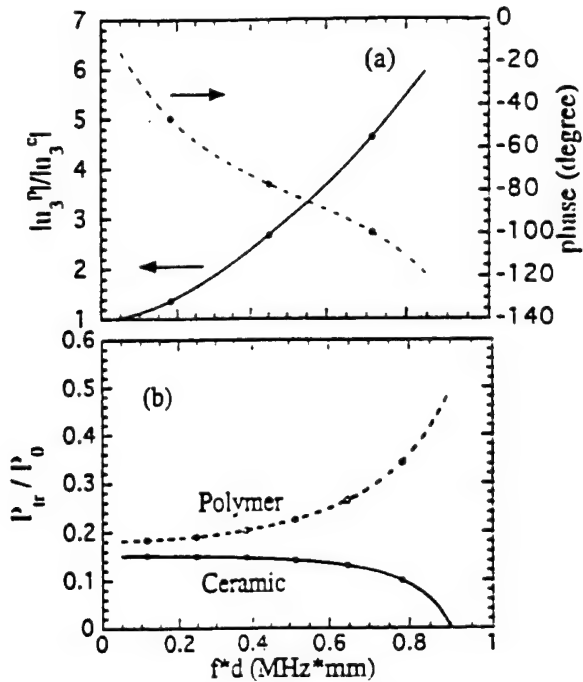
Fig. 4. (a) The surface vibration distribution as a function of frequency for the 2-2 composite with 44% ceramic content at the interface with water and under an acoustic field. u_3^p and u_3^c are the displacement at the center of the polymer plate ($x_1 = d/2$) and ceramic plate ($x_1 = 0$). (b) The acoustic energy (in reduced units) entering the ceramic and polymer regions as a function of frequency evaluated at the interface ($x_3 = 0$) where P_0 is the total energy in the incident wave.

Fig. 5. The energy redistribution inside the composite along the x_3-direction where $x_3 = 0$ is the interface. There is an energy transfer from the polymer to the ceramic inside the composite. As shown in the figures, the width of the transition region increases as the frequency increases (in reduced length unit).

shown in Fig. 2.

As has been pointed out in the introduction, for an ultrasonic piezoceramic polymer composite, one of the most important factors in determining the performance is the effective acoustic energy exchange between the ceramic and the external medium. As seen in Fig. 3 where at frequencies near the lateral mode, the input acoustic impedance of the composite is close to that of water and hence, the reflection coefficient reaches a minimum, the question is how much of that energy enters into the ceramic plates. Figure 4(b) shows how the total acoustic powers entering into the ceramic region and polymer region vary with frequency. Clearly, at the high frequency region, in spite of the fact that the effective transmission coefficient of the composite increases, the amount entering into the ceramic plate actually decreases.

It is also interesting to examine how this acoustic energy distribution in the polymer and ceramic regions changes along the x_3-direction since the interaction between the ceramic and polymer through the joint region will cause the acoustic energy transfer between the two. In Fig. 5, the acoustic energy distribution along the x_3-direction at three frequencies ($f \ll f_t$, $f = f_t/2$, and $f = f_t$, where f_t is the first lateral mode frequency) is shown. In all the cases, there is a redistribution of the acoustic energy along the x_3-axis and the acoustic energy in the polymer is gradually transferred to the ceramic plate. However, at low frequencies, the transition region is much shorter than that at high frequencies (with
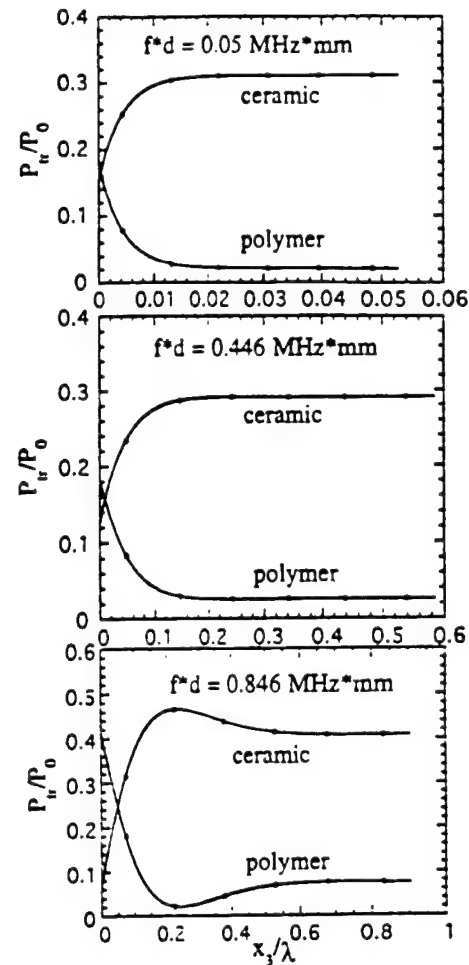
respect to the wave length at that frequency). For instance, in Fig. 5(a), the reduced length x_3/λ is about 0.01 for the acoustic power in the ceramic to reach 90% of the final value, while in Fig. 5(b), this region increases to about 0.1, and in Fig. 5(c), it becomes near 0.2. It should be reminded that in a thickness mode transducer, the thickness of the piezocomposite is $\lambda/2$.

In Fig. 6, the change of the displacement u_3 in the polymer and ceramic regions along the x_3-direction at the three frequencies is presented and it shows that at high frequencies, the displacement amplitude in the polymer and ceramic regions is no longer the same even deep inside the composite.

The change of the input acoustic impedance from eq. (7) along the x_3-direction in the composite is also evaluated. Figure 7 are the results of the 2-2 composite with 44% ceramic content at different frequencies. Apparently, at high frequencies there is a large change of the effective acoustic impedance from the surface into the interior of the composites and even in the interior of the composite, the effective impedance is not the same as that derived from the effective medium theory.[18,19]
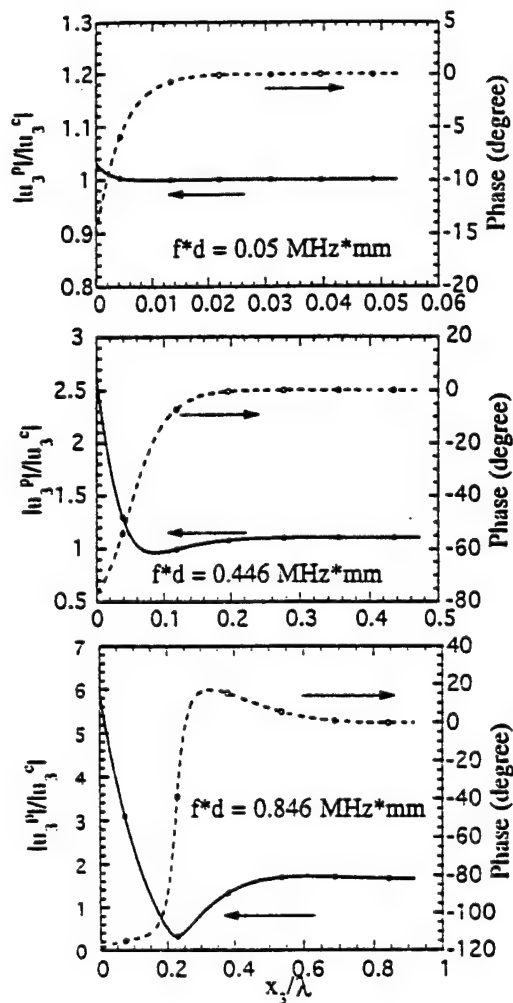
Fig. 6. The vibration profile as a function of the distance from the interface with water ($x_3 = 0$) where u_3^p and u_3^c are the displacement at the center of the polymer plate ($x_1 = d/2$) and ceramic plate ($x_1 = 0$). At low frequencies, the polymer and ceramic vibrate with the same amplitude and phase while at high frequencies, even far away from the interface, the vibration amplitude of the two is still not the same while the phase becomes the same.

3. Wave Reflection and Transmission at Solid-2-2 Composite Interfaces

The issues investigated in this section are quite similar to those studied in the preceding section. The difference is that a solid medium can support shear waves while a fluid cannot. Due to this difference, the boundary conditions (4) must be modified to:

$$T_{33}^{Cm} = T_{33}^{S}, \quad T_{13}^{Cm} = T_{13}^{S}, \quad u_3^{Cm} = u_3^{S}, \quad u_1^{Cm} = u_1^{S}$$
$$\Phi^{Cm} = \Phi^{S}, \quad D_3^{Cm} = D_3^{S}. \tag{8}$$

where the superscript S refers to the variables in the solid medium.

As we have shown in a previous paper,[3] the input acoustic impedance of 2-2 composites calculated here is different from that in the fluid case. In addition, it is also found that at a solid medium-2-2 composite interface, the input acoustic impedance seems to depend on the characteristic impedance of the solid medium at the
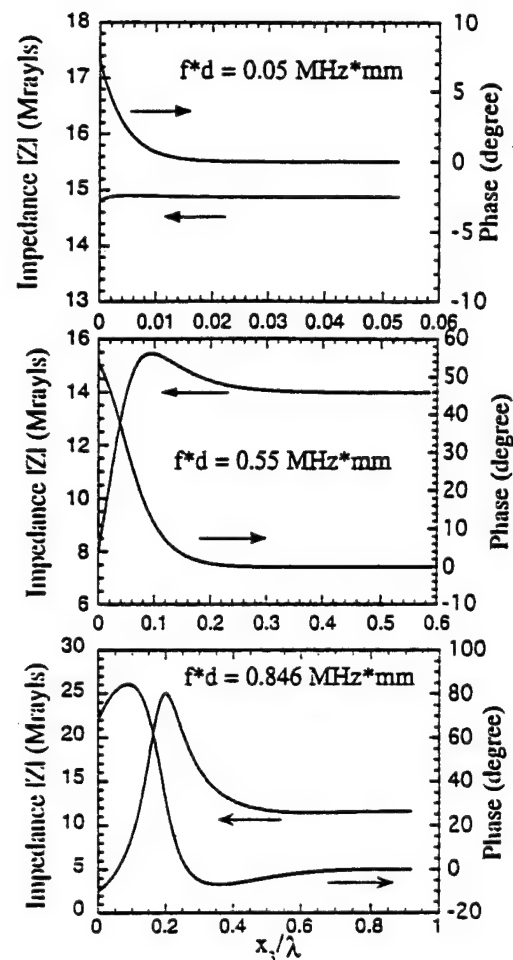
Fig. 7. The effective input impedance from eq. (7) as a function of the distance from the interface with water ($x_3 = 0$) at three typical frequencies: far below the lateral mode, at about the half of the lateral mode frequency, and near the lateral mode frequency.

interface, which is quite different from the fluid medium-composite interface.

To understand this phenomenon, we notice that the difference between a solid medium and a fluid one is that a solid medium has a non-zero shear stiffness constant. Therefore, Z_{in} for a 2-2 composite (44% ceramic content) in contact with solid medium is evaluated where ρ (mass density) and c_{11} are kept as constant and c_{44} is varied and the results are presented in Fig. 8(a). Similarly, Z_{in} for a 2-2 composite in contact with solid medium is also evaluated where ρ and c_{44} are kept constant and c_{11} is varied and the results are shown in Fig. 8(b). The results demonstrate that for a plane incident wave, even if the characteristic longitudinal impedance of the solid medium is kept constant, the effective input impedance of a composite and, hence, the reflection coefficient of a pure longitudinal wave incident normally at the interface will change if the shear stiffness coefficient of the solid medium changes. On the other hand, if the shear stiffness constant is kept constant and the characteristic longitudinal impedance is varied in the solid medium, the effective input acoustic impedance of a composite will not
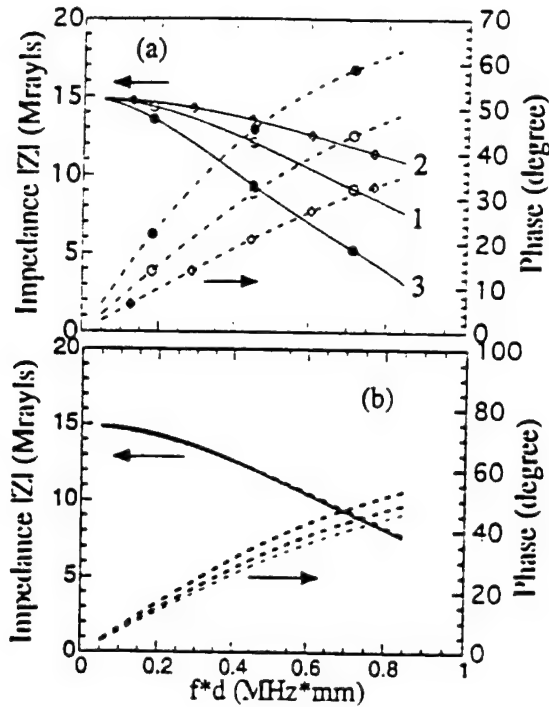
Fig. 8. Data illustrate the dependence of Z_{in} of a composite on the shear elastic constant of the solid medium at the interface. (a) The solid medium for the curve 1 is $\rho = 1.61\,\mathrm{g/cm^3}$. $c_{11} = 1.36 \times 10^{10}\,\mathrm{N/m^2}$. and $c_{44} = 3.43 \times 10^9\,\mathrm{N/m^2}$. and for curve 2 and curve 3. both ρ and c_{11} are kept constant and $c_{44} = 6.86 \times 10^9\,\mathrm{N/m^2}$ and $c_{44} = 1.72 \times 10^9\,\mathrm{N/m^2}$. (b) Here both ρ and c_{44} are kept constant. and $c_{11} = 0.68 \times 10^{10}$. $c_{11} = 1.36 \times 10^{10}$, and $c_{11} = 2.72 \times 10^{10}\,\mathrm{N/m^2}$. The amplitude of Z_{in} does not change much with c_{11} except a small change in the phase.

Fig. 9. The figures illustrate the effect of c_{11} and c_{44} of the solid medium on the surface vibration profile of the composite. (a) The parameters of the solid medium for the data of dashed curve is $\rho = 1.61\,\mathrm{g/cm^3}$. $c_{11} = 1.36 \times 10^{10}\,\mathrm{N/m^2}$. and $c_{44} = 3.43 \times 10^9\,\mathrm{N/m^2}$. and for the solid curve, both ρ, c_{44} are the same except $c_{11} = 2.72 \times 10^{10}\,\mathrm{N/m^2}$. (b) The parameters for the solid medium is $\rho = 1.61\,\mathrm{g/cm^3}$. $c_{11} = 1.36 \times 10^{10}\,\mathrm{N/m^2}$, and $c_{44} = 6.86 \times 10^9\,\mathrm{N/m^2}$. Notice the effect of c_{44} on the surface vibration profile of the composite.

have much change. This phenomenon is directly related to the surface uniformity of the composite which depends on the stress transfer between the two constituents in the composite through the solid medium in contact. It can be shown that this stress transfer is through the shear action in the solid medium.

To illustrate this. the surface vibration distribution in the ceramic and polymer regions is also evaluated for the 2-2 composite in contact with solid media of different c_{11} and c_{44} and the results are presented in Fig. 9. There is very little difference in the surface vibration profile for solid media with the same c_{44} and different c_{11}. In contrast. the surface vibration profile will change as c_{44} is changed [Figs. 9(a) and 9(b)].

Figure 10 illustrates the input acoustic impedance of a composite as a function of x_3 for different solid media at the interface. It shows the length of the transition region in the composite where the evanescent waves are important decreases as the acoustic impedance of the medium. especially the shear modulus, increases.

4. Reflection and Transmission from the Boundary between Fluid and Acoustic Impedance Matching Layer

We now proceed to investigate how the various effects observed in the preceding sections affect the selection of anti-reflection matching layers at the interface. Figure
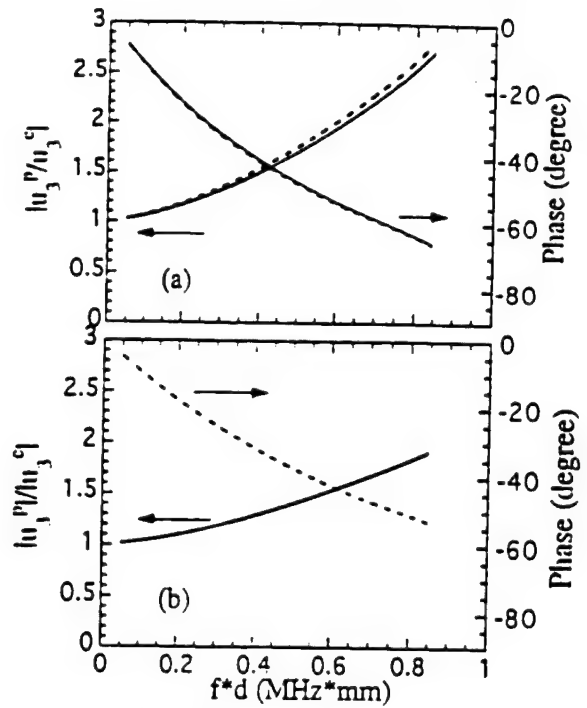
11 is a schematic of an acoustic system which consists of a fluid medium. a matching layer and a 2-2 composite. In this case. there are two interfaces with different boundary conditions to be treated. One of the interfaces is between the 2-2 composite and matching layer where the boundary conditions are those of eq. (8). Another one is the fluid and matching layer interface where the boundary conditions are:

$$T_{33}^s = T_{33}^w, \quad T_{13}^s = 0. \quad u_3^s = u_3^w, \quad \Phi^s = \Phi^w,$$
$$D_3^s = D_3^w \quad \text{at} \quad x_3 = -t \tag{9}$$

where t is the thickness of the matching layer and the other notations are the same as before.

In general. for homogeneous materials. the reflection coefficient from the boundary between a fluid and a matching layer will be zero when the thickness of the matching layer is quarter wavelength and its acoustic impedance Z^M is

$$Z^M = \sqrt{Z^W Z^S} \tag{10}$$

where Z^W and Z^S are the acoustic impedance of the media on the two sides of the matching layer. respectively.[1,2]

For a composite material. from the results obtained in the preceding sections, it is expected that the parameters of the anti-reflection matching layer will be modified. Figure 12 illustrates the derived reflection coefficient from the boundary between the fluid and match-
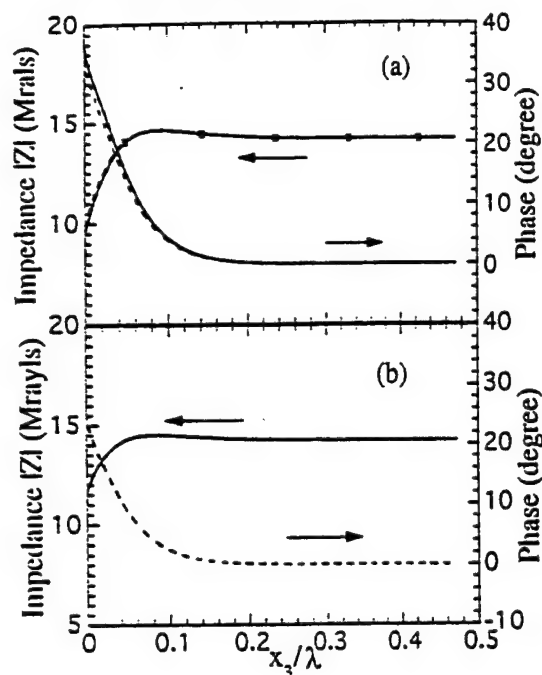
Fig. 10. The figures illustrate the effect of the elastic properties of the solid medium at the interface on the effective input impedance distribution along the x_3-axis at a frequency $f \cdot d = 0.446$ MHz·mm where $x_3 = 0$ is the interface. (a) The dashed line: $\rho = 1.16$ g/cm^3, $c_{11} = 7.72 \times 10^9$ N/m^2, and $c_{44} = 1.588 \times 10^9$ N/m^2. The solid line: $\rho = 1.1$ g/cm^3, $c_{11} = 5.41 \times 10^9$ N/m^2, and $c_{44} = 1.307 \times 10^9$ N/m^2 (Spurrs epoxy). (b) The parameters for the solid medium is: $\rho = 1.61$ g/cm^3, $c_{11} = 1.36 \times 10^{10}$ N/m^2, and $c_{44} = 3.43 \times 10^9$ N/m^2.
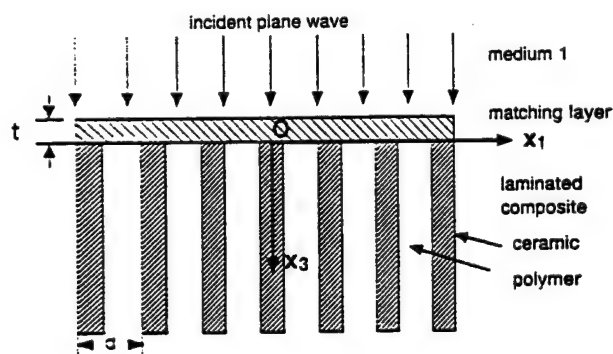
Fig. 11. Schematic of an interface system consisting of a fluid medium (medium 1), a matching layer, and a 2-2 composite. The thickness of the matching layer is t and the period of the composite is d.

Fig. 12. The reflection coefficient from the matching layer system where the total transmission occurs at $f \cdot d = 0.334$ MHz·mm for the matching layer with $t = 2.02 \times d = 0.91 \times (\lambda/4)$ (at $f \cdot d = 0.334$ MHz·mm) and $Z^M = 4.68$ MRayls ($\rho = 1.61$ g/cm^3, $c_{11} = 1.36 \times 10^{10}$ N/m^2, and $c_{44} = 3.43 \times 10^9$ N/m^2) (curve 1). For the comparison, the reflection coefficient from the matching layers with other parameters is also shown here: for curve 2, $Z^M = 3.0$ Mrayls and $t = 1.35 \times d$, and for curve 3, $Z^M = 2.44$ MRayls and $t = 1.58 \times d$.

Fig. 13. The required parameters for (a) Z^M and (b) t of the matching layer to have total transmission as a function of frequency for a water-2-2 composite (44% ceramic volume content) interface (solid lines are the theoretical predictions). The experimental data was presented in (b) as open circles.

ing layer for different matching layer materials where the thickness of the matching layer is chose so that the frequency of the reflection coefficient minimum is at $fd = 0.335$ MHz·mm. From results, it is found that the acoustic impedance of the matching layer from which the reflection coefficient becomes zero satisfies approximately eq. (10) if Z^s is replaced by the effective input acoustic impedance of the 2-2 composite at the low frequency. However, the thickness of the matching layer is no longer quarter wavelength and in fact, it is shorter
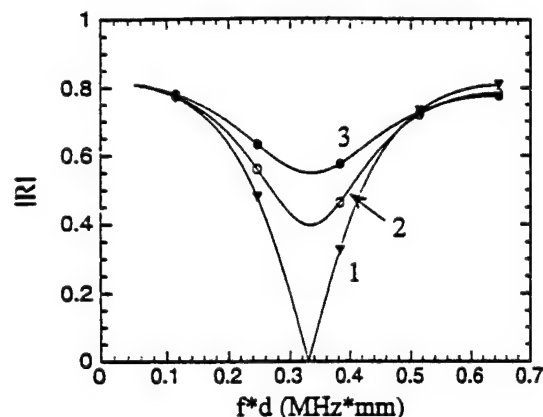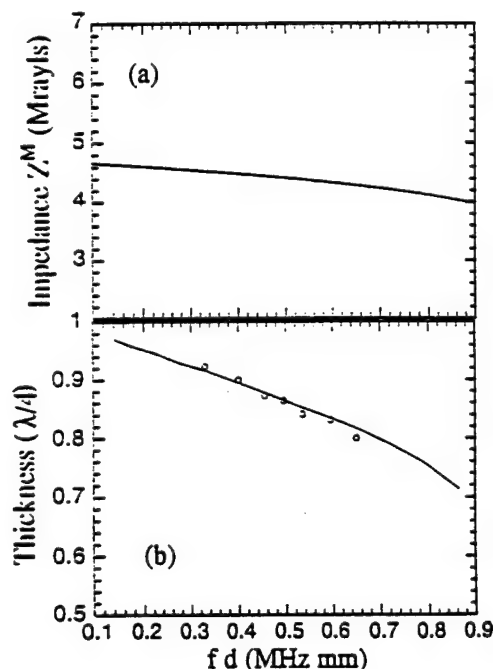
than $\lambda/4$. These results are summarized in Fig. 13. The data in Fig. 13(a) is the acoustic impedance of the matching layer in order for the reflection coefficient to be zero as a function of frequency. In Fig. 13(b), the change of the matching layer thickness as a function of frequency is presented where $t = 1$ corresponds to the thickness of $\lambda/4$ at that frequency. Therefore, as the frequency increases, both the acoustic impedance and the thickness of

the matching layer decrease. For example, when the frequency changes from 0.05 MHz·mm to 0.5 MHz·mm, the acoustic impedance of the matching layer changes from 4.70 MRayls to 4.45 MRayls and the thickness t changes from about $\lambda/4$ to $0.86 \times \lambda/4$. The reduction in the matching layer thickness is a direct result of the fact that the incident plane wave suffers more than $180°$ phase loss upon the reflection from the interface.

From the fact that in the frequency range of interesting, the evanescent waves at the interface will decay approximately as $\exp(-2n\pi x_3/d)$, the effect of the interface of $x_3 = -t$, where t is approximately $\lambda/4$, to the surface vibration distribution at the composite-matching layer interface will be quite small. Therefore, the reflection coefficient between a solid medium and a composite can be used to approximate the reflection at the matching layer-composite interface. Hence, the reflection coefficient R from the system in Fig. 11 can be approximated as:

$$R = \frac{R_{12} + R_{23}e^{2j\beta_0^z t}}{1 - R_{12}R_{23}e^{2j\beta_0^z t}} \qquad (11)$$

where R_{12} is the reflection coefficient from the interface of two semi-infinite media of the fluid and solid (to approximate the reflection coefficients at the fluid-matching layer interface), and R_{23} is that from the solid medium-composite interface (to approximate the reflection coefficient at the matching layer-2-2 composite interface). From eq. (11), the requirements to the matching layer to achieve the total transmission ($R = 0$) can be derived. The acoustic impedance of the matching layer is

$$Z^M = \sqrt{Z^W|Z^{Cm}|\frac{|Z^{Cm}| - Z^W\cos(\theta)}{|Z^{Cm}|\cos(\theta) - Z^W}} \qquad (12)$$

where θ is the phase angle of the acoustic impedance of the 2-2 composite. The thickness of the matching layer is

$$t = \frac{\lambda}{4}\left\{1 - \frac{1}{\pi}\arctan\left(\frac{2Z^M|Z^{Cm}|\sin(\vartheta)}{|Z^{Cm}|^2 - (Z^M)^2}\right)\right\} \qquad (13)$$

In the frequency range of interest, the results from eqs. (12) and (13) are almost identical to those derived from the numerical calculation presented in Fig. 13.

In order to verify the theoretical predictions, the reflection coefficient from a fluid-matching layer interface was measured as a function of frequency utilizing the experimental set-up shown in Fig. 14 where a stainless steel standard was used as the reference. For a 2-2 composite with 44% PZT-5H ceramic in a Spurr epoxy matrix, the required acoustic impedance for the matching layer in frequencies near $fd = 0.5$ (MHz·mm) is about 4.45 MRayls. A series of polymer were examined and the acoustic velocity was determined from the time of flight technique. Combined with the data on the density, the acoustic impedance of the material can be obtained. A Hysol epoxy (EE1068) was chosen because the acoustic impedance $Z = 4.68$ MRayls ($\rho = 1610 \text{ kg/m}^2$, $c_{11} = 1.3634 \times 10^{10} \text{ N/m}^2$, and $c_{44} = 3.432 \times 10^9 \text{ N/m}^2$) is quite close to the required value.[20] For a fixed thickness t of the matching layer, the frequency position of the minimum reflection can be determined and the ratio of
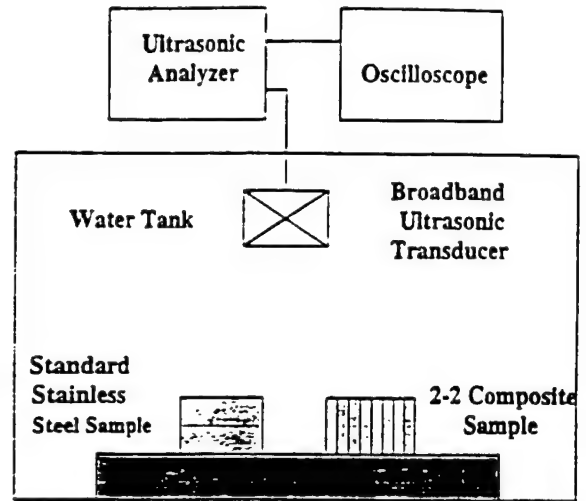

Fig. 14. Schematic of the set-up used to measure the reflection coefficient of 2-2 composites and matching layer system. In order to obtain the phase information of the reflection coefficient, the distance between the probe transducer and the 2-2 composite is maintained the same as that between the probe and the stainless steel standard.

$4t/\lambda$ is obtained. By varying the thickness of the matching layer, the dependence of $4t/\lambda$ on the frequency can be obtained. The data is presented in Fig. 13(b) (open circles) and apparently, there is an excellent accord between the theoretical prediction and experimental data.

5. Summary

The reflection and transmission of a plane acoustic wave at a medium-composite interface and the issues related to the design of matching layer for a composite are analyzed based on an approach developed recently, which can address explicitly the non-uniform field distributions due to the heterogeneity structure of a piezoceramic polymer composite. The effective input acoustic impedance Z_{in} of the composite at the interface was evaluated and both the amplitude and phase show a strong frequency dependence. It was found that for a solid medium, Z_{in} will change if the shear stiffness constant of the medium changes. It was demonstrated that this difference originates from the non-uniformity of the surface vibration distribution of the composite at the interface which depends crucially on the shear stiffness constant of the medium.

Since for a piezoceramic polymer composite, it is the ceramic phase which performs the energy conversion between the acoustic and electric forms, how much acoustic energy can enter the ceramic region is one of the most important parameters in a composite transducer design. In the paper, we show that even though the effective transmission coefficient increases as the frequency is increased, the amount of acoustic energy entering the ceramic region actually decreases. Therefore, there may be a trade-off between the bandwidth, which is related to the transmission coefficient, and the sensitivity in the composite transducer design.

From the fact that there is more than $180°$ phase change in the reflection from the medium-composite in-

Jpn. J. Appl. Phys. Vol. 36 (1997) Pt. 1, No. 11

Q. ZHANG and X. GENG   6861

terface. it is shown that the matching layer thickness is no longer equal to the quarter wavelength but smaller than that. In addition, the acoustic impedance of the matching layer will also be affected by the phase of Z_{in} of the composite, although the effect is not as significant as that in the thickness of the matching layer. These results are confirmed experimentally.

Acknowledgement

1) L. M. Berkhovskikh: *Waves in Layered Media* (Academic Press, New York 1980).
2) B. A. Auld: *Acoustic Fields and Waves in Solids* (John Wiley & Sons, New York 1973), Vols. I and II.
3) T. R. Gururaja, W. A. Schulze, L. E. Cross, R. E. Newnham, B. A. Auld and J. Wang: IEEE Trans. Ultrason. Ferroelectr. & Freq. Control 32 (1985) 481.
4) W. A. Smith: Proc. 1990 IEEE 7th ISAF, Urbana, Illinois, 1990. p. 145.
5) R. E. Newnham, D. P. Skinner and L. E. Cross, Mater. Res. Bull. 13 (1978) 525.
6) B. A. Auld: Mater. Sci. & Eng. A 122 (1989) 65.
7) H. F. Tiersten: *Linear Piezoelectric Plate Vibrations* (Plenum, New York, 1969).
8) Q. M. Zhang and Xuecang Geng: J. Appl. Phys. 80 (1996) 5503.
9) PZT-5H is the trade-mark of Morgan Mattroc Inc. (Beddford, OH 44146) for one of its PZT piezoceramics. Spurr epoxy is the trade-mark of Polysciences. Inc. (Warrington, PA 18976, USA). Their parameters are: PZT-5H: $e_{33} = 23.09 \, C/m^2$, $e_{31} = -6.603 \, C/m^2$, $e_{15} = 17.0 \, C/m^2$, $c_{11} = 12.72 \times 10^{10} \, N/m^2$, $c_{44} = 2.3 \times 10^{10} \, N/m^2$, $c_{33} = 11.74 \times 10^{10} \, N/m^2$, $c_{13} = 8.47 \times 10^{10} \, N/m^2$, $K_{11} = 1700$, $K_{33} = 1470$, $\rho = 7500 \, kg/m^3$. Spurr epoxy: $c_{11} = 5.4 \times 10^9 \, N/m^2$, $c_{44} = 1.3 \times 10^9 \, N/m^2$, $\rho = 1100 \, kg/m^3$.
10) G. S. Kino: *Acoustic Waves: Devices, Imaging, and Analog Signal Processing* (Prentice-Hall, Englewood Cliffs, 1987).
11) Xuecang Geng and Q. M. Zhang: Appl. Phys. Lett. 67 (1996) 3093.
12) D. E. Hall: *Basic Acoustics* (Happer & Row, New York 1987).
13) G. F. Miller and H. Pursey: Proc. R. Soc. London 223 (1954) 521.
14) C. S. Desilets: Ph.D. Thesis, Stanford University, 1978.
15) A. H. Nayfeh, R. L. Crane and W. C. Hoppe: J. Appl. Phys. 55 (1984) 685.
16) D. A. Berlincourt, D. R. Curran and H. Jaffe: *Physical Acoustics*. ed. W. P. Mason (Academic Press, New York, 1964) Vol. I. Pt. A.
17) D. Leedom, R. Krimholtz and G. Matthaei: IEEE Trans. Sonics & Ultrason. 18 (1971) 123.
18) W. A. Smith and B. Auld: IEEE Trans. Ultrason. Ferroelectr. & Freq. Control 38 (1988) 40.
19) K. Y. Hashmoto and M. Yamaguchi: Proc. 1986 IEEE Ultrasonics Symp., Williamsburg, VA, 1986, p. 697.
20) Hysol epoxy is from Hysol electronic chemicals division, CA 91746. USA.

APPENDIX 84

Analysis of the Resonance Modes and Losses in 1-3 Composites for Ultrasonic Transducer Applications

Xuecang Geng and Q. M. Zhang

Materials Research Laboratory and Department of Electrical Engineering

The Pennsylvania State University, University Park, PA 16802

Abstract:

A model is derived for the analysis of the resonance behavior of 1-3 piezocomposites, including the thickness mode and lateral mode. The influence of various losses in a 1-3 composite on the dispersion curves and the quality factor for the thickness mode is examined. It is found that the elastic loss in the polymer has a marked effect on the lateral mode such as reducing the cut-off frequency to zero and producing a large attenuation to the wave propagation. For the thickness mode, it is found that the reduction in the quality factor of a composite compared with piezoceramic is mainly due to the coupling between the two constituents. Even for a composite with the mechanical Q of the polymer higher than that of the ceramic, the mechanical Q of the composite is still lower than that of the ceramic except when the ceramic volume content is very low. Hence, in most of the situations, the mechanical Q of the ceramic phase plays a major role in determining the quality factor of a 1-3 composite transducer.

I. INTRODUCTION

Piezoceramic polymer composites offer many advantages over single phase materials for many transducer applications such as underwater sonar, ultrasonic imaging for medical and NDE applications, and stress sensors [1], [2]. The complementary properties of the polymer and ceramic phases in the electric and mechanical responses make it possible to tune the composite properties over a wide range. On the other hand, in order to fully make use of these advantages and to reduce the manufacture costs of composite, it is necessary and still a challenge to establish a quantitatively structure-property relationship which links various design parameters in the constituents to the final device performance and reveals new properties of composites that are absent in single phase materials.

In the past two decades, a great deal of effort have been devoted to analyze and model the transducer performance of piezocomposites [3]-[9]. The model (quasi-static model) developed by Smith et al. [3] and Hashimoto et al. [4] based on the isostrain and isostress concepts in treating the coupling between the constituent phases provided a qualitative prediction on the effective piezoelectric properties of 1-3 composites as a thickness resonator. It was shown from the model that the thickness coupling factor k_t of a composite can approach the longitudinal coupling factor k_{33}^1 of the piezoceramic rod, which agrees with experiments for composites with a high aspect ratio t/d, where t is the thickness and d is the periodicity of the composites. Because of its simplicity, the quasi-static model offers a convenient means for a quick estimation of the composite parameters. Auld et al. pointed out the existence of the stop band edge resonance in both 2-2 and 1-3 composites due to the periodic arrangement of the ceramic elements in these composites [5], [6]. However, in order to address quantitatively many realistic issues of a composite material such as the influence of the aspect ratio and shape

2

of the ceramic rod in a 1-3 composite on the performance, finite element method (FEM) is often used [7]-[9].

More recently, based on the guided wave approach, an analytical model was developed which is capable of treating many practical issues related to the ultrasonic performance of a 2-2 composite. By combining this with the eigenmode expansion, the ultrasonic properties of a finite thickness 2-2 composite can be analyzed quantitatively and many new features were predicted and confirmed experimentally [10], [11] Compared with FEM, the model offers physical insight into the ultrasonic performance of a 2-2 piezocomposite. It is the objective of this work to extend the model to 1-3 piezocomposites.

In general, a 1-3 composite manufactured by the commonly used dice-and-fill technique [12], as shown in Fig. 1(a), has a three dimensional structure which, although can be treated using the approach in references [13] and [14], is quite complicated mathematically. To simplify the mathematics of the problem, we will make use of the concentric unit cell to approximate the unit cell of a 1-3 composite which has the ceramic rods arranged in a hexagonal lattice, as schematically drawn in Fig. 1(b). Such an approximation has been used in treating a 1-3 composite for hydrostatic applications earlier which reduces the problem to a two dimensional one [15]. We will briefly derive the guided wave solution for a 1-3 composite with the unit cell in Fig. 1(c) which is unbounded in the z-direction. Based on this, the ultrasonic properties related to the thickness resonance will be evaluated and compared with experiment. Comparison will also be made with the quasi-static model to show the range of its validity. We will pay special attention to the mechanical Q in a composite material and show that the mechanical Q of a composite is not a simple extrapolation between the two end

constituents and can be much smaller than those of both end constituent phases (ceramic and polymer).

II. WAVE PROPAGATION IN AN UNBOUNDED 1-3 PIEZOCOMPOSITE

For the unit cell shown in Fig. 1(c), the axial-symmetry along the poling direction of piezoceramic (the z-direction) reduces this three dimensional problem to a two dimensional one. The cylindrical coordinate system is chosen such that the z-axis is along the poling direction of the piezoceramic rod, the r-axis is along the radial direction and the θ-axis is perpendicular to the r-z plane, respectively. Because of the axial-symmetry, all the properties do not depend on the θ-coordinate and hence, the governing equations for the dynamics of a 1-3 piezo-composite become

$$\frac{\partial T_{rr}}{\partial r} + \frac{\partial T_{rz}}{\partial z} + \frac{1}{r}(T_{rr} - T_{\theta\theta}) = \rho \frac{\partial^2 u_r}{\partial t^2} \qquad (1a)$$

$$\frac{\partial T_{rz}}{\partial r} + \frac{T_{rz}}{r} + \frac{\partial T_{zz}}{\partial z} = \rho \frac{\partial^2 u_z}{\partial t^2} \qquad (1b)$$

$$\frac{\partial D_r}{\partial r} + \frac{1}{r} D_r + \frac{\partial D_z}{\partial z} = 0 \qquad (1c)$$

The symbols adopted in this paper are summarized as follows: T_{ij} and S_{ij} are the stress and strain tensor components, u_i is the elastic displacement vector, ρ is the density, D_i is the electric displacement vector and E_i the electric field. The relevant material coefficients are: e_{ij} is the piezoelectric coefficient, c_{ij} is the elastic stiffness, and ε_i the dielectric permittivity. Equation (1) holds for both polymer and piezoceramic phases.

The constitutive equations for the piezoceramic in the cylindrical coordinate system are

$$T_{rr} = c_{11}^E \frac{\partial u_r}{\partial r} + c_{12}^E \frac{u_r}{r} + c_{13}^E \frac{\partial u_z}{\partial z} - e_{31} E_z \tag{2a}$$

$$T_{\theta\theta} = c_{12}^E \frac{\partial u_r}{\partial r} + c_{11}^E \frac{u_r}{r} + c_{13}^E \frac{\partial u_z}{\partial z} - e_{31} E_z \tag{2b}$$

$$T_{zz} = c_{13}^E \frac{\partial u_r}{\partial r} + c_{13}^E \frac{u_r}{r} + c_{33}^E \frac{\partial u_z}{\partial z} - e_{33} E_z \tag{2c}$$

$$T_{rz} = c_{44}^E (\frac{\partial u_r}{\partial z} + \frac{\partial u_z}{\partial r}) - e_{15} E_r \tag{2d}$$

$$D_r = e_{15} (\frac{\partial u_r}{\partial z} + \frac{\partial u_z}{\partial r}) + \varepsilon_{11}^S E_r \tag{2e}$$

$$D_z = e_{31} (\frac{\partial u_r}{\partial r} + \frac{u_r}{r}) + e_{33} \frac{\partial u_z}{\partial z} + \varepsilon_{33}^S E_z \tag{2f}$$

For the polymer phase, e_{ki} in (2) is zero. The superscripts E and S indicate that the coefficients are under the constant E field and constant strain conditions, respectively. Under the quasi-electrostatic approximation, the electric field E is related to the electrical potential Φ

$$\vec{E} = -\nabla\Phi . \tag{3}$$

Combining (1), (2), and (3) yields differential equations governing the elastic displacement u_r, u_z, and the electrical potential Φ in the piezoceramic rod and in the polymer, respectively [11]. The general solutions for the piezo-active modes in the ceramic rod have the form:

$$u_z^c = \sum_i R_i^c f_i^c J_0 (h_i^c r) sin(\beta z)$$

$$u_r^c = \sum_i R_i^c g_i^c J_1 (h_i^c r) cos(\beta z) \tag{4}$$

$$\Phi^c = \sum_i R_i^c t_i^c J_0 (h_i^c r) sin(\beta z)$$

where i runs from 1 to 3 and the superscript c denotes the ceramic. J_0 and J_1 are the zeroth and first order Bessel functions. For each β, there are three h, h_1^c, h_2^c and h_3^c, corresponding to the

quasi-electromagnetic, quasi-longitudinal, and quasi-shear waves in the piezoceramic rod, respectively. f_i^c, g_i^c and t_i^c are the cofactors of $A_{k_1}(i)$, $A_{k_2}(i)$, and $A_{k_3}(i)$ of the determinant:

$$[M_{ij}] = \begin{bmatrix} c_{33}^E \beta^2 + c_{44}^E h^2 - \rho\omega^2 & (c_{13}^E + c_{44}^E)h\beta & e_{33}\beta^2 + e_{15}h^2 \\ (c_{13}^E + c_{44}^E)h\beta & c_{11}^E h^2 + c_{44}^E \beta^2 - \rho\omega^2 & (e_{15} + e_{31})h\beta \\ e_{33}\beta^2 + e_{15}h^2 & (e_{15} + e_{31})h\beta & -(\varepsilon_{11}^S h^2 + \varepsilon_{33}^S \beta^2) \end{bmatrix} \quad (5)$$

(where h is replaced by h_i^c for i=1, 2, and 3, respectively). The time dependent term exp(-jωt) is omitted in (4), where ω is the angular frequency [11].

Similarly, the solutions for the polymer phase can be obtained [11]

$$u_z^P = \sum_i f_i^P (R_i^P J_0(h_i^P r) + Q_i^P Y_0(h_i^P r)) \sin(\beta z)$$

$$u_r^P = \sum_i g_i^P (R_i^P J_1(h_i^P r) + Q_i^P Y_1(h_i^P r)) \cos(\beta z) \quad (6)$$

$$\Phi^P = (C_1^P J_0(h_3^P r) + C_2^P Y_0(h_3^P r)) \sin(\beta z)$$

where i=1, 2 and the superscript p denotes the polymer. Y_0 and Y_1 are the zeroth and first order Hankel functions. f_i^P and g_i^P are the cofactors of $A_{k_1}(i)$, $A_{k_2}(i)$ of (5) with all the material parameters replaced by those of polymer phase, and

$$(h_1^P)^2 = (k_L^P)^2 - \beta^2 , \ (h_2^P)^2 = (k_T^P)^2 - \beta^2 \ and \ (h_3^P)^2 = -\beta^2 \quad (7)$$

where $k_L^P = \dfrac{\omega}{v_L^P}$, $k_T^P = \dfrac{\omega}{v_T^P}$, v_L^P and v_T^P are the longitudinal and shear wave velocities in the polymer phase, respectively.

The expressions of the stresses and electric displacement in the ceramic rod and the polymer phase can be obtained by substituting the equations of the elastic displacement and electric potential into the constitutive equations (2) (for the ceramic rod) [11]

The boundary conditions at the ceramic polymer interface ($r=r_1$) are

$$u_r^c = u_r^p, \ u_z^c = u_z^p, \ T_{rr}^c = T_{rr}^p, \ T_{rz}^c = T_{rz}^p \quad (8a)$$

$$\Phi^c = \Phi^p, \ D_r^c = D_r^p \quad\quad\quad (8b)$$

and the symmetry conditions at r=r$_2$ require

$$T_{rz}^p = 0, \ u_r^p = 0, \ D_r^p = 0 \quad\quad (8c)$$

From (8), the relationship between ω and β, the dispersion relations, can be determined. For each pair of ω and β, the relationships among R_i^c, R_j^p, Q_j^p and C_j^p (in (4) and (6)) can be obtained [11]

III. DISPERSION CURVES, RESONANCE MODES, AND EFFECTIVE ELECTROMECHANICAL PROPERTIES OF A 1-3 PIEZOCOMPOSITE

Shown in Fig. 2 are the two lowest branches of the dispersion curves for a 1-3 piezocomposite which has the parameters of PZT-5H piezoceramic and Spurr epoxy with ceramic volume fraction of 40.5%. In this paper, except otherwise specified, the composites have PZT-5H as the piezoceramic and Spurr epoxy as polymer matrix. The parameters of the PZT-5H piezoceramic and the Spurr epoxy are presented in table I, where the real part of the material parameters is from [16]. The general trend of the dispersion curves in the Fig. 2 resembles that of the 2-2 piezocomposite [11]. At small βr_2 limit, the first branch corresponds to the longitudinal wave propagation along the z-direction, that is, u$_z$ is the dominant displacement which is more or less uniform and in phase along the r-direction. The phase velocity V$_{ph}$ =ω/β is the effective longitudinal wave velocity of the 1-3 piezo-composite. The second branch corresponds to the lateral resonance arose from the periodic structure of the 1-3

7

piezocomposite in the plane perpendicular to the z-axis. The displacement u_z of the polymer is much larger than that of the ceramic and the phase difference between them is 180°.

Under the assumption that the wave length λ in the z-direction ($\beta=2\pi/\lambda$) is equal to two times the thickness t of the 1-3 piezocomposite plate (the condition for the thickness resonance), the theoretical dispersion curves can be compared with the experimental results which are obtained from the 1-3 piezocomposite samples with different thickness [17]. The 1-3 composites were fabricated using dice-and-fill technique and hence, have a unit cell of Fig. 1(a). In the comparison, the composite with the same ceramic volume content is compared. As a result, the lateral mode resonance from the experimental data which is from composites with the unit cell of Fig. 1(a) is lower than that from the model which is based on the composites with unit cell of Fig. 1(c). Due to this reason, no direct comparison can be made on the lateral mode frequency. In an earlier publication [17], it has been shown that over a large volume fraction range (in the ceramic volume content range approximately from 20% to 75%), the lateral mode frequency is mainly determined by the width of the polymer gap. For the composites with the same ceramic volume content, the polymer gap width responsible for the lowest frequency lateral mode for a composite with the unit cell of Fig. 1(a) (experimental composites) is 0.866 times that of a composite with the unit cell of Fig. 1(b) (composites in the model). By taking this factor into consideration in the comparison, the experimental and model results can be compared, which is shown in Fig. 2(b) and apparently, the agreement between the two is quite satisfactory.

The evolution of the resonance modes with βr_2, where r_2 is the half of the period d ($d=2r_2$) of the 1-3 piezocomposite, can be summarized as following. At small βr_2 on the dispersion curves, the frequency of the fundamental thickness mode from the experiment falls on the first

branch as marked by the black dots, and the frequency of the first lateral mode should fall on the second branch. After the crossover region B, the modes interchange the positions on the dispersion curves where the thickness mode is in the second branch while there is a weak resonance at a frequency below the thickness mode and it falls on the first branch. Here, the thickness mode is defined as the one with higher electromechanical coupling factor. The results presented in the Fig. 2 show that there is an excellent accord between the theoretically derived thickness resonance frequencies and the experimentally observed ones when $\beta r_2 < 1$. The discrepancy at $\beta r_2 > 1$ is due to the lower lateral mode frequency in the experimental samples which have a square shaped unit cell. The coupling between the two modes near the cross over region results in a lowering of the resonance frequency of the thickness mode at $\beta r_2 > 1$.

The longitudinal wave velocity of a 1-3 piezocomposite is determined from the dispersion curves using $V_{ph} = \omega/\beta$. Presented in Fig. 3(a) are the comparison of the theoretical and experimental results of the longitudinal wave velocity V^D as a function of d/t (t is the thickness of the composite) for a 1-3 piezocomposite with 40.5% ceramic volume fraction. The experimental results are obtained by the resonance method using HP 4194 Impedance Analyzer for the 1-3 piezocomposite plate at different thickness t and $V^D = 2 f_p t$ (f_p is the parallel resonance frequency). The agreement is very good when d/t is less than 0.65. At d/t higher than 0.65, the experimental values deviate from that of the theoretical one. As has been pointed out earlier, this is due to the lower lateral mode frequency from the experimental samples.

Shown in Fig. 3(b) is the dependence of the longitudinal wave velocity on ceramic volume fraction for a 1-3 piezocomposite with different βr_2, a parameter inversely proportional to the

9

aspect ratio of the unit cell. The lowering of V^D for $\beta r_2 = 1.0$ shown at the low ceramic volume content region in the figure is due to the coupling of the thickness mode with the lateral mode. For composites with higher ceramic volume content, this coupling will occur at higher βr_2 and correspondingly, the lowering of V^D with βr_2 will occur at higher values. Away from the coupling region (the region marked by B in the Fig. 2), V^D exhibits very little dependence on βr_2 which is consistent with the data in Fig. 3(a) and earlier experiment results [18] For the comparison, V^D from quasi-static model are also shown in Fig. 3(b) [3], [4]. Clearly, V^D from the quasi-static model is higher than that determined from this model and experimental data.

The thickness mode electromechanical coupling coefficient of a 1-3 piezocomposite is derived in the model from [16]

$$k_t^2 = 1 - (\frac{v_l^E}{v_l^D})^2 \qquad (9)$$

where v_l^E *and* v_l^D are the longitudinal wave velocity under constant E and constant D conditions, respectively. Presented in Fig. 4(a) is the dependence of k_t on ceramic volume fraction for a 1-3 piezocomposite with different βr_2. Again, the reduction in k_t at the low ceramic volume fraction region for the curve with $\beta r_2 = 1$ is due to the coupling to the lateral mode. At βr_2 away from the coupling region, k_t exhibits very little dispersion. For the comparison, the results from the quasi-static model is also presented in the figure and k_t from the quasi-static model is less than that from this model even when r_2/t approaches zero, where the thickness of the composite is much larger than the period.

The thickness coupling factor for a 1-3 piezocomposite with 40.5% ceramic volume content was evaluated experimentally using the relation [19]:

$$k_t = \frac{\pi}{2}\frac{f_s}{f_p} tan(\frac{\pi}{2}\frac{f_p - f_s}{f_p}) \qquad (10)$$

where f_s and f_p are the series and parallel resonance frequencies of the 1-3 piezocomposite plate, respectively. The dependence of the theoretical and experimental electromechanical coupling coefficient k_t on the aspect ratio t/d is shown in Fig. 4(b) for composites with 40.5% ceramic content. The agreement between the two is excellent for d/t less than 0.65. At d/t above 0.65, the deviation of the theoretical value from the experimental one is due to the lower lateral mode frequency of the experimental samples (Fig. 2) as has been pointed out earlier.

IV. LOSSES IN 1-3 PIEZOCOMPOSITES

In the previous sections, the losses in the materials have not been included. However, as has been demonstrated in many experiments, loss in a 1-3 piezocomposite is much higher than that in piezoceramic, and therefore, it is very important to include the losses in the analysis.

In general, there are three kinds of losses in a piezoelectric material, i.e. mechanical loss, dielectric loss and piezoelectric loss. In the polymer phase, there are only mechanical loss and dielectric loss. The losses in the ceramic phase can be expressed by complex constants [20],

$$\begin{aligned} c_{ij}^E &= c_{ij}^{E'} + jc_{ij}^{E''} \\ e_{ij} &= e_{ij}' + je_{ij}'' \\ \varepsilon_{ij}^S &= \varepsilon_{ij}^{S'} - j\varepsilon_{ij}^{S''} \end{aligned} \qquad (11)$$

and the losses in the polymer phase can be expressed as

$$c_{ij} = c_{ij}' + jc_{ij}''$$

$$\varepsilon = \varepsilon' - j\varepsilon'' \qquad (12)$$

From the fact that the attenuation in piezoceramic is proportional to frequency, the imaginary part of the parameters in the ceramic can be assumed constants [21]. While in the polymer phase, the main loss mechanism is due to viscosity, therefore, $c_{ij}'' = \omega\eta_{ij}$, where η_{ij} is the viscosity coefficient of the polymer.

Fig. 5 illustrates the effect of polymer loss on the dispersion curves of a 1-3 piezocomposite with 40.5% of ceramic volume content. In the calculation, the losses from the ceramic region are assumed to be zero. In comparison with Fig. 2, it is found that the first branch of the dispersion curves are not strongly affected by the loss in the polymer phase. However for the second branch, which corresponds to the lateral mode resonance, there exists no cut-off frequency when loss is introduced, and this branch represents the attenuated guided wave propagation because the imaginary part of the wave vector increases rapidly when real(βr_2) reaches zero as shown in Fig. 5(b). In contrast, the losses in the ceramic phase (when the loss in the polymer is assumed to be zero) do not produce marked changes in the first two branches.

The quality factor Q (or the mechanical Q) for the thickness mode of a 1-3 piezocomposite is evaluated from the dispersion curves from the relation:

$$Q = \frac{\beta_r}{2\beta_i} \tag{13}$$

Where β_r and β_i are the real and imaginary part of the wave vector β, respectively. Presented in Fig. 6 is the Q of a 1-3 piezocomposite as a function of the ceramic volume fraction evaluated at $\beta r_2=0.1$. The loss parameters used in the calculation are those of PZT-5H for the ceramic phase and Spurr epoxy for the polymer (listed in table I). Those parameters are obtained from several sources. The dielectric losses for the PZT-5H ceramic and the elastic losses in Spurr

epoxy were measured. The elastic losses and the piezoelectric losses for the PZT-5H ceramic are taken from [22] and [23]. For the loss part of the elastic compliance s_{33}^E and s_{13}^E which is not available, it is assumed that s_{11}^E and s_{33}^E have the same loss tangent and the loss tangent of s_{13}^E is the same as that of s_{12}^E. The quality factor calculated based on these parameters for a PZT-5H ceramic plate is 75, which is close to that measured directly (Q=60) based on IEEE standard [19]. The elastic loss for the polymer is evaluated at 117 kHz which yields a mechanical Q=2222 for the polymer. The mechanical Q in the polymer phase is inversely proportional to frequency while in the ceramic phase it is a constant.

The results in Fig. 6 show that the quality factor of a 1-3 piezocomposite is less than that of both the ceramic and polymer for the composites evaluated. For the comparison, the quality factor for the thickness mode of several 1-3 composites with different ceramic content and single phase PZT-5H ceramic plate was experimentally determined [19]. The experiment data is also presented in the figure which is consistent with the theoretical results. The lower value of the experimental Q for single phase PZT-5H ceramic plate compared with that from the model may be the main reason for the lower Q of the experimental samples compared with model results. The result here is quite different from the real part of the elastic constant of a 1-3 composite which always lies in between the two end phases. This is also in contrary to the common belief that the low mechanical Q in a 1-3 composite is a result of the loss in the polymer phase. In fact, in the composite evaluated, the mechanical Q of the polymer phase (Spurr epoxy) is much higher than that of the piezoceramic, while the Q of the 1-3 composite is lower than that of the pizeoceramic. The similar conclusion can also be obtained from the

13

quasi-static model. which is presented in Fig. 6, where the quality factor is equal to $1/\tan\delta$ of $\bar{c}_{33}^D$ (the effective elastic constant of the composite at the constant electric displacement D).

To examine whether the observed effect is due to the piezoelectric coupling, the quality factor for a 1-3 composite without piezoelectricity is also evaluated and the results are presented in Fig. 7 where the parameters are taken from Spurr epoxy and unpoled PZT-5H ceramic (no piezoelectric effect) and the mechanical Q of the ceramic is about 200. Apparently, the quality factor here is still less than that of both ceramic and polymer when the Q of the polymer phase is larger than that of the ceramic. On the other hand, when the Q of the polymer phase becomes smaller than that of the ceramic, the quality factor of the composite lies between that of the polymer and ceramic.

To elucidate how different losses of the ceramic phase in a composite influence the quality factor of the composite transducer, calculation is carried out for model composites with different losses in the ceramic. Presented in Fig. 8 is for a 1-3 piezocomposite in which the piezoceramic has dielectric loss only (no piezoelectric and elastic losses) and piezoelectric loss only (the dielectric and elastic losses are assumed to be zero). In both cases, the trend of quality factor with the ceramic volume fraction is quite similar to those in the pure elastic case as shown in Fig. 7. Apparently, through the piezoelectric coupling in the material, both the piezoelectric and dielectric losses reduces the mechanical Q of a 1-3 composite. It should be pointed out that in general, a piezoelectric loss may not imply a real energy loss. Although for the materials examined here, the piezoelectric loss reduces the mechanical Q of the thickness resonance mode, it can also be an energy gain in other cases which means an increase in the mechanical Q, as has been pointed out by Holland [22]

Presented in Fig. 9(a) are the results when all the losses in a 1-3 composite are included (data in table I), where the different polymer loss can be corresponding to different thickness resonance frequency since the elastic loss in the polymer increases linearly with frequency. It can be seen that at high ceramic volume content (for example, >40%), the polymer loss does not have a significant effect on the quality factor of a composite transducer. For example, as the mechanical Q of the polymer is reduced from more than 2000 down to about 10, the Q of the composite changes only from about 63 to 47 for a composite of 40% ceramic volume content. On the other hand, the losses in the ceramic phase seem to play a more important role in determining the mechanical Q of the composite. To illustrate that, in Fig. 9(b), the Q for a composite with losses from the polymer phase only, i.e., there is no loss in the piezoceramic, and for a composite with all the losses included is plotted as a function of frequency, where the ceramic volume content is 40% and the quality factor of the ceramic (PZT-5H) is 75. This is understandable. Since the quality factor is defined as the ratio of stored mechanical energy vs. mechanical energy loss in one cycle and as seen from table I, the elastic constants of the ceramic are more than 10 times higher than those of the polymer, only when the loss in the polymer becomes much higher than that of the ceramic, will it have significant effect on the quality factor of a piezocomposite, as shown in Fig. 9(b).

Clearly, the coupling between the ceramic and polymer in a composite changes the phase relationship between the stress and strain in both phases. Shown in Figs. 10 and 11 are the phase angle δ between the stress (T_{zz}) and strain (S_{zz}) along the z-direction at the polymer center ($r=r_2$) and ceramic rod center ($r=0$) as a function of Q^p/Q^c, the ratio of the mechanical Q in the two phases. Two compositions are examined, one with the ceramic content at 10% (Fig. 10) and the other at 40% (Fig. 11). In the figures, the dashed lines are the δ in the single phase

material and the solid lines are the δ in the composites. Apparently, for the polymer phase, the δ is reduced when the polymer is in the composite, and for the ceramic, it is increased in the composite. Further more, the reduction of δ in the polymer increases with ceramic volume content of the composite, and as shown in Fig. 12, composites with ceramic volume fraction higher than 45%, the phase delay in the polymer becomes positive. Hence, the large increase of the δ in the ceramic phase of the composite is the main reason for the drop in the quality factor of composites since, as pointed out, the high elastic constants in the ceramic phase implies that in most cases, the loss in the ceramic region plays a dominant role in controlling the mechanical Q of the thickness mode of a composite.

V. SUMMARY

A dynamic model is derived for the analysis of the ultrasonic performance of 1-3 piezocomposites. To simplify the mathematics, 1-3 composites with the concentric unit cell was treated in the model which should closely resemble the unit cell of a 1-3 composite with ceramic rods arranged in a hexagonal lattice. It is shown that the model can describe the thickness resonance of a general 1-3 composite quite well in the frequency range away from the mode coupling region. By taking into account of the difference in the width of the polymer gap between composites with different rods arrangements, the model may be used to describe the lateral mode for composites in the volume fraction region (about 20% to 75% ceramic volume fraction range) where the lateral mode frequency is mainly determined by the width of the polymer gap responsible for the mode.

In the paper, special attention is paid to the losses in a 1-3 composite and it is found that the mechanical loss in the polymer has a marked effect on the cut-off frequency of the lateral

mode. For the thickness resonance, the quality factor of a composite is largely determined by the mechanical Q of the ceramic and its coupling to the polymer phase, which seem to be in contrary to the common belief that the low Q in a composite is due to the loss in the polymer. Even for a composite with the mechanical Q of the polymer larger than that of the ceramic, the quality factor (or mechanical Q) of the composite is lower than both constituents. It is found that the phase delay between the strain S_{zz} and stress T_{zz} in the ceramic increases significantly in the composite compared with the single ceramic material, which is the main reason for the reduction of the quality factor Q in a composite. On the other hand, the coupling with the ceramic phase reduces the phase delay between the strain S_{zz} and stress T_{zz} in the polymer when compared with that in the single phase polymer. Due to the piezoelectric coupling, both the dielectric and piezoelectric losses affect the quality factor of a piezocomposite.

Table I. The material parameters for the PZT-5H and Spurr epoxy used in the model calculation

---

Ceramic: $c_{11}^E = 12.72 \times 10^{10}(1.0 + j8.0 \times 10^{-3})$ N/m², $c_{33}^E = 11.74 \times 10^{10}(1.0 + j8.0 \times 10^{-3})$ N/m²,

$c_{12}^E = 7.95 \times 10^{10}(1.0 + j6.5 \times 10^{-3})$ N/m², $c_{13}^E = 8.47 \times 10^{10}(1.0 + j6.5 \times 10^{-3})$ N/m²,

$c_{44}^E = 2.3 \times 10^{10}(1.0 + j1.2 \times 10^{-2})$ N/m²; $\varepsilon_{11}^S = 1700\varepsilon_0(1.0 - j2.7 \times 10^{-2})$, $\varepsilon_{33}^S = 1470\varepsilon_0(1.0 - j2.7 \times 10^{-2})$,

$e_{33} = 23.09(1.0 - j5.4 \times 10^{-5})$ C/m², $e_{15} = 17.0(1.0 - j5.0 \times 10^{-5})$ C/m².

$e_{31} = -6.6(1.0 - j7.2 \times 10^{-3})$ C/m², $\rho^c = 7500$ kg/m³.

Polymer: $c_{11}^P = 5.41 \times 10^9$ N/m², $c_{44}^P = 1.307 \times 10^9$ N/m². $\eta_{11} = 20.74$ N/m²s, $\eta_{44} = 11.0$ N/m²s;

$\varepsilon_{11}^P = 4.0\varepsilon_0$, $\rho^r = 1100$ kg/m³.

REFERENCES:

[1]. R. Newnham, "Composite Electroceramics", Ann. Rev. Mater. Sci., Vol. 16, pp. 47-68, 1986.

[2]. W. A. Smith, " The application of 1-3 piezocomposites in acoustic transducers," Proc. IEEE ISAF, Urbana, Illinois, 1990, pp. 145-152.

[3]. W. A. Smith and B. A. Auld, "Modeling 1-3 composite piezoelectrics: Thickness-mode oscillations," IEEE Trans. Ultrason., Ferroelect., Freq. Contr., Vol. 38, pp. 40-47, 1988.

[4]. K. Y. Hashimoto and M. Yamaguchi, "Elastic, piezoelectric and dielectric properties of composite materials," Proc. IEEE Ultrason. Symp., Williamsburg, VA, 1986, pp. 697-702.

[5]. B. A. Auld, H. Kunkel, Y. A. Shui, and Y. Wang, "Dynamic behavior of periodic piezoelectric composites," Proc. IEEE Ultrason., Symp., Atlanta, GA, 1983, pp. 554-558.

[6]. B. A. Auld, Y. A. Shui, and Y. Wang, "Elastic wave propagation in three-dimensional periodic composite materials," J. Physique, Vol. 45, pp. 159-163, 1984.

[7]. M. Yamaguchi, K. Y. Hashimoto, and H. Makita, "Finite element method analysis of dispersion characteristics for the 1-3 type piezoelectric composites," Proc. IEEE Ultrason., Symp., Denver, CO, 1987, pp. 657-661.

[8]. J. A. Hossack and G. Hayward, "Finite element analysis of 1-3 composite transducers," IEEE Trans. Ultrason., Ferroelect., Freq. Contr., Vol. 38, pp. 618-629, 1991.

[9]. Anne-Christine, Hladky-Hennion, and Jean-Noel Decarpigny, "Finite element modeling of active periodic structures: Application to 1-3 piezocomposites," J. Acoust. Soc. Amer., Vol. 94, pp. 621-635, 1993.

[10]. X. Geng and Q. M. Zhang, "Dynamic Behavior of Periodic Piezoceramic-Polymer Composite Plates", Appl. Phys. Lett. Vol. 67, pp. 3093-3095, 1995.

[11]. X. Geng and Q. M. Zhang, "Evaluation of Piezocomposites for Ultrasonic Transducer Applications—Influence of the Unit Cell Dimensions and the Properties of Constituents on the Performance of 2-2 composites", IEEE Trans. Ultrason., Ferroelect., Freq. Contr., Vol. 44, pp. 857-872, 1997.

[12]. J. W. Sliwa, Jr., A. Ayter, and J. P. Mohr III., "Method for Making Piezoelectric Composite", US Pat. No. 5239736, 1993.

[13]. Kosuke Nagaya, "Method for Solving Vibration Problem of a Plate with Arbitrary Shape", J. Acoust. Soc. Amer., Vol. 67, pp. 2029-2033, 1980.

[14]. H. S. Paul and M. Venkatesan, "Wave Propagation in a Piezoelectric Ceramic Cylinder of Arbitrary Cross Section with a Circular Cylindrical Cavity", J. Acoust. Soc. Amer. Vol. 85, pp. 163-170, 1989.

[15]. H. Jensen, "Determination of Macroscopic Electro-Mechanical Characteristics of 1-3 Piezoceramic/Polymer Composites by a Concentric Model", IEEE Trans. Ultrason., Ferroelect., Freq. Contr., Vol. 38, pp. 591-594, 1991.

[16]. Q. M. Zhang and Xuecang Geng, ìDynamic Modeling of Piezoceramic Polymer Composite with 2-2 Connectivity", J. Appl. Phys. Vol. 76, pp. 6014-6016, 1994.

[17]. Yongan Shui, X. Geng, and Q. M. Zhang, "Theoretical Modeling of Resonant Modes of Composite Ultrasonic Transducers", IEEE Trans. Ultrason., Ferroelect., Freq. Contr., Vol. 42, pp. 766-773, 1995.

[18]. T. R. Gururaja, W. A. Schulze, L. E. Cross, R. E. Newnham, B. A. Auld, and J. Wang, "Piezoelectric Composite Materials for Ultrasonic Transducer Applications. Part I: Resonant

Modes of Vibration of PZT-Rod-Polymer Composites," IEEE Trans. Sonics and Ultrasonics, Vol. SU-32, pp. 481-498, 1985.

[19]. IEEE Standard on Piezoelectricity, ANSI/IEEE Std 176-1987.

[20]. R. Holland, "Representation of Dielectric, Elastic, and Piezoelectric Losses By Complex Coefficients," IEEE Trans. on Sonics and Ultrasonics, Vol. SU-14, pp. 18-20, 1967.

[21]. A. G. Evans, B. R. Tittman, L. Ahlberg, B. T. Khuri-Yakub and G. S. Kino, "Ultrasonic Attenuation in Ceramics," J. Appl. Phys. Vol. 49(5), pp. 2669-2679, 1978.

[22]. R. Holland, "Design of Resonant Piezoelectric Devices", MIT Press, Cambridge, MA 1969.

[23]. H. Wang, Q. M. Zhang, and L. E. Cross, "A High Sensitivity, Phase Sensitive d_{33} Meter for Complex Piezoelectric Constant Measurement", Jpn. J. Appl. Phys., Vol. 32, L1281, 1993.

Figure captions

Fig. 1. (a) Schematic drawing of a 1-3 piezocomposite fabricated from the Dice-and-Fill technique and having a square unit cell. (b) Schematic drawing of a 1-3 composite with ceramic rods arranged in a hexagonal periodic array. A concentric unit cell can be used to approximate hexagonal unit cell. (c) A concentric unit cell and the coordinate system for a 1-3 composite.

Fig. 2. Dispersion curves of a 1-3 piezocomposite with 40.5% ceramic volume fraction. The dots are experimental results from composites as in figure 1(a) and solid lines are from the model for composite as in Figs. 1(b) and 1(c). Region B represents the mode coupling region.

Fig. 3. (a) Longitudinal wave velocity of a 1-3 piezocomposite with 40.5% ceramic content as a function of d/t. The open circles are the experimental results and solid line is from the model. (b) The longitudinal wave velocity as a function of ceramic volume fraction for composites with different βr_2. For the comparison, the result from the quasi-static model is also included.

Fig. 4. (a) The electromechanical coupling coefficient k_t as a function of ceramic volume fraction for composites with different βr_2. For the comparison, the result from the quasi-static model is also included as the solid line. (b) The electromechanical coupling coefficient k_t of a 1-3 piezocomposite with 40.5% ceramic content as a function of d/t. The open circles are the experimental results and solid line is from the model.

Fig. 5. Effect of the loss in the polymer phase on the dispersion curves of 44% 1-3 piezocomposite. Solid lines are from η_{11}=20.737 N/m^2 s and η_{44}=10.994 N/m^2 s, and dotted lines are from η_{11}=8×20.737 N/m^{2}s and η_{44}=8×10.994 N/m^{2}s.

Fig. 6.   Quality factor Q of 1-3 piezocomposites as a function of ceramic volume fraction. Q is evaluated at $\beta r_2 = 0.1$ and f=117 kHz (η_{11}=20.737 N/m²s and η_{44}=10.994 N/m²s for the polymer). The result from the quasi-static model is included as the dashed line. The experimental data is represented as black dots.

Fig. 7.   The influence of elastic loss of polymer on the quality factor of a 1-3 piezocomposite as a function of ceramic volume fraction, where Q_m^P for each curve (from top to bottom) is 2222, 222, 111, 22.2, and 11.1 respectively. The losses for the ceramic phase is from depoled PZT-5H where the piezoelectric coefficients are zero.

Fig. 8.   The contribution of dielectric loss (no elastic and piezoelectric losses) and piezoelectric loss (no dielectric and elastic losses) of piezoceramic to the quality factor of a 1-3 piezocomposite as a function of ceramic volume fraction, where the tanδ of dielectric constant is 2% and the tanδ of the piezoelectric coefficient e_{ij} is 2%. The curves are evaluated at βr_2=0.1 and Q_m=2222 for polymer.

Fig. 9. (a)   The quality factor of a 1-3 piezocomposite with both the elastic loss of the polymer and the elastic, dielectric and piezoelectric losses of the piezoceramic, where the quality factor Q_m^P (polymer) for each curve (from the top to the bottom) is 2222, 222, 111, 44.4, 22.2, and 11.1, respectively. (b) The quality factor of a 1-3 composite with 40% ceramic content as a function of frequency when the loss is from the polymer only (dashed line) and when all the losses are included (solid line).

Fig. 10.   (a) Comparison of the phase delay between the strain and stress in polymer as a single phase material (dashed line) and in composite (solid line). (b) Comparison of the phase delay between the strain and stress in ceramic as a single phase material (dashed line) and in

composite (solid line). Apparently, by compositing, the phase delay in the polymer is reduced while in the ceramic, it is increased. The ceramic volume content is 10%.

Fig. 11. (a) Comparison of the phase delay between the strain and stress in polymer as a single phase material (dashed line) and in composite (solid line). (b) Comparison of the phase delay between the strain and stress in ceramic as a single phase material (dashed line) and in composite (solid line). The ceramic volume content is 40%.

Fig. 12. The change of the phase delay δ in the center of the polymer region and the center of the ceramic region of a composite as a function of the ceramic volume content. The polymer has a Q=2222 and the calculation is carried out at $\beta r_2 = 0.1$. The corresponding quality factor of the composite is also included in the figure.

(a)

(b)

(c)

4

(a)

f*r$_2$ (MHz*mm)

real(β)*r$_2$

(b)

imaginary(β)*r$_2$

the second branch

the first branch

real(β)*r$_2$

7

_Q_ plotted against Volume Fraction, showing two curves: "dielectric loss only" (dotted) and "piezoelectric loss only" (solid).

8

(a)

Q

Volume Fraction

(b)

Q

polymer loss only

all losses included

f^*r_2(MHz*mm)

9

10

(a) polymer phase in the composite / single polymer phase

(b) single ceramic phase / ceramic phase in the composite

11

phase delay in the polymer

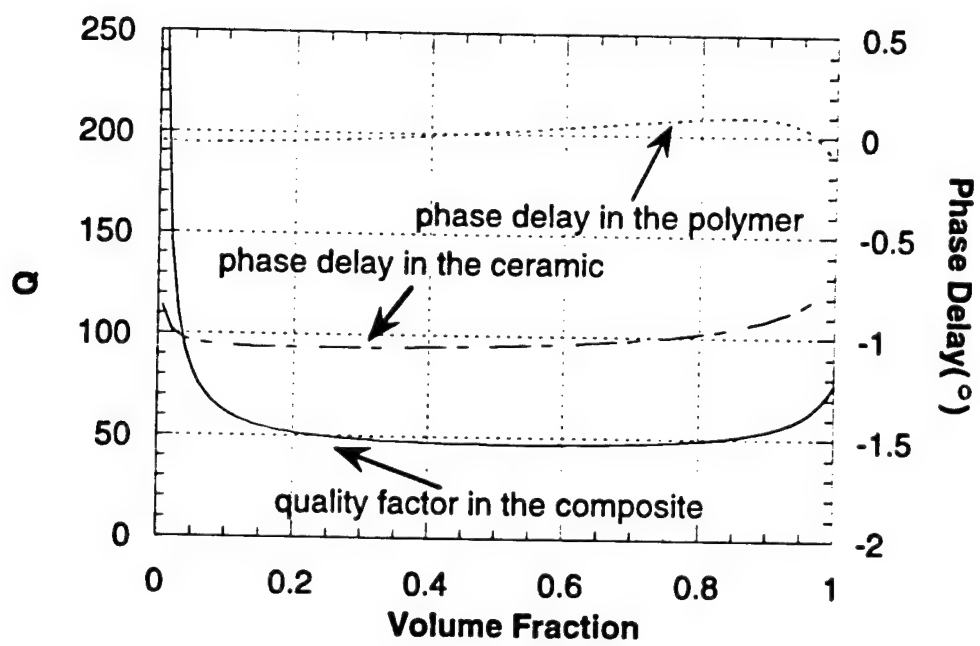phase delay in the ceramic

quality factor in the composite

12

Relaxor Ferroelectrics

APPENDIX 85

Diffuse phase transition in ferroelectrics with mesoscopic heterogeneity: Mean-field theory

Shaoping Li and J. A. Eastman

Material Science Division, Argonne National Laboratory, 9700 South Cass Avenue, Argonne, Illinois 60439

R. E. Newnham and L. E. Cross

Materials Research Laboratory, Pennsylvania State University, University Park, Pennsylvania 16802

(Received 3 September 1996; revised manuscript received 8 January 1997)

The diffuse phase transition in ferroelectrics with mesoscopic heterogeneity has been discussed within the context of a superparaelectric model by using the Ginzburg-Landau formalism. In the Curie region ferroelectrics with mesoscopic heterogeneity are treated as "superparaelectrics" consisting of a mass of polar clusters, each of which has Ising character. Based on the mean-field theory, the influence of the finite-size effects of polar clusters on their structural instability has been discussed by considering a coherent lattice coupling between two structurally different regions. In particular, we have analytically derived the explicit solutions of the distribution of local polarizations. In turn, the processes of polar nanophase precipitation and coarsening have been also discussed in conjunction with the local chemical or structural inhomogeneity. Moreover, we have also analyzed the relationship between the local polarization distribution and the static dielectric susceptibility in ferroelectrics with the nanometric scale heterogeneity. The width of the Curie region is dependent upon the distribution of the sum of localized correlation length, which reflects the size distribution of heterogeneity. The presented analysis reveals that the diffuse phase transition is closely associated with the existence of nanometric polar clusters and their physical size distribution. Intriguingly, our theoretical results bear a very close resemblance to most experimental observations. [S0163-1829(97)03518-2]

I. INTRODUCTION

The dielectric response in ferroelectrics is mainly determined by the characteristics of transverse-optic phonons or soft modes, which virtually reflect the relative movement between cations and anions. Usually the dielectric constants in ferroelectrics can be estimated by the Lyddane-Sachs-Teller (LST) relation, or their phase transition behavior can be quite accurately described by mean-field theories, such as the Landau theory.[1] In normal ferroelectrics, as a rule, the dielectric coefficient peaks at the transition temperature T_c showing a typical Landau behavior. However, a variety of ferroelectrics, such as dielectric composites,[1-3] complex perovskite ferroelectrics,[4,5] disorder or random dipole ferroelectrics,[6,7] ferroelectrics with graded compositions,[8,9] and even nanostructured ferroelectrics and ceramics with ultrafine grains.[10-12] exhibit a very broad peak near their Curie temperatures, whose dielectric coefficients often are larger than those suggested by the LST relation. The phase transitions in these materials are called as the diffuse phase transition (DPT) because they are characterized by broad anomalies in the dielectric response near transition temperature regions, resulting in an exceeding enhancement of dielectric, pyroelectric, elastic-electric, and optoelectric properties within a wide temperature range. More precisely, the principal signature of the DPT is based on the fact that the dielectric susceptibility near the Curie region is governed by the relation[10,13,14]

$$\frac{1}{\chi} = \frac{1}{M} + \frac{(T - T_c)^\alpha}{N}, \quad 1 \leqslant \alpha \leqslant -2 \tag{1}$$

rather than the usual Curie-Weiss law obeyed by normal ferroelectrics. The coefficient α in Eq. (1) increases when the transition becomes more diffused.

In general, the common feature shared by all ferroelectrics with the DPT is that they possess compositional variations, structural inhomogeneities, or phase heterogeneities in the physical scale from micron or submicron range to the atomic level. In fact, physically the inhomogeneity within ferroelectrics influences the manner in which the materials exhibit ferroelectricity.

Experimentally it has been substantially reported that a variety of complex mixed perovskite ferroelectrics with DPT behavior, such as Pb(Mg, Nb)O$_3$ (PMN), (Pb, La)(Zr, Ti)O$_3$ (PLZT), or (Sr, Ba)Nb$_2$O$_6$, have a truly nanometer scale heterogeneity in composition. These types of ferroelectrics are also called ferroelectric relaxors because they also exhibit a significant dispersion of dielectric response near the Curie range, giving rise to sizable nonlinear dielectric and electromechanical phenomena.

The nature of the diffuse phase transition in ferroelectric relaxors has been a long standing puzzle since their detection nearly four decades ago. The high interest in the phase-transition behavior of ferroelectric relaxors not only resides in their fundamental significance, but also it is due to their practical importance[15] because ferroelectric relaxors have the largest intrinsic dielectric constants among all materials on earth.

Forty years ago Smolenskii and co-workers[13,16-18] provided an intuitive picture of the diffuse phase transition in complex ferroelectrics. Through the assumption of a local distribution of phase-transition points and the concept of microregion (Kanzig region), they empirically estimated the broadening of the phase transition, although they could not
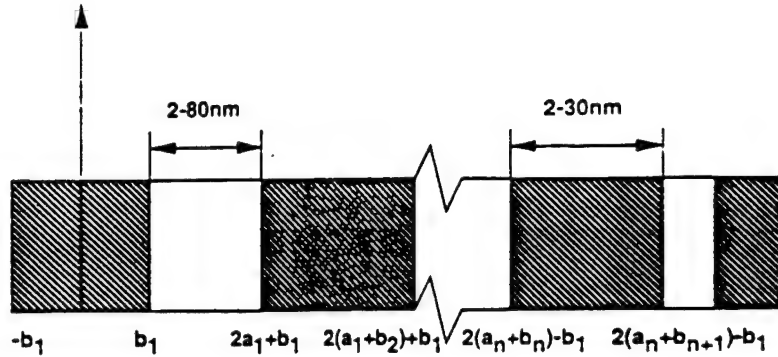
FIG. 1. Schematic representation of the distribution of local order parameters in an inhomogeneous system.

offer a solid physical ground about their assumption. Following Smolenskii's pioneer work, many important researches about ferroelectric relaxors were carried out in the 1960's–1990's, and a number of models have been proposed for interpreting the dielectric response of the relaxors. Here we do not attempt to review the enormously voluminous experimental and theoretical literature in this area. However, it should be emphasized that Cross[19] proposed a superparaelectric model which suggested that the DPT in the relaxors is generated by their mesoscopic heterogeneity.

Nevertheless so far the detailed physical process of the diffuse phase transition in these materials has not been understood completely yet. Unresolved questions include, the exact nature of the diffuse phase transition and the intrinsic connection between the heterogeneity and their dielectric response. Particularly interesting is the phase-transition width or the diffuseness of the phase transition, which influences practical applications. An intriguing question here is: does the width of the Curie region really, as expected before, depend on the dipole-dipole interaction between clusters, or does another generic cause related with the microstructure itself govern the diffuseness of the phase transition? As a matter of fact, a more profound fundamental issue is: is it possible to artificially engineer and manipulate ferroelectric phase transition by controlling the mesoscopic heterogeneity in order to tailor and design dielectric properties of ferroelectric dielectrics?

It is the thesis of this paper that the origin of the diffuse phase transition in ferroelectric relaxors lies in a size effect and ties up with their heterogeneity and relevant physical scale. In this work, we attempt to quantify the correlation between the diffuse phase transition in relaxors and their mesoscopic heterogeneity, although experimentally enormous evidence has strongly suggested that the formation of polar clusters with nanometer size, on a scale significantly larger than the lattice constant, is responsible for their diffuse phase transition.[1]

In light of the complexity of the topic, we have organized this paper as follows. In Sec. II, we present an extended Ginzburg-Landau model for the case of the inhomogeneous system by constructing a simple but rather realistic free-energy equation for such a system. In Sec. III, we evaluate the shift of local phase-transition points, and the explicit solutions of polarization distribution are given by a continuum theory. Section IV contains a quantitative analysis of the features of diffuse phase transition of ferroelectric relaxors, in which we discuss the relationship between the behavior of local polarization and overall dielectric response. We calculate the temperature variation of order parameters along with the responses to a weak external field, and we show how the overall phase transition is controlled through mesoscopic heterogeneities. Finally our conclusions are summarized in Sec. V.

II. THEORETICAL ANALYSIS: FREE-ENERGY EQUATION IN A COHERENT SYSTEM

The essence of the present work, as will emerge below, is an effort to quantitatively analyze the dielectric response and the phase stability of polar clusters in relaxors in connection with their physical sizes and the features of their diffuse phase transition. One of the primary difficulties concerning DPT in relaxors is to describe spatial inhomogeneities in the system analytically. For simplicity let us first envisage an inhomogeneous system consisting of two different chemical regions. One is subsystem A as the matrix phase and another is denoted as subsystem B as illustrated in Fig. 1, each of which behaves as a "Devonshire ferroelectric." In reality, the subsystems A and B are interconnected with one another as a 0-3 nanocomposite. To constructing an analytic expression of total free energy, we introduce two local order parameters, $P_a(r)$ and $P_b(r)$, corresponding to the polarization of subsystems A and B. Both localized order parameters together can describe the polarization behavior in a medium, i.e., an ensemble of clusters within a matrix, on the mesoscopic scale, over which there are enough atoms present so that the order parameters have thermodynamic meaning, and they can be described in the approximation of a continuous medium. In the following analysis, we restrict ourselves to the following conditions. (i) Two local scale order parameters correspond to a one-component representation, such as the case of the (111) direction in PMN system. The two order parameters have their intrinsic bulk Curie points when the physical sizes of two subsystems are infinitely large; and (ii) there is a direct coherent coupling between two order parameters at interfaces and the phase transition in each subsystem is of the second order. By following the free-energy expressions in the literature,[20-23] the thermodynamic potential of an inhomogeneous system can be constructed in a Landau-Ginzburg form.

$$\Phi = \int \left\{ \Phi_{a0} + \Phi_{b0} + \frac{1}{2}\xi_1(\nabla P_a)^2 - \frac{1}{2}\xi_2(\nabla P_b)^2 + \frac{A}{2}P_b^2(r) + \frac{B}{4}P_b^4(r) + \frac{C}{6}P_b^6 + \frac{\alpha}{2}P_{pa}^2(r) - \frac{\beta}{4}P_a^4(r) + \frac{\gamma}{6}P_a^6(r) \right.$$

$$\left. - \frac{Q_2}{2}P_b^2\delta\left\{r = b_{n+1} + \left[\sum_n 2n(a_n+b_n) - b_1 + b_{n-1}\right]\right\} + \frac{Q_1}{2}P_a^2\delta\left(r = a_{n+1} + \left[\sum_n 2n(a_n+b_{n-1}) - b_1 + a_{n+1}\right]\right)\right\} dr,$$

$$n=0; \pm 1; \pm 2; \pm 3; \dots, \quad (2)$$

where Φ_{a0} and Φ_{b0} denote the thermodynamic potential of subsystems A and B in the paraelectric phase state. α, β, γ, A, B, and C are coefficients in the thermodynamic expansion, and especially $\alpha = \alpha_0(T-T_1)$, and $A = A_0(T-T_2)$. T_1 and T_2 are the bulk phase transition temperatures in each subsystem, respectively. $T_2 > T_1$ is defined in the following discussion. ξ_1 and ξ_2 are the coefficients of gradient terms of order parameters. The Ginzburg term $\xi_i(\nabla P_i)$ reflects the presence of polarization inhomogeneities in the material. $\delta(r)$ is a delta function which describes the coordinates of the interface between two subsystems. The δ function is commonly used to represent the coupling terms at the interface in ferroelectric media.[7,23-25] Although, in principle, the general conclusion of our theoretical results will not be affected by choosing the δ function as a connection function, it simplifies the analytical and numerical calculations.

The integral of Eq. (2) is over all space since the order parameters vary spatially. Thus, the local order parameters $P_a(r)$ and $P_b(r)$ are the functions of space coordinates. a_n and b_n are the radius of domains of subsystems in one of their polar axes. More precisely, b_n is defined as the size of subsystem B, representing high-temperature ordered clusters within ferroelectric relaxors, which is on a mesoscopic scale, i.e., $b_n = 2-30$ nm. The matrix phase is in fact a three-dimensional network, and the dimensional scale of the matrix phase A. a_n essentially stands for the minimum distance between two clusters, which ranges around 2 to 80 nm, from a nanometer size up to a submicron level. In reality the average size of a_n is relatively larger than b_n. The two order parameters which appear in the invariant free-energy function can possess different sequences of irreducible representations of symmetry groups in the certain temperature range. Q_1 and Q_2 are defined as the coherent coupling coefficients, which characterize the coherent coupling at the interfaces between different regions. Physically the coupling terms can be related to the stored elastic and electrostatic energy caused by coherency coupling. The coefficients Q_1 and Q_2 structurally allow the polar cluster to coherently conjugate to the other local order parameter. The spatial distribution of the polarization can be obtained by solving the Euler-Lagrange equations

$$\xi_1\frac{d^2P_a}{dr^2} - (\alpha P_a + \beta P_a^3 - \gamma P_a^5) = 0, \quad (3a)$$

$$\xi_2\frac{d^2P_b}{dr^2} - (AP_b - BP_b^3 - CP_b^5) = 0, \quad (3b)$$

with associated periodic boundary conditions

$$\left[\xi_1\frac{dP_a}{dr} + Q_1P_a\right]\delta P_a\Big|_{r=\Sigma_n 2(a_n+b_n)-b_1} = 0, \quad (4a)$$

$$\left[\xi_1\frac{dP_a}{dr} - Q_1P_a\right]\delta P_a\Big|_{r=\Sigma_n 2(a_n-b_{n+1})-b_1} = 0, \quad (4b)$$

$$\left[\xi_2\frac{dP_b}{dr} + Q_2P_b\right]\delta P_b\Big|_{r=\Sigma_n 2(a_n-b_{n+1})-b_1} = 0, \quad (4c)$$

$$\left[\xi_2\frac{dP_b}{dr} - Q_2P_b\right]\delta P_b\Big|_{r=\Sigma_n 2(a_n-b_n)-b_1} = 0. \quad (4d)$$

Equations (3) and (4) are obtained by functional differentiation of Eq. (2). If there does not exist a mutual coupling at interfaces between two subsystems, the thermodynamic behavior of each subsystem will become independent of each other. And then these equations would be exactly identical with those in the model of Tilley and Zeks[21,22] for describing the behavior of finite ferroelectric systems.

By considering the interactions between two subsystems, a coherent interface state is assumed to be present at the boundaries of two subsystems. The coherency is defined by the requirement that the local order parameters from one subsystem to another subsystem are continuous across all interfaces. In this case, the order parameter in one subsystem will appear as the exact same as the order parameter of the second subsystem at interfaces, i.e.,

$$P_a(r)\Big|_{r=\Sigma_n 2(a_n+b_{n+1})-b_1} = P_b(r)\Big|_{r=\Sigma_n 2(a_n+b_{n+1})-b_1}, \quad (5a)$$

$$P_a(r)\Big|_{r=\Sigma_n 2(a_n+b_n)-b_1} = P_b(r)\Big|_{r=\Sigma_n 2(a_{n+1}+b_{n+1})-b_1}. \quad (5b)$$

Accordingly Eqs. (5) become

$$\frac{dP_b}{dr} - \frac{P_b}{d_2}\Big|_{r=\Sigma_n 2(a_n-b_n)-b_1} = 0, \quad (6)$$

$$\frac{dP_b}{dr} + \frac{P_b}{d_2}\Big|_{r=\Sigma_n 2(a_n-b_{n-1})-b_1} = 0, \quad (7)$$

$$\frac{dP_a}{dr} - \frac{P_a}{d_1}\Big|_{r=\Sigma_n 2(a_n-b_{n-1})-b_1} = 0. \quad (8)$$

$$\frac{dP_a}{dr} + \frac{P_a}{d_1}\Bigg|_{r=\Sigma_n 2 \cdot a_{n-1} - b_{n-1}) - b_1} = 0, \qquad (9)$$

with the condition $d = -d_1 = d_2$. $\qquad$ (10)

Here $Q_1 = \xi_1/d_1$ and $Q_2 = \xi_2/d_2$. d_1 and d_2 are defined as the extrapolation lengths, which reflect the strength of the coherent coupling at interfaces. Conceptually d is similar to the extrapolation length in the case of an isolated small particle,[21] measuring the strength of the surface effect. We will discuss this aspect in detail later on.

One of the implications in Eqs. (5)–(10) is that localized phonon modes in adjacent chemically different regions can be coupled to one another via an interface coupling. The polar clusters might create highly nonlocalized electric and strain fields at interfaces, and these fields might be conjugated to the other local order parameter in the vicinity of interfaces. Two points should be stressed here. (a) The coherent coupling resulting in a mutual interaction at interfaces is arising from matching the cluster phase with the parent phase at interfaces, which leads to minimizing the interfacial energy. Interfacial energy can be elastic or electrostatic in nature. (b) In reality, the interfaces between two chemically different regions are quite fuzzy. In the continuous-medium approximation it is difficult to describe the immediate vicinity of the interface boundary between two structurally different regions explicitly. However, the main concern regarding the imposed boundary conditions is only to ensure that the order parameters match exactly at the interface. other than the exact location of the interface.

III. LOCAL POLARIZATION AND LOCAL PHASE TRANSITION

A. Local polarization distribution

We next examine the influence of heterogeneity on the distribution of local polarizations. The explicit nontrivial solutions of Eqs. (3). i.e.. spatial distribution of polarization $P_a(r)$ and $P_b(r)$, can be obtained precisely with the help of Eqs. (5)–(10), although. in general. they are quite cumbersome.[26] Specifying a chosen area $(-b_n, 2a_n - b_n)$. we now find the space profile of the local order parameter analytically. Focusing attention on the temperature region from $T \ll T$. we consider that the induced local polarization $P_a(r)$ in subsystem A is small. while in subsystem B the polarization P_b deviates from P_{b0}, i.e., $P_b = (P_{b0} - \Delta P_b)$. P_{b0} is the polarization at the coordinate origin. ΔP_b is the polarization variant, primarily due to the size effect and interface interactions. By assuming $\Delta P_b / P_{b0} < 1$ if the physical dimension of b is small enough, Eqs. (3) can be approximately written as

$$\xi_2 \nabla^2 P_a = (A - B P_{0b}^2 - C P_{0b}^4) P_a, \quad P_b \in (-b_n, b_n); \qquad (11a)$$

$$\xi_1 \nabla^2 P_a = \alpha P_a, \quad P \in (b_n, 2a_n \pm b_n). \qquad (11b)$$

Note that the validity of the solution of Eq. (11a) can be inspected by integrating Eq. (3a) with additional symmetric boundary conditions $dP_b/dr \to 0$ and $P_b \to P_{0b}$ as $r \to 0$.

From the coherent boundary conditions of Eqs. (5). the special solutions for Eq. (11) can be approximately written as

$$P_b = P_{b0} \cos(k_2 r), \quad P \in (-b_n, b_n), \qquad (12a)$$

$$P_a = \frac{P_{b0} \cos(\kappa_2 b_n)}{\cosh(k_1 a_n)} \cosh\{k_1[r - (a_n + b_n)]\},$$

$$P_a \in (b_n, 2a_n + b_n), \qquad (12b)$$

with

$$\kappa_1^2 = \frac{\alpha_0(T - T_1)}{\xi_1}, \qquad (12c)$$

$$P_{b0} \pm \left\{ -\frac{B}{2C}\left[1 - \sqrt{1 - \frac{4A_0 C}{B^2}(T - T_{2c})}\right]\right\}^{1/2},$$

and

$$T_{2c} = T_2 - (\xi_2 \kappa_2^2 / A_0), \qquad (12d)$$

where κ_1 and κ_2 are defined as the characteristic lengths, which reflect the correlation radius of the order parameters and describe the breath of polarization fluctuation in each subsystem. Inserting Eq. (12b) into Eqs. (8) or (9), one obtains

$$\kappa_1 \tanh(\kappa_1 a_n) = \frac{1}{d}. \qquad (13)$$

Since $T \gg T_1$ and thus $\kappa_1 a_n \gg 1$. one further has

$$\kappa_1 = \frac{1}{d}. \qquad (14)$$

Equation (14) implies that the extrapolation length of d in this case is associated with the physical properties of the adjacent phase and temperature as well. On the contrary, in the situation of free surfaces (air-solid interface), the extrapolation length of an isolated nanometric particle can be mainly considered as a constant.[21,22] This argument in fact makes sense by considering the fact that the coherent coupling strength at solid-solid interfaces should be closely associated with the surrounding interfacial environment or the feature of lattice vibrations in the adjacent phase. Likewise, inserting Eq. (12a) into Eqs. (6) or (7), one has

$$\tan(\kappa_2 b_n) = \frac{1}{\kappa_2 d}. \qquad (15)$$

When the physical size of polar cluster b_n is small, the term $\tan(\kappa_2 b_n)$ in Eq. (15) can be expanded as a Taylor series. By neglecting the higher-order terms of $(\kappa_2 b_n)$ in Eq. (15) and using Eq. (14), Eq. (12d) will become

$$T_{2c} = T_2 - (\xi_2 \sqrt{\alpha}i / \sqrt{\xi_1} b_n A_0). \qquad (16a)$$

Equation (16a) can approximately estimate the shift of the Curie point in the cluster phase B. Clearly, the original Curie transition points are modified by the physical size and the coherent coupling strength. Figure 2 shows the transition temperature dependence of the physical size b_n of nanomet-
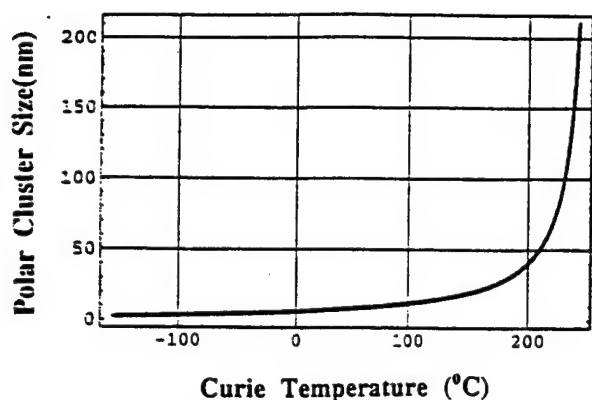
FIG. 2. The physical sizes of polar clusters as a function of their size-induced phase transition point. The free-energy parameters for this calculation can be found in Tables I and II, which have the cgs unit unless specified.

ric clusters. Essentially the phonon modes of one region can couple to the soft mode in the adjacent region locally to perturb the stability of polar phase and soft-mode transition. giving rise to a disturbance of the correlation of dipoles, and thus leading to a shift of the Curie temperature.

On the other hand. when temperature is below or near to T_1, the polarization variant ΔP_2 in the cluster domain becomes negligibly small. And then from Eqs. (3) and (10), the shift of the Curie point of the matrix phase A near interfaces can be also estimated by

$$T_{1c} = T_1 + (\xi_1 \sqrt{A} \overline{\Lambda \xi_2} a_\pi \alpha_0).   (16b)$$

The underlying physics here is that two local order parameters are reconciled by a coherent interface boundary condition. The coherent coupling between these order parameters influences the softening of local phonon modes. leading to a shifting of the Curie temperatures of both the nanometric cluster phase and the matrix phase. respectively.

The variations of polarization in polar clusters are plotted as the functions of temperature and their physical size in Fig. 3. The induced polarization P_a in subsystem A is also numerically plotted as the functions of both the normalized
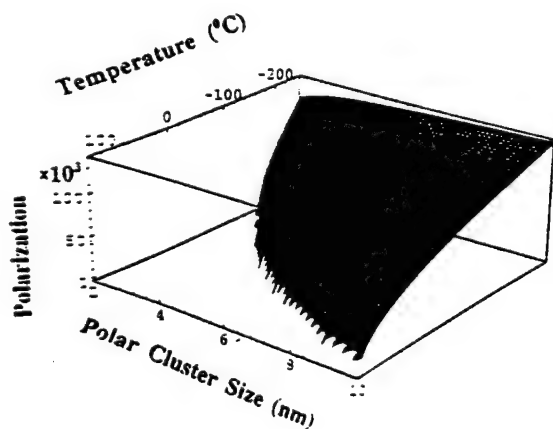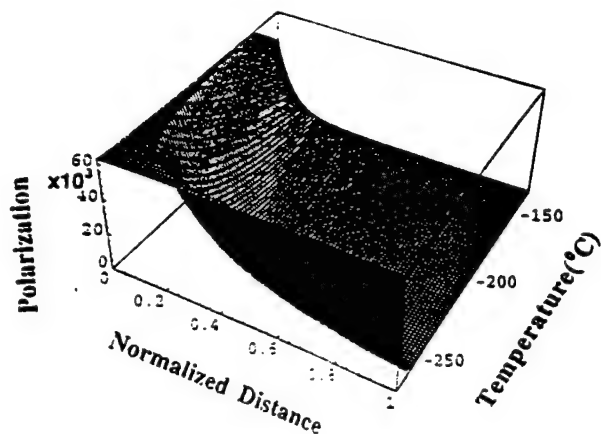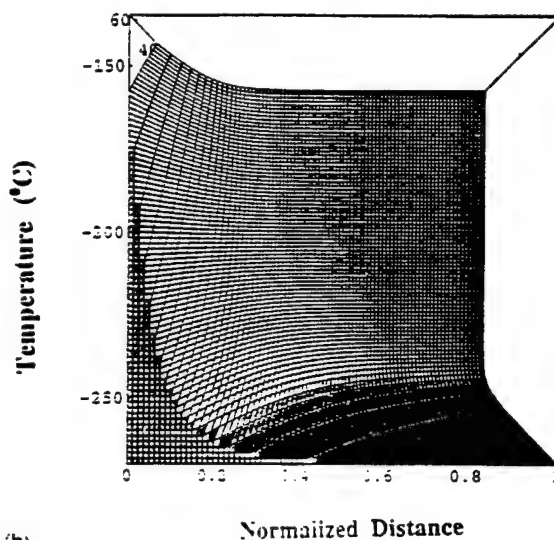

FIG. 3. Calculated polarization of a polar cluster as functions of both temperature and its physical size.

(a)

(b)

Normalized Distance

FIG. 4. Different views of the induced polarization at the interface. The normalized distance stands for $(r - b_n)/b_n$. b_n is the physical size of polar clusters and we take $b_n = 5$ nm here for the calculation. (a) The spatial profile of induced polarization in the matrix as a function of temperature and the normalized distance. (b) The local transition temperature is defined as one at which the induced polarization approaches zero. i.e. $P = 0$. The distribution of the local Curie temperatures in subsystem A near the interface is illustrated here.

coordinate and temperature in Fig. 4. It can be seen that the polarization in polar clusters P decreases at interfaces. while induced polarization P_a increases near interfaces. Several important features are apparent. i) The cluster phase B can induce the polarization in the periphery of subsystem A, even though the temperature is above the original local Curie temperature of subsystem A. In other words. a polarization $P_a(r)$ occurring in subsystem A is caused by the coherent coupling from subsystem B. ii) The initial size of a polarized cluster is determined by the spatial inhomogeneity. As the temperature decreases. the size of the polarized regions will grow. forming a polar nanodomain with a size almost twice as large (8–10 nm) as the initial one (4–5 nm) at low temperature. The temperature evolution of the spatial
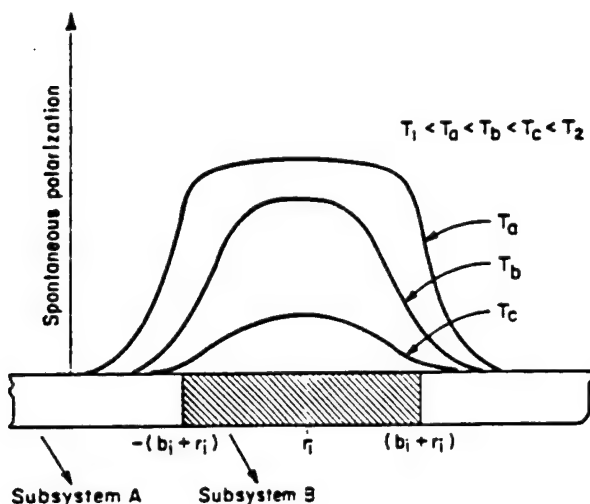
FIG. 5. Illustration of the growth pattern of polar clusters by the polarization spatial profile at different temperatures.

profile of a cluster polarization is schematically depicted in Fig. 5. It is clear that upon cooling the region near the boundary between two subsystems can no longer sustain a structure with zero polarization, even within subsystem A. As expected, the ferroelectric phase transition can be nucleated in this region, even though this region is intrinsically the paraelectric phase. The polarization occurring in subsystem A is extrinsic in nature at this temperature stage. Experimentally the growth of polar microregions in PLZT and other relaxors has been observed as temperature decreases,[27-29] which is quite consistent with our theoretical description. From the lattice vibration point of view, the two subsystems have different characteristics of phonon modes because of differences in composition. The coherent coupling can link two local order parameters coherently and influences the softening of the local phonon modes upon one another in some degree.

B. Local phase transition

We now look at the distribution of local Curie temperatures at interfaces. Figure 4(a) shows that as the boundary between polar cluster and nonpolar matrix moves into sub-

system A, the size of polarized region increases. If we define the local Curie temperature as the point at which the local spontaneous polarization just approaches zero, one can find in Fig. 4(b) that the local Curie temperature will drop rapidly from the periphery of subsystem A to the interior of subsystem A where the chemical composition favors an unpolarized state in this temperature range. Quite clearly, at the exact interface, the local Curie point is the transition temperature of polar clusters, and then it decreases quickly as a function of the space coordinates.[19] The essential point here is that the coupling-induced polar structure in a paraelectric matrix phase can exist even above its intrinsic Curie temperature. The local Gibbs free energy in subsystem A as a function of space-polarization coordinate can be obtained by substituting Eq. (12b) into Eq. (2), as illustrated in Fig. 6. The evolution of potential wells represents the magnitude of induced polarization in subsystem A.

Lastly, we close this section by making some comments on the coherent coupling and the range of applicability of the Landau theory. The so-called coherent coupling between two localized order parameters means that discontinuities in the distribution of order parameters are not permitted along interfaces. The lattice coupling plays an important role in the coherent coexistence of two phases with slightly different lattice parameters and symmetry. There are two fundamental reasons why the coherent coupling would occur in real systems. Since incoherent interfaces usually have higher interfacial energies than coherent interfaces, the coherent equilibrium at the interfaces is actually the stable state if the lattice match is close enough.[30,31]

On the other hand, in its main approximation, the Landau theory of phase transitions ignores long-wave fluctuations of order parameters. However, it is important to realize that one can calculate contributions from the long-wave fluctuations as long as the contributions are small enough.[32-36] The critical range is proven to be very narrow in ferroelectrics[32-34] because the smoothly varying Coulomb force is responsible for establishing the polar phase. In fact, the logarithmic corrections have been proven to be difficult to detect experimentally. In experiments, the observed phase-transition behavior generally appears in agreement with the results of Landau theory. Practically, in most of cases, one can use the Landau theory to describe the phase transition for the entire phase-transition region. Therefore, it appears safe to assume that
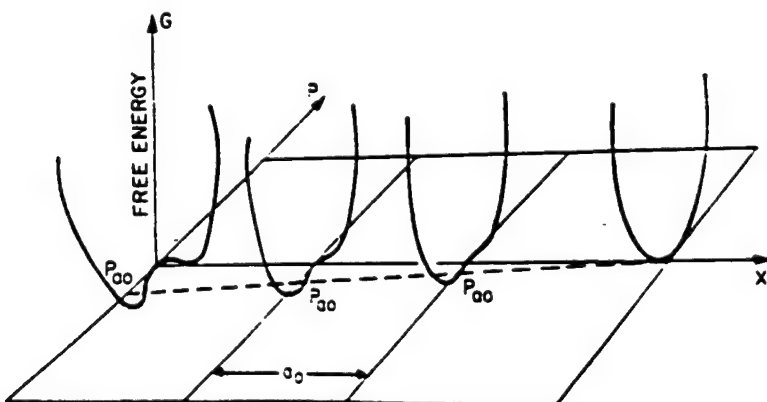

FIG. 6. The local Gibbs free energy in subsystem A as a function of the distance away from the interface at 40 K. The scale of a_0 is in range of 1 nm.

Landau theory will describe the principal physical features of polarization processes in this study.

IV. DIFFUSE PHASE TRANSITION

Next we explore the connection between the nature of diffuse phase transformation and the compositional inhomogeneity. One of the important properties for ferroelectric relaxors is their mean static susceptibility $\chi(T)$ near the Curie range. The static susceptibility of ferroelectrics is defined as

$$\chi_i = \frac{\partial P_i}{\partial E}\bigg|_{E=0} = \left[\frac{\partial^2 \Phi}{\partial P_i^2}\right]^{-1} \quad (i = a, b). \tag{17}$$

Varying the total free energy of Eq. (2) with respect to P, one can obtain a variation equation,

$$\hat{\delta}\Phi = \Sigma_n \int_{-r_{1n}}^{r_{1n}} \{[AP_b + BP_b^3 + CP_b^5 + Q_2 P_b \delta(r \pm r_{1n})]\hat{\delta}P_b + \xi_2(\nabla P_b)\hat{\delta}(\nabla P_b)\}dr$$

$$+ \int_{-r_{2n}}^{r_{2n}} \{[\alpha P_a + \beta P_a^3 + \gamma P_a^5 + Q_1 \delta(r \pm r_{2n})]\hat{\delta}P_a + \xi_1(\nabla P_a)\hat{\delta}(\nabla P_a)\}dr, \tag{18}$$

where

$$r_{1n} = b_{n+1} + \Sigma 2(a_n + b_{n+1}) - b_1 + b_{n+1} \quad \text{and} \quad r_{2n} = a_{n-1} + \Sigma 2(a_n + b_{n+1}) - b_1 + a_{n+1}.$$

With the help of the integral formula

$$\int_{-r_{in}}^{r_{in}} \{\xi_i(\nabla P_i)\hat{\delta}(\nabla P_i)\}dr = \xi_i(\nabla P_i)\hat{\delta}P_i \bigg|_{-r_{in}}^{r_{in}} - \int_{-r_{in}}^{r_{in}} \{\xi_i(\nabla P_i)\hat{\delta}(\nabla P_i)\}dr, \quad (i = 1, 2) \tag{19}$$

Eq. (18) gives

$$\hat{\delta}\Phi = \Sigma_n \int_{-r_{1n}}^{r_{1n}} \{-\xi_2(\nabla^2 P_b) + AP_b + BP_b^3 + CP_b^5 + [= \xi_2(\nabla P_b) + Q_2 P_b]\delta(r \pm r_{1n})]\}\hat{\delta}P_b dr$$

$$+ \int_{-r_{2n}}^{r_{2n}} \{-\xi_1(\nabla^2 P_a) + \alpha P_a + \beta P_a^3 + \gamma P_a^5 + [= \xi_1(\nabla P_a) + Q_1 P_a]\delta(r \pm r_{2n})]\}\hat{\delta}P_a dr. \tag{20}$$

Therefore, the average local inverse susceptibilities of polar clusters and the nearby matrix phase can be expressed as

$$\langle \chi_{bn}^{-1} \rangle = \frac{1}{2b_n} \int_{-r_{1n}}^{r_{1n}} \{A + 3BP_b^2 + 5CP_b^4 + Q_2 \delta(r \pm r_{1n})\}dr, \tag{21a}$$

$$\langle \chi_{an}^{-1} \rangle = \frac{1}{2a_n} \int_{-r_{2n}}^{r_{2n}} \{\alpha + 3\beta P_a^2 + 5\gamma P_a^4 + Q_1 \delta(r \pm r_{2n})\}dr, \tag{21b}$$

respectively. The identical equation

$$\int dr\{\partial^2(\nabla P_i)^2/\partial P_i^2\} \equiv 0, \tag{22}$$

is used for derivation of Eqs. (21). As a straightforward consequence of Eqs. (21), the *average* susceptibility of matrix and local susceptibilities of clusters can be written as

$$\langle \chi_{\bar{a}_n} \rangle \sim \frac{1}{\alpha_0(T - T_{1c})} \quad T > T_{1c}, \tag{23a}$$

$$\langle \chi_{\bar{a}_n} \rangle \sim \frac{1}{-2\alpha_0(T - T_{1c})} \quad T < T_{1c}, \tag{23b}$$

$$\langle \chi_{bn} \rangle = \frac{1}{A_0(T - T_{2c}^n)} \quad T > T_{2c}^n, \tag{23c}$$

$$\langle \chi_{bn} \rangle = \frac{1}{-2A_0(T - T_{2c}^n)} \quad T < T_{2c}^n, \tag{23d}$$

with

$$T_{1n} = T_1 + (\xi_1\sqrt{|A|}/\sqrt{\xi_2}\alpha_0\bar{a}_n),$$

$$T_{2c}^n = T_2 - (\xi_2\sqrt{|\alpha|}/\sqrt{\xi_1}A_0 b_n). \tag{23e}$$

Here $\bar{a}_n$ is the average minimum distance between clusters. Note that when the physical sizes a_n and b_n of cluster domains and matrix phase become very large, Eqs. (23) degenerate into expressions of susceptibility for normal ferroelectrics.[37,38]

Generally the dielectric properties of dielectric composites could be estimated by an empirical relationship[39]

$$\epsilon_{tot}^k = x\epsilon_1^k + (1-x)\epsilon_2^k, \tag{24}$$

where ϵ_{tot} is the dielectric constant of an entire multiphase system. Essentially Eq. (24) is too crude to assess the dielectric response in ferroelectric relaxors because it neglects the fact that the impedance of polar clusters is relatively larger than that of the matrix and overlooks the microstructure details. In order to obtain a realistic dielectric response of ferro-

electric relaxors, according to a simple Maxwell-Wagner calculation from Eq. (A2) (see the Appendix) for multiphase dielectric systems, the effective mean static dielectric susceptibility of the entire system can be written as

$$\langle \chi \rangle \cong \sum_n \left[\frac{a_n \sigma_a}{b_n \sigma_b} \right]^2 f_{1n} \langle \chi_{an} \rangle - \sum_n \frac{b_n f_{2n}}{a_n} \langle \chi_{bn} \rangle, \quad (25a)$$

with

$$f_{1n} = \frac{a_n}{\sum_n 2(a_n + b_n)}, \quad \text{and} \quad f_{2n} = \frac{b_n}{\sum_n 2(a_n + b_n)}. \quad (25b)$$

Here f_{1n} is the volume fraction of the local matrix phase with a minimum distance a_n between two clusters, while f_{2n} is the volume fraction of cluster domains with a specific size b_n. For simplicity, by assuming $a_n \cong a_{n+1}$, a conservative estimation of Eqs. (25) can be approximately obtained from Eq. (A3) as

$$\langle \chi \rangle \sim f_1 h \langle \chi_{\bar{a}_n} \rangle + \sum_n k f_{2n} \langle \chi_{bn} \rangle, \quad (26)$$

with

$$f_1 = \frac{2 n \bar{a}_n}{\sum_n 2(\bar{a}_n - b_n)}, \quad k = (\bar{a}_n - b_n)/b_n, \quad \text{and} \quad h = \left(\frac{b_n \sigma_a}{\bar{a}_n \sigma_b} \right)^2.$$

Here f_1 is the total volume fraction of the matrix. h is a constant about 0.01–0.1, and k is a constant of 3–10, depending upon the ratio of $\bar{a}_n/b_n$ and σ_a/σ_b. The actual information about f_{1n}, f_{2n}, $\bar{a}_n$, and b_n can be estimated directly from the microstructure characterization done by transmission-electron microscope (TEM).[27–29,40–50]

Now we consider a PMN crystal consisting of a mass of clusters within a matrix. Based on Eq. (26), the overall dielectric response of a PMN system is calculated and is illustrated in Fig. 7. The calculated ϵ data yielded an excellent fit to the experimental data,[13,51] showing a typical smeared dielectric response over a broad temperature range. The thermodynamic parameters used for our calculation are listed in Tables I and II. A salient feature demonstrated in Fig. 7 is that the overall dielectric behavior of the PMN is controlled by its heterogeneity. A set of localized phase transitions, arising from an intrinsic size effect, superpose together and coherently form a giant dielectric response over a very broad temperature range. The overall dielectric coefficient in this case is exceedingly larger than that suggested by the LST relation. The distribution of physical sizes of heterogeneity used in our calculation was roughly estimated from the microstructure information offered by the TEM characterization, and it is plotted in Fig. 8. The basic physical picture
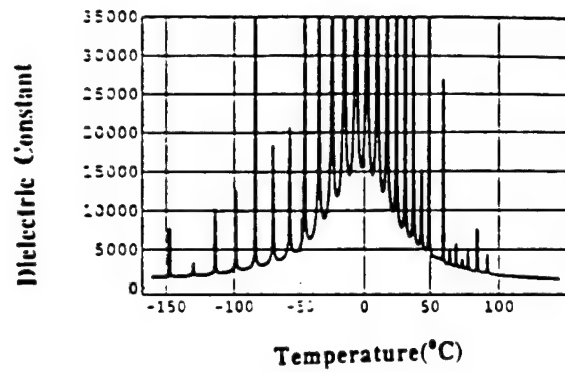

FIG. 7. The calculated temperature dependence of the mean susceptibility in a Pb(Mg.Nb) crystal.

presented in this section is straightforward: the polar phase transition tends to be confined in many localized cluster regions, ranging from a few nanometers up to more than ten nanometers, and the localized Curie points are virtually related to their physical sizes as well as the associated coherent coupling at interfaces, leading to the localized polarization fluctuation spreading over a broad temperature range. As a result, the overall phase transition will be no longer a single Curie temperature point but a continuum temperature range when the physical sizes of the polar phases form a continuum distribution.

On the other hand, the correlation lengths of localized order parameters are limited by the physical sizes of heterogeneities. The local soft modes will not propagate beyond the physical scale of the clusters. There exist a distribution of the localized correlation volumes covering a broad temperature range. It can be seen that the sum of the localized correlation volume (or length) is a function of temperature, as shown in Fig. 9, which determines the difussness of the Curie range in the dielectric response. In fact, a giant dielectric (pyroelectric) response is created by a set of localized dielectric singularities in a broad range of temperature.

Figure 10 shows the mean polarization of ferroelectric nanocomposite, significantly deviating from the normal ferroelectric behavior. It is found that the calculated polarization is gradually weakening and depressing, exhibiting a typical characteristic of diffuse phase-transition behavior. Quite obviously, the local polarization exists well above the temperature, at which the dielectric constant exhibits its maximum. This helps explain the experimental results that the polar regions exist well above the transition temperature, together with the absence of any evidence from x rays or neutron diffraction for a sudden structural change in going to the low-temperature phase.

TABLE I. Parameters of the free-energy expression for the polar clusters $Pb(Mg_{0.3}Nb_{0.6})O_3$ in PMN. Since currently there are no free-energy parameters for $Pb(MgNb)O_3$ available, the free-energy parameters of $Pb(Zr,Ti)O_3$ are adopted for our calculation [60] (cgs unit unless specified).

T_0	A	B	C	ξ_0 (cm)
250 °C[a]	3×10^{-5} (Ref. 52)	0.738×10^{-12} (Ref. 52)	2.3×10^{-23} (Ref. 52)	5×10^{-16} (Ref. 53)

[a]T_0 here is set without reference.

TABLE II. Parameters of the free-energy expression for the matrix phase in the PMN. Since currently there are no free-energy parameters for the matrix phase of $Pb(Mg, Nb)O_3$ available, the free-energy parameters of $SrTiO_3$ are adopted for our calculation.

T_{c0}	α_0	β	γ	ξ_1 (cm)^2
35 K (Ref. 54)	1.57×10^{-4} (Ref. 55)	$4.73(T+15.6)\times 10^{-12}$ (Ref. 54)	2.96×10^{-21} (Ref. 54)	5×10^{-16} (Ref. 53)

Equation (23e) is exactly identical with Eqs. (16). Apparently T_{1c} and T_{2c} are not only related to the physical sizes a_n and b_n of heterogeneities, but also they are associated with the elastic coefficients, and therefore their values are dependent upon a driving frequency. Qualitatively it can be seen in Eq. (23e) that T_{2c} will become larger when $|\alpha|$ gets smaller in the case of a higher driving frequency. In other words, the whole Curie range will consequently shift towards a higher temperature range under a higher driving frequency. Therefore it may be reasonably believed that significant dispersion of dielectric response near the Curie range is originated from the microstructure effect. More detailed discussions about the dynamic behavior and other aspects of ferroelectric relaxors will be discussed in several other separate papers.

In closing, we would like to make a final remark about this approach. Basically, relaxor ferroelectrics exhibit an unusual variety and richness of phase-transition features. The present approach is a quite general one, which might not explain all experimental results for all kinds of material systems in details. Nevertheless, generally, our main calculated results are consistent with the principal experimental results for some typical relaxor systems, such as PLZT(8/65/35) or $Pb(Mg_{1/3}Nb_{2/3})O_3$.

V. SUMMARY

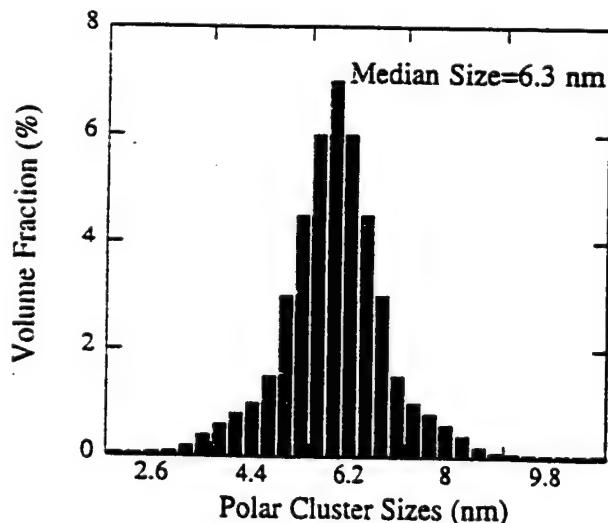Beginning from a basic formulation of the Ginzburg-Landau free-energy equation with physically allowed order parameters in an inhomogeneous medium, we have presented a straightforward thermodynamic approach to diffuse phase transitions in ferroelectrics with mesoscopic inhomogeneities. In our view, this approach provides important insights into the basic physics of the DPT in ferroelectric relaxors, and it contributes to the understanding of the structural instabilities in inhomogeneous ferroic materials. Despite a number of simplifications, the presented analysis can still explain the principal characteristics of phase transformation in ferroelectrics relaxors. Moreover, the model can account well for a number of the electrical, thermal, and microstructural observations in relaxor ferroelectrics. Next we summarize our main results.

(i) A determined effort has been made to study the dielectric behavior of a system with mesoscopic heterogeneity. The evolution of the polarization process of the coherent polar phase within a paraelectric medium has been discussed based on coherent lattice coupling and its heterogeneity. The process includes coherent precipitation and nanopolar cluster coarsening in an inhomogeneous medium. According to our model, the coherent lattice coupling between different phases imposes a critical constraint on the characteristics of local soft-mode phonons and the behavior of the phase transition in inhomogeneous media with nanopolar clusters. The local paraelectric-ferroelectric transition can be thought of as a perturbing influence of localized chemistry on localized soft-mode phonons. The unique feature in this approach is that coherent coupling is maintained across interfaces between two chemically different ordering regions.

(ii) On the basis of the spatial heterogeneity, we have

FIG. 8. The volume fraction distribution of polar clusters with different physical sizes.
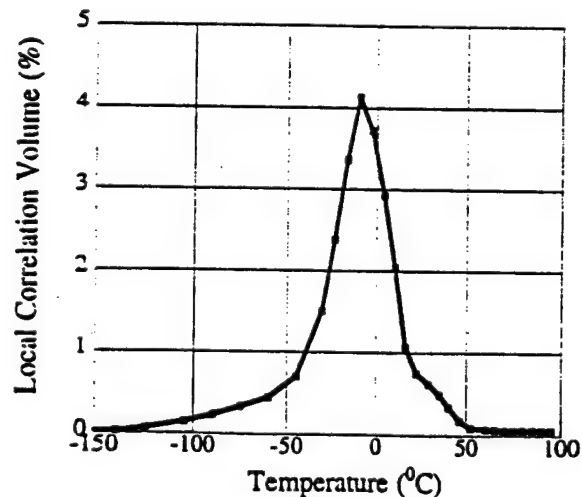

FIG. 9. The sum of the local correlation volume as a function of temperature.
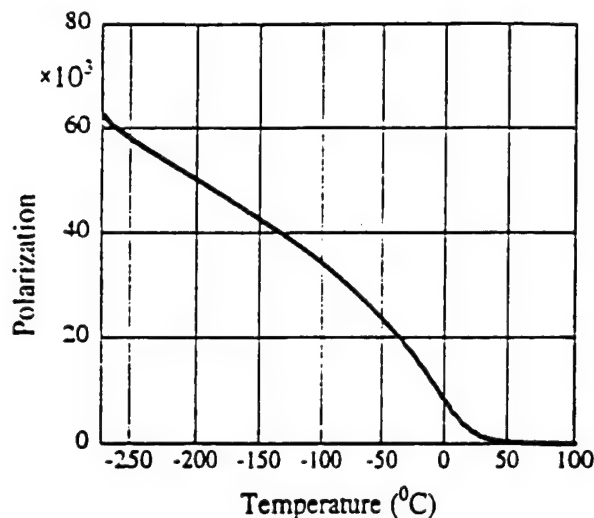
FIG. 10. The calculated temperature dependence of the mean polarization of a PMN crystal.

FIG. 11. Equivalent circuit diagram of a cluster with its surrounding matrix phase.

derived both the overall dielectric response and the local polarization distributions. We consider that each localized cluster has a mean-field character and it can be described by the Ginzburg-Landau formalism at its own "fixed point." We connect all these localized clusters, which have size-dependent phase-transition points, to their matrix phase to describe the overall dielectric response of the entire system over a wide temperature region. Based on this approach, the diffuse phase transition in the relaxors could be understood as an inhomogeneous condensation of localized soft modes.

The analysis presented here, we believe, is the first to demonstrate how the gradual crossover characteristics of the relaxors evolve, which is inherently consistent with most of the experimental observations, and explains well the general principle of diffuse phase transition in relaxor ferroelectrics, thereby deepening our understanding of the spectacular properties of these industrially important materials.

ACKNOWLEDGMENTS

APPENDIX

The localized dielectric susceptibility of a cluster with a surrounding matrix layer can be estimated by a Maxwell-Wagner formalism.[56,57] Here we take a PMN crystal as a typical example of ferroelectric relaxors with a 0-3 microstructural connection. In the cluster phase of the PMN, the Mg^{2+} and Nb^{5+} ion order is in fact in a 1:1 ratio on the B-site sublattice of the PMN. Since the Mg/Nb ratio is 1:1 within the ordered domains (as opposed to 1:2 for the average composition) the clusters have a net negative charge with respect to the matrix phase in order to preserve stoichiom-
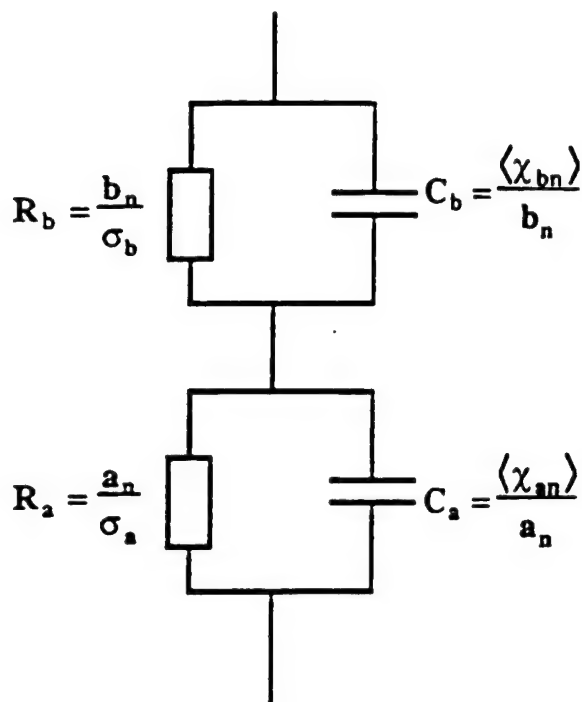
etry. It follows that the matrix must be a Mg-rich region and positively charged.

Clusters and the matrix phase can be considered as acceptor and donor-type semiconductors, respectively. The resultant pure Schottky barriers at interface boundaries between the matrix and clusters can reduce the effective conductivity of clusters drastically, quite analogous to the situation of a doped $BaTiO_3$ ceramic.[58-60] It should be noticed that this interface effect does not essentially affect the conductivity of the matrix because its geometry connection is three-dimensional in character.

A cluster with its surrounding matrix phase can be described by an equivalent circuit as shown in Fig. 11.[61,62] According to the equivalent circuit diagram, the local static susceptibility can be written as[23,64]

$$\chi_{1n} = \frac{(b_n \langle \chi_{bn} \rangle \sigma_a^2 + a_n \langle \chi_{an} \rangle \sigma_b^2)(b_n + a_n)}{(b_n \sigma_a - a_n \sigma_b)^2}. \quad (A1)$$

Here χ_{1n} is the localized susceptibility and $\bar{a}_n$ is the average minimum size between two clusters. By considering that the effective conductivity of the cluster phase is much smaller than that of the matrix phase, $\sigma_b \ll \sigma_a$ near the cluster phase transition, the static localized susceptibility in whole temperature range can be written as

$$\langle \chi_{1n} \rangle \approx \frac{(a_n + b_n)}{b_n} \langle \chi_{bn} \rangle + \left(\frac{b_n \sigma_a}{a_n \sigma_b} \right)^2 \langle \chi_{an} \rangle. \quad (A2)$$

Equation (A2) shows an interesting reverse effect of the barrier layer capacitors, similar to that of the well-known conventional interfacial capacitors,[65,66] leading to significant enhancement of local effective dielectric properties. A quite

conservative estimation of Eq. (A2) can be obtained by assuming $\bar{a}_n \approx b_n$ and $10\sigma_a = \sigma_b$, i.e.,

$$\langle \chi_{1n} \rangle \approx 2\langle \chi_{bn} \rangle + 0.04\langle \chi_{an} \rangle. \qquad (A3)$$

At the optical frequency, the localized susceptibility in the whole temperature range can be written as

$$\langle \chi_{1n} \rangle = \frac{(a_n + b_n)\langle \chi_{an} \rangle}{(a_n + b_n\langle \chi_{an} \rangle / \langle \chi_{bn} \rangle)} + \frac{(a_n + b_n)\langle \chi_{bn} \rangle}{(b_n + a_n\langle \chi_{bn} \rangle / \langle \chi_{an} \rangle)}. \qquad (A4)$$

Equation (A4) implies that the dielectric constant of ferroelectric relaxors will be reduced at least as much as 50% when the driving frequency increases to an optical frequency level.

[1] L. E. Cross, in *Ferroelectric Ceramics*, edited by N. Setter and E. L. Colla (Birkhaus, Basel, 1993), p. 15.

[2] J. Herber, *Ceramic Dielectrics and Capacitors* (Gordon and Breach, London, 1985), Vol. 6; Y. Park, and Y. Kim, J. Mater. Res. 10, 2779 (1995).

[3] L. P. Goulpeau, Ferroelectrics 9, 11 (1975); D. Hennings and A. Schneil, J. Am. Ceram. Soc. 67, 249 (1984).

[4] C. A. Randall and A. S. Bhalla, Jpn. J. Appl. Phys. 29, 327 (1990).

[5] G. A. Smolenskii, J. Phys. Soc. Jpn. Suppl. 28, 26 (1970); Sov. Phys. Solid State 23, 783 (1981); Ferroelectrics 53, 129 (1984).

[6] B. Vugmeister and M. Glinchuk, Rev. Mod. Phys. 82, 993 (1990); U. Hochli, K. Knorr, and A. Loidl, Adv. Phys. 39, 405 (1990).

[7] A. P. Levanyuk and A. S. Sigov, *Defects and Structural Phase Transitions* (Gordon and Breach, London, 1989).

[8] J. V. Mantese et al., Appl. Phys. Lett. 67, 721 (1995).

[9] N. W. Schubring et al., Phys. Rev. Lett. 68, 1778 (1992).

[10] S. Chattopadhyay, P. Ayyub, V. R. Palkar, and M. Multani, Phys. Rev. B. 52, 13 177 (1995); P. Marguardt and H. Gleiter, Phys. Rev. Lett. 48, 1423 (1982).

[11] C. R. Cho et al., Ferroelectrics 152, 37 (1994); and T. Nagatomo et al., ibid. 152, 133 (1994).

[12] A. Shaikh, R. Vest, and G. Vest, IEEE Trans. Ultrason. Ferroelectr. Freq. Control 36, 407 (1989); K. Kinoshita and A. Yamaji, J. Appl. Phys. 47, 371 (1976); G. Arlt, D. Hennings, and G. de With, ibid. 58, 1619 (1985).

[13] G. A. Smolenskii, V. A. Isupov, A. Agranovskaya, and S. N. Popov, Fiz. Tverd. Tela. 2, 2906 (1960); G. A. Smolenskii and V. A. Isupov, Sov. J. Techn. Phys. 24, 1375 (1954); G. A. Smolenskii and A. Agranovskaya, Sov. Phys. Solid State 1, 1429 (1960).

[14] S. M. Pilgrim, A. E. Sutherland, and S. R. Winzer, J. Am. Ceram. Soc. 73, 3122 (1990); K. Uchino and S. Nmura, Ferroelectr. Lett. 44, 55 (1982); J. C. Burfoot and G. W. Taylor, *Polar Dielectrics and Their Applications* (MacMillan, London, 1979), p. 128.

[15] L. Sheppard, Am. Ceram. Bull. 72(3), 45 (1993).

[16] G. A. Smolenskii et al., Ferroelectrics 54, 119 (1984).

[17] V. A. Isupov, Sov. Phys. Tech. Phys. 1, 1846 (1956); Sov. Solid State Phys. 5, 136 (1963); Ferroelectrics 90, 113 (1989); 143, 109 (1993).

[18] V. V. Kirillov and V. A. Isupov, Ferroelectrics 5, 3 (1971); V. A. Isupov and P. Pronin, Jpn. J. Phys. Soc. Suppl. B 49, 53 (1980).

[19] L. E. Cross, Ferroelectrics 76, 241 (1987).

[20] R. W. Wang and D. L. Mills, Phys. Rev. B 46, 11 681 (1992).

[21] D. R. Tilley and B. Zeks, Solid State Commun. 49, 823 (1984); *Ferroelectric Ceramics*, edited by N. Setter and E. L. Colla (Birkhaus, Basel, 1993), p. 163.

[22] D. R. Tilly, Solid State Commun. 65, 657 (1988).

[23] D. Schwenk, F. Fishman, and F. Schwabl, Ferroelectrics 104, 349 (1990); J. Phys. C 2, 5409 (1990); Phys. Rev. B 38, 11 618 (1988).

[24] B. E. Vugmeister and M. D. Glinchuk, Sov. Phys. Usp. 28, 589 (1985); Sov. Phys. Solid State 31, 1871 (1989).

[25] T. C. Lubensky and M. H. Rubin, Phys. Rev. B 3, 3885 (1975).

[26] F. Falk, Z. Phys. B 51, 177 (1983).

[27] J. Chen, H. M. Chan, and M. P. Harmer, J. Am. Ceram. Soc. 72, 593 (1989).

[28] C. A. Randall, D. J. Barber, and R. W. Whatmore, J. Microsc. 145, 275 (1987); J. Mater. Sci. 21, 4456 (1986); Ferroelectrics 76, 311 (1987).

[29] K. Z. BaBa-Kishi, I. M. Reaney, and D. J. Barber, J. Mater. Sci. 26, 1654 (1990).

[30] J. W. Cahn and F. Larche, Acta Metal. 32, 1915 (1984).

[31] M. F. Ashby and L. Johnson, Philos. Mag. 30, 1009 (1969).

[32] V. L. Ginzburg, Sov. Phys. Solid State 2, 1824 (1961); Ferroelectrics 11, 451 (1976).

[33] V. L. Ginzburg, A. P. Levanynk, and A. Sobyanin, Ferroelectrics 73, 171; 76, 3 (1987).

[34] L. Kadanoff et al., Rev. Mod. Phys. 39, 395 (1967).

[35] A. P. Levanyuk, Izv. Akad. Nauk SSSR, Ser. Fiz. 28, 879 (1965); A. P. Levanyuk and A. Sobyanin, JETP Lett. 11, 371 (1970).

[36] J. Villain, Solid State Commun. 8, 295 (1970); R. A. Cowely, Phys. Rev. B 13, 4877 (1976).

[37] T. Mitui, I. Tatsuzaki, and E. Nakamira, *An Introduction to Physics of Ferroelectrics* (Gordon and Breach, New York, 1974), p. 151.

[38] A. F. Devonshire, Philos. Mag. 40, 1040 (1949).

[39] S. P. Mitoff, Adv. Mater. Res. 3, 305 (1968).

[40] K. Z. BaBa-Kishi and D. J. Barber, Ferroelectrics 93, 321 (1989); J. Appl. Crystallogr. 23, 43 (1990); K. Z. BaBa-Kishi, G. K. Z. Cressey, and R. J. Cernik, ibid. 25, 477 (1992).

[41] Song Xiang-Yun et al., Science (in Chinese) 33, 238 (1990).

[42] C. Caranoni et al., Phys. Status Solidi A 130, 25 (1992).

[43] L. G. Siny and T. A. Smirnova, Ferroelectrics 90, 191 (1989).

[44] U. Bismaryer, V. Devarajan, and P. Groves, J. Phys. Condens. Matter 1, 6977 (1989).

[45] P. Lampin, N. Menguy, and C. Caranoni, Philos. Mag. Lett. 72, 215 (1995).

[46] M. P. Harmer et al., Mater. Lett. 2, 278 (1984); Ferroelectrics 97, 263 (1989).

[47] A. A. Bokov and V. Y. Shonov, Ferroelectrics 108, 237 (1990).

[48] C. C. F. Stenger and A. J. Burggraaf, Phys. Status Solidi 61, 653 (1980).

[49] A. D. Hilton, D. J. Barber, C. A. Randall, and T. R. Shrout, J. Mater. Sci. 25, 3461 (1990).

[50] H. M. Chen et al., Jpn. J. Appl. Phys. 24, 550 (1985).

[51] V. A. Bokov and I. E. Myl'nikova, Sov. Phys. Solid. State 1, 1429 (1960).

[52] M. J. Haun *et al.*, Ferroelectrics 99, 45 (1989).

[53] V. A. Zhirnov, Sov. Phys. JETP 35, 822 (1959).

[54] K. A. Muller and H. Burkard, Phys. Rev. B 19, 3593 (1979).

[55] W. N. Lawless and A. J. Morrow, Ferroelectrics 15, 159 (1977).

[56] J. Volger, Prog. Semiconduct. 4, 207 (1960).

[57] G. Goodman, *Ceramic Materials For Electronics*, edited by R. C. Buchanan (Dekker, New York, 1986), p. 115.

[58] W. Heywang, J. Mater. Sci. 6, 1214 (1971).

[59] J. Daniels, Philips Res. Rep. 31, 516 (1976).

[60] H. Ihring and W. Puschert, J. Appl. Phys. 48, 3081 (1977).

[61] W. Heywang, J. Amer. Ceram. Soc. 47, 484 (1964).

[62] I. Burn and S. Neirman, J. Mater. Sci. 17, 3510 (1982).

[63] J. C. Anderson, *Dielectrics* (Spottiswoode and Ballantyne, London, 1964), p. 93.

[64] R. Coelho, *Physics of Dielectrics for the Engineer* (Elsevier, Amsterdam, 1977), p. 89.

[65] P. F. Bongers and P. E. C. Franken, in *Grain Boundary Phenomena in Electronic Ceramics*, edited by C. M. Levinson (American Ceramic Society, Columbus, OH, 1981), p. 38.

[66] R. Wernicke, *Grain Boundary Phenomena in Electronic Ceramics* (Ref. 65), p. 261.

APPENDIX 86

Dielectric response in ferroelectric superlattices

By SHAOPING LI. J. A. EASTMAN, J M. VETRONE

Materials Science Division. Argonne National Laboratory, 9700 South Cass Ave, Argonne. Illinois 60439

R. E. NEWNHAM and L. E. CROSS

Materials Research Laboratory, Pennsylvania State University, University Park, Pennsylvania 16802, USA

ABSTRACT

The dielectric response of a ferroelectric multilayer, having a designed heterogeneity, has been studied near its phase transition range by use of the Landau–Ginzburg theory. The coherent lattice coupling between ultrathin layers can be significantly strong, resulting in a broad phase transition of the superlattice system as a whole. The thickness of layers and their spatial distribution hold the keys for enhancing dielectric properties in a broad temperature range.

§ 1. INTRODUCTION

There is a fundamental interest in the study of ferroelectric superlattices because their mesoscope structures drastically differ from bulk homogeneous materials. Normally the dielectric constants in ferroelectrics can be estimated by the Lyddane–Sachs–Teller (LST) relation. and the phase transition behaviour of ferro-electrics can be quite accurately described by mean-field theories. such as the Landau theory (Cross 1993). However, experimentally it has long been found that in reality ferroelectrics with inhomogeneities exhibit a very broad dielectric peak near their Curie temperature, whose dielectric coefficients often are larger than those suggested by the LST relation (Burns and Burnstein 1973, Cross 1993). The phase transitions in these materials are called diffuse phase transitions (DPTs) because they are char-acterized by broad anomalies in the dielectric response near the transition tempera-ture region. exhibiting unusually large values of dielectric coefficients in a wide temperature range.

It has been expected that dielectric characteristics of ferroelectrics could be manipulated by controlling the material's heterogeneity at a mesoscopic level (5–80 nm) (Cross 1993), leading to artificially engineering ferroelectric phase transi-tions and ferroelectric dielectrics with exceedingly larger dielectric coefficients. Basically the dielectric response in ferroelectrics can be virtually altered by intro-ducing local modifications of lattice structures because dielectric characteristics in ferroelectrics are mainly determined by the collective movement of transverse optic phonons or soft modes, which reflects the relative vibrations of cations and anions in ferroelectrics. Nevertheless, despite numerous experiments over several decades,

it is still not clear what is the exact link between the localized soft modes and the anomalous dielectric behaviour manifested by ferroelectrics with heterogeneities. Recently experimental efforts synthesizing ferroelectric superlattices have been initiated by several groups (Wiener-Avnear 1994, Hayashi and Tanaka 1995, Kanno *et al.* 1996, Christem *et al.* 1996) in order to produce ferroelectrics with novel dielectric properties through control of heterogeneities.

However, all these efforts overlooked a critical aspect: the heterogeneity in ferroelectrics with a DPT is inhomogeneous in nature. From the phase transition point of view, the inhomogeneous heterogeneity is most likely a key to causing the dielectric anomalies in ferroelectrics. As is well known, in normal systems, the spatial correlation length of order parameters (such as polarization) diverges at the Curie point, resulting in one and only one dielectric singularity in materials while, in inhomogeneous systems, the situation is quite different. The phase transitions in this case tend to be confined in localized regions, ranging from a few nanometres up to a submicron level in scale. Additionally, the correlation lengths of local order parameters are limited by the physical sizes of heterogeneities. The soft modes will not propagate beyond the physical scale of the heterogeneity. In this case the localized transition points should be intimately influenced by the physical sizes of the heterogeneity, and the size effect of the heterogeneity should, in principle, also have a critical influence on the overall dielectric response of ferroelectrics.

In this work, for the first time, we present a quantitative connection between the heterogeneity and dielectric response in inhomogeneous ferroelectric systems and report a theoretical estimation of dielectric response in a ferroelectric multilayer system with designed heterogeneity, based on an extended Ginzburg–Landau model. Our numerical results predicate that a giant dielectric susceptibility might be obtained in ferroelectric superlattices or ultrathin multilayer systems with the desirable heterogeneities.

§ 2. Model

The Landau theory has long been successfully used to explain the phase transition behaviour of ferroelectrics, and it has proved to be a good description of the phase transition behaviour in ferroelectrics because the smoothly varying Coulomb force is mainly responsible for establishing the polar phase. Recently it has been extended to study the surface and size effect on nanostructured ferroelectrics (Tilley 1993). Following the expressions for the free energy in the literature, we now consider the O_h–C_{4v} proper ferroelectric phase transitions in a multilayer system with 60 alternating layers of $SrTiO_3$ (STO) and $Pb(Ti_{0.5}Zr_{0.5})O_3$ (PZT), in which each layer has Ising character. For simplicity, let us assume that the order parameters of local polarizations are always oriented along the z axis, that is $P = \{0, 0, P(z)\}$, and the superlattice dimensions along the x axis and y axis are infinite. The free energy of the superlattice system with alternating slabs of thicknesses a_n and b_n can be written as (Tilley and Zeks 1984, Schwenk *et al.* 1990, Wang and Mills 1992)

$$\Phi = \frac{F}{S} = \int_{-L/2}^{L/2} \left\{ \Phi_{a0} + \Phi_{b0} + \frac{\xi_1}{2}(\nabla P_a)^2 + \frac{\xi_2}{2}(\nabla P_b)^2 + \frac{1}{2}\alpha P_a^2 + \frac{1}{4}\beta P_a^4 + \frac{1}{6}\gamma P_a^6 \right.$$

$$+ \frac{1}{2}Q_1 P_a^2 \delta \left[z \pm a_{n+1} + \left(\sum_n 2(a_n + b_{n+1}) - b_1 + a_{n+1} \right) \right] + \frac{1}{2}A P_b^2 + \frac{1}{4}B P_b^4$$

$$\left. + \frac{1}{6}C P_b^6 + \frac{1}{2}Q_2 P_b^2 \delta \left[z \pm b_{n+1} + \left(\sum_n 2(a_n + b_{n+1}) - b_1 + b_{n+1} \right) \right] \right\} dz, \qquad (1)$$

where S is the surface area of the superlattice with plane surfaces at $z = \pm L/2$. Φ_{a0} and Φ_{b0} denote the thermodynamic potentials of STO and PZT layers in their para-electric phase states. $\alpha, \beta, \gamma, A, B$ and C are normalized free-energy coefficients, in which elastic coefficients and other relevant coupling parameters are tacitly included, and especially $\alpha = \alpha_0(T - T_1)$ and $A = A_0(T - T_2)$. T_1 and T_2 are phase transition temperatures in the bulk materials of layers STO and PZT respectively. ξ_1 and ξ_2 are the gradient terms of order parameters, describing the polarization inhomogeneity. Q_1 and Q_2 are defined as the coherent coupling coefficients, which are not indepen-dent parameters and characterize the coherent coupling at the interfaces between different regions. Physically the coupling terms can be related to the stored elastic and electrostatic energy caused by coherency coupling. $\delta(z)$ is a delta function which describes the coordinates of the interface between two layers.

The integral in eqn. (1) is over all space since the order parameters vary spatially, which is illustrated in fig. 1. The spatial distribution of the polarization can be obtained by solving the Euler–Lagrange equations
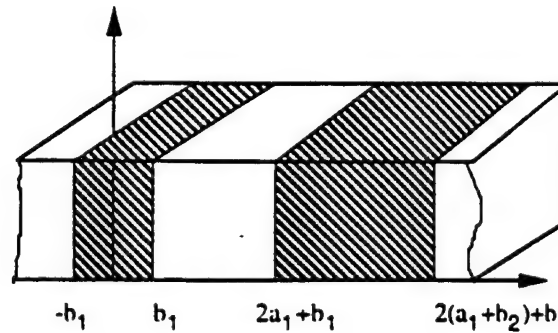
$$\xi_1 \frac{d^2 P_a}{dr^2} - (\alpha P_a + \beta P_a^3 + \gamma P_a^5) = 0, \qquad (2a)$$

$$\xi_2 \frac{d^2 P_b}{dr^2} - (A P_b + B P_b^3 + C P_b^5) = 0. \qquad (2b)$$

with the following coherent boundary conditions at the interfaces:

$$P_a(z) = P_b(z)|_{z = \left[\sum_n 2(a_n + b_{n-1}) - b_1 \right]}, \qquad P_a(z) = P_b(z)|_{z = \left[\sum_n 2(a_n + b_n) - b_1 \right]}, \qquad (3a)$$

Fig. 1

Model superlattice structure described in the text. Here a_n and b_n are the thicknesses of STO and PZT layers. respectively.

$$\left(\frac{dP_a}{dz} + \frac{P_a}{d_1}\right)\Bigg|_{z=[\sum_n 2(a_n+b_n)-b_1]} = 0, \quad \left(\frac{dP_a}{dz} - \frac{P_a}{d_1}\right)\Bigg|_{z=[\sum_n 2(a_n+b_{n-1})-b_1]} = 0, \quad (3b)$$

$$\left(\frac{dP_b}{dz} + \frac{P_b}{d_2}\right)\Bigg|_{z=[\sum_n 2(a_n+b_{n-1})-b_1]} = 0, \quad \left(\frac{dP_b}{dz} - \frac{P_b}{d_2}\right)\Bigg|_{z=[\sum_n 2(a_n+b_n)-b_1]} = 0. \quad (3c)$$

Here $d_1 = -d_2$, and $d_1 = \xi_1/Q_1$, $d_2 = \xi_2/Q_2$, which reflect the strength of the interface effect (Tilley and Zeks 1984). The coherency is defined by the requirement that the local order parameters from one subsystem to another subsystem is continuous across all interfaces.

§ 3. LOCAL PHASE TRANSITION

The non-trivial solutions of eqns. (2) can be derived exactly although, in general, they are quite cumbersome. For brevity, focusing on only the temperature region $T_1 < T < T_2$, the approximate solutions of eqns. (2) can be written as

$$P_b = P_{b0} \cos\left\{k_2\left[r - \left(\sum_n 2(a_n + b_{n+1}) - b_1 - b_{n+1}\right)\right]\right\}, \quad (4a)$$

$$P_a = \frac{P_{b0}\cos(\kappa_2 b_{n+1})}{\cosh(k_1 a_{n+1})} \cosh\left[k_1\left(r - \sum_n (a_n + b_{n+1}) - b_1 + a_{n+1}\right)\right], \quad (4b)$$

with

$$P_{b0} = \pm\left\{-\frac{B}{2C}\left[1 + \left(1 - \frac{4A_0 C}{B^2}(T - T_{2c})\right)^{1/2}\right]\right\}^{1/2} \quad \text{(the first-order transition)}, \quad (4c)$$

$$P_{b0} = \pm\left\{-\frac{B}{2C}\left[1 - \left(1 - \frac{4A_0 C}{B^2}(T - T_{2c})\right)^{1/2}\right]\right\}^{1/2} \quad \text{(the second-order transition)}, \quad (4d)$$

$$\kappa_1 = \left(\frac{\alpha_0(T - T_1)}{\xi_1}\right)^{1/2} = \frac{1}{|d_1|\tanh(\kappa_1 a_{n+1})}, \quad (4e)$$

$$\kappa_2 = \frac{1}{|d_2|\tan(\kappa_2 b_{n+1})} \quad (4f)$$

and

$$T_{2c} = T_2 - \frac{\xi_2 \kappa_2^2}{A_0}, \quad (4g)$$

where κ_1 and κ_2 are defined as the characteristic lengths, which describe the breadth of polarization fluctuation in the two types of layer. In the case of the first-order phase transition, the size-induced phase transition can be written as

$$T_2^* = T_2 + \frac{3B^2}{16A_0C} - \frac{\xi_2\kappa_2^2}{A_0}. \tag{5}$$

Equations (4) represent the spatial variations in local order parameters of the super-lattice system. The polarization in PZT layers is plotted as functions of both temperature and their physical sizes in fig. 2. Quite apparently an important feature is that the phase transition temperature of each layer is virtually related to its physical size and the associated coherent coupling at the interfaces. As a result, the phase transition in the inhomogeneous system will no longer be a temperature point but a continuum temperature range when the physical sizes of polar phase form a continuum distribution.

The spatial profile of polarization P_a in the STO of layers is also numerically plotted as the functions of both the normalized coordinate and the temperature in fig. 3. One can find that the PZT layers with higher phase transition points can induce polarization in the peripheries of the STO layers, even though the temperature is above the original bulk Curie point of STO layers. The local polarization $P_a(r)$ occurring in STO layers is caused by the coherent coupling from PZT layers. In other words, the ferroelectric phase transition can be nucleated in the region which is intrinsically the paraelectric phase. In this case, the polarization occurring in the STO layers is extrinsic in nature.

Fig. 2
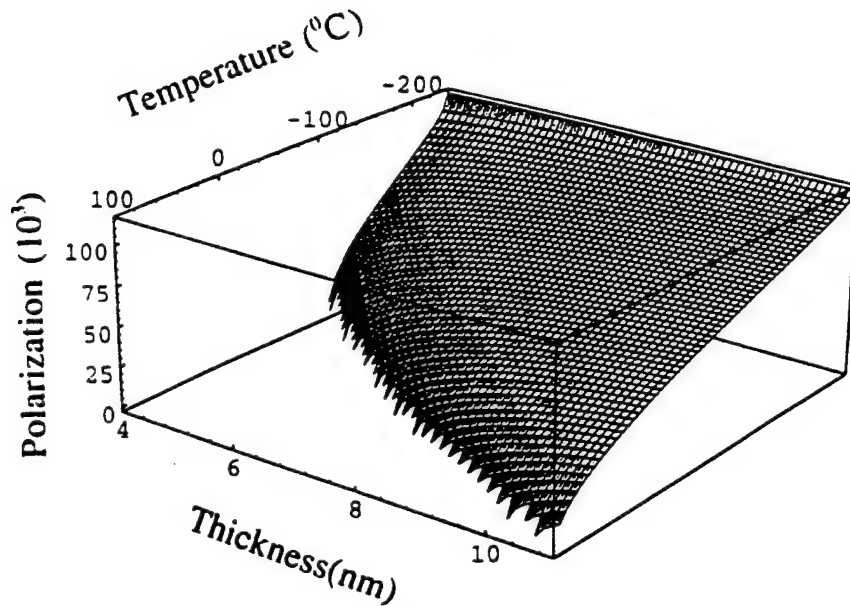
Calculated polarization in PZT layers as the functions of both temperature and their thickness. In our calculation, we take $a_n = a_{n+1} = 5\,\mathrm{nm}$ for STO layers.

Fig. 3
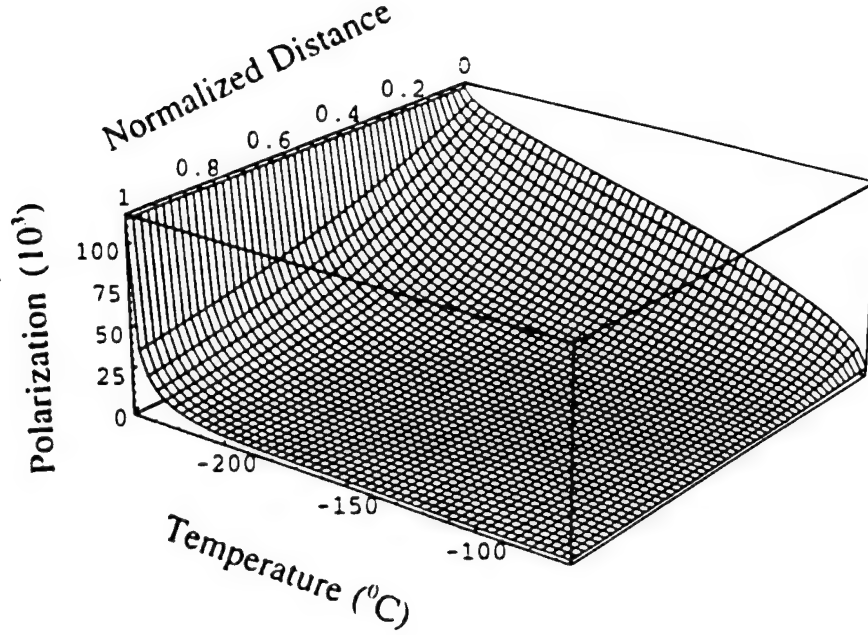
The view of the induced polarization in the STO layers as the functions of both temperature and the normalized distance away from the interfaces.

§ 4. Diffuse Phase Transition

One of the important properties of ferroelectrics is their static susceptibility $\chi(T)$ near the Curie range. Next we examine the static dielectric responses in our super-lattice system. The *average* local inverse susceptibilities of the PZT and STO layers can be expressed as

$$
\begin{aligned}
\langle \chi_{b_n}^{-1} \rangle &= \frac{1}{2b_n} \frac{\partial^2 \Phi}{\partial P_b^2} \\
&\approx \frac{1}{2b_n} \int_{-b_n}^{b_n} A + 3BP_b^3 + 5CP_b^4 + Q_2\delta \left[z = \pm b_{n+1} \right. \\
&\quad \left. + \left(\sum_n 2(a_n + b_{n-1}) - b_1 + b_{n+1} \right) \right].
\end{aligned}
\tag{6a}
$$

$$
\begin{aligned}
\langle \chi_{a_n}^{-1} \rangle &= \frac{1}{2a_n} \frac{\partial^2 \Phi}{\partial P_a^2} \\
&\approx \frac{1}{2a_n} \int_{-a_n}^{a_n} \alpha + 3\beta P_a^3 + 5\gamma P_a^4 + Q_1\delta \left[z = \pm a_{n+1} \right. \\
&\quad \left. + \left(\sum_n 2(a_n + b_{n-1}) - b_1 + a_{n+1} \right) \right]
\end{aligned}
\tag{6b}
$$

respectively. According to the Maxwell–Wagner formalism (Volger 1960, Anderson 1964) the effective static dielectric susceptibility of the entire system can be approximately expressed as

$$\langle \chi \rangle = \sum_n \left(\frac{a_n}{a_n + b_n} \right)^2 f_{1n} \langle \chi_{a_n} \rangle + \sum_n \left(\frac{b_n}{a_n + b_n} \right)^2 f_{2n} \langle \chi_{b_n} \rangle, \tag{7}$$

where

$$f_{1n} = a_n \Big/ \sum_n 2(a_n + b_n), \quad f_{2n} = b_n \Big/ \sum_n 2(a_n + b_n), \tag{8}$$

$$\langle \chi_{a_n} \rangle \approx \begin{cases} \dfrac{1}{\alpha_0(T - T_{1c}^n)}, & T > T_{1c}^n, \tag{9a} \\[4mm] \dfrac{-1}{2\alpha_0(T - T_{1c}^n)}, & T < T_{1c}^n, \tag{9b} \end{cases}$$

$$\langle \chi_{b_n} \rangle \approx \begin{cases} \dfrac{1}{A_0(T - T_{2c}^n)}, & T > T_{2c}^n, \tag{9c} \\[4mm] \dfrac{-1}{2A_0(T - T_{2c}^n)}, & T < T_{2c}^n, \tag{9d} \end{cases}$$

with

$$T_{1c}^n = T_1 + \frac{\xi_1 |A|^{1/2}}{\xi_2^{1/2} \alpha_0 a_n}, \quad T_{2c}^n = T_2 - \frac{\xi_2 |\alpha|^{1/2}}{\xi_1^{1/2} A_0 b_n}. \tag{10}$$

Here f_{1n} is the volume fraction of the nth STO layer, while f_{2n} is the volume fraction of the nth PZT layer. For a conservative estimation, we have tacitly assumed that both layers have the same conductivity. Note that, if choosing the layers with different conductivity, the effective dielectric response will increase even more drastically (Volger 1960). We shall not discuss this situation here. The thermodynamic parameters used for our calculation are listed in tables 1 and 2.

By designing a special distribution for the thickness of PZT layers, as illustrated in fig. 4, the overall temperature dependence of the average dielectric susceptibility and the spontaneous polarization are numerically presented in fig. 5 and fig. 6

Table 1. Parameters of the free energy expression for PZT (cgs units unless specified).

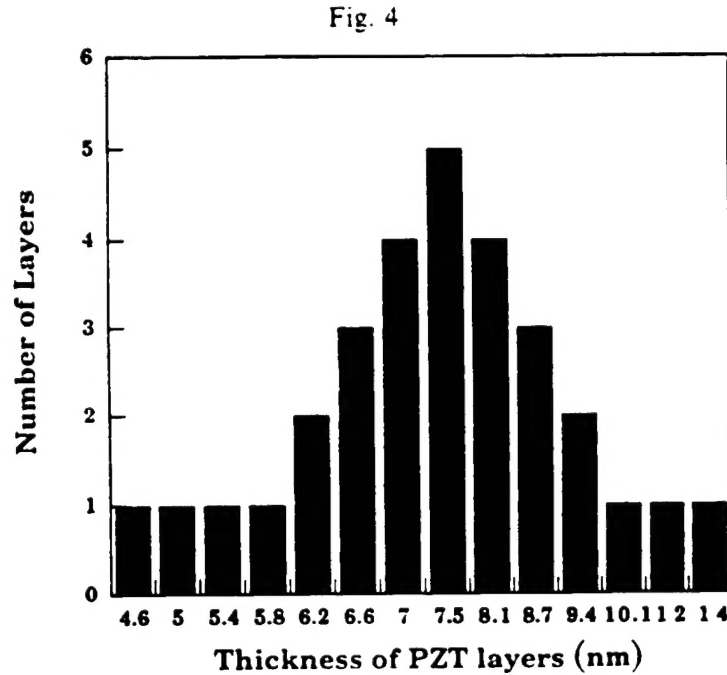| T_{c0}(°C)	A_0	B	C	ξ_i
392[a]	1.63×10^{-5b}	0.738×10^{-12a}	2.3×10^{-23a}	5×10^{-16c}

[a] The free-energy parameters from Haun *et al.* (1989).
[b] The free-energy parameters from Amin *et al.* (1985).
[c] Data from Ginzburg (1961).

Table 2. Parameters of the free-energy expression for STO.

T_{c0} (K)	A_0	B	C
35·5[a]	$1·57 \times 10^{-4}$[a]	$4·73(T - 15·6) \times 10^{-12}$[b]	$2·96 \times 10^{-21}$[b]

[a] Data from Muller and Burkard (1979).
[b] Data from Lawless and Morrow (1977).

Fig. 4

The thickness distribution of PZT layers in the STO/PZT multilayer system.

respectively. It can be found that the polarization is gradually weakening and depressing, displaying a significant deviation from the normal ferroelectric behaviour. On the other hand, since the thickness of PZT layers has a distribution, the local phase transition points in the superlattice are spread into a temperature range, and in fact these local phase transitions are superposed in some degree so as to make the entire superlattice system on the verge of structural instability under a broad temperature range. As is evident in fig. 6, the overall dielectric behaviour of the superlattice demonstrates a giant response, showing that dielectric constant in the practically useful range can be well above a value of 5000. This illustrates a salient feature of dielectric behaviour in superlattices with inhomogeneous heterogeneity; a set of localized phase transitions, arising from an intrinsic size effect, slightly superpose together and coherently form a giant dielectric response over a very broad temperature range. More precisely, there exist a distribution of localized correlation lengths covering a temperature range in the superlattice, and a set of localized dielectric singularities in a broad range of temperature which create a giant dielectric (pyroelectric) response. The overall dielectric coefficient in this case is considerably

Fig. 5
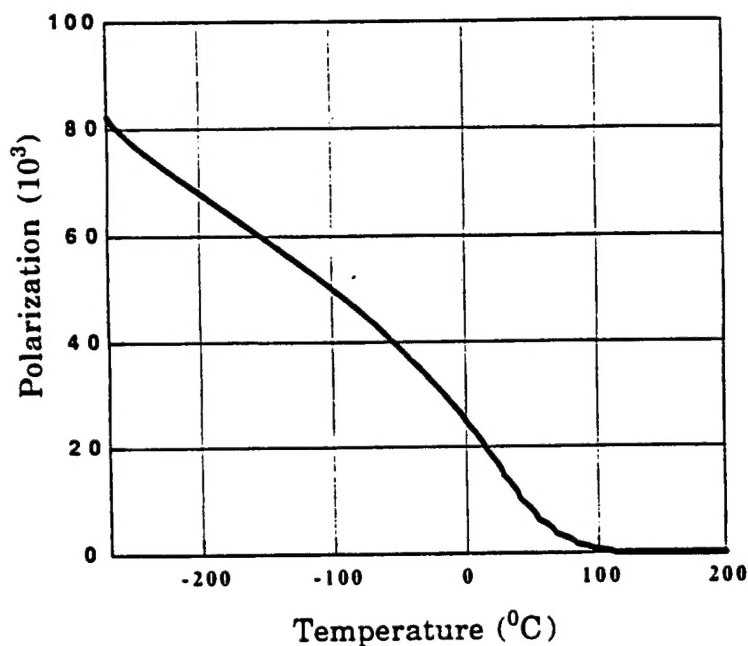
The temperature dependence of the mean polarization of the STO/PZT superlattice with a total thickness of 0·407 μm.
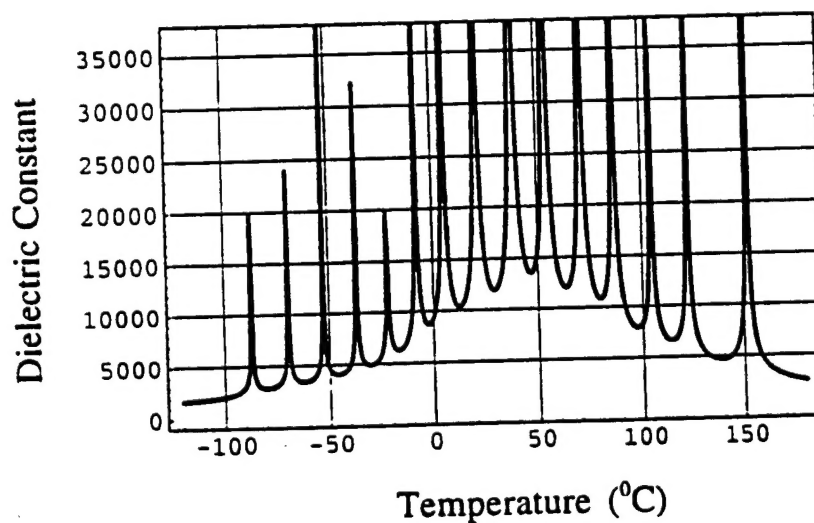
Fig. 6

The temperature dependence of the mean susceptibility of the STO/PZT superlattice.

larger than that suggested by the LST relation. It can also be clearly seen in both fig. 5 and fig. 6 that the local polarization can exist well above the temperature at which the dielectric constant exhibits its maximum, exhibiting a typical characteristic of the DPT. Note that in our calculation we do not consider the elastic stress induced by the lattice mismatch at interfaces. which could significantly affect the values of the

free-energy parameters and the overall dielectric response of superlattice systems as well. One typical example for this situation. in reality, is the interface influence on properties of the $BaTiO_3/SrTiO_3$ system. Nevertheless. we believe that the general conclusion of our results should still hold qualitatively. A potential application for this intrinsic size effect is to make supercapacitors with ultrathin (ferroelectric/conductor) or (ferroelectric–insulator ferroelectric–semiconductor) multilayer structures for energy storage and wireless applications. which might possess the highest possible electric charge density that one could ever achieve.

From the experimental point of view. it is better to synthesize $STO/PbTiO_3$ and $KTaO_3/KNbO_3$ superlattice systems because only a small lattice mismatch at interfaces will result in these systems. Another way to make thin films with giant dielectric constants is to synthesize multilayer or graded systems with a step and continuing change in Curie points within the system (Mantese *et al.* 1995). We shall discuss this case in a separate paper.

As a final remark. we would like to address the applicability of Landau theory to ultrathin films. In general. the validity of the Landau theory for ferroelectric phase transitions has been roughly justified and discussed by Ginzburg (1961, 1976, 1987a.b). The critical range for bulk ferroelectric perovskite has been proven to be very narrow. and the logarithmic corrections have proven to be difficult to detect experimentally. The physical reason for this is that the Coulomb force. which is responsible for establishing the order phase. varies smoothly. Moreover. the critical fluctuation can also be suppressed by strain fields since most ferroelectric perovskites are involved with strong couplings of elastic strains.

However. in the main approximation. the Landau theory of phase transitions is equivalent to the theory of self-consistent field (mean-molecular-field) theory, ignoring long-wave fluctuations of the order parameter. which is supposed to be quite significant in the case of thin films. In other words. in the case of ultrathin films, it should be expected that polarization fluctuations will become more significant. even though the true critical region in ferroelectric perovskites is quite narrow. Therefore, in principle. an even more significant overall dielectric enhancement might be expected for our studied heterogeneous structures. In fact the power-law singularity obtained from the Landau model can be modified by a logarithmic correction factor via a renormalization group technique. and the relevant formulae for the critical behaviour of ferroelectric thin films can be found in the literature (Kretschmer and Binder 1979). In the work presented. we perform only a quite crude estimation of dielectric behaviour for a specially designed heterogeneous structure. It is necessary to make a more rigorous evaluation of the dielectric susceptibility for ferroelectric superlattices of this type. It would be extremely helpful to evaluate directly the leading fluctuation corrections for ultrathin layers of ferroelectric perovskites based on a pertinent microscopic model. It is possible that critical properties of ultrathin perovskite layers might significantly deviate from the Landau behaviour, for example. exhibiting a Kosterlitz–Thouless (1973) like critical characteristic.

§ 5. Conclusions

In summary, a calculation of the dielectric behaviour of ferroelectric superlattices with inhomogeneous heterogeneity has been performed. On the basis of the spatial heterogeneity, we have derived both the overall dielectric response and the local polarization distributions. We consider that each localized layer has an Ising character and it can be described by the Ginzburg–Landau formalism at its own 'fixed

point'. We connect all these localized ultrathin polar layers, which have thickness-dependent phase transition points, to their neighbouring non-polar layers to describe the overall dielectric response of the entire superlattice system over a wide temperature region. The coherent coupling between different layers can lead to a huge enhancement of the dielectric properties in a broad temperature range. The overall dielectric response in the superlattice is controlled by the distribution of thicknesses of PZT of layers, that is the heterogeneity, as well as the associated coherent coupling effect. The spirit of our approach is akin to a kind of inhomogeneous renormalization procedure at mesoscopic scale. Based on this procedure, the DPT in this type of superlattice could be understood as a result of the inhomogeneous condensation of localized soft modes.

REFERENCES

ANDERSON, J. C., 1964, *Dielectrics* (London: Spottiswoode, Ballantyne & Co), p. 93.
AMIN, A., HAUN, M. J., BADGER, B., McKINSTRY, H. A., and CROSS, L. E., 1985, *Ferroelectrics*, **65**, 107.
BURNS, G., and BURSTEIN, E., 1973, *Ferroelectrics*, **7**, 297.
CHRISTEM, H.-M., BOATNER, L. A., BUDAI, J. D., CHISHOLM, J. D., GEA, L. A., MARRERO, P. J., and NORTON, D. P., 1996, *Appl. Phys. Lett.*, **68**, 1488.
CROSS, L. E., 1993, *Ferroelectric Ceramics*, edited by N. Setter and E. L. Colla (Basel: Birkhaus), p. 15.
GINZBURG, V. L., 1961, *Soviet Phys. Solid St.*, **2**, 1824; 1976, *Ferroelectrics*, **11**, 451; 1987a, *ibid.*, **73**, 171; 1987b, *ibid.*, **76**, 3.
HAUN, M. J., FURMAN, E., JANG, S. J., and CROSS, L. E., 1989, *Ferroelectrics*, **99**, 45.
HAYASHI, T., and TANAKA, T., 1995, *Jap. J. appl. Phys.*, **34**, 5100.
KANNO, I., HAYASHI, S., TAKAYAMA, R., and HIRAO, T., 1996, *Appl. Phys. Lett.*, **68**, 328.
KOSTERLITZ, J. M., and THOULESS, D. J., 1973, *J. Phys.* C, **6**, 1181.
KRETSCHMER, R., and BINDER, K., 1979, *Phys. Rev.* B, **20**, 1065.
LAWLESS, W. N., and MORROW, A. J., 1977, *Ferroelectrics*, **15**, 159.
MANTESE, J. V., SCHUBRING, N. W., MICHELI, A. L., and CATALAN, A. B., 1995, *Appl. Phys. Lett.*, **67**, 721.
MULLER, K. A., and BURKARD, H., 1979, *Phys. Rev.*, **19**, 3593.
SCHWENK, D., FISHMAN, F., and SCHWABL, F., 1990, *J. Phys.* C, **2**, 5409.
TILLEY, D. R., 1993, *Ferroelectric Ceramics*, edited by N. Setter and E. L. Colla (Basel: Birkhaus), p. 163.
TILLEY, D. R., and ZEKS, B., 1984, *Solid St. Commun.*, **49**, 823.
VOLGER, J., 1960, *Prog. Semiconduct.*, **4**, 207.
WANG, R. W., and MILLS, D. L., 1992, *Phys. Rev.* B, **46**, 11 681.
WIENER-AVNER, E., 1994, *Appl. Phys. Lett.*, **65**, 1784.